

UNIVERSITÄTSKLINIKUM HAMBURG-EPPENDORF

Institut für Entwicklungsneurophysiologie

Leiterin: Prof. Dr. Ileana L. Hanganu-Opatz

**Sparser and less efficient connectivity account
for developmental network dysfunction in a
mouse model of psychiatric disorders**

Dissertation

zur Erlangung des Doktorgrades PhD

an der Medizinischen Fakultät der Universität Hamburg

vorgelegt von:

Lingzhen Song
aus Shandong, China

Hamburg 2021

Angenommen von der

Medizinischen Fakultät der Universität Hamburg am: 06.12.2021

Veröffentlicht mit Genehmigung der

Medizinischen Fakultät der Universität Hamburg.

Prüfungsausschuss, der/die Vorsitzende: Prof. Dr. Ileana Hanganu-Opatz

Prüfungsausschuss, zweite/r Gutachter/in: Prof. Dr. Dietmar Kuhl

Prüfungsausschuss, dritte/r Gutachter/in: _____

1 Table of Contents

1 Table of Contents	3
2 Introduction	5
2.1 Oscillations and synchrony in the adult brain	5
2.2 Anatomical organization of lateral entorhinal-hippocampal-prefrontal (LEC-HP-PFC) network	8
2.3 Developmental origins of psychiatric disorders	10
2.3.1 Neurodevelopmental hypothesis	10
2.3.2 Genetic and environmental risk factors interplay in psychiatric disorders	11
2.4 HP-PFC network abnormalities as a hub for psychiatric disorders	12
2.5 Oscillatory activity in developing brain	14
2.6 Thesis overview and summary of results	16
3 Materials and Methods	19
3.1 Animals	19
3.2 Stereotaxic injections	19
3.3 <i>In utero</i> electroporation	20
3.4 Electrophysiological recordings and optogenetic manipulation <i>in vivo</i>	21
3.5 Electrophysiological recordings and optogenetic manipulation <i>in vitro</i>	22
3.6 Behavioral experiments	23
3.7 Histology and image analysis	26
3.8 Data Analysis	28
4 Articles	32
4.1 Article 1	32
4.2 Article 2	57
4.3 Article 3	77
4.4 Article 4	133
5 Discussion	196
5.1 Cellular substrates of functional LEC-HP-PFC network	196
5.2 LEC acts as an upstream region for the HP-PFC network	199
5.3 Excitation-inhibition imbalance in psychiatric disorders	201
5.4 Concluding remarks	203
6 General Summary	204
6.1 English summary	204
6.2 German summary	205
7 Bibliography	207

8 List of abbreviations.....	220
9 Acknowledgements	222
10 Curriculum Vitae	223
11 Eidesstattliche Versicherung	224

2 Introduction

The brain serves as center of the nervous system to control every process of our body by rapid and coordinated responses to environmental changes. From the fundamental aspect, brain can be treated as a biological computer: it acquires input from the surrounding world, stores it and processes it in various ways (Von Neumann, 1958; Bota et al., 2005). Neurons, as individual computational elements of brain structure and function, organize into infinite networks and give rise to coordinated and synchronized oscillatory activity (Buzsaki et al., 2012; Cox and Dean, 2014). Neural oscillations and synchronization support flexible and efficient information processing within and between cortical areas. Direct oscillatory coupling within brain networks is vital to performing high-order cognitive abilities (Buzsaki and Draguhn, 2004; Buzsáki and Watson, 2012) and has been extensively investigated in adults. More importantly, disturbances of brain oscillations are demonstrated across psychiatric diseases.

2.1 Oscillations and synchrony in the adult brain

Neural oscillations (nearly interchangeably with 'rhythms') impose a spatio-temporal structure on neural ensembles within and across networks. Information processing closely correlates with rhythmic activities that are represented as large-amplitude periodically fluctuating waves of local field potential (LFP) (Buzsaki et al., 2012). Brain rhythm does not reflect activity from an individual neuron but synchronous electric current of a population of neurons, thus is capable of carrying out complex cognitive operations (Colgin, 2016). The relevance exemplifies in hippocampus (HP), prefrontal cortex (PFC) and entorhinal cortex (EC).

The HP is required for several types of memory, where exhibits three major rhythm patterns correlated with different behavioral and cognitive states: theta (~4-12 Hz), gamma (~25-100 Hz) and sharp waves-ripples complexes (SPW-Rs, ~110-250 Hz ripples superimposed on ~1-10 Hz sharp waves (SPWs)) (Buzsáki et al., 1983). Theta rhythms occur during active exploration and rapid eye movement (REM) sleep (Vanderwolf, 1969; Buzsáki, 2002), while intermittent SPW-Rs emerge during slow-wave sleep, consummatory states or immobility (Buzsáki, 1986). Functionally, theta oscillations are believed to be critical for modulating synaptic strength and thereby for spatiotemporal coding of memory engrams (Buzsáki, 2002), and SPW-Rs for stabilizing and consolidating offline memories (Fernández-Ruiz et al., 2019).

Gamma oscillations, whose regularity is affected by theta and SPW-Rs, are faster waves with lower amplitude and are largest when theta rhythms are present (Bragin et al., 1995). There is less agreement about the functional significances of gamma rhythms, however, including memory retrieval (Colgin, 2016). A general principle of an oscillatory cycle is that temporally protracted recruitment of pyramidal neurons and terminated by the build-up of inhibition. Although theta waves are regularly observed in HP and other cortical regions, such as entorhinal cortex (EC), PFC and amygdala (Buzsáki, 2002), these structures cannot generate theta waves themselves. The medial septal (MS) interneurons that function as theta generators and pacemakers target interneurons in HP, rhythmically disinhibit hippocampal pyramidal cells, and thereby promote their theta rhythmic firing (Freund and Antal, 1988). Gamma activity can also be detected in HP, medial entorhinal cortex (MEC), PFC and other brain regions (Buzsaki and Wang, 2012). In intact brains, gamma oscillations are mainly generated by the interaction between pyramidal cells and interneurons. Much evidence indicate that HP interneurons drive slow gamma (~30-80 Hz), and MEC interneurons generate fast gamma (~60-100 Hz) (Lasztoczi and Klausberger, 2014; Schomburg et al., 2014). Moreover, interneuron spikes consistently phase lock to gamma oscillations, whereas pyramidal cell spikes do not (Buzsaki and Wang, 2012).

Each of those rhythms plays a unique role in coordinating interactions between HP and systems it communicates, e.g., PFC and lateral entorhinal cortex (LEC). Slow theta rhythms coordinate the activity across widespread on a relatively slow time scale. A theta cycle is undoubtedly capable of coordinating monosynaptic activations between two regions (~15 ms) and plausibly tolerates polysynaptic interactions as well. Coherent theta rhythms between PFC and HP and correlations between prefrontal spike times and hippocampal theta phase have been observed (Hartwich et al., 2009; Adhikari et al., 2010; Benchenane et al., 2010). Approximately 40% of PFC neurons are significantly phase-locked to hippocampal theta rhythms, which is reported to be associated with spatial navigation tasks and working memory (Siapas et al., 2005; Benchenane et al., 2010). It has been shown that PFC gamma power is modulated by hippocampal theta phase (Sirota et al., 2008; Adhikari et al., 2010), with localized gamma bursts transiently occurring at different PFC subregions. Another prominent example of this cross-frequency coupling that hippocampal theta oscillations enable is the entorhinal system (Bragin et al., 1995; Colgin et al., 2009).

Oscillatory coupling at ~20-40 Hz across CA1 and LEC activity and phase-locking of LEC and CA1 spikes to ~20-40 Hz oscillations are present and develop with odor-place association learning and memory retrieval (Igarashi et al., 2014). These interactions are likely to involve both theta and slow gamma, with slow gamma activating cell assemblies representing a particular memory within a given theta cycle (Colgin, 2015). Gamma oscillations in HP co-occur with theta rhythms and are coherent with fast gamma oscillations in MEC (Colgin et al., 2009) and low gamma oscillations in LEC (Takahashi et al., 2014), which facilitate retrieval of previously learned memories. PFC gamma oscillations may be coherent with that in both HP and EC. If so, coherent gamma oscillations in the entorhinal-hippocampal-prefrontal network could coordinate information flow across three areas during information processing related to external environment (Hafting et al., 2005). Hippocampal-neocortical information transfer happens during SPW-Rs. Sleep spindle activity and increased firing rate in PFC have occurred shortly following SPWs (Siapas and Wilson, 1998; Wierzynski et al., 2009). This mechanism plays a critical role in transferring transient memories from HP to neocortices for permanent storage, thus memory consolidation (Girardeau et al., 2009; Wierzynski et al., 2009; Maingret et al., 2016). The organization of neuronal assemblies in multiple-timescale allows for information processing and enables effective communication, which has been shown to correlate with memory performance in both animals and humans (Tort et al., 2009; Axmacher et al., 2010).

Deficits in temporal coordinating properties of neural oscillations are relevant to pathological processes of psychiatric diseases (Buzsáki and Watson, 2012). Reduced hippocampal theta phase-locking of PFC neurons and decreased theta coherence between HP and PFC are found in schizophrenia mice (Sigurdsson and Duvarci, 2015). Furthermore, reduced power of local gamma oscillations and reductions in low-frequency gamma coherence across hemispheres or other large anatomical distances have been reported in patients (Maharajh et al., 2010). Therefore, research is highly needed to understand consistently shared fundamental properties of brain networks, including basic connectivity principles, oscillatory activity and oscillation-related control of spiking.

2.2 Anatomical organization of lateral entorhinal-hippocampal-prefrontal (LEC-HP-PFC) network

Hippocampus (derived from the Greek word for seahorse) curls into an S-shaped structure on edge of the temporal lobe as an extension of cerebral cortex. Though HP lies subcortically, it is not considered a subcortical structure but a part of the limbic system (Anderson et al., 2006). It constitutes three subregions: cornu ammonis (CA), dentate gyrus (DG) and subiculum (Amaral and Witter, 1989). The CA can be distinguished by a layer of densely packed pyramidal neurons, consisting of subfields CA1, CA2, CA3 and CA4 in sequence along the distal-proximal direction (Amaral and Lavenex, 2006). CA1 serves as the main output region of HP, and CA2 receives input from entorhinal cortex (EC) via perforant path. CA3 ramifies extensively with local subregions within HP, e.g., receives projections from DG via Mossy fibers, sends axons to CA2 and CA1 via Schaffer collaterals (Witter, 2010). CA4 has usually named hilus or hilar region if considered as a part of DG. Neurons primarily receive inputs from granule cells in DG (Insausti and Amaral, 2004). Subiculum (Latin for support), which lies between EC and CA1 subfield, is the most inferior region of HP. It receives input from CA1 and EC and is another output region of HP (O'Mara et al., 2001). The HP is generally described as consisting of anterior (septal) and posterior (temporal) parts in humans or ventral and dorsal parts in rodents (Fanselow and Dong, 2010; Strange et al., 2014). The dorsal hippocampus (dHP) is primarily associated with spatial location and object-representation, while the intermediated-ventral hippocampus (i/vHP) is involved in context representation, emotion and stress regulation (Bannerman et al., 2004; Kjelstrup et al., 2008; Lee et al., 2017).

The PFC is most prominent in primates, especially humans, and plays critical roles in executive functions, such as working memory, decision making, language comprehension, attention maintenance, social and coordination of goal-directed behaviors (Miller and Cohen, 2001; Fuster and Bressler, 2015). Therefore, functions of PFC are the most crucial point of what we think of as "human" in cognition (Fuster, 2000). While these functions are not fully present in rodents, their PFC underlies most (Carlen, 2017). In rodents, medial PFC (mPFC) comprises anterior cingulate (ACC), prelimbic (PL) and infralimbic (IL) regions, while each has distinct connectivity and functional properties. The present thesis focuses on PL subregion, which roughly corresponds to dorsal anterior cingulate cortex (dACC) of humans (Laubach et al., 2018). The organization of PL laminar follows the same inside-out migration pattern as

other neocortical areas, which is early-born neurons forming deep layers (layer V/VI) and late-born neurons bypassing early-born neurons and locating in upper layers (layer II/III) (Nadarajah and Parnavelas, 2002). Layer II/III pyramidal neurons tend to fire in beta rhythm, facilitate the generation of beta oscillations and increase intra- (beta band) and interlayer (gamma band) synchrony (Bitzenhofer et al., 2017). However, stimulation of pyramidal neurons in layer V/VI activates the prelimbic network in all frequency bands and synchronizes solely deeper layers. In adult mice, besides interconnections between deep layers and upper layers (Cheriyian et al., 2016), pyramidal neurons within PL send branching projections to multiple long-range targets, such as contralateral PFC, mediodorsal (MD) and ventromedial (VM) thalamus, basolateral amygdala (BLA), contralateral and ipsilateral claustrum (CLA), contralateral and ipsilateral striatum (STR) and ventral tegmental area (VTA) (McGarry and Carter, 2017; Collins et al., 2018; Anastasiades et al., 2019). In the meantime, PL receives extensive reciprocal connections from most areas mentioned above and from HP. PL receives dense monosynaptic hippocampal projections but does not project back (Jay and Witter, 1991; Hoover and Vertes, 2007), making hippocampal-prefrontal (HP-PFC) connection an enthralling topic to investigate. Of note, differences in distribution and laminar organization of projecting neurons and axonal innervation patterns in PL exist as well (Gabbott et al., 2005; Anastasiades et al., 2019).

The EC is located in medial temporal lobe, defining the interface between the HP and neocortex (Witter et al., 2000). Functions of EC include being a widespread network hub for spatial and temporal memory, navigation, and integrating different sensory inputs into higher-order mnemonic representations (Eichenbaum et al., 2007; Montchal et al., 2019). In humans, EC has anterior-lateral and posterior-medial subregions defined by their cytoarchitectural and heterological features (Suzuki and Amaral, 1994; Witter et al., 2017). In rodents, related to its function and input-output connectivity, EC is usually divided into medial (MEC) and lateral (LEC) entorhinal cortex (Kerr et al., 2007). The MEC contains numerous head-direction and grid cells, whose activity is involved in spatial navigation and spatial memory (Hafting et al., 2005; Sargolini et al., 2006). In contrast, cells in LEC respond to item-related information and context-related locations, being critical for coding context and temporal information in associative recognition memory (Deshmukh and Knierim, 2011; Knierim et al., 2014). LEC is conceived as the critical area between hippocampal formation and various association domains of neocortex, including PFC (Canto et al., 2008). Neurons in layer

II/ III of LEC are significant sources of entorhinal projections to all subdivisions of HP, accompanied with the contribution of a small number of neurons in layers V and VI (Strange et al., 2014; Cappaert et al., 2015). In contrast, layer V neurons are the central origin of LEC projections to widespread cortical areas, such as perirhinal and parahippocampal cortices (Witter et al., 2000; Nilssen et al., 2019). Exceptions are entorhinal-prelimbic and entorhinal-olfactory projections, which appear to arise in layers II/III (Insausti et al., 1997; Witter et al., 2017). Regarding entorhinal afferents, it is clear that most show a dominant distribution confined to superficial layers I-III, such as olfactory projections from mitral cells in olfactory bulb (OB) (Xu and Wilson, 2012; Gretenkord et al., 2019). While inputs from HP, PFC, cingulate cortex (Cg) and retrosplenial cortex (RSC) show a striking preference for deep layers of LEC (Jones and Witter, 2007).

2.3 Developmental origins of psychiatric disorders

2.3.1 Neurodevelopmental hypothesis

Weinberger explicitly proposes the neurodevelopmental hypothesis for schizophrenia (Weinberger, 1987). This hypothesis is fueled by subsequent studies assessing participants from birth -be able to identify alterations much earlier- and show that poor cognitive performance related to later schizophrenia occur during early teens (at age 13, and possible at age 4 or 8) (Poulton et al., 2000; Reichenberg et al., 2010). In most patients, the formal onset of schizophrenia is preceded by a prodromal phase (a so-called at-risk mental state), symptoms and behaviors include attenuated positive, mood, cognitive symptoms and social withdrawal (McGlashan, 1996). In some instances, premorbid impairments in cognition can manifest many years before the first psychotic episode (Lieberman et al., 2001). The hypothesis is later confirmed in many other psychiatric disorders include ASD, intellectual disability, cerebral palsy and attention deficit hyperactivity disorder (ADHD) (American Psychiatric Association, 2013). Minor psychotic symptoms showed in early development can predict increased risk of adult psychosis and are dynamic and progressive decline with advancing age (Meier et al., 2014; Kahn, 2020).

The neurodevelopmental hypothesis also combines the view that critical process might be aberrant synaptic pruning, a process of synapse elimination, during adolescence (Feinberg, 1982; Sekar et al., 2016). Longitudinal neuroimaging studies have consistently reported a global increase in cortical volume, surface area and

thickness during development, typically peak in late childhood and decrease in adolescence (Wierenga et al., 2014; Tamnes et al., 2017). These dynamic changes of cortical morphometry have been linked to increasing synaptic pruning, which enables refinement of brain circuits and is critical in the pathology of psychiatric disorders (Prins et al., 2018; Sellgren et al., 2019). The neurodevelopmental hypothesis emphasizes the need for more remarkable integration studies among mental illnesses of all ages.

2.3.2 Genetic and environmental risk factors interplay in psychiatric disorders

Proximal events that trigger the onset of psychiatric disorders are not clear but seem to originate from disruption of brain development caused by genetic or environmental factors, or both (Owen et al., 2016). The HP-PFC interactions in at-risk individuals are either similar to patients (Benetti et al., 2009) or in intermediate between healthy controls and patients (Rasetti et al., 2011), which suggests that mental disorders have genetic bases that be directly inherited, or for *de novo* during development. Genome-wide association studies (GWAS) have detected many common genetic variants of small effect - primarily single nucleotide polymorphisms (SNPs), rare copy number variants (CNVs), single-nucleotide variants (SNVs), small insertions and deletions-associated with neurodevelopmental disorders (Grayton et al., 2012; Schizophrenia Working Group of the Psychiatric Genomics, 2014; Genovese et al., 2016; Rein and Yan, 2020). Of particular, there are no single causal "disease genes" *per se*, but rather many genetic variants contribute small increments of risk (Birnbaum and Weinberger, 2017). These related genes are involved in multiple developmental processes, affecting brain maturation and vulnerability to environmental effects.

Several environmental interactions, especially those directly affecting early brain development, e.g., gestational insults, maternal stress, maternal infections, nutritional deficiencies, are associated with the onset of schizophrenia (McGrath et al., 2010; Brown, 2012). The underlying mechanism is that a large number of molecular pathways for development and synaptic function maintenance, particularly those involving inflammatory processes and oxidative stress, are affected by several environmental factors (Owen et al., 2016). Maternal immune activation (MIA) animal models show that maternal infection elevates expression of cytokines, upregulates microglial markers and astrogliosis and reduces white matter myelination in newborn rodents (Bell and Hallenbeck, 2002; Paintlia et al., 2004; Rousset et al., 2006). Of particular, microglia (glial cells that mediate brain inflammation) involve in synaptic

maintenance and deterioration, particularly synaptic pruning in adolescence (Paolicelli et al., 2011; Ji et al., 2013). Furthermore, fast-spiking parvalbumin (PV) interneurons and myelination are particularly vulnerable to oxidative stress (Behrens et al., 2007; Cabungcal et al., 2014). Prenatal factors and prepubertal stressors have been found to interact cumulatively affect neurobiological and behavioral variables that model aspects of mental disorders (Giovanoli et al., 2013; Knuesel et al., 2014). Maternal infectious exposure is also associated with epilepsy, Alzheimer's, Parkinson's diseases, and to a lesser extent, cerebral palsy (Ribiani et al., 2007; Hirvonen et al., 2012; Krstic et al., 2012; Lema Tome et al., 2013). These findings provide a putative link between earlier immune disturbance and psychiatric pathogenesis.

Disrupted in schizophrenia 1 (Disc1) is perhaps the most widely known genetic cause of mental disorders and is identified in a Scottish family who had schizophrenia and subsequently other families in America (Millar et al., 2000; Sachs et al., 2005). The role of DISC1 in dendritic development and axonal development is well established (Morris et al., 2003; Kvajo et al., 2011), and mutations in Disc1 lead to alterations in neuronal architecture and cognition (Kvajo et al. 2008; Kvajo et al. 2011; Crabtree et al. 2017). These deficits are more prominent when additional environmental stressors disrupt the Disc1 locus, as shown by previous lab studies (Hartung et al., 2016b; Oberlander et al., 2019; Xu et al., 2019; Chini et al., 2020). The concept of gene-environment interactions, in its broadest sense, means that the effect of a genetic variant depends on one or more environmental factors and *vice versa* (Uher, 2014).

2.4 HP-PFC network abnormalities as a hub for psychiatric disorders

While different mental disorders such as schizophrenia, autism spectrum disorders (ASD) and depression manifest diverse clinical phenotypes and features, cognitive impairment emerges as a shared trait of their pathophysiology (Godsil et al., 2013). The common element of pathophysiology, disruption in the HP-PFC pathway, underlies overlap of cognitive symptoms among various psychiatric disorders (Godsil et al., 2013; Sigurdsson and Duvarci, 2015; Spellman et al., 2015). Using functional magnetic resonance imaging (fMRI) and electroencephalography (EEG), communication between HP and PFC is reported to be enhanced during working tasks (Bahner et al., 2015), fear extinction recall (Milad et al., 2007) and contextual information processing (Herweg et al., 2016). In rodents, investigations of the HP-PFC pathway has been studied intensively, including during spatial working memory (O'Neill

et al., 2013; Spellman et al., 2015), contextual information flow (Place et al., 2016), reward learning (Benchenane et al., 2010), anxiety and avoidance behavior (Adhikari et al., 2010; Padilla-Coreano et al., 2019). Of particular relevance is oscillations synchrony in theta range.

Studies of human patients and rodent disease models have revealed that abnormalities of the HP-PFC pathway manifest at different levels, ranging from large-scale brain network dysfunctions to anatomical abnormalities in local microcircuits. Aberrant HF-PFC functional synchrony during memory tasks is reported in ASD and schizophrenia patients and rodent models (Meyer-Lindenberg et al., 2005; Sigurdsson et al., 2010; Cooper et al., 2017; Phillips et al., 2019). Investigations measuring effective connectivity further reveal a decrease in HP influence over PFC in schizophrenia patients (Benetti et al., 2009). Moreover, anatomical and electrophysiological abnormalities exist in these two regions. Decreased neocortical and hippocampal volumes have been reported in individuals with schizophrenia, along with the potential progression of volumetric loss and ventricular enlargement throughout illness (Nelson et al., 1998; Yan et al., 2019). However, hippocampal volume significantly increased around birth in ASD patients and animal models (Barnea-Goraly et al., 2014; Cloarec et al., 2019). Reduced activation of dorsolateral PFC during cognitive tasks has also been revealed in patients with mental disorders (Minzenberg et al., 2009; Long et al., 2016). Postmortem studies show alterations in the structure and synaptic connectivity of excitatory and inhibitory neurons within PFC (Chao et al., 2010; Lazaro et al., 2019; Spratt et al., 2019). These deficits are not excluding the involvement of PV interneurons, which are believed to contribute to disrupted gamma oscillations and cognitive impairments (Buzsaki and Wang, 2012). Notably, structural abnormalities in fornix were observed (Zhou et al., 2008), the fiber bundle that connects HP with neocortical areas, including PFC. In addition, altered HP innervation patterns of mPFC neurons and increased synaptic strength contribute to aberrant HP-PFC signaling in ASD mice (Phillips et al., 2019). Another important observation is that hippocampal projections form fewer branches within PFC in a schizophrenia mouse model (Mukai et al., 2015), suggesting a possible anatomical basis for synchrony deficits between HP and PFC.

2.5 Oscillatory activity in developing brain

Brain development is a protracted process that begins with neurulation, proliferation, migration and differentiation during the embryonic period, then follows synaptogenesis, synaptic pruning, and myelination till late adolescence, arguably throughout lifespan (Stiles and Jernigan, 2010). Imaging intracellular calcium transients discovered electrical activity at early development (Blanton et al., 1990; Flint et al., 1999). The synchronous activity engages many neurons of developing networks shortly after reaching their final destination and forming synaptic contact with neighbors or other neurons in distant regions (Tau and Peterson, 2010).

In HP, three sequential patterns dominate early activity: spontaneous calcium spikes, synchronous plateau assemblies (SPAs) and giant depolarizing potentials (GDPs) from late embryonic stage to end of the first postnatal week (Crepel et al., 2007). At the early stage before synapse formation, calcium fluctuations exist uncorrelated. Soon the activity patterns shift from intrinsic voltage-gated calcium currents to large calcium plateaus mediated by gap junctions to widespread synapse-driven synchrony activities. Similar to HP, neuronal synchrony in the neocortex is low and spatially restricted at early stages. Soon after birth, it becomes more heterogeneous concerning electrographic patterns and underlying mechanisms (Garaschuk et al., 2000; Dupont et al., 2006; Blankenship and Feller, 2010). Moreover, the rapid transition from gap junction-mediated coupling to synaptic connections involves excitatory and inhibitory synapses (McCabe et al., 2007; Allene et al., 2008). Events that depend on glutamatergic and GABAergic transmission have been termed cortical early network oscillations (ENOs) and cortical GDP (cGDP). ENOs and cGDPs are sequentially expressed in immature neocortex since ENOs precede cGDPs (McCabe et al., 2007). These early activity transients ensure efficiency and fidelity of brain assembly via refining proliferation, migration and ion channel expression (Komuro and Rakic, 1996; Behuet et al., 2019), providing an initial landscape that reshapes subsequent oscillatory activity at later stages (Spitzer, 2006).

Oscillatory activity in the immature brain is characterized by its discontinuity of electrical activity, which means oscillatory bursts intermit with long periods of silence. These early transient bursts activity is named delta brushes in humans (Anderson et al., 1985) and spindle bursts in rodents (Khazipov et al., 2004). It has been suggested that ENOs and cGDPs represent "spindle bursts" and "long oscillations" in neocortex

in vivo, respectively (Allene et al., 2008; Yang et al., 2009), and GDPs represent early sharp-wave complex (eSPW) in HP *in vivo* (Leinekugel et al., 2002). These synchronized oscillatory activities are linked with activity-dependent synaptic modifications based on Hebbian learning rules, and more importantly, with subsequent experience (i.e., visual and sensory)-dependent "critical period" refinement (Feller and Scanziani, 2005). Oscillatory activity in brain smoothly evolves, becoming longer, faster, of higher power (Bitzenhofer et al., 2020), accompanied with massive synaptogenesis, synaptic pruning, and myelination, and in the end, be replaced by more elaborate behavioral-relevant continuous oscillations (Buzsaki and Draguhn, 2004; Bitzenhofer et al., 2020).

Different cortical regions have marked differences regarding cell layers organization, cell types, connectivity and developmental time course (Hanganu-Opatz, 2010; Kilb et al., 2011). Large-scale coherent calcium waves in immature EC start earlier than in HP (Garaschuk et al., 2000), suggesting that EC acts as an upstream region of HP. This process might be through direct synaptic connections already present before birth (Supèr and Soriano, 1994). Moreover, layer III neurons in developing EC spontaneously generate prolonged (2-20 s) intrinsic bursting activity that peaks around the end of the first postnatal week (Sheroziya et al., 2009). This early synchrony activity in EC might drive the emergence of burst activity in hippocampal CA1 (Karlsson et al., 2006; Hartung et al., 2016a; Valeeva et al., 2019). Bursts of oscillatory activity display shortly after birth in HP (Leinekugel et al., 2002; Brockmann et al., 2011), where diverse patterns of activity (eSPWs, theta and gamma oscillations, ripples) start to emerge during the first postnatal week (Sipilä et al., 2009; Mohs and Blumberg, 2010). Likewise, intrinsic bursting of CA3 pyramidal neurons may also shape hippocampal GDPs (Sipilä et al., 2005). Many cortical networks activities have capitulated to drive or shaping of HP (Griguoli and Cherubini, 2017). Among them, PFC is of particular interest. PFC seems to mature particularly late in parallel with other brain areas. Spindle bursts present at birth in somatosensory and visual cortex (Khazipov et al., 2004; Hartung et al., 2016a) and postnatal day (P) 3 in PFC (Brockmann et al., 2011). The oscillatory coupling within the HP-PFC network emerges during the first two postnatal weeks. Hippocampal discontinuous theta bursts drive oscillatory activity in PFC, and the communication peaks in beta-low gamma frequency band via a unidirectional monosynaptic pathway present in the first postnatal week (Brockmann et al., 2011; Hartung et al., 2016a). The intrinsic bursting activity

disappears during the third postnatal week, suggesting a selective contribution of this phenomenon to early cortical development (Sheroziya et al., 2009).

Developmental changes in construction and synchronous patterns of brain circuits are probably driving the ontogeny of learning and memory (Ngo et al., 2017; Keresztes et al., 2018). Recent studies have pointed out that early postnatal and adolescence period is of high vulnerability, whose disturbance ultimately leads to life-long consequences (Paus et al., 2008; Bitzenhofer et al., 2021).

2.6 Thesis overview and summary of results

Diminished HP-PFC coupling through synchrony of oscillatory activity and reduction of direct HP and PFC interactions have emerged at the first postnatal week in a mouse model of gene-environment interaction (dual-hit genetic-environmental (GE) mice) of combined both genetic (mutation of *Disc1* gene) and environmental (challenge by MIA) psychiatric risk factors (Hartung et al., 2016b; Xu et al., 2019; Chini et al., 2020), at a developmental stage corresponding to the third gestational trimester in humans (Clancy et al., 2001). Four mechanisms might cause these early deficits: (i) local disruption of prefrontal circuits, (ii) local disruption of hippocampal circuits, (iii) abnormal long-range communication between HP and PFC and (iv) abnormal regulation of their upstream networks, such as LEC. The first mechanism is confirmed by findings showing that layer II/III pyramidal neurons in PFC of GE mice experience excessive microglia-induced synaptic pruning, which leads to impaired beta-gamma oscillations and subsequent cognitive disabilities (Xu et al., 2019; Chini et al., 2020). The principal aim of the present thesis is to investigate physiological patterns characterizing early LEC-HP-PFC network oscillatory activity, their connectivity during development, their abnormalities under pathological conditions, how they relate to later cognitive deficits, and most importantly, cellular and synaptic mechanisms that underlie them. A vast array of techniques was performed to examine the LEC-HP-PFC network characteristics.

Characterization of cellular substrates involved in the emergence of early oscillatory synchrony between HP and PFC was first investigated during neonatal period (**Ahlbeck et al., 2018**). In order to meet this aim, *in vivo* electrophysiological recordings of either dHP or i/vHP and PFC combined with optogenetic stimulation were performed simultaneously to explore how communication properties vary along the hippocampal septo-temporal axis in P8-10 mice. It reveals differences in early

oscillatory patterns between dHP and i/vHP, which are dHP displaying higher LFP power and larger sharp-wave ripples. Conversely, i/vHP displays a stronger connection and communication with PFC. By optogenetic stimulating CA1 pyramidal neurons in i/vHP, but not dHP, 8 Hz elicited hippocampal oscillation is particularly effective in entraining prefrontal activity. Finally, it shows that gamma aminobutyric acid (GABA) exerts an inhibitory function in HP at the beginning of second postnatal week.

We next sought to further characterize early oscillatory activity patterns of HP in dual-hit GE mice and further identify cellular mechanisms behind it (**Xu et al., 2021**). Combined *in vivo* electrophysiological recordings, optogenetics, morphological and behavioral assessment were used to investigate immune-challenged mice with DISC1 knock-down either in the whole brain (GE) or restricted to hippocampal CA1 pyramidal neurons ($G_{HP}E$). The HP exhibits abnormal network activity, reduced SPWs and neuronal firing in CA1 at neonatal age in GE mice. Morphological deficits of CA1 neurons are shown, characterized by simplified dendritic arborization and reduced synaptic density. These functional and morphological disturbances are replicated in $G_{HP}E$ and persist until pre-juvenile age, complementing deficits in layer II/III of PFC. Moreover, optogenetic activating CA1 pyramidal neurons fail to activate local prefrontal circuits in GE and $G_{HP}E$. As a long-term consequence, DISC1 knock-down in HP leads to poorer recognition memory at pre-juvenile age. Therefore, DISC1-controlled developmental processes in HP in immune-challenged mice are critical for circuit function and cognitive behavior.

Furthermore, two studies aimed to investigate the long-range connectivity in the LEC-HP-PFC network throughout development and its deficits in dual-hit GE mice are presented (**Song et al., revision; Xu et al., revision**). *In vivo* electrophysiological recordings, *in vitro* patch-clamp recordings and optogenetics with in-depth tracing of projections were employed to examine morphology and function of hippocampal afferents in PFC throughout development (**Song et al., revision**). It reveals that projections from hippocampal CA1 area preferentially target layer 5/6 pyramidal neurons and interneurons and, to a lesser extent, layer 2/3 neurons of PL subdivision of PFC. In neonatal GE mice, sparser axonal projections from CA1 pyramidal neurons with abnormal excitability reach PL. Their short-term synaptic plasticity alters to the direction of more synaptic depression. Their ability in entraining layer 5/6 firing and oscillatory activity decreases. These structural and functional deficits persist yet are less prominent in pre-juvenile GE mice. Thus, besides local dysfunction of HP and PL,

sparser and less efficient connectivity between two brain areas is present in GE mice throughout development and might cause lifelong miswiring and ultimately cognitive disruption. The contribution of LEC, an upstream region of HP and PFC, to early dysfunction was investigated (*Xu et al., revision*). It shows that poorer LEC-involved recognition memory is detectable in GE mice at pre-juvenile age, preceded by abnormal communication within LEC-HP-PFC networks from neonatal age. The prominent entorhinal drive to HP is weaker in GE mice as a result of sparser projections from LEC to CA1 and decreased efficiency of axonal terminals to activate hippocampal circuits. In contrast, direct entorhinal drive to PFC is not affected in GE mice, yet PFC is compromised indirectly as a target of under-activated HP. Thus, already at neonatal age, the entorhinal-hippocampal circuit is impaired in a mouse model of psychiatric disease and further contributes to disruption of HP-PFC communication, which underlies long-term cognitive abnormalities.

3 Materials and Methods

3.1 Animals

All experiments were performed in compliance with German laws and guidelines of the European Community for using animals in research and were approved by the local ethical committee (G17/015, N18/015). Timed-pregnant mice from the University Medical Center Hamburg-Eppendorf animal facility were housed individually at a 12 h light/12 h dark cycle and were given access to water and food *ad libitum*. The day of vaginal plug detection was considered embryonic day (E) 0.5, the day of birth was considered P 0. The heterozygous offspring carrying a DISC1 allele (DISC1^{Tm1Kara}) on a C57BL/6J background, whose dams were injected at E9.5 with viral mimetic polyinosinic-polycytidylic acid (poly I:C, 4 mg/kg, i.p.), were classified as dual-hit genetic-environmental (GE) mice. Nontreated wildtype C57BL/6J mice and offspring of dams injected at E9 with saline (0.9%) were used as controls (CON) and combined, as no difference between the two groups was found. C57BL/6J mice with DISC1 knockdown confined to HP (G_{HP}E) were engineered through *in utero* electroporation (IUE) transfection with DISC1 shRNA (5'-GGCAAACACTGTGAAGTGC-3' under H1 promoter-driven pSuper plasmid) + pAAV-CAG-tDimer2 or DISC1 shRNA + pAAV-CAG-ChR2(ET/TC)-2A-tDimer2 at E15.5. All experiments were performed on pups of both sexes during neonatal development at P8–P10 and during pre-juvenile development at P20–P24.

3.2 Stereotaxic injections

Pups were placed in a stereotactic apparatus and kept under anesthesia with isoflurane (induction: 5%, maintenance: 2.5%). Fluorogold (FG, 2.5%) or biotinylated dextran amine (BDA, 5%) was injected iontophoretically into PFC (0.5 mm anterior to bregma, 0.3 mm right to the midline) or i/vHP (0.7 mm anterior to lambda, 2.3 mm right to the midline) of P7 or P21 mice. A glass capillary (~25 µm tip diameter) was filled with ~1 µl FG or ~1 µl BDA, and a silver wire was inserted into FG or BDA solution. Anodal current (6 s on/off, 6 mA) was applied for 10 min. In some anterograde tracing experiments, a total volume of 100 nl Alexa Fluor conjugated cholera toxin subunit B (CTB555, CTB488, 1%) was injected into PFC or i/vHP at a rate of 50 µl/min with a 10 µl syringe controlled by a microsyringe pump controller. For trans-synaptic labeling, 200 nl wheat germ agglutinin (WGA, 4%) was injected at a rate of 80 µl/min into i/vHP

(0.7 mm anterior to lambda, 2.3 mm right to the midline) or LEC (4 mm posterior to bregma, 6 mm right to the midline) with a 10 μ l syringe controlled by a pump. The capillary or syringe was lowered carefully into PFC (~1.9 mm dorsal from the dura) or i/vHP (~1.5 mm dorsal from dura) or LEC (~0.1 mm dorsal from dura). To locate innervated neurons in HP by LEC, mixed WGA and FG were used. For labeling hippocampal or entorhinal axons with opsins, the same procedure was used to inject AAV9-hSyn-hChR2(H134R)-EYFP (2.67×10^{13} GC/ μ l) virus or AAV9-CamKII-hChR2(H134R)-mCherry (3.17×10^{13} GC/ μ l) virus into HP or LEC (80 nl, 50 nl/min for P1 mice and 150 nl, 80 nl/min for P13-P15 mice). Following injection, the capillary or syringe was left in place for at least 5 min and withdrew slowly. The scalp was closed by tissue adhesive glue. Pups were warmed on a heating pad and returned to the dam until complete recovery of motor activity. Pups were perfused three days later for FG and BDA staining and 8-9 days later for recordings. The perfusion occurred 30 h after WGA injection, in line with literature that showed trans-synaptic transfer to the 1st order neurons (Phillips et al., 2019).

3.3 *In utero* electroporation

Timed-pregnant CON or GE mice (E15.5) were injected with buprenorphine (0.05 mg/kg body weight) subcutaneously 30 min before surgery. Surgery was performed under isoflurane anesthesia (induction: 5%, maintenance: 3.5%) on a heating blanket. The eyes of the dam were covered with eye ointment to prevent damage. The uterine horns were exposed and moistened with warm sterile phosphate buffered saline (PBS, 37°C). DNA solution containing 1.25 μ g/ μ l pAAV-CAG-tDimer2, pAAV-CAG-ChR2(ET/TC)-2A-tDimer2, or a mixture of DISC1 shRNA + pAAV-CAG-tDimer2 (molar ratio = 3:1) and 0.1% fast green dye at a volume of 0.75-1.25 μ l was injected into right lateral ventricle of embryos using glass capillaries. To target dHP, the embryo was placed between electroporation tweezer-type paddles (5 mm diameter) that were oriented at a 25° leftward angle from the midline and a 0° angle downward from anterior to posterior. To target i/vHP, a tri-polar approach was used (Szczerkowska et al., 2016). The embryo was placed between tweezer-type paddles (5 mm diameter, both positive poles), oriented at a 90° leftward angle from the midline and a 0° angle downward from anterior to posterior. A third custom built negative pole was positioned on top of the head roughly between eyes. Electrode pulses (30 V, 50 ms) were applied 6 times at an interval of 950 ms controlled by an electroporator. Uterine horns were placed back into the abdominal cavity after electroporation. The abdominal

cavity was filled with warm PBS, and abdominal muscles and skin were sutured with absorbable and non-absorbable suture thread, respectively. After recovery, dams were returned to their home cages, which were half placed on a heating blanket for two days, and received additional wet food supplemented with Metacam (0.5 mg/ml).

3.4 Electrophysiological recordings and optogenetic manipulation *in vivo*

Multisite extracellular recordings were performed in PL of PFC, dHP, i/vHP and/or LEC from P8-10 or P20-P24 mice. For recordings in awake P8-P10 mice, 0.5% bupivacaine / 1% lidocaine was applied locally on neck muscles. For recordings in anesthetized P20-P24 mice, mice were injected intraperitoneally with urethane (1 mg/g body weight) before surgery. Surgery was performed under isoflurane anesthesia (induction: 5%; maintenance: 2.5-3%). The bone over PFC (0.8 mm anterior to bregma, 0.1-0.5 mm right to the midline), dHP (2.0 mm posterior to bregma, 1.0 mm right to the midline), i/vHP (3.5-3.7 mm anterior to lambda, 3.5-3.8 mm right to the midline), LEC (4 mm posterior to bregma, 6 mm right to the midline) was removed carefully by drilling holes of 0.5 mm diameter. The head of the pup was fixed into a stereotaxic apparatus with two plastic bars mounted on nasal and occipital bones using dental cement. A four-shank optoelectrode with 4 × 4 recording sites (0.4-0.8 MΩ impedance, 0.1 mm spacing, 0.125 mm inter-shank spacing) was inserted into PL at a depth of 2.0 mm from the skull surface. A one-shank optoelectrode with 1 × 16 recordings sites (0.4-0.8 MΩ impedance, 50 μm spacing) was inserted into HP with a 20° angle. A one-shank optoelectrode with 1 × 16 recordings sites (0.4-0.8 MΩ impedance, 100 μm spacing) was inserted into LEC horizontally. One silver wire was inserted into the cerebellum to serve as ground and reference electrode. Before the signal acquisition, a recovery period of 15 min after electrode insertion was provided. Extracellular signals were band-pass filtered (0.1 Hz to 5 kHz) and digitized (32 kHz) with a multichannel extracellular amplifier and Cheetah acquisition software.

Pulsatile (laser on-off, 5 ms, 8 Hz, 3 s) or ramp (linearly increasing power, 3 s) light stimulations *in vivo* were performed with an Arduino uno controlled laser system (473 nm), which was coupled with a 50 μm (four-shank electrodes) or a 100 μm (one-shank electrodes) diameter light fiber. Each type of stimulation was repeated 60 times with an interval of 7 s. Laser power was measured and adjusted to a range of 0.75-2.5 mW at the fiber tip. The light fiber ended 200 μm above the top recording site aligned with each recording shank.

3.5 Electrophysiological recordings and optogenetic manipulation *in vitro*

For patch-clamp recordings, pups were anesthetized with 5% isoflurane and decapitated. Brains were rapidly removed and placed in ice-cooled oxygenated (95% O₂/5% CO₂) high-sucrose-based artificial cerebral spinal fluid (ACSF) containing (in mM): 228 sucrose, 2.5 KCl, 1 NaH₂PO₄, 26.2 NaHCO₃, 11 glucose and 7 MgSO₄ (310 mosmol/kg H₂O). Coronal brain slices (300 μm) were prepared using a vibratome. Slices were allowed to recover in oxygenated ACSF containing (in mM): 119 NaCl, 2.5 KCl, 1 NaH₂PO₄, 26.2 NaHCO₃, 11 glucose, 1.3 MgSO₄ (310 mOsmol/kg H₂O) at 33 °C for at least 30 min, then kept at room temperature (~22 °C) for another 60 min before recordings. Slices were transferred to the recording chamber and continuously perfused with oxygenated standard ACSF (2–3 ml/min) at room temperature.

Whole-cell recordings were made from neurons located in PL, CA1, or LEC. Two to three coronal slices were used per animal and chosen according to the coordinates (PL: 0.7-1.7 mm anterior to bregma; HP: 3.0-4.0 mm posterior to bregma; LEC: 4.0-5.0 mm posterior to bregma). Slices were visualized using an upright microscope and with infrared and differential interference contrast optics. All recordings were performed from pyramidal neurons identified according to their shape, spiking pattern and action potential width. Borosilicate glass patch pipettes (4-8 MΩ) were filled with K-gluconate-based solution containing (in mM): 130 K-gluconate, 10 HEPES, 0.5 EGTA, 4 Mg-ATP, 0.3 Na-GTP, 8 NaCl (285 mosmol/kg H₂O, pH adjusted to 7.4 with KOH) and 0.3%-0.5% biocytin for post hoc morphological identification of recorded cells. Recordings were performed with an EPC 10 amplifier and PatchMaster software v2x73.1, filtered at 2.9 kHz using a Bessel filter and sampled at 10 kHz. All potentials were corrected for the liquid junction potential of gluconate-based electrode solution (-8.65 mV at our measurement). The resting membrane potential (RMP) was measured immediately after obtaining the whole-cell configuration. 600 ms hyperpolarizing or depolarizing current pulses ranging from -100 pA to 120 pA in a 20 pA step were applied to calculate basic membrane properties. Under voltage-clamp conditions, access resistance (R_s) was monitored by analyzing capacitive transients during 5 ms-long depolarizing pulses. Recordings were included only when a GΩ seal formed before whole-cell access with R_s of less than 30 MΩ. Cells with R_s changes > 25% were excluded from further investigation.

For optogenetic stimulation *in vitro*, 470 nm light pulses were applied with a CoolLED system (pE-2) attached to an upright microscope. Maximal light output at 470 nm was measured at 10 mW/mm² with an optical power meter. For stimulation of hippocampal afferents in PL, light pulses (3 ms, 5 ms 10 ms, 15 s interval) were applied repetitively up to 10 times. For investigation of short-term synaptic plasticity, train pulses consisted of 2 s-long light pulses at 2 Hz, 4Hz, 8 Hz repeated every 15 s for up to 5 times. The evoked excitatory postsynaptic current (EPSC) and inhibitory postsynaptic current (IPSCs) were voltage-clamp recorded at -70 mV and +10 mV, respectively. To block AMPA/kainate receptors, 6-cyano-7-nitroquinoxaline-2, 3-dione (CNQX, 10 μ M) was added to the recording solution. For stimulation of entorhinal afferents in HP, the light was centered on stratum lacunosum-moleculare (SLM) region (~150-200 μ m below stratum pyramidale (SP)) and light pulses (10 ms, 15 s interval) were applied repetitively for up to 20 times. To block AMPA and NMDA receptors, 6-cyano-7-nitroquinoxaline-2, 3-dione (NBQX, 10 μ M), and amino-5-phosphonovaleric acid (AP5, 50 μ M) were added to the recording solution. Experiments of stimulating entorhinal afferents were voltage-clamp recorded at -65 mV.

3.6 Behavioral experiments

The exploratory behavior and recognition memory of CON, G_{HP}E and GE mice were tested at pre-juvenile age (P16-20) using previously established experimental protocols (Kruger et al., 2012). Briefly, all behavioral tests were conducted in a custom-made circular white arena, whose size (D: 34 cm, H: 30 cm) maximized exploratory behavior while minimizing incidental contact with testing objects (Heyser and Ferris, 2013). Objects used for testing novelty recognition were six differently shaped, textured and colored, easy to clean items provided with magnets to fix them to the bottom of the arena. Object sizes (H: 3 cm, diameter: 1.5-3 cm) were smaller than the twice size of a mouse and did not resemble living stimuli (no eyespots, predator shape). Objects were positioned at 10 cm from the borders and 8 cm from the center of the arena. After every trial, objects and the arena were cleaned with 0.1 % acetic acid to remove all odors. A black and white CCD camera was mounted 100 cm above the arena and connected to a PC via a PCI interface serving as frame grabber for Video Mot2 video tracking software.

Exploratory behavior in the open field (OF). Pre-juvenile mice (P16) habituated to the arena by freely exploring the arena for 10 min (two times) one day before the OF task.

The next day, mice (P16) were allowed to explore the testing arena for 10 minutes freely. Additionally, the floor area of the arena was digitally subdivided into 8 zones (4 center zones and 4 border zones) using the zone monitor mode of the VideoMot 2 analysis software. Time spent by pups in the center and border zones and running distance and velocity were quantified.

Novelty recognition paradigms. All protocols for assessing item recognition memory in P17 mice consisted of familiarization and testing trials (Ennaceur and Delacour, 1988). During familiarization trials in the novel object recognition (NOR) task, each mouse was placed into the arena containing two identical objects and released against the center of the opposite wall with the back to objects. After 10 min of free exploration of objects, the mouse was returned to a temporary holding cage. Subsequently, a test trial was performed after a delay of 5 min post-familiarization. Mice were allowed to investigate one familiar and one novel object with a different shape and texture for 5 min. Since some mice lost interest in achieving tasks even before investigation time, object interaction during the first 3 minutes was analyzed and compared between the groups. A discrimination ratio was calculated as $(\text{Time spent interacting with novel object} - \text{time spent interacting with familiar object}) / (\text{Time spent interacting with novel object} + \text{time spent interacting with familiar object})$.

Recency recognition (RR) task. Mice of P19-20 age experienced two 10 min-long familiarization trials with two different sets of identical objects that were separated by a delay of 30 min. The second familiarization trial was followed after 5 min by a test trial in which one object was used in the first and one object used in the second more recent familiarization trial were placed in the arena at same positions as during familiarization trials. Object interaction during the first 3 min was analyzed and compared between groups. All trials were video-tracked, and analysis was performed using Video Mot2 analysis software. The object recognition module of the software was used, and a 3-point tracking method identified the head, the rear end and the center of gravity of the mouse. Digitally, a circular zone of 1.5 cm was created around each object, and every entry of the head point into this area was considered object interaction. Climbing or sitting on the object, mirrored by the presence of both head and center of gravity points within the circular zone, were not counted as interactions. Discrimination ratios were calculated as $(\text{Time spent interacting with more recent object} - \text{time spent interacting with less recent object}) / (\text{Time spent interacting with more recent object} + \text{time spent interacting with less recent object})$.

Novel object preference (distinct objects) (NOPd) and object-location preference (OLP) tasks. All protocols for assessing associative recognition memory in P17 (NOPd) and P18 (OLP) mice consisted of familiarization and test trials. During the familiarization trial, each mouse was placed into the arena containing two different objects and released against the center of the opposite wall with the back to objects. After 10 min of free exploration of objects, the mouse was returned to a temporary holding cage. Subsequently, a test trial was performed after a delay of 5 min post-familiarization. In the NOPd task, mice were allowed to investigate one familiar and one novel object with a different shape and texture for 5 min. The nature of this test is similar to the novel object preference test, except that the test trial involves an association between two different objects (an association of object-object). In the OLP task, mice were allowed to investigate one familiar and a copy of the old object presented previously for 5 min. This test examines whether animals recognize the location once occupied by a particular object (an association of object-location). Object interaction during the first 4 min was analyzed and compared between groups. All trials were video-tracked and the analysis was performed using Video Mot2 analysis software. The object recognition module of the software was used, and a 3-point tracking method identified the head, the rear end and the center of gravity of the mouse. Digitally, a circular zone of 1.5 cm was created around each object, and every entry of the head point into this area was considered object interaction. Climbing or sitting on the object, mirrored by the presence of both head and center of gravity points within the circular zone, were not counted as interactions. Mouse with exploration distance in familiarization or test trials lower than (20 cm/min) was excluded. The object discrimination was computed for NOPd as $(\text{time at novel object} - \text{time at old object}) / \text{time at both objects}$ and for OLP as $(\text{time at displaced object} - \text{time at stationary object}) / \text{time at both objects}$.

Behavioral protocols for quantifying the cFos expression in mice doing NOPd or OLP task. P16 CON mice were divided randomly into 4 groups (n = 4 mice/group). Mice were allowed to freely explore the arena containing two different objects for 10 mins. This familiarization process continued for 3 days with 2 trials per day. On the third day (P18), 5 mins after the last familiarization trial, 3 mice from two groups were signed to perform the test trial (5 mins) of the NOPd task, whereas one mouse performs the familiarization trial. Similarly, for the other 2 groups, 3 mice were assigned to perform the test trial (5 mins) of the OLP task and one mouse to perform the familiarization trial. Mice were perfused ~90 min after the last behavioral trial.

3.7 Histology and image analysis

Perfusion and slicing. Briefly, P8–P10 and P20–P24 mice were anesthetized with 10% ketamine / 2% xylazine in 0.9% NaCl solution (10 µg/g body weight, *i.p.*) and transcardially perfused with Histofix containing 4% paraformaldehyde (PFA). Brains were postfixed with 4% PFA for 24 h and sectioned coronally at 100 µm for the reconstruction of the position of electrodes or 50 µm for further staining. Sections for staining were collected in three equally spaced series. To reduce the redundancy of information of neighbor slices, only one of three series was mounted or used for subsequent staining and analysis.

Immunohistochemistry. Free-floating slices were permeabilized and blocked with PBS containing 0.3% Triton X-100, 5% normal bovine serum. Subsequently, slices were incubated overnight with mouse monoclonal Alexa Fluor-488-conjugated antibody against NeuN, Alexa Fluor-488-conjugated streptavidin, or rabbit polyclonal primary antibody against DISC1, rabbit polyclonal primary antibody against GABA, polyclonal guinea-pig antibody against vGLUT1, rabbit polyclonal primary antibody against cFos, rabbit polyclonal primary antibody against lectin followed by 2 h incubation with Alexa Fluor-568 goat anti-rabbit secondary antibody, Alexa Fluor-568 goat anti-rabbit IgG secondary antibody, Alexa Fluor-568 goat anti-guinea pig, Alexa Fluor-568 goat anti-rabbit, biotinylated donkey anti-rabbit and Alexa Fluor-568-conjugated streptavidin. 4,6-diamidino-2-phenylindole (DAPI) was added to the second antibody for nuclear labeling. Finally, slices were transferred to glass slides and covered with Vecta-Shield. To avoid cross-reactivity between anti-lectin primary antibody and other antibodies, sections were firstly incubated with anti-lectin and then underwent subsequent biotinylation and streptavidin treatment steps. Following the last wash, sections were again blocked for 2 h.

Diaminobenzidine (DAB) staining. For BDA staining, sections (prepared as described above) were rinsed in PBS (0.125 M, pH 7.4-7.6) for 10 min, treated with peroxide solution (3% peroxide, 10% methanol in 0.125 M PBS) for 10 min to quench any endogenous peroxidases within tissue and rinsed again in PBS three times for 10 minutes each. Subsequently, sections were washed in PBS containing 0.5% Triton-X and incubated with avidin biotinylated enzyme complex for 90 min at room temperature or overnight at 4°C according to the manufacturer's instructions. After rinsing in Tris-HCl (pH 7.4), sections were incubated further with DAB working buffer at room

temperature for 2–10 min. After the signal was detected, all sections were rinsed with Tris-HCl, mounted on slides, dehydrated, cleared in xylenes, coverslipped and viewed with brightfield microscopy. In some cases, nuclear staining was necessary to aid the delineation of brain regions.

Imaging. Wide-field fluorescence was performed to reconstruct the position of the recording electrode in brain slices of investigated pups. Higher magnification images were acquired by confocal microscopy. Microscopic stacks were acquired as 2048×2048-pixel images (pixel size, 78 nm; Z-step, 500 nm) for quantification analysis.

Quantification of axonal density. For DAB staining, all bright-field images were obtained using a Zeiss imager M1 microscope with identical settings. Bright-field photomicrographs were imported into FIJI, and their contrast and brightness were adjusted. Axons were traced manually using FIJI. Area and layer borders were set by superimposing photomicrographs of BDA sections with another series of sections that processed for nuclear staining. For each experiment, one series of sections of HP was stained with streptavidin and DAPI, injection sites in HP were examined and the number of injected neurons was counted. Statistical tests were conducted on the density of axons ($\mu\text{m}/\text{mm}^2$) when normalized to the number of stained neurons in CA1 of HP, resulting in a unit of $\mu\text{m} / \text{mm}^2/\text{cell}$. For quantification of LEC axonal terminals labeled by mCherry, high magnification stacks were acquired by confocal microscopy from SLM of CA1. The intensity of the mCherry signal in slices from a similar coordinate was measured and compared between groups. All images were similarly processed and analyzed using ImageJ software.

Quantification of cFos and tracer labeled neurons. Photographs of relevant areas (LEC for cFos, CTB488, CTB555; HP for FG; PFC for WGA) were taken with a light microscope at a consistent light level. 3–4 slices per animal were used. Images were processed using FIJI software. The number of cFos positive neurons, CTB488 positive neurons, CTB555 positive neurons, FG-positive cells and WGA positive neurons were automatically quantified using custom-written algorithms in FIJI and confirmed manually. All cell number quantifications were carried out blind to experimental conditions.

Sholl analysis and spine density quantification. Sholl analysis and spine density quantification were carried out in the FIJI environment. For Sholl analysis, images were binarized (*auto threshold*), and dendrites were traced using the semi-automat

plugin *Simple Neurite Tracer*. The traced dendritic tree was analyzed with the plugin *Sholl Analysis* after the geometric center was identified using the *blow/lasso* tool. For spine density quantification, the length (*line*) and the number of spines (*point picker*) on the dendrite of interest (apical, basal, proximal oblique, or secondary apical) were quantified.

3.8 Data Analysis

Electrophysiological data were imported and analyzed offline using custom-written tools (<https://github.com/OpatzLab/HanganuOpatzToolbox>) in MATLAB software. Data were band-pass filtered (500–5000 Hz for spike analysis or 1–100 Hz for LFP) using a third-order Butterworth filter forward and backward to preserve phase information before down-sampling to 1000 Hz to analyze local field potential (LFP). For the analysis of hippocampal LFP, the recording site was located in the pyramidal layer where eSPWs reverse was selected. In PL, two medial shanks were located in layer II/III, whereas lateral shanks were located in layer V/VI. In LEC, the recording site that was 700 μm above the pyramidal layer of CA1 was selected.

Detection of neonatal oscillatory activity. Discontinuous oscillatory events were detected using a previously developed unsupervised algorithm (Cichon et al., 2014) and confirmed by visual inspection. Briefly, deflections of the root-mean-square of band-pass (3–100 Hz) filtered signals exceeding a variance-dependent threshold were assigned as network oscillations. The threshold was determined by a Gaussian fit to values ranging from 0 to the global maximum of the root-mean-square histogram. Only oscillatory events >1 s were considered for further analysis. Time-frequency plots were calculated by transforming the data using Morlet continuous wavelet.

Power spectral density. For power spectral density analysis, 1 s-long window of network oscillations was concatenated, and power was calculated using Welch's method with non-overlapping windows. For optical ramp stimulation, we compared the average power during the 1.5 s-long time window preceding stimulation to the last 1.5 s-long time window of light-evoked activity.

Single unit activity (SUA). SUA was detected and clustered using *klusta* and manually curated using *phy* (<https://github.com/cortex-lab/phy>). Data were imported and analyzed using custom-written tools in MATLAB.

Firing rate. The firing rate was computed by dividing the total number of spikes by the duration of the analyzed time window. For optical pulsatile stimulations, the modulation index (MI) of firing rate was calculated as $(\text{Firing}_{\text{during-stimulation}} - \text{Firing}_{\text{pre-stimulation}}) / (\text{Firing}_{\text{during-stimulation}} + \text{Firing}_{\text{pre-stimulation}})$.

Inter-spike-interval. ISI was calculated at 1 ms resolution in the range of 10-200 ms.

Spike-triggered LFP power. Spike-triggered LFP spectra were calculated as

$$(\text{Power}_{\text{spike}} - \text{Power}_{\text{baseline}}) / \text{Power}_{\text{baseline}}$$

where the spike-triggered power spectrum ($\text{Power}_{\text{spike}}$) was calculated using Welch's method for a 200 ms-long time window centered on each spike, and the power spectrum of baseline LFP ($\text{Power}_{\text{baseline}}$) was averaged for two-time windows, 100-300 ms and 200-400 ms before each spike.

Detection of SPWs in HP. The filtered signal (1-300 Hz) was subtracted from the signal recorded 100 μm above and 100 μm below SP. SPWs were detected as peaks above 5 times the standard deviation of the subtracted signal.

Phase locking value (PLV). PLV was developed to analyze the strength of phase synchronization. The analytic phase has a precise meaning only at a narrow frequency band. Therefore, we first filtered the signal into a narrow frequency band (bandwidth=1Hz, step=1Hz, for example, 1-2 Hz, 2-3 Hz, ...49-50 Hz) in a phase preserving manner. Then, we applied the Hilbert transform to extract the phase of two signals. PLV was defined as follows,

$$PLV = |\text{mean}(\exp(i * \Delta\phi_t))|$$

with $\Delta\phi_t$ stands for the phase difference between two signals at time point t. The value of PLV ranged between 0 (no synchrony) and 1 (max synchrony).

Spectral coherence. Coherence was calculated using the coherency method. Briefly, the coherence was calculated (using MATLAB build-in functions: *cpsd.m* and *pwelch.m*) by cross-spectral density between two signals and normalized by the power spectral density. The computation of the coherence over frequency (f) for the power spectral density P of signal X and Y was performed according to the formula:

$$C_{XY}(f) = \left| \left(\frac{P_{XY}(f)}{\sqrt{P_{XX}(f)P_{YY}(f)}} \right) \right|$$

Directionality methods. To investigate the directionality of functional connectivity between PFC and HP, generalized partial directed coherence (gPDC) was used. gPDC is based on a linear Granger causality measure in the frequency domain. The method attempts to describe the causal relationship between multivariate time series based on the decomposition of multivariate partial coherence computed from multivariate autoregressive models. The LFP signal was divided into 1s-long segments containing oscillatory activity. After de-noising using MATLAB wavelet toolbox, gPDC was calculated using a previously described algorithm (Baccalá and Sameshima, 2001).

Estimation of light propagation. The spatial pattern of light propagation *in vivo* was estimated using a previously developed model (Stujenske et al., 2015) based on Monte Carlo simulation (probe parameters: light fiber diameter: 50 μm , numerical aperture: 0.22, light parameters: 594 nm, 0.6 mW).

Pearson's correlation. For correlation between gPDC and NOR/RR, we computed Pearson's correlation using *corrplot.m* in MATLAB.

Generalized linear model (GLM). GLM was performed to predict the behavioral performance of animals in NOR and RR tasks by gPDC. Group comparisons were performed with GLM by including the factor of the group as a predictor variable.

Membrane properties. Analysis of data resulted from patch-clamp recordings was performed offline using custom-written scripts in MATLAB. For all recorded neurons, RMP, input resistance (R_{in}), membrane time constant (τ_m), membrane capacity (C_m), R_s , action potential amplitude, halfwidth and firing threshold were calculated. R_{in} was calculated according to Ohm's law by dividing resulting potential changes by the amplitude of applied current (-60 pA). τ_m was calculated by fitting a monoexponential function to the induced potential deflection. C_m was calculated by dividing τ_m by R_{in} . The firing threshold voltage was considered when depolarization speed first exceeded 10 mV/ms. Action potential amplitude was measured from threshold to peak, with half-width measured at half this distance. The firing rate was calculated during a 600 ms-long depolarization of cells by 80 pA current injection. Sag amplitude was calculated for each cell as the proportional difference between the initial voltage response (averaged for the first 200 ms) and the steady-state response (averaged for the last 100 ms) to a -100 pA hyperpolarizing current pulse.

Synaptic activity. Synaptic events were detected automatically on template parameters and examined manually to exclude false-positive events. Events were excluded if

amplitude was < 3 pA. Light-evoked EPSCs were averaged over 10-20 stimuli. Their peak amplitude and onset (i.e., the delay between light stimulus and the time point at which response speed exceeded 10 pA/ms) were calculated. The coefficient of variation (CV) for a given measured variable was defined as the ratio between the standard deviation and the average value of 10-20 individual responses to light stimulation.

Statistical analysis. Statistical analyses were performed in the MATLAB environment. Paired t-test or one-way analysis of variance (ANOVA) followed with Bonferroni-corrected post hoc analysis was performed to detect significant differences when the variance was normally distributed (Kolmogorov-Smirnov test). The effect of experimental groups and layers on spontaneous EPSC (sEPSC) properties was tested using two-way ANOVA followed by Bonferroni-corrected post hoc analysis. Investigators were blinded to the group allocation when quantifications of cFos expression, FG positive neurons in HP, CTB488 and CTB555 positive neurons in LEC and WGA positive neurons in PFC were performed. A Chi-square test was used to detect the significant difference between the two proportions. Values were considered outliers and removed when their distance from the 25th or 75th percentile exceeded 1.5 times the interquartile interval. Data are presented as mean \pm SEM. Significance levels of $p < 0.05$ (*), $p < 0.01$ (**) or $p < 0.001$ (***) were used.

4 Articles

4.1 Article 1

Glutamatergic drive along the septo-temporal axis of hippocampus boosts prelimbic oscillations in the neonatal mouse

Ahlbeck J¹, **Lingzhen Song**¹, Mattia Chini¹, Sebastian H Bitzenhofer¹, Ileana L Hanganu-Opatz¹

¹ Developmental Neurophysiology, Institute of Neuroanatomy, University Medical Center Hamburg-Eppendorf, 20251 Hamburg, Germany

eLife, 2018, 7:e33158, DOI: 10.7554/eLife.33158

Personal contribution

I carried out tracing experiments. I assisted with formal analysis. I discussed, reviewed and commented on the manuscript.

Glutamatergic drive along the septo-temporal axis of hippocampus boosts prelimbic oscillations in the neonatal mouse

Joachim Ahlbeck[†], Lingzhen Song, Mattia Chini, Sebastian H Bitzenhofer, Ileana L Hanganu-Opatz*

Developmental Neurophysiology, Institute of Neuroanatomy, University Medical Center Hamburg-Eppendorf, Hamburg, Germany

Abstract The long-range coupling within prefrontal-hippocampal networks that account for cognitive performance emerges early in life. The discontinuous hippocampal theta bursts have been proposed to drive the generation of neonatal prefrontal oscillations, yet the cellular substrate of these early interactions is still unresolved. Here, we selectively target optogenetic manipulation of glutamatergic projection neurons in the CA1 area of either dorsal or intermediate/ventral hippocampus at neonatal age to elucidate their contribution to the emergence of prefrontal oscillatory entrainment. We show that despite stronger theta and ripples power in dorsal hippocampus, the prefrontal cortex is mainly coupled with intermediate/ventral hippocampus by phase-locking of neuronal firing via dense direct axonal projections. Theta band-confined activation by light of pyramidal neurons in intermediate/ventral but not dorsal CA1 that were transfected by *in utero* electroporation with high-efficiency channelrhodopsin boosts prefrontal oscillations. Our data causally elucidate the cellular origin of the long-range coupling in the developing brain.

DOI: <https://doi.org/10.7554/eLife.33158.001>

*For correspondence:
hangop@zmnh.uni-hamburg.de

Present address: [†]Department of Neurophysiology and Pathophysiology, University Medical Center Hamburg-Eppendorf, Hamburg, Germany

Competing interests: The authors declare that no competing interests exist.

Funding: See page 20

Received: 27 October 2017

Accepted: 06 March 2018

Published: 10 April 2018

Reviewing editor: Marlene Bartos, University of Freiburg, Germany

© Copyright Ahlbeck et al. This article is distributed under the terms of the [Creative Commons Attribution License](https://creativecommons.org/licenses/by/4.0/), which permits unrestricted use and redistribution provided that the original author and source are credited.

Introduction

In the adult rodent brain, coordinated patterns of oscillatory activity code in a frequency-specific manner for sensory and cognitive performance. For example, learning and memory critically depend on oscillations within theta frequency band (4–12 Hz) that functionally couple the medial prefrontal cortex (PFC) and hippocampus (HP) (*Siapas and Wilson, 1998; Benchenane et al., 2010; Brincat and Miller, 2015; Backus et al., 2016; Eichenbaum, 2017; Wirt and Hyman, 2017*). These frequency-tuned brain states are present already during early development, long before the memory and attentional abilities have fully matured. They have been extensively characterized and categorized according to their spatial and temporal structure (*Lindemann et al., 2016*). Network oscillations during development have a highly discontinuous and fragmented structure with bursts of activity alternating with ‘silent’ periods (*Hanganu et al., 2006; Seelke and Blumberg, 2010; Shen and Colonnese, 2016; Luhmann and Khazipov, 2018*). The most common oscillatory pattern, spindle bursts, synchronizes large cortical and subcortical networks within theta-alpha frequency range. It is accompanied by slow delta waves as well as by faster discharges (beta and gamma oscillations) that account for local activation of circuits (*Brockmann et al., 2011; Yang et al., 2016*).

In the absence of direct behavioral correlates, a mechanistic understanding of oscillatory rhythms in the developing brain is currently lacking. In sensory systems, spindle bursts have been proposed to act as a template facilitating the formation of cortical maps (*Dupont et al., 2006; Hanganu et al., 2006; Tolner et al., 2012*), whereas early gamma oscillations seem to control the organization of

eLife digest When memories are stored, or mental tasks performed, different parts of the brain need to communicate with each other to process and extract information from the environment. For example, the communication between two brain areas called the hippocampus and the prefrontal cortex is essential for memory and attention. However, it is still unclear how these interactions are established when the brain develops.

Now, by looking at how the hippocampus and the prefrontal cortex 'work' together in newborn mouse pups, Ahlbeck et al. hope to understand how these brain areas start to connect. In particular, the groups of neurons that kick start the development of the circuits required for information processing need to be identified.

Recording the brains of the pups revealed that electrical activity in a particular sub-division of the hippocampus activated neurons in the prefrontal cortex. In fact, a specific population of neurons in this area was needed for the circuits in the prefrontal cortex to mature.

In further experiments, the neurons from this population in the hippocampus were manipulated so they could be artificially activated in the brain using light. When stimulated, these neurons generated electrical activity, which was then relayed through the neurons all the way to the prefrontal cortex. There, this signal triggered local neuronal circuits. Thanks to this activation, these circuits could 'wire' together, and start establishing the connections necessary for mental tasks or memory in adulthood.

The brain of the mouse pups used by Ahlbeck et al. was approximately in the same developmental state as the brain of human fetuses in the second or third trimester of pregnancy. These findings may therefore inform on how the hippocampus and the prefrontal cortex start connecting in humans. Problems in the way brain areas interact during early development could be partly responsible for certain neurodevelopmental disorders and mental illnesses, such as schizophrenia. Understanding these processes at the cellular level may therefore be the first step towards finding potential targets for treatment.

DOI: <https://doi.org/10.7554/eLife.33158.002>

thalamocortical topography (Minlebaev et al., 2011; Khazipov et al., 2013). In limbic systems dedicated to mnemonic and executive abilities, the knowledge on the relevance of early network oscillations is even sparser. Few lesion studies, yet without selectivity for specific activity patterns, suggested that prefrontal-hippocampal communication during development might be necessary for the maturation of episodic memory (Krüger et al., 2012). Temporal associations between the firing and synaptic discharges of individual neurons and network oscillations in different frequency bands gave first insights into the cellular substrate of coordinated activity in neonates. Whereas in sensory systems, endogenous activation of sensory periphery drives entrainment of local circuitry through gap junction coupling as well as glutamatergic and GABAergic transmission (Dupont et al., 2006; Hanganu et al., 2006; Minlebaev et al., 2009), in developing prefrontal-hippocampal networks, the excitatory drive from the HP has been proposed to activate a complex layer- and frequency-specific interplay in the PFC (Brockmann et al., 2011; Bitzenhofer and Hanganu-Opatz, 2014; Bitzenhofer et al., 2015).

While most of this correlative evidence put forward the relevance of early oscillations beyond a simple epiphenomenal signature of developing networks, direct evidence for their causal contribution to circuit maturation is still missing. This is mainly due to the absence of a causal interrogation of developing networks, similarly to the investigations done in adult ones. Only recently the methodological difficulties related to area-, layer- and cell type-specific manipulations at neonatal age have been overcome (Bitzenhofer et al., 2017a; Bitzenhofer et al., 2017b). By these means, the local neuronal interplay generating beta-gamma oscillations in the PFC has been elucidated. However, the long-range coupling causing the activation of local prefrontal circuits is still unresolved. We previously proposed that the hippocampal CA1 area drives the oscillatory entrainment of PFC at neonatal age (Brockmann et al., 2011). Here, we developed a methodological approach to optically manipulate the neonatal HP along its septo-temporal axis. We provide causal evidence that theta frequency-specific activation of pyramidal neurons in the CA1 area of intermediate and ventral (i/

vHP), but not of dorsal HP (dHP) elicits broad band oscillations in the PFC of neonatal mice via dense axonal projections.

Results

Neonatal dorsal and intermediate/ventral hippocampus are differently entrained in discontinuous patterns of oscillatory activity

While different organization and function of dHP vs. i/vHP of adults have been extensively characterized (Thompson *et al.*, 2008; Dong *et al.*, 2009; Patel *et al.*, 2013), their patterns of structural and functional maturation are still poorly understood. To fill this knowledge gap, we firstly examined the network oscillatory and firing activity of CA1 area of either dHP or i/vHP by performing extracellular recordings of the local field potential (LFP) and multiple unit activity (MUA) in neonatal [postnatal day (P) 8–10] non-anesthetized and urethane-anesthetized mice ($n = 153$). While urethane anesthesia led to an overall decrease of amplitude and power of oscillatory activity when compared to the non-anesthetized state of the same group of pups, the firing rate and timing as well as the synchrony and interactions within prefrontal-hippocampal networks were similar during both states (Figure 1—figure supplement 1). Due to the close proximity and the absence of reliable anatomical and functional borders between iHP and vHP at neonatal age, data from the two areas were pooled and referred as from i/vHP. The entire investigation was performed at the age of initiation of coupling between HP and PFC, that is, P8–10 (Brockmann *et al.*, 2011). Independent of the position along the dorsal-ventral axis, the CA1 area was characterized by discontinuous oscillations with main frequency in theta band (4–12 Hz) and irregular low amplitude beta-gamma band components, which have been previously categorized as theta oscillations (Brockmann *et al.*, 2011). They were accompanied by prominent sharp-waves (SPWs) reversing across the pyramidal layer (str. pyr.) and by strong MUA discharge (Figure 1A and E). While the general patterns of activity were similar in dHP and i/vHP, their properties significantly differed between the sub-divisions. The theta bursts in i/vHP had significantly higher occurrence (i/vHP: 8.1 ± 0.2 oscillations/min, $n = 103$ mice vs. dHP: 5.2 ± 0.3 oscillations/min, $n = 41$ mice; $p < 0.001$), larger amplitude (i/vHP: 110.6 ± 5.6 μ V vs. dHP: 92.9 ± 2.6 μ V; $p = 0.015$), and shorter duration (i/vHP: 3.5 ± 0.1 s vs. dHP: 4.3 ± 0.1 s, $p < 0.001$) when compared with dHP (Figure 1B, Figure 1—figure supplement 2A). Investigation of the spectral composition of theta bursts revealed significant differences within theta band with a stronger activation of dHP (relative power: dHP: 13.0 ± 1.3 , $n = 41$ mice; i/vHP: 10.3 ± 0.5 , $n = 103$ mice; $p = 0.026$), whereas the faster frequency components were similar along the septo-temporal axis (relative power: 12–30 Hz: dHP, 15.0 ± 1.6 , $n = 41$ mice; i/vHP, 13.2 ± 0.7 , $n = 103$ mice, $p = 0.22$; 30–100 Hz: dHP, 6.3 ± 0.6 , $n = 41$ mice; i/vHP: 5.2 ± 0.3 , $n = 103$ mice; $p = 0.073$) (Figure 1C, Figure 1—figure supplement 2B).

Differences along the septo-temporal axis were detected both in hippocampal spiking and population events SPWs. Overall, pyramidal neurons in i/vHP fired at higher rates (0.45 ± 0.01 Hz, $n = 557$ units from 103 mice) than in the dHP (0.35 ± 0.02 Hz, $n = 158$ units from 41 mice; $p = 0.025$) (Figure 1D). SPW in neonatal HP were more prominent in the dHP (712.8 ± 31.5 μ V, $n = 41$ mice) when compared with those occurring in the i/vHP (223.8 ± 6.3 μ V, $n = 103$ mice, $p < 0.001$), yet their occurrence increased along the septo-temporal axis (dHP: 6.6 ± 0.5 , $n = 41$ mice; i/vHP: 8.6 ± 0.2 , $n = 103$ mice, $p < 0.001$) (Figure 1E and F, Figure 1—figure supplement 2D). In line with our previous results (Brockmann *et al.*, 2011), SPWs were accompanied by prominent firing centered around the SPW peak (dHP, 232 units; i/vHP, 670 units) that were phase-locked to hippocampal ripples (Figure 1—figure supplement 2C). The power of ripples decreased along the septo-temporal axis (relative power: dHP, 24.4 ± 3.3 , $n = 41$ mice; i/vHP, 6.1 ± 0.60 , $n = 103$ mice, $p < 0.001$) (Figure 1G,H). Similarly, the ripple-related spiking was stronger in dHP when compared with i/vHP (peak firing: dHP: 1.13 ± 0.09 Hz, $n = 232$ units; i/vHP 0.84 ± 0.03 , $n = 670$, $p < 0.001$) (Figure 1I and J).

These data show that the activity patterns in the dorsal and intermediate/ventral CA1 area differ in their properties and spectral structure.

Theta activity within dorsal and intermediate/ventral hippocampus differently entrains the neonatal prelimbic cortex

The different properties of network and neuronal activity in dHP vs. i/vHP led us to question their outcome for the long-range coupling in the developing brain. Past studies identified tight

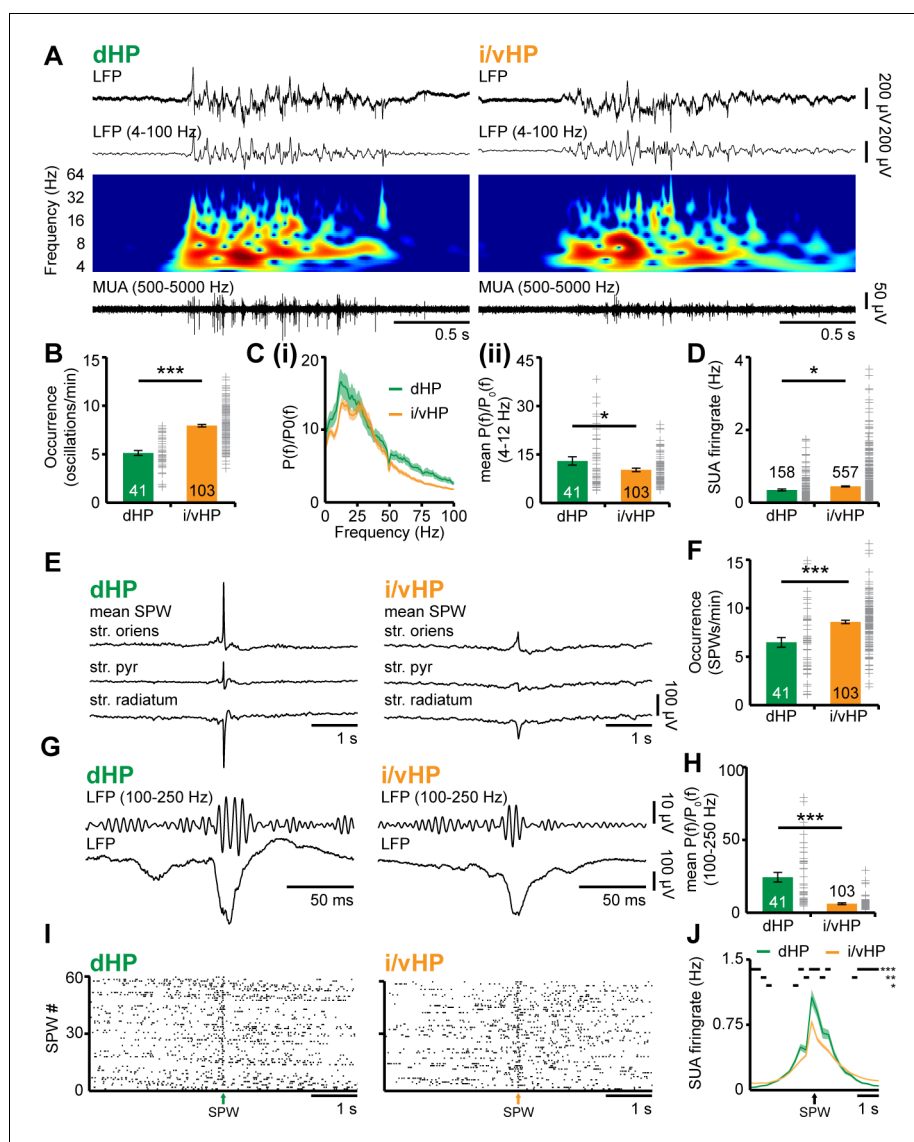


Figure 1. Patterns of discontinuous oscillatory activity in the CA1 area of the neonatal dHP and i/vHP in vivo. (A) Characteristic theta burst activity recorded in the CA1 area of the dHP (left) and i/vHP (right) of a P9 mouse displayed after band-pass filtering (4–100 Hz) and the corresponding MUA (500–5000 Hz). Color-coded frequency plots show the wavelet spectrum of LFP at identical time scale. (B) Bar diagram (mean \pm SEM) displaying the occurrence of discontinuous theta bursts in dHP ($n = 41$ mice) and i/vHP ($n = 103$ mice). (C) Power analysis of discontinuous oscillatory activity $P(f)$ normalized to the non-oscillatory period $P_0(f)$ in dHP and i/vHP. (i) Power spectra (4–100 Hz) averaged for all investigated mice. (ii) Bar diagrams quantifying the mean power within theta frequency band (4–12 Hz) in dHP ($n = 41$ mice) and i/vHP ($n = 103$ mice) (D) Bar diagram displaying the SUA of dHP ($n = 158$ units) and i/vHP ($n = 557$ units) after clustering of spike shapes. (E) Characteristic SPWs and ripple events recorded in dHP (left) and i/vHP (right). (F) Bar diagrams (mean \pm SEM) displaying the SPWs occurrence in dHP and i/vHP. (G) Characteristic SPW-ripple events recorded in dHP (left) and i/vHP (right). (H) Bar diagram displaying the mean power of ripples in dHP and i/vHP. (I) Spike trains from neurons in dHP (left) and i/vHP (right) aligned to SPWs. (J) Histograms of SUA aligned to SPWs ($n = 232$ units for dHP, $n = 670$ for i/vHP). Data are represented as mean \pm SEM. * $p < 0.05$, ** $p < 0.01$, *** $p < 0.001$.

DOI: <https://doi.org/10.7554/eLife.33158.003>

The following figure supplements are available for figure 1:

Figure supplement 1. Properties of network and neuronal activity in i/vHP of neonatal non-anesthetized and urethane-anesthetized mice.

DOI: <https://doi.org/10.7554/eLife.33158.004>

Figure supplement 2. Properties of network and neuronal activity in dHP vs. i/vHP of neonatal mice.

Figure 1 continued on next page

Figure 1 continued

DOI: <https://doi.org/10.7554/eLife.33158.005>

interactions between HP and PFC, which emerge already at neonatal age (Brockmann et al., 2011; Hartung et al., 2016) and are in support of memory at adulthood (Krüger et al., 2012; Spellman et al., 2015; Place et al., 2016). The discontinuous theta oscillations in HP have been proposed to drive the activation of local circuits in the PFC. To assess the coupling of dHP and i/vHP with PFC, we recorded simultaneously LFP and MUA in the corresponding hippocampal CA1 area and the prelimbic subdivision (PL) of the PFC of P8-10 mice. The entire investigation focused on PL, since in adults it is the prefrontal subdivision with the most dense innervation from HP (Jay and Witter, 1991; Vertes et al., 2007). In a first step, we examined the temporal correspondence of discontinuous oscillations recorded simultaneously in the PL and dHP, as well as in the PL and i/vHP. We previously characterized the network activity in the PL and showed that spindle-shaped oscillations switching between theta (4–12 Hz) and beta-gamma (12–40 Hz) frequency components alternate with periods of silence (Brockmann et al., 2011; Cichon et al., 2014; Bitzenhofer et al., 2015). The majority of prelimbic and hippocampal oscillations co-occurred within a narrow time window (Figure 2A). The temporal synchrony between prelimbic and hippocampal oscillations was assessed by performing spectral coherence analysis (Figure 2B). The results revealed a stronger coupling for PL-i/vHP (4–12 Hz: 0.17 ± 0.0069 ; 12–30 Hz: 0.31 ± 0.011 ; 30–100 Hz: 0.11 ± 0.0069 , $n = 103$ mice) when compared with PL-dHP (4–12 Hz: 0.12 ± 0.0081 ; 12–30 Hz: 0.18 ± 0.0094 ; 30–100 Hz: 0.084 ± 0.004 , $n = 41$ mice). In line with previous investigations, this level of coherence is a genuine feature of investigated neonatal networks and not the result of non-specific and conduction synchrony, since we considered only the imaginary component of the coherence spectrum, which excludes zero time-lag synchronization (Nolte et al., 2004).

Due to the symmetric interdependence of coherence, it does not offer reliable insights into the information flow between two brain areas. Therefore, in a second step, we estimated the strength of directed interactions between PL and HP by calculating the generalized partial directed coherence (gPDC) (Baccala et al., 2007; Rodrigues and Baccala, 2016) (Figure 2C). The method bases on the notion of Granger causality (Granger, 1980) and avoids distorted connectivity results due to different scaling of data in HP and PL (Baccala et al., 2007; Taxidis et al., 2010). Independent of the position along the septo-temporal axis, the information flow in theta or beta frequency band from either dorsal or intermediate/ventral HP to PL was significantly stronger than in the opposite direction. However, mean gPDC values for i/vHP \rightarrow PL were significantly ($p < 0.001$) higher (0.069 ± 0.003 , $n = 103$ mice) when compared with those for dHP \rightarrow PL (0.053 ± 0.003 , $n = 41$ mice). Cross-correlation analysis confirmed these results (Figure 2—figure supplement 1). The stronger information flow from i/vHP to PL was confined to theta frequency range and was not detected for 12–30 Hz frequencies (i/vHP \rightarrow PL: 0.048 ± 0.001 ; dHP \rightarrow PL: 0.043 ± 0.002 , $p = 0.16$). Correspondingly, the firing of individual prelimbic neurons was precisely timed by the phase of oscillations in i/vHP but not dHP (Figure 2D). Almost 20% of clustered units (52 out of 310 units) were locked to theta phase in i/vHP, whereas only 6.5% of units (3 out of 46 units) were timed by dHP. The low number of locked cells in dHP precluded the comparison of coupling strength between the two hippocampal sub-divisions.

These results indicate that the distinct activity patterns in dHP and i/vHP at neonatal age have different outcomes in their coupling with the PL. Despite higher power, theta oscillations in dHP do not substantially account for prelimbic activity. In contrast, i/vHP seems to drive neuronal firing and network entrainment in the PL.

SPWs-mediated output of intermediate/ventral but not dorsal hippocampus times network oscillations and spiking response in the neonatal prelimbic cortex

Since SPWs and ripples in dHP significantly differ from those in i/vHP, they might have a distinct impact on the developing PFC. While abundant literature documented the contribution of SPW-spindles complex to memory-relevant processing in downstream targets, such as PFC (Colgin, 2011; Buzsáki, 2015; Colgin, 2016), it is unknown how these complexes affect the development of cortical activation. Simultaneous recordings from neonatal CA1 area either in dHP or i/vHP and PL showed

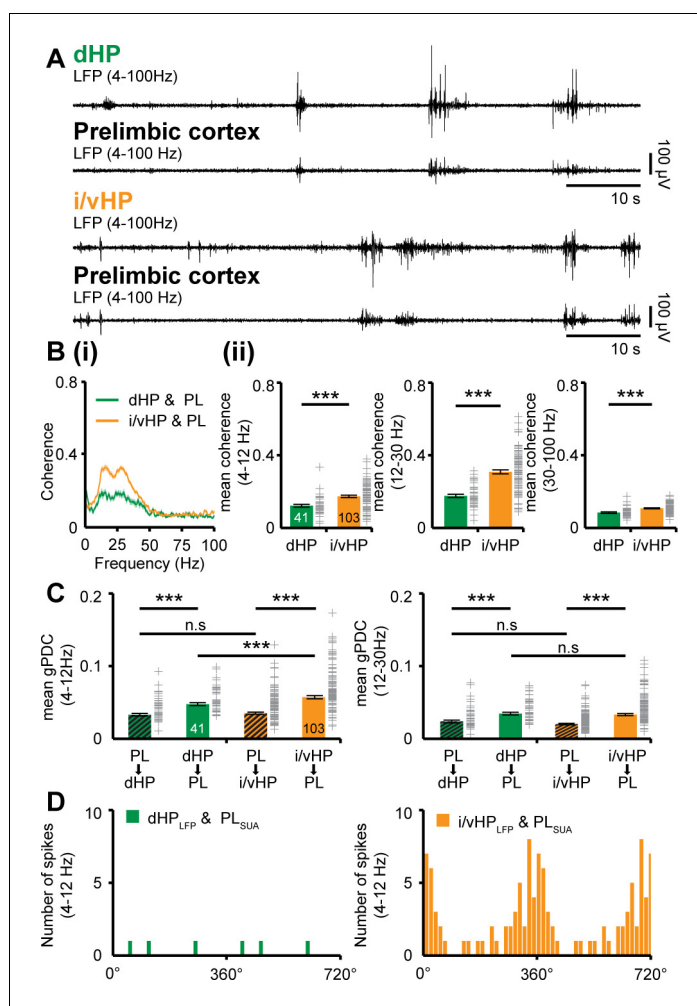


Figure 2. Dynamic coupling of hippocampal and prefrontal oscillatory activity along septo-temporal axis during neonatal development. (A) Simultaneous LFP recordings of discontinuous oscillatory activity in dHP and PL (top) and i/vHP and PL (bottom). (B) Long-range synchrony within prefrontal-hippocampal networks. (i) Average coherence spectra for simultaneously recorded oscillatory events in dHP and PL as well as i/vHP and PL. (ii) Bar diagrams (mean \pm SEM) displaying the coherence in theta (4–12 Hz), beta (12–30 Hz), and gamma (30–100 Hz) band when averaged for all investigated mice. (C) Directed interactions between PL and either dHP or i/vHP monitored by general Partial Directed Coherence (gPDC). Bar diagrams displaying the gPDC calculated for theta (4–12 Hz, left) and beta (12–30 Hz, right) frequency and averaged for all investigated animals ($n = 41$ mice for dHP and PL, $n = 103$ mice for i/vHP and PL). (D) Histograms displaying the phase-locking of prelimbic spikes to theta oscillations in dHP (left) and i/vHP (right). Note the different proportion of spikes significantly locked along the septo-temporal axis (dHP, 3 of 46 units; i/vHP, 52 of 310 units). Data are represented as mean \pm SEM. * $p < 0.05$, *** $p < 0.001$.

DOI: <https://doi.org/10.7554/eLife.33158.006>

The following figure supplement is available for figure 2:

Figure supplement 1. Cross-correlation of the amplitudes of band pass (4–12 Hz)-filtered LFP recorded from dHP and PL (green) as well as from i/vHP and PL (orange).

DOI: <https://doi.org/10.7554/eLife.33158.007>

that already at neonatal age, prefrontal oscillations are generated shortly (~ 100 ms) after hippocampal SPWs-ripples. This prelimbic activation is significantly stronger when induced by SPWs-ripples emerging in i/vHP than in dHP as reflected by the significantly higher power of oscillatory activity in theta (PL for dHP: $186.9 \pm 12.5 \mu\text{V}^2$; PL for i/vHP: $249.5 \pm 14.5 \mu\text{V}^2$, $p = 0.0088$), beta (PL for dHP: $34.3 \pm 3.3 \mu\text{V}^2$; PL for i/vHP: $48.1 \pm 2.8 \mu\text{V}^2$, $p = 0.0049$), and gamma (PL for dHP: $11.3 \pm 0.9 \mu\text{V}^2$; PL for i/vHP: $17.4 \pm 1.2 \mu\text{V}^2$, $p = 0.0026$) frequency band (Figure 3A). The SPWs-ripple-induced

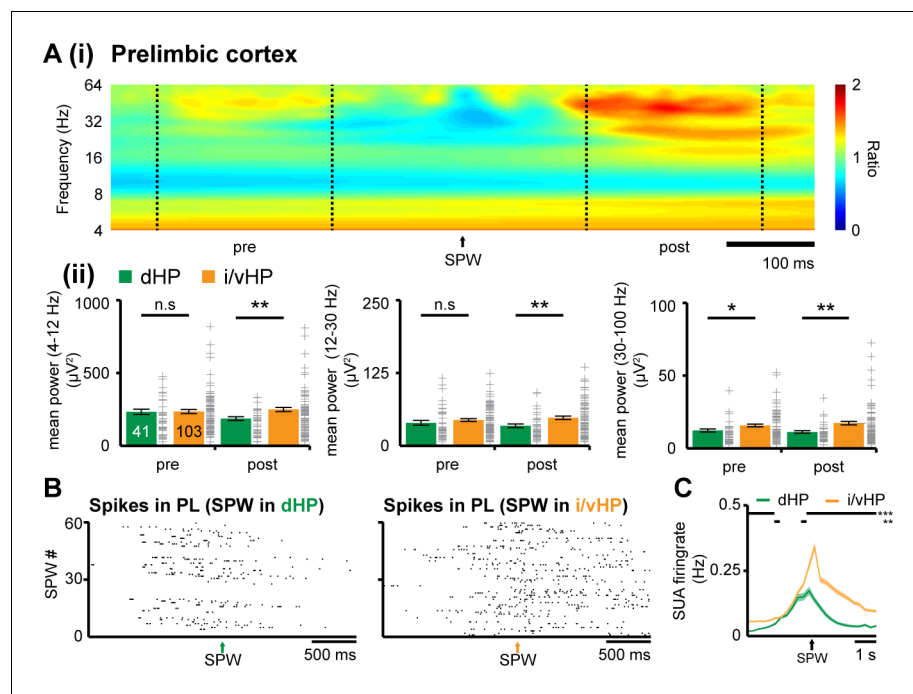


Figure 3. Coupling between neonatal PFC and HP during hippocampal SPWs. (A) Power changes in the PL during hippocampal SPWs. (i) Color-coded frequency plot showing the relative power in the PL aligned to the onset of SPWs detected in i/vHP when normalized to the power change caused in the PL by SPWs in the dHP. All other colors than green represent power augmentation (red) or decrease (blue). (ii) Bar diagrams displaying mean power changes of prelimbic activity in different frequency bands (left, theta; middle, beta; right, gamma) before (pre) and after (post) hippocampal SPWs in the dHP and i/vHP ($n = 41$ mice for dHP, $n = 103$ mice for i/vHP). (B) Spike trains recorded in the PL before and after SPWs occurring either in the dHP (left) or i/vHP (right). (C) Histograms of prelimbic spiking in relationship with hippocampal SPWs ($n = 148$ units for dHP, $n = 560$ units for i/vHP). Data are represented as mean \pm SEM. * $p < 0.05$, ** $p < 0.01$, *** $p < 0.001$.

DOI: <https://doi.org/10.7554/eLife.33158.008>

The following figure supplement is available for figure 3:

Figure supplement 1. Phase-locking of SUA in PL before (pre) and after (post) SPWs detected in dHP (top, green) and i/vHP (bottom, orange).

DOI: <https://doi.org/10.7554/eLife.33158.009>

oscillatory activity in the PL of neonatal mice was accompanied by augmentation of firing rates. While the induced firing in i/vHP peaked (≈ 90 ms) after SPWs-ripples and remained significantly ($p < 0.001$) elevated for several seconds, a less prominent peak was observed following SPW-ripples in dHP (Figure 3B and C). The phase-locking of prelimbic units was similar before and after SPWs (Figure 3—figure supplement 1).

These data reveal that SPWs-ripples from intermediate/ventral but less from the dorsal part of hippocampal CA1 correlate with pronounced neuronal firing and local entrainment in the PL of neonatal mice.

Pyramidal neurons in intermediate/ventral but not dorsal hippocampus densely project to the prefrontal cortex at neonatal age

To identify the anatomical substrate of different coupling strength between i/vHP - PL and dHP - PL, we monitored the projections that originate from the CA1 area in both hippocampal subdivisions and target the PFC. The direct unilateral projections from hippocampal CA1 area to PL have been extensively investigated in adult brain (Swanson, 1981; Jay and Witter, 1991; Vertes et al., 2007) and are present already at neonatal age (Brockmann et al., 2011; Hartung et al., 2016). We tested for sub-division-specific differences by using retrograde and anterograde tracing. First, we injected unilaterally small amounts of the retrograde tracer Fluorogold (FG) into the PL of P7 mice ($n = 8$

mice). Three days after FG injections, labeled cells were found in str. pyr. of CA1 in both dHP and i/vHP (**Figure 4A**). However, their density was significantly different ($p < 0.001$); whereas in dHP very few cells were retrogradely labeled ($0.15 \times 10^3 \pm 0.074 \times 10^3$ cells/mm²), a large proportion of pyramidal-shaped cells in the CA1 area of i/vHP projects to PL ($3.29 \times 10^3 \pm 0.19 \times 10^3$ cells/mm²).

Second, the preferential innervation of PL by pyramidal neurons from CA1 area of i/vHP was confirmed by anterograde staining with BDA ($n = 9$ mice). Small amounts of BDA were injected into the CA1 area of i/vHP (**Figure 4B**). They led to labeling of the soma and arborized dendritic tree of pyramidal neurons in str. pyr. with the characteristic orientation of axons. In 7 out of 9 mice anterogradely-labeled axons were found in the PL, preferentially within its deep layers V and VI.

Thus, the dense axonal projections from CA1 area of i/vHP might represent the substrate of HP-induced oscillatory entrainment of prelimbic circuits.

Selective light manipulation of pyramidal neurons and interneurons in CA1 area of intermediate/ventral but not dorsal hippocampus causes frequency-specific changes in the oscillatory entrainment of neonatal prelimbic circuits

The tight coupling by synchrony and the directed information flow from hippocampal CA1 area to PL via direct axonal projections suggest that the HP acts already at neonatal age as a drive for prelimbic activation. Moreover, the differences identified between the dHP – PL and i/vHP – PL communication argue for prominent augmentation of driving force along the septo-temporal hippocampal

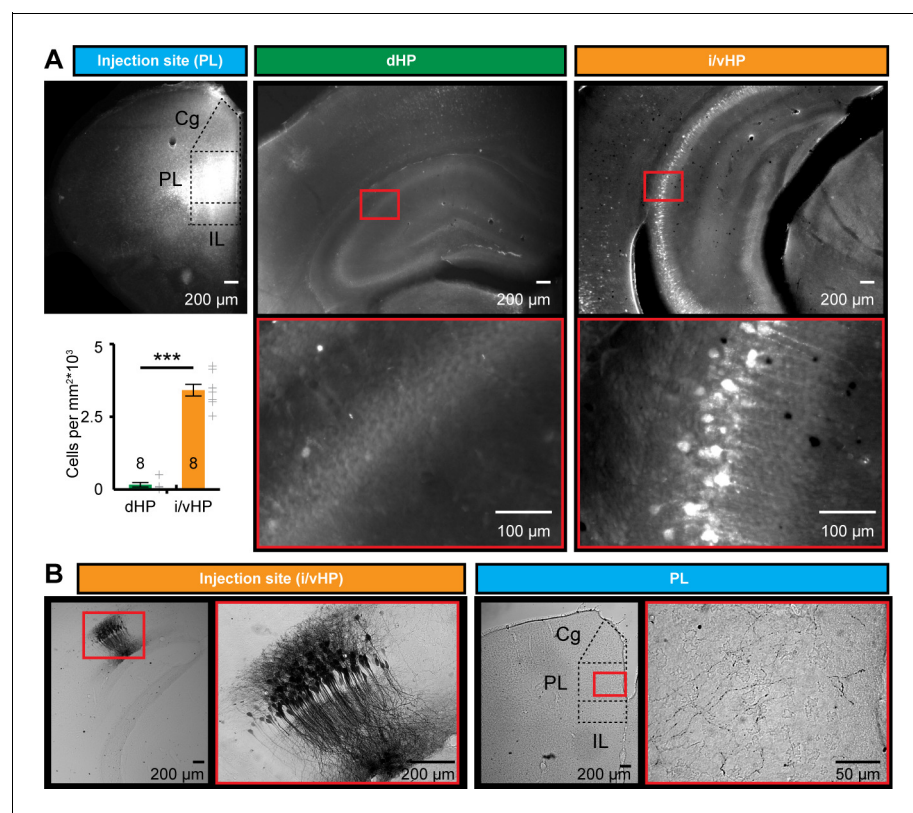


Figure 4. Long-range monosynaptic axonal projections connecting the neonatal PFC and hippocampal CA1 area along the septo-temporal axis. (A) Photomicrographs depicting dense retrogradely labelled neurons in the CA1 area of i/vHP (right) but not dHP (middle) after FG injection into PL at P1 (left). Bar diagram displays the overall density of retrogradely stained neurons when averaged for all investigated pups ($n = 8$ mice). (B) Photomicrographs depicting anterogradely labeled axons targeting the PL of a P10 mouse (right) after iontophoretic BDA injection into the CA1 area of i/vHP at P7 (left). The site of injection and the area with the highest axonal density are depicted at higher magnification. Data are represented as mean \pm SEM. *** $p < 0.001$.

DOI: <https://doi.org/10.7554/eLife.33158.010>

axis. To causally confirm these correlative evidences, we selectively activated by light the pyramidal neurons in the CA1 area of either dHP or i/vHP that had been transfected with a highly efficient fast-kinetics double mutant ChR2E123T/T159C (ET/TC) (Berndt et al., 2011) and the red fluorescent protein tDimer2 by *in utero* electroporation (IUE) (Figure 5—figure supplement 1A). This method enables stable area and cell type-specific transfection of neurons already prenatally without the need of cell-type specific promoters of a sufficiently small size (Baumgart and Grebe, 2015; Szczurkowska et al., 2016). To target neurons along the septo-temporal axis, distinct transfection protocols were used. When the IUE was performed with two paddles placed 25° leftward angle from the midline and a 0° angle downward from anterior to posterior, tDimer-positive neurons were mainly found in the CA1 area of the dHP, as revealed by the analysis of consecutive coronal sections from IUE-transfected P8-10 mice. Targeting of i/vHP succeeded only when three paddles were used, with both positive poles located at 90° leftward angle from the midline and the third negative pole at 0° angle downward from anterior to posterior (Figure 5A, S2B). Staining with NeuN showed that a substantial proportion of neurons in str. pyr. of CA1 area (dHP: $18.3 \pm 1.0\%$; $n = 36$ slices from 13 mice; i/vHP: $14.5 \pm 1.5\%$, $n = 12$ slices from 11 mice) were transfected by IUE. The shape of tDimer2-positive neurons, the orientation of primary dendrites, and the absence of positive staining for GABA confirmed that the light-sensitive protein ChR2(ET/TC) was integrated exclusively into cell lineages of pyramidal neurons (Figure 5A). Omission of ChR2(ET/TC) from the expression construct (i.e. opsin-free) yielded similar expression rates and distribution of tDimer2-positive neurons (Figure 5—figure supplement 1C).

To exclude non-specific effects of transfection procedure by IUE on the overall development of mice, we assessed the developmental milestones and reflexes of electroporated opsin-expressing and opsin-free mice (Figure 5—figure supplement 1D). While IUE caused significant reduction of litter size (non-electroporated 6.5 ± 0.7 pups/litter, electroporated: 4.5 ± 0.5 pups/litter, $p=0.017$), all investigated pups had similar body length, tail length, and weight during early postnatal period. Vibrissa placing, surface righting and cliff aversion reflexes were also not affected by IUE or transfection of neurons with opsins. These data indicate that the overall somatic development during embryonic and postnatal stage of ChR2(ET/TC)-transfected mice is unaltered.

We first assessed the efficiency of light stimulation in evoking action potentials in hippocampal pyramidal neurons *in vivo*. Blue light pulses (473 nm, 20–40 mW/mm²) at different frequencies (4, 8, 16 Hz) led shortly (<10 ms) after the stimulus to precisely timed firing of transfected neurons in both dHP and i/vHP. Our previous experimental data and modeling work showed that the used light power did not cause local tissue heating that might interfere with neuronal spiking (Stujenske et al., 2015; Bitzenhofer et al., 2017b). For both hippocampal sub-divisions the efficiency of firing similarly decreased with augmenting frequency (Figure 5B). For stimulation frequencies >16 Hz, the firing lost the precise timing by light, most likely due to the immaturity of neurons and their projections.

To decide whether activation of HP boosts the entrainment of prelimbic circuits, we simultaneously performed multi-site recordings of LFP and MUA in PL and HP during pulsed light stimulation of CA1 area of dHP ($n = 22$ mice) or i/vHP ($n = 9$ mice) (Figure 5C). The firing in i/vHP timed by light at 8 Hz, but not at 4 Hz or 16 Hz, caused significant (theta: $p=0.039$, beta: $p=0.030$, gamma: $p=0.0036$) augmentation of oscillatory activity in all frequency bands as reflected by the higher power in the PL during the stimulation when compared with the time window before the train of pulses (Figure 5D, Table 1). In contrast, stimulation by light of dHP left the prelimbic activity unaffected. In opsin-free animals, stimulation of dHP and i/vHP led to no significant changes in the oscillatory activity (Figure 5—figure supplement 2A, Table 1). Rhythmic firing of prelimbic neurons was not detected after light activation of hippocampal subdivisions, most likely because hippocampal axons were rather sparse.

To confirm the driving role of i/vHP for the generation of oscillatory activity in PL, we selectively transfected Dlx5/6 positive interneurons with either ChETA or archaerhodopsin (ArchT). Blue light stimulation (473 nm) confined to i/vHP of Dlx5/6–ChETA mice ($n = 19$) led to a significant reduction of hippocampal power in all frequency bands (theta: $p=0.024$, beta: $p=0.018$, gamma: $p=0.044$). Correspondingly, the oscillatory activity in PL diminished (theta: $p=0.027$, beta: $p=0.077$, gamma: $p=0.019$) (Figure 6A,B). Silencing of interneurons in Dlx5/6–ArchT mice ($n = 13$) by yellow light (600 nm) had an opposite effect and caused augmentation of oscillatory activity both within i/vHP (theta:

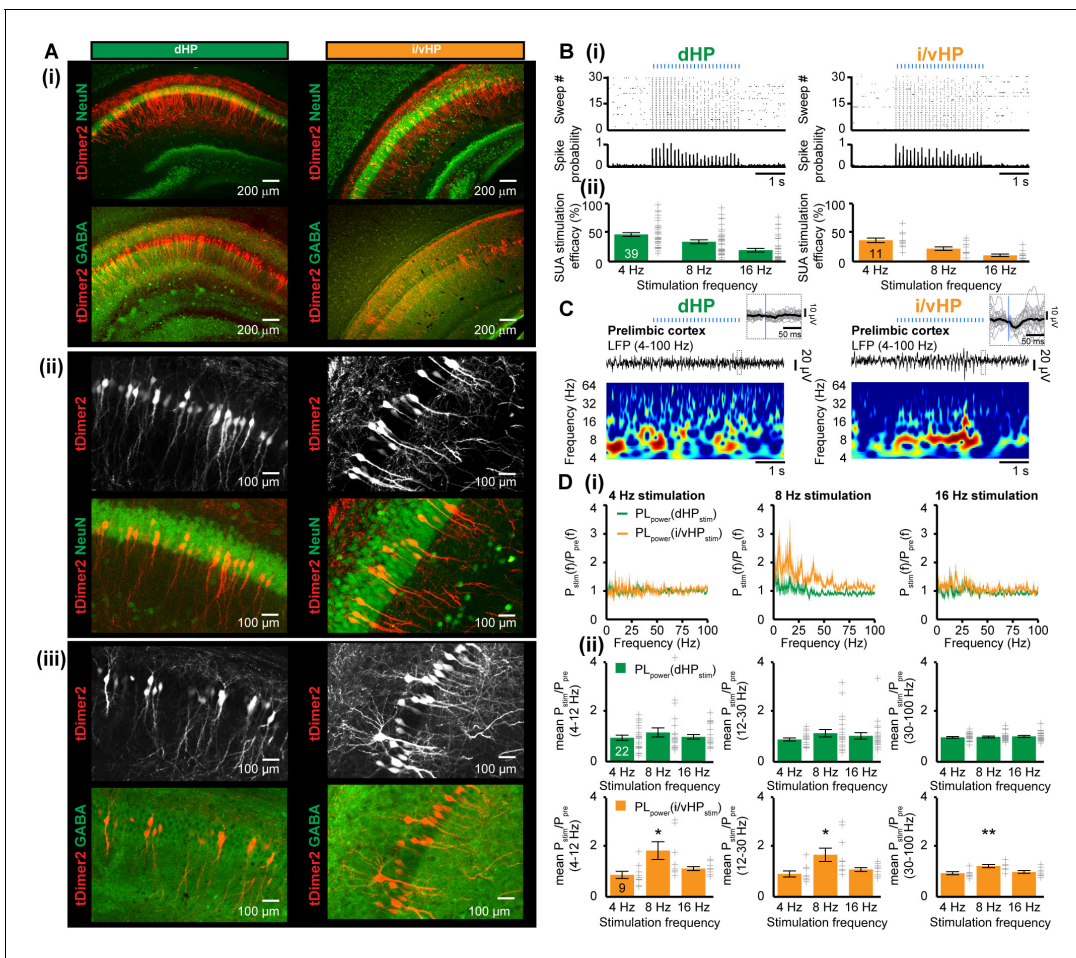


Figure 5. Optogenetic activation of pyramidal neurons in the CA1 area of dHP and i/vHP has different effects on the network activity of neonatal PL. (A) Cell- and layer-specific transfection of dHP or i/vHP with CAG-ChR2(ET/TC)–2A-tDimer2 by site-directed IUE. (i) Photomicrographs depicting tDimer2-expressing pyramidal neurons (red) in the CA1 region of dHP (left) and i/vHP (right) when stained for NeuN (green, top panels) or GABA (green, bottom panels). (ii) Photomicrographs depicting the transfected hippocampal neurons when co-stained for NeuN and displayed at larger magnification. (iii) Photomicrographs depicting transfected hippocampal neurons when co-stained for GABA and displayed at larger magnification. (B) Optogenetic activation of pyramidal neurons in CA1 area along septo-temporal axis. (i) Representative raster plot and corresponding spike probability histogram for dHP (left) and i/vHP (right) in response to 30 sweeps of 8 Hz pulse stimulation (3 ms pulse length, 473 nm). (ii) Bar diagram displaying the efficacy of inducing spiking in dHP and i/vHP of different stimulation frequencies. (C) Characteristic light-induced discontinuous oscillatory activity in the PL of a P10 mouse after transfection of pyramidal neurons in the CA1 area of the dHP (left) or i/vHP (right) with ChR2(ET/TC) by IUE. The LFP is displayed after band-pass filtering (4–100 Hz) together with the corresponding color-coded wavelet spectrum at identical time scale. Inset, individual (gray) and averaged (black) prelimbic LFP traces displayed at larger time scale in response to light stimulation in HP. (D) Power analysis of prelimbic oscillatory activity $P_{stim}(f)$ after light stimulation of dHP (green) and i/v HP (orange) at different frequencies (4, 8, 16 Hz) normalized to the activity before stimulus $P_{pre}(f)$. (i) Power spectra (0–100 Hz) averaged for all investigated mice. (ii) Bar diagrams displaying mean power changes in PL during stimulation of either dHP (top panels) or i/vHP (bottom panels). Data are represented as mean \pm SEM. * $p < 0.05$, ** $p < 0.01$.

DOI: <https://doi.org/10.7554/eLife.33158.011>

The following figure supplements are available for figure 5:

Figure supplement 1. Experimental protocol for *in utero* electroporation of the hippocampus.

DOI: <https://doi.org/10.7554/eLife.33158.012>

Figure supplement 2. Response in prelimbic cortex for opsin-free animals.

DOI: <https://doi.org/10.7554/eLife.33158.013>

$p < 0.001$, beta: $p = 0.0012$, gamma: $p < 0.001$) and PL (theta: $p < 0.001$, beta: $p < 0.001$, gamma: $p < 0.001$) (Figure 6A,C).

Table 1. Mean power changes in PL after light stimulation of dHP or i/vHP in ChR2(ET/TC)-containing and opsin-free animals.

*p<0.05, **p<0.01.

	dHP			i/vHP		
	Stimulation frequency			Stimulation frequency		
ChR2(ET/TC)	4 Hz	8 Hz	16 Hz	4 Hz	8 Hz	16 Hz
Theta	0.97 ± 0.10	1.19 ± 0.19	1.0 ± 0.093	0.90 ± 0.15	1.89 ± 0.36 (*)	1.16 ± 0.08
Beta	0.91 ± 0.06	1.17 ± 0.15	1.06 ± 0.13	0.94 ± 0.12	1.72 ± 0.27 (*)	1.12 ± 0.08
Gamma	1.0 ± 0.035	1.00 ± 0.19	1.04 ± 0.38	0.97 ± 0.06	1.26 ± 0.06 (**)	1.02 ± 0.06
Opsinfree						
Theta	1.11 ± 0.14	1.09 ± 0.19	1.14 ± 0.22	1.17 ± 0.27	1.17 ± 0.20	1.16 ± 0.12
Beta	1.13 ± 0.15	0.99 ± 0.16	1.11 ± 0.11	1.05 ± 0.22	0.95 ± 0.18	1.08 ± 0.13
Gamma	1.08 ± 0.06	0.93 ± 0.04	1.03 ± 0.03	0.89 ± 0.09	0.94 ± 0.07	0.97 ± 0.04

DOI: <https://doi.org/10.7554/eLife.33158.014>

Taken together, these data reveal the critical role of hippocampal activity for the oscillatory entrainment of PL and identify pyramidal neurons in CA1 area of i/vHP but not dHP as drivers for the broad activation of local prelimbic circuits.

Discussion

Combining selective optogenetic activation with extracellular recordings and tracing of projections in neonatal mice in vivo, we provide causal evidence that theta activity in the CA1 area of i/vHP but not dHP drives network oscillations within developing prefrontal cortex. Despite stronger theta power in the dHP, solely optical activation of the pyramidal neurons in i/vHP at theta frequency range (8 Hz) boosted the emergence of discontinuous oscillatory activity in theta and beta-gamma bands in the neonatal PFC. These data identify the cellular substrate of the directed interactions between neonatal hippocampus and prefrontal cortex and offer new perspectives for the interrogation of long-range coupling in the developing brain and its behavioral readout.

Distinct patterns of functional maturation in dorsal and intermediate/ventral hippocampus

The abundant literature dedicated to the adult hippocampus mainly deals with a single cortical module (Amaral *et al.*, 2007). However, an increasing number of studies in recent years revealed distinct organization, processing mechanisms and behavioral relevance for dHP vs. i/vHP (Fanselow and Dong, 2010; Bannerman *et al.*, 2014; Strange *et al.*, 2014). For example, the dHP, which receives dense projections from the entorhinal cortex (Witter and Amaral, 2004), is mainly involved in spatial navigation (O'Keefe and Nadel, 1978; Moser *et al.*, 1995; Moser *et al.*, 1998). In contrast, the ventral part receives strong cholinergic and dopaminergic innervation (Witter *et al.*, 1989; Pitkänen *et al.*, 2000) and contributes to processing of non-spatial information (Bannerman *et al.*, 2003; Bast *et al.*, 2009). Correspondingly, the network and neuronal activity changes along the septo-temporal axis. The power of the most prominent activity pattern in the adult HP, the theta oscillations, as well as the theta timing of the neuronal firing was found to be substantially reduced in the i/vHP when compared with dHP (Royer *et al.*, 2010). By these means, the precise spatial representation deteriorates along the septo-temporal axis, since theta activity is directly linked to place cell representation (O'Keefe and Recce, 1993; Geisler *et al.*, 2007). In contrast, SPWs are more frequent and ripples have higher amplitude and frequency in the ventral HP than in the dHP (Patel *et al.*, 2013).

Our data uncovered that some of these differences in the activity patterns along the septo-temporal axis emerge already during early neonatal development. Similar to findings from adult rodents, the power of theta bursts at neonatal age was higher in dHP than in i/vHP. The amplitude of SPWs and the power of ripples decreased along the septo-temporal axis. These findings give insights into the mechanisms underlying the early generation of activity patterns. It has been proposed that the differences in theta dynamics along the septo-temporal axis result from distinct innervation, on the

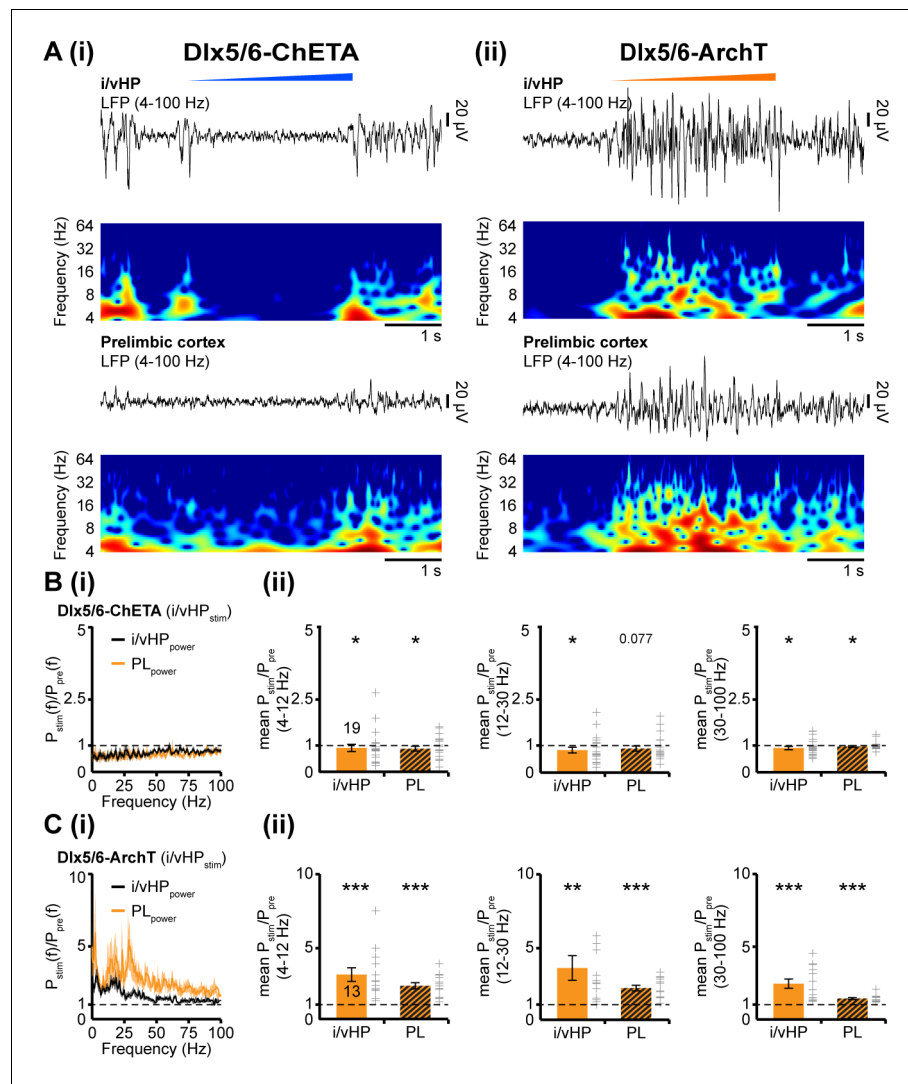


Figure 6. Modulation of oscillatory activity in i/vHP by optogenetic manipulation of interneurons affects the entrainment of neonatal PL. (A) Light-induced modulation of oscillatory activity in i/vHP and PL of a P9 mouse after transfection of interneurons in the CA1 area of the i/vHP with ChETA (i) or ArchT (ii). The LFP is displayed after band-pass filtering (4–100 Hz) together with the corresponding color-coded wavelet spectrum at identical time scale. (B) Power of oscillatory activity in i/vHP and PL after optogenetic activation of interneurons in i/vHP ($P_{stim}(f)$) normalized to the activity before stimulus $P_{pre}(f)$. (i) Power spectra (0–100 Hz) averaged for all investigated mice. (ii) Bar diagrams displaying mean power changes in theta, beta, and gamma frequency bands for the oscillations recorded in i/vHP and PL during light stimulation in i/vHP. (C) Same as (B) for silencing of ArchT-transfected interneurons in i/vHP by yellow light. Data are shown as mean \pm SEM. * $p < 0.05$, ** $p < 0.01$, *** $p < 0.001$. DOI: <https://doi.org/10.7554/eLife.33158.015>

one hand, and from specific intrinsic properties of hippocampal neurons, on the other hand. Cholinergic projections of different origin in the dHP and i/vHP (Stewart and Fox, 1990; Amaral et al., 2007) as well as maturational differences in the intrinsic resonant properties of hippocampal neurons and notable gradients of parvalbumin immunoreactivity along the septo-temporal axis (Honeycutt et al., 2016) may contribute to the observed differences.

Quantification along the septo-temporal axis revealed that, similar to adults, the occurrence of SPWs was higher in the i/vHP and their amplitude was larger in the neonatal dHP (Patel et al., 2013). It is still an issue of debate when exactly ripples emerge in the developing hippocampus, although it is obvious that they appear later than theta bursts and SPWs, most likely towards the end of the first and during second postnatal week (Buhl and Buzsáki, 2005; Brockmann et al.,

2011). Their underlying mechanisms at neonatal age remain also largely unknown and need to be related to age-dependent changes in gap junctional coupling and GABA switch (Ben-Ari et al., 1989; Zhang et al., 1990; Yuste et al., 1995). The organization of SPWs and ripples is of particular relevance when considering their impact on the early activity of PFC. Already at neonatal age, the prelimbic firing and oscillatory entrainment is timed by SPWs-ripples. Of note, the degree of timing varies along the septo-temporal axis and is much higher for the i/vHP.

Optogenetic interrogation of long-range coupling in the developing brain

At adult age the communication between PFC and HP has been investigated in relationship with memory tasks both under physiological and disease-related conditions (Sirota et al., 2008; Adhikari et al., 2010; Sigurdsson et al., 2010; Eichenbaum, 2017). Depending on the phase of memory processing, the prefrontal-hippocampal coupling via oscillatory synchrony has been found to be either unidirectional from the HP to PFC or bidirectional (Siapas et al., 2005; Hallock et al., 2016; Place et al., 2016). Both theta and gamma network oscillations contribute to the functional long-range coupling. The model of prefrontal-hippocampal communication has been initially built based on experimental evidence correlating the temporal organization of neuronal and network activity in the two brain areas. The time delay between spike trains and oscillatory phase or between oscillations enabled to propose that the information flows in one direction or the other via mono- or polysynaptic axonal projections. More recently, a direct causal assessment of the coupling became possible through optogenetic interrogation of neural circuits. In a seminal study, Spellman and colleagues used light-driven inhibition of axonal terminals for dissecting the directionality of interactions between PFC and HP during different phases of memory retrieval (Spellman et al., 2015).

We previously showed that at neonatal age, long before full maturation of memory and attentional abilities, discontinuous theta bursts in i/vHP are temporally correlated to the network oscillations in the PFC and time the prefrontal firing (Brockmann et al., 2011; Hartung et al., 2016). Moreover, the temporal delay of 10–20 ms between prefrontal and hippocampal spike trains as well as the estimated directionality of information flow between the two areas suggested that hippocampal theta drives the oscillatory entrainment of the local circuits in the PFC. The present data directly prove this hypothesis, taking advantage of the recently developed protocol for optogenetic manipulation of neuronal networks at neonatal age (Bitzenhofer et al., 2017a, 2017b). We observed that prelimbic circuits were effectively entrained when the stimulation of pyramidal neurons in i/vHP occurred at 8 Hz but not at 4 Hz or 16 Hz. Such frequency-specific effect might result from intrinsic resonance properties of neurons mediated through hyperpolarization-activated cyclic nucleotide-gated (HCN) channels (Hu et al., 2002; Stark et al., 2013). It has been previously proposed that oscillatory activity in cortical regions may be entrained due to the rhythmic theta-band output from the hippocampus (Stark et al., 2013; Colgin, 2016).

Several considerations regarding the technical challenges of optogenetic manipulation of HP along the septo-temporal axis need to be made. Besides the inherent difficulties related to the specificity of promoters for selective transfection and the targeting procedure that are ubiquitous for all developing networks and have been addressed elsewhere (Bitzenhofer et al., 2017a), confinement of light-sensitive proteins to pyramidal neurons of either dHP or i/vHP required special attention. In a previous study (Bitzenhofer et al., 2017b), we developed a selective targeting protocol of neonatal neurons that relies on the combination of CAG promoter and IUE. By these means, the expression of light-sensitive proteins in the neurons located in the neocortical layer and area of interest was sufficiently high to ensure their reliable activation. Similarly, the expression of ChR2(ET/TC) in the pyramidal neurons of hippocampal CA1 area under the CAG promoter was sufficiently high to reliably cause network and neuronal activity. Taking into account that viral transduction, which usually requires 10–14 days for stable expression, is only of limited usability to investigate local network interactions during development, IUE seems to represent the method of choice for manipulating circuits at this early age. IUE enables targeting of precursor cells of neuronal and glial subpopulations, based on their distinct spatial and temporal patterns of generation in the ventricular zone (Tabata and Nakajima, 2001; Borrell et al., 2005; Niwa et al., 2010; Hoerder-Suabedissen and Molnár, 2015). IUE based on two electrode paddles enabled selective targeting of pyramidal neurons in the CA1 area of dHP in more than half of the pups per litter (Figure 5—figure supplement 1), but it completely failed (0 out of 32 mice) to target these neurons in i/vHP. Therefore, it was

necessary to use a modified IUE protocol based on three electrodes. This protocol, although more complicated and time consuming, allows reliable transfection at brain locations that are only able to be sporadically targeted by two electrodes. The IUE-induced expression of light sensitive proteins enables the reliable firing of neurons in both dHP and i/vHP in response to light pulses. One intriguing question is how many pyramidal neurons in str. pyr. of CA1 area must be synchronously activated to drive the oscillatory entrainment of prelimbic circuitry. Anterograde and retrograde tracing demonstrated the density increase along the septo-temporal axis of hippocampal axons targeting the PL. Light activation/inhibition of these axonal terminals paired with monitoring of network oscillations in the PFC might offer valuable insights into the patterns of coupling sufficient for activation.

Functional relevance of frequency-specific drive within developing prefrontal-hippocampal networks

Abundant literature links theta frequency coupling within prefrontal-hippocampal networks to cognitive performance and emotional states of adults (*Adhikari et al., 2010; Xu and Südhof, 2013; Spellman et al., 2015; Hallock et al., 2016; Place et al., 2016; Ye et al., 2017*). The early emergence of directed communication between PFC and i/vHP raises the question of functional relevance of this early coupling during development and at adulthood.

The maturation of cognitive abilities is a process even more protracted than sensory development and starts during second-third postnatal week (*Hanganu-Opatz, 2010; Cirelli and Tononi, 2015*). Some of these abilities, such as recognition memory, can be easily monitored at early age and seems to critically rely on structurally and functionally intact prefrontal-hippocampal networks (*Krüger et al., 2012*). Direct assessment of the role of neonatal communication for memory performance as performed for adult circuits is impossible due to the temporal delay of the two processes. The alternative is to manipulate the activity of either PFC, HP or the connectivity between them during defined developmental time windows and monitor the juvenile and adult consequences at structural, functional and behavioral levels. The present data and optogenetic protocol represent the prerequisite of this investigation, opening new perspectives for assessing the adult behavioral readout of long-range communication in the developing brain.

One question that remains to be addressed is how the hippocampal theta drive shapes the maturation of prefrontal-hippocampal networks. Following the general rules of activity-dependent plasticity (*Hubel et al., 1977; Huberman et al., 2006; Xu et al., 2011; Yasuda et al., 2011*), the precisely timed excitatory inputs from the i/vHP to the PL might facilitate the wiring of local prefrontal circuitry and enable the refinement of behaviorally relevant communication scaffold between the two regions. By these means, the prefrontal activity driven by projection neurons in the HP act as a template, having a pre-adaptive function that facilitates the tuning of circuits with regard to future conditions. This instructive role of theta activity for the prefrontal circuits needs to be proven by manipulation of temporal structure of the hippocampal drive without affecting the overall level of activity. Understanding the rules that govern the early organization of large-scale networks represents the pre-requisite for identifying the structural and functional deficits related to abnormal behavior and disease.

Materials and methods

Key resources table

Reagent type (species) or resource	Designation	Source or reference	Identifiers	Additional information
antibody	mouse monoclonal Alexa Fluor-488 conjugated antibody against NeuN	Merck Millipore	MAB377X	1:200 dilution
antibody	rabbit polyclonal primary antibody against GABA	Sigma-Aldrich	A2052	1:1000 dilution
antibody	Alexa Fluor-488 goat anti-rabbit IgG secondary antibody	Merck Millipore	A11008	1:500 dilution

Continued on next page

Continued

Reagent type (species) or resource	Designation	Source or reference	Identifiers	Additional information
chemical compound, drug	Isoflurane	Abbott	B506	
chemical compound, drug	Urethane	Fluka analytical	94300	
chemical compound, drug	Fluorogold	Fluorochrome, LLC	52-9400	
chemical compound, drug	Biotinylated dextran amine, 10.000 MW	Thermo Fisher Scientific	D1956	
commercial assay or kit	NucleoBond PC 100	Macherey-Nagel	740573	
strain, strain background (mouse, both genders)	C57Bl/6J	Universitätsklinikum Hamburg-Eppendorf – Animal facility	C57Bl/6J	https://www.jax.org/strain/008199
strain, strain background (mouse, both genders)	Tg(dlx5a-cre)1MekkJ	The Jackson Laboratory	Tg(dlx5a-cre)1MekkJ	https://www.jax.org/strain/017455
strain, strain background (mouse, both genders)	R26-CAG-LSL-2XChETA-tdTomato	The Jackson Laboratory	R26-CAG-LSL-2XChETA-tdTomato	https://www.jax.org/strain/021188
strain, strain background (mouse, both genders)	Ai40(RCL-ArchT/EGFP)-D	The Jackson Laboratory	Ai40(RCL-ArchT/EGFP)-D	
recombinant DNA reagent	pAAV-CAG-ChR2 (E123T/T159C) –2AtDimer2	Provided by T. G. Oertner	pAAV-CAG-ChR2 (E123T/T159C) –2AtDimer2	http://www.oertner.com/
recombinant DNA reagent	pAAV-CAG-tDimer2	Provided by T. G. Oertner	pAAV-CAG-tDimer2	http://www.oertner.com/
software, algorithm	Matlab R2015a	MathWorks	Matlab R2015a	https://www.mathworks.com
software, algorithm	Offline Sorter	Plexon	Offline Sorter	http://www.plexon.com/
software, algorithm	ImageJ 1.48 c	ImageJ	ImageJ 1.48 c	https://imagej.nih.gov/ij/
software, algorithm	SPSS Statistics 21	IBM	SPSS Statistics 21	https://www.ibm.com/analytics/us/en/technology/spss/
software, algorithm	Cheetah 6	Neuralynx	Cheetah 6	http://neuralynx.com/
other	Arduino Uno SMD	Arduino	A000073	A000073
other	Digital Lynx 4SX	Neuralynx	Digital Lynx 4SX	http://neuralynx.com/
other	Diode laser (473 nm)	Omicron	LuxX 473-100	
other	Electroporation device	BEX	CUY21EX	
other	Electroporation tweezer-type paddles	Protech	CUY650-P5	
other	Recording electrode (1 shank, 16 channels)	Neuronexus	A1 × 16-3 mm-703-A16	
other	Recording optrode (1 shank, 16 channels)	Neuronexus	A1 × 16-5 mm-703-OA16LP	
other	Digital midgard precision current source	Stoelting	51595	

Experimental model and subject details

Mice

All experiments were performed in compliance with the German laws and the guidelines of the European Union for the use of animals in research and were approved by the local ethical committee (111/12, 132/12). Timed-pregnant C57Bl/6J mice from the animal facility of the University Medical Center Hamburg-Eppendorf were housed individually in breeding cages at a 12 hr light/12 hr dark cycle and fed *ad libitum*. The day of vaginal plug detection was defined E0.5, while the day of birth was assigned as P0. Both female and male mice underwent light stimulation and multi-site electrophysiological recordings at P8-10 after transfection with light-sensitive proteins by IUE at E15.5. For monitoring of projections, tracers were injected at P7 and monitored in their distribution along the axonal tracts at P10. For specifically addressing interneurons by light, the *Dlx5/6-Cre* drive line (Tg(*dlx5a-cre*)1MekkJ, Jackson Laboratory) was crossed with either ArchT (Ai40(RCL-ArchT/EGFP)-D,

Jackson Laboratory) or ChETA (R26-CAG-LSL-2XChETA-tdTomato, Jackson Laboratory) reporter line.

Methods details

Surgical procedures

In utero electroporation

Starting one day before and until two days after surgery, timed-pregnant C57Bl/6J mice received on a daily basis additional wet food supplemented with 2–4 drops Metacam (0.5 mg/ml, Boehringer-Ingelheim, Germany). At E15.5 randomly assigned pregnant mice were injected subcutaneously with buprenorphine (0.05 mg/kg body weight) 30 min before surgery. The surgery was performed on a heating blanket and toe pinch and breathing were monitored throughout. Under isoflurane anesthesia (induction: 5%, maintenance: 3.5%) the eyes of the dam were covered with eye ointment to prevent damage before the uterine horns were exposed and moistened with warm sterile phosphate buffered saline (PBS, 37°C). Solution containing 1.25 µg/µl DNA [pAAV-CAG-ChR2(E123T/T159C)–2A-tDimer2, or pAAV-CAG-tDimer2] (**Figure 5—figure supplement 1A**) and 0.1% fast green dye at a volume of 0.75–1.25 µl were injected into the right lateral ventricle of individual embryos using pulled borosilicate glass capillaries with a sharp and long tip. Plasmid DNA was purified with NucleoBond (Macherey-Nagel, Germany). 2A encodes for a ribosomal skip sentence, splitting the fluorescent protein tDimer2 from the opsin during gene translation. Two different IUE protocols were used to target pyramidal neurons in CA1 area of either dHP or i/vHP. To target dHP, each embryo within the uterus was placed between the electroporation tweezer-type paddles (5 mm diameter, Protech, TX, USA) that were oriented at a 25° leftward angle from the midline and a 0° angle downward from anterior to posterior. Electrode pulses (35 V, 50 ms) were applied five times at intervals of 950 ms controlled by an electroporator (CU21EX, BEX, Japan) (**Figure 5—figure supplement 1B(ii)**) (**Baumgart and Grebe, 2015**). To target i/vHP, a tri-polar approach was used (**Szczurkowska et al., 2016**). Each embryo within the uterus was placed between the electroporation tweezer-type paddles (5 mm diameter, both positive poles, Protech, TX, USA) that were oriented at 90° leftward angle from the midline and a 0° angle downward from anterior to posterior. A third custom build negative pole was positioned on top of the head roughly between the eyes. Electrode pulses (30 V, 50 ms) were applied six times at intervals of 950 ms controlled by an electroporator (CU21EX, BEX, Japan). By these means, neural precursor cells from the subventricular zone, which radially migrate into the HP, were transfected. Uterine horns were placed back into the abdominal cavity after electroporation. The abdominal cavity was filled with warm sterile PBS (37°C) and abdominal muscles and skin were sutured individually with absorbable and non-absorbable suture thread, respectively. After recovery, pregnant mice were returned to their home cages, which were half placed on a heating blanket for two days after surgery.

Retrograde and anterograde tracing

For retrograde tracing, mice were injected at P7 with Fluorogold (Fluorochrome, LLC, USA) unilaterally into the PFC using iontophoresis. The pups were placed in a stereotactic apparatus and kept under anesthesia with isoflurane (induction: 5%, maintenance: 2.5%) for the entire procedure. A 10 mm incision of the skin on the head was performed with small scissors. The bone above the PFC (0.5 mm anterior to bregma, 0.3 mm right to the midline) was carefully removed using a syringe. A glass capillary (≈20 µm tip diameter) was filled with ≈1 µL of 5% Fluorogold diluted in sterile water by capillary forces, and a silver wire was inserted such that it was in contact with the Fluorogold solution. For anterograde tracing, mice were injected at P7 with the anterograde tracer biotinylated dextran amine (BDA) (Thermo Fisher Scientific, USA) unilaterally into i/vHP using iontophoresis and surgery protocols as described above. The bone above i/vHP (0.7 mm anterior to lambda, 2.3 mm right to the midline) was carefully removed using a syringe. A glass capillary (≈30 µm tip diameter) was filled with ≈1 µL of 5% BDA diluted in 0.125 M phosphate buffer by capillary forces, and a silver wire was inserted such that it was in contact with the BDA solution. For both anterograde and retrograde tracing, the positive pole of the iontophoresis device was attached to the silver wire, the negative one was attached to the skin of the neck. The capillary was carefully lowered into the PFC (≈1.5 mm dorsal from the dura) or HP (≈1.5 mm dorsal from the dura). Iontophoretically injection by applying anodal current to the pipette (6 s on/off current pulses of 6 µA) was done for 5 min.

Following injection, the pipette was left in place for at least 5 min and then slowly retracted. The scalp was closed by application of tissue adhesive glue and the pups were left on a heating pad for 10–15 min to fully recover before they were given back to the mother. The pups were perfused at P10.

Surgical preparation for acute electrophysiological recording and light delivery

For recordings in non-anesthetized state, 0.5% bupivacain/1% lidocaine was locally applied on the neck muscles. For recordings under anesthesia, mice were injected i.p. with urethane (1 mg/g body weight; Sigma-Aldrich, MO, USA) prior to surgery. For both groups, under isoflurane anesthesia (induction: 5%, maintenance: 2.5%) the head of the pup was fixed into a stereotaxic apparatus using two plastic bars mounted on the nasal and occipital bones with dental cement. The bone above the PFC (0.5 mm anterior to bregma, 0.5 mm right to the midline for layer V/VI), hippocampus (2.0 mm posterior to bregma, 1.0 mm right to the midline for dHP, 3.5 mm posterior to bregma, 3.5 mm right to the midline for i/vHP) was carefully removed by drilling a hole of <0.5 mm in diameter. After a 10–20 min recovery period on a heating blanket mice were moved to the setup for electrophysiological recording. Throughout the surgery and recording session the mouse was positioned on a heating pad with the temperature kept at 37°C.

Perfusion

Mice were anesthetized with 10% ketamine (aniMedica, Germany)/2% xylazine (WDT, Germany) in 0.9% NaCl solution (10 µg/g body weight, i.p.) and transcardially perfused with Histofix (Carl Roth, Germany) containing 4% paraformaldehyde for 30–40 min. Brains were postfixed in 4% paraformaldehyde for 24 hr.

Behavioral testing

Examination of developmental milestones

Mouse pups were tested for their somatic development and reflexes at P2, P5 and P8. Weight, body and tail length were assessed. Surface righting reflex was quantified as time (max 30 s) until the pup turned over with all four feet on the ground after being placed on its back. Cliff aversion reflex was quantified as time (max 30 s) until the pup withdrew after snout and forepaws were positioned over an elevated edge. Vibrissa placing was rated positive if the pup turned its head after gently touching the whiskers with a toothpick.

Electrophysiology

Electrophysiological recording

A one-shank electrode (NeuroNexus, MI, USA) containing 1×16 recording sites (0.4–0.8 MΩ impedance, 100 µm spacing) was inserted into the layer V/VI of PFC. One-shank optoelectrodes (NeuroNexus, MI, USA) containing 1×16 recordings sites (0.4–0.8 MΩ impedance, 50 µm spacing) aligned with an optical fiber (105 µm diameter) ending 200 µm above the top recording site was inserted into either dHP or i/vHP. A silver wire was inserted into the cerebellum and served as ground and reference electrode. A recovery period of 10 min following insertion of electrodes before acquisition of data was provided. Extracellular signals were band-pass filtered (0.1–9,000 Hz) and digitized (32 kHz) with a multichannel extracellular amplifier (Digital Lynx SX; Neuralynx, Bozeman, MO, USA) and the Cheetah acquisition software (Neuralynx). Spontaneous (i.e. not induced by light stimulation) activity was recorded for 15 min at the beginning and end of each recording session as baseline activity. Only the baseline prior to stimulation epochs was used for data analysis. The position of recording electrodes in PL and CA1 area of dHP or i/vHP was confirmed after histological assessment post-mortem. For the analysis of prelimbic LFP, the recording site centered in PL was used, whereas for the analysis of spiking activity two channels above and two channels below this site were additionally considered. Recording site in cingulate or infralimbic sub-divisions of the PL were excluded from analysis. For the analysis of hippocampal LFP, the recording site located in *str pyr*, where sharp-waves reverse (*Bitzenhofer and Hanganu-Opatz, 2014*), was used to minimize any non-stationary effects of the large amplitude events. For the analysis of hippocampal firing, two channels below and two channels above this site were additionally considered.

Light stimulation

Pulsed (laser on-off) light or ramp (linearly increasing power) stimulations were performed with an arduino uno (Arduino, Italy) controlled diode laser (473 nm or 600 nm; Omicron, Austria). Laser power was adjusted to trigger neuronal spiking in response to >25% of 3-ms-long light pulses at 16 Hz. Resulting light power was in the range of 20–40 mW/mm² at the fiber tip. For each frequency used (4, 8 and 16 Hz), stimuli (3 ms pulse length, 3 s stimulation duration, 6 s inter stimulation interval) were repeated (30 times) in a randomized order.

Histology

Immunohistochemistry

Brains were sectioned coronally at 50 μ m. Free-floating slices were permeabilized and blocked with PBS containing 0.2% Triton X 100 (Sigma-Aldrich, MO, USA), 10% normal bovine serum (Jackson Immuno Research, PA, USA) and 0.02% sodium azide. Subsequently, slices were incubated overnight with mouse monoclonal Alexa Fluor-488 conjugated antibody against NeuN (1:200, MAB377X, Merck Millipore, MA, USA) or rabbit polyclonal primary antibody against GABA (1:1,000, A2052; Sigma-Aldrich), followed by 2 hr incubation with Alexa Fluor-488 goat anti-rabbit IgG secondary antibody (1:500, A11008; Merck Millipore). Slices were transferred to glass slides and covered with Fluoromount (Sigma-Aldrich, MO, USA).

For 3,3'-diaminobenzidine (DAB) staining sections (prepared as described above) were rinsed in PBS (0.125 M, pH 7.4–7.6) for 10 min, treated with peroxide solution (3% peroxide, 10% methanol in 0.125 M PB) for 10 min to quench any endogenous peroxidases within the tissue, and rinsed again. Subsequently, the sections were washed in PBS containing 0.5% Triton-X and incubated with avidin biotinylated enzyme complex (ABC, VECTASTAIN ABC Kit, USA) at room temperature or overnight at 4°C. After rinsing in Tris-HCl (pH 7.4), the sections were further incubated with DAB working buffer (DAB peroxidase substrate kit, Vector Laboratories, USA) at room temperature for 2–10 min. After the signal was detected, all sections were rinsed with Tris-HCl.

Imaging

Wide field fluorescence was performed to reconstruct the recording electrode position in brain slices of electrophysiologically investigated pups and to localize tDimer2 expression in pups after IUE. High magnification images were acquired with a confocal microscope (DM IRBE, Leica, Germany) to quantify tDimer2 expression and immunopositive cells (1–4 brain slices/investigated mouse). For DAB staining, brightfield images were obtained using Zeiss imager M1 microscope (Zeiss, Oberkochen, Germany) and enhanced using the National Institutes of Health (NIH) Image program.

Quantification and statistical analysis

Immunohistochemistry quantification

All images were similarly analyzed with ImageJ. For quantification of fluorogold tracing automatic cell counting was done using custom-written tools. To quantify tDimer2, NeuN and GABA-positive neurons, manual counting was performed, since the high neuronal density in str. pyr. prevented reliable automatic counting.

Spectral analysis of LFP

Data were imported and analyzed offline using custom-written tools in the Matlab environment (MathWorks). Data were processed as follows: band-pass filtered (500–5,000 Hz) to analyze MUA and low-pass filtered (<1,400 Hz) using a third-order Butterworth filter before downsampling to 3.2 kHz to analyze LFP. All filtering procedures were performed in a manner preserving phase information.

Detection of oscillatory activity

The detection and of discontinuous patterns of activity in the neonatal PL and HP were performed using a modified version of the previously developed algorithm for unsupervised analysis of neonatal oscillations (Cichon *et al.*, 2014) and confirmed by visual inspection. Briefly, deflections of the root mean square of band-pass filtered signals (1–100 Hz) exceeding a variance-depending threshold

were assigned as network oscillations. The threshold was determined by a Gaussian fit to the values ranging from 0 to the global maximum of the root-mean-square histogram. If two oscillations occurred within 200 ms of each other, they were considered as one. Only oscillations lasting >1 s was included.

Detection of sharpwaves

Sharpwaves were detected by subtracting the filtered signal (1–300 Hz) from the recording sites 100 μm above and 100 μm below the recording site in str. pyr. Sharpwaves were then detected as peaks above five times the standard deviation of the subtracted signal.

Power spectral density

Power spectral density was calculated using the Welch's method. Briefly, segments of the recorded signal were glued together (1 s segments for oscillatory activity; 300 ms segments for sharpwave pre/post comparison; 100 ms segments for ripple comparison; 3 s for light evoked activity) and power were then calculated using non-overlapping windows. Time–frequency plots were calculated by transforming the data using Morlet continuous wavelet.

Coherence

Coherence was calculated using the imaginary coherency method (Nolte *et al.*, 2004). Briefly, the imaginary coherence was calculated by taking the imaginary component of the cross-spectral density between the two signals and normalized by the power spectral density of each. The computation of the imaginary coherence C over frequency (f) for the power spectral density P of signal X and Y was performed according to the formula:

$$C_{XY}(f) = \text{Im} \left(\frac{|P_{XY}(f)|^2}{P_{XX}(f)P_{YY}(f)} \right)$$

General partial directed coherence

gPDC is based on linear Granger causality measure. The method attempts to describe the causal relationship between multivariate time series based on the decomposition of multivariate partial coherences computed from multivariate autoregressive models. The LFP signal was divided into segments containing the oscillatory activity. Signal was de-noised using wavelets with the Matlab wavelet toolbox. After de-noising, gPDC was calculated using the gPDC algorithm previously described (Baccala *et al.*, 2007).

Single unit activity analysis

SUA was detected and clustered using Offline Sorter (Plexon, TC, USA). 1–4 single units were detected at each recording site. Subsequently, data were imported and analyzed using custom-written tools in the Matlab software (MathWorks). The firing rate temporally related to SPWs was calculated by aligning all units to the detected SPWs. For assessing the phase locking of units to LFP, we firstly used the Rayleigh test for non-uniformity of circular data to identify the units significantly locked to network oscillations. The phase was calculated by extracting the phase component using the Hilbert transform of the filtered signal at each detected spike. Spikes occurring in a 15 ms-long time window after the start of a light pulse were considered to be light-evoked. Stimulation efficacy was calculated as the probability of at least one spike occurring in this period.

Statistical analysis

Statistical analyses were performed using SPSS Statistics 21 (IBM, NY, USA) or Matlab. Data were tested for normal distribution by the Shapiro–Wilk test. Normally distributed data were tested for significant differences (* $p < 0.05$, ** $p < 0.01$ and *** $p < 0.001$) using paired t-test, unpaired t-test or one-way repeated-measures analysis of variance with Bonferroni-corrected post hoc analysis. Not normally distributed data were tested with the nonparametric Mann–Whitney U-test. The circular statistics toolbox was used to test for significant differences in the phase locking data. Data are presented as mean \pm SEM. No statistical measures were used to estimate sample size since effect size was unknown. Investigators were not blinded to the group allocation during the experiments.

Unsupervised analysis software was used if possible to preclude investigator biases. Summary of performed statistical analysis is summarized in **Supplementary file 1**.

Acknowledgements

We thank Nadine Faesel for the establishment of tracing technique, Antonio Candela for preliminary tracing data, Drs. L Cancedda and A Cwetsch for help with the *in utero* electroporation, Drs. S Wiegert, T Oertner, and C Gee for help with the development of opsin constructs as well as A Marquardt, P Putthoff, A Dahlmann and I Ohmert for excellent technical assistance. ILH-O acknowledges support by the ERC (ERC Consolidator Grant 681577) and by the German Research Foundation (SFB 936 (B5) and SPP 1665 (Ha4466/12-1)). ILH-O is the member of the FENS Kavli Network of Excellence. In memoriam of Howard Eichenbaum

Additional information

Funding

Funder	Grant reference number	Author
European Research Council	681577	Ileana L Hanganu-Opatz
Deutsche Forschungsgemeinschaft	SFB 936	Ileana L Hanganu-Opatz
Deutsche Forschungsgemeinschaft	SPP 1665	Ileana L Hanganu-Opatz

The funders had no role in study design, data collection and interpretation, or the decision to submit the work for publication.

Author contributions

Joachim Ahlbeck, Data curation, Formal analysis, Investigation, Methodology, Writing—original draft, Writing—review and editing; Lingzhen Song, Data curation, Formal analysis, Writing—review and editing; Mattia Chini, Data curation, Formal analysis, Investigation, Methodology, Writing—review and editing; Sebastian H Bitzenhofer, Data curation, Validation, Investigation, Visualization, Methodology, Writing—review and editing; Ileana L Hanganu-Opatz, Conceptualization, Data curation, Supervision, Funding acquisition, Validation, Investigation, Methodology, Writing—original draft, Project administration, Writing—review and editing

Author ORCIDs

Joachim Ahlbeck  <https://orcid.org/0000-0002-4439-0798>

Mattia Chini  <http://orcid.org/0000-0002-5782-9720>

Ileana L Hanganu-Opatz  <http://orcid.org/0000-0002-4787-1765>

Ethics

Animal experimentation: All experiments were performed in compliance with the German laws and the guidelines of the European Community for the use of animals in research and were approved by the local ethical committee (111/12, 132/12).

Decision letter and Author response

Decision letter <https://doi.org/10.7554/eLife.33158.022>

Author response <https://doi.org/10.7554/eLife.33158.023>

Additional files

Supplementary files

• Supplementary file 1. (table supplement 1 for **Figures 1–5** and supplementary figures 1–4) Summary of statistics for all experiments. (A) Statistical testing, number of investigated mice and p-values for the analyses displayed in **Figure 1**. (B)–(I) Same as (A) for analyses in **Figures 2–6**, S1–4.

DOI: <https://doi.org/10.7554/eLife.33158.016>

• Source code 1. Matlab source code for the analysis of discontinuous oscillatory activity.

DOI: <https://doi.org/10.7554/eLife.33158.017>

• Transparent reporting form

DOI: <https://doi.org/10.7554/eLife.33158.018>

Major datasets

The following dataset was generated:

Author(s)	Year	Dataset title	Dataset URL	Database, license, and accessibility information
Ahlbeck J, Song L, Chini M, Candela A, Bitzenhofer S, Hanganu-Opatz I	2018	Data from: Glutamatergic drive along the septo-temporal axis of hippocampus boosts prelimbic oscillations in the neonatal mouse	http://dx.doi.org/10.5061/dryad.52fh	Available at Dryad Digital Repository under a CC0 Public Domain Dedication

References

- Adhikari A**, Topiwala MA, Gordon JA. 2010. Synchronized activity between the ventral hippocampus and the medial prefrontal cortex during anxiety. *Neuron* **65**:257–269. DOI: <https://doi.org/10.1016/j.neuron.2009.12.002>, PMID: 20152131
- Amaral DG**, Scharfman HE, Lavenex P. 2007. The dentate gyrus: fundamental neuroanatomical organization (dentate gyrus for dummies). *Progress in Brain Research* **163**:3–22. DOI: [https://doi.org/10.1016/S0079-6123\(07\)63001-5](https://doi.org/10.1016/S0079-6123(07)63001-5), PMID: 17765709
- Baccala LA**, Sameshima K, Takahashi DY. 2007. Generalized Partial Directed Coherence. 15th International Conference on Digital Signal Processing 163–166.
- Backus AR**, Schoffelen JM, Szebényi S, Hanslmayr S, Doeller CF. 2016. Hippocampal-Prefrontal Theta Oscillations Support Memory Integration. *Current Biology* **26**:450–457. DOI: <https://doi.org/10.1016/j.cub.2015.12.048>, PMID: 26832442
- Bannerman DM**, Grubb M, Deacon RM, Yee BK, Feldon J, Rawlins JN. 2003. Ventral hippocampal lesions affect anxiety but not spatial learning. *Behavioural Brain Research* **139**:197–213. DOI: [https://doi.org/10.1016/S0166-4328\(02\)00268-1](https://doi.org/10.1016/S0166-4328(02)00268-1), PMID: 12642189
- Bannerman DM**, Sprengel R, Sanderson DJ, McHugh SB, Rawlins JN, Monyer H, Seeburg PH. 2014. Hippocampal synaptic plasticity, spatial memory and anxiety. *Nature Reviews Neuroscience* **15**:181–192. DOI: <https://doi.org/10.1038/nrn3677>, PMID: 24552786
- Bast T**, Wilson IA, Witter MP, Morris RG. 2009. From rapid place learning to behavioral performance: a key role for the intermediate hippocampus. *PLoS Biology* **7**:e1000089. DOI: <https://doi.org/10.1371/journal.pbio.1000089>, PMID: 19385719
- Baumgart J**, Grebe N. 2015. C57BL/6-specific conditions for efficient in utero electroporation of the central nervous system. *Journal of Neuroscience Methods* **240**:116–124. DOI: <https://doi.org/10.1016/j.jneumeth.2014.11.004>, PMID: 25445056
- Ben-Ari Y**, Cherubini E, Corradetti R, Gaiarsa JL. 1989. Giant synaptic potentials in immature rat CA3 hippocampal neurones. *The Journal of Physiology* **416**:303–325. DOI: <https://doi.org/10.1113/jphysiol.1989.sp017762>, PMID: 2575165
- Benchenane K**, Peyrache A, Khamassi M, Tierney PL, Gioanni Y, Battaglia FP, Wiener SI. 2010. Coherent theta oscillations and reorganization of spike timing in the hippocampal- prefrontal network upon learning. *Neuron* **66**:921–936. DOI: <https://doi.org/10.1016/j.neuron.2010.05.013>, PMID: 20620877
- Berndt A**, Schoenenberger P, Mattis J, Tye KM, Deisseroth K, Hegemann P, Oertner TG. 2011. High-efficiency channelrhodopsins for fast neuronal stimulation at low light levels. *PNAS* **108**:7595–7600. DOI: <https://doi.org/10.1073/pnas.1017210108>, PMID: 21504945
- Bitzenhofer SH**, Hanganu-Opatz IL. 2014. Oscillatory coupling within neonatal prefrontal-hippocampal networks is independent of selective removal of GABAergic neurons in the hippocampus. *Neuropharmacology* **77**:57–67. DOI: <https://doi.org/10.1016/j.neuropharm.2013.09.007>, PMID: 24056266
- Bitzenhofer SH**, Sieben K, Siebert KD, Spehr M, Hanganu-Opatz IL. 2015. Oscillatory activity in developing prefrontal networks results from theta-gamma-modulated synaptic inputs. *Cell Reports* **11**:486–497. DOI: <https://doi.org/10.1016/j.celrep.2015.03.031>, PMID: 25865885

- Bitzenhofer SH**, Ahlbeck J, Hanganu-Opatz IL. 2017a. Methodological Approach for Optogenetic Manipulation of Neonatal Neuronal Networks. *Frontiers in Cellular Neuroscience* **11**:239–252. DOI: <https://doi.org/10.3389/fncel.2017.00239>, PMID: 28848399
- Bitzenhofer SH**, Ahlbeck J, Wolff A, Wiegert JS, Gee CE, Oertner TG, Hanganu-Opatz IL. 2017b. Layer-specific optogenetic activation of pyramidal neurons causes beta-gamma entrainment of neonatal networks. *Nature Communications* **8**:14563. DOI: <https://doi.org/10.1038/ncomms14563>, PMID: 28216627
- Borrell V**, Yoshimura Y, Callaway EM. 2005. Targeted gene delivery to telencephalic inhibitory neurons by directional in utero electroporation. *Journal of Neuroscience Methods* **143**:151–158. DOI: <https://doi.org/10.1016/j.jneumeth.2004.09.027>, PMID: 15814147
- Brincat SL**, Miller EK. 2015. Frequency-specific hippocampal-prefrontal interactions during associative learning. *Nature Neuroscience* **18**:576–581. DOI: <https://doi.org/10.1038/nn.3954>, PMID: 25706471
- Brockmann MD**, Pöschel B, Cichon N, Hanganu-Opatz IL. 2011. Coupled oscillations mediate directed interactions between prefrontal cortex and hippocampus of the neonatal rat. *Neuron* **71**:332–347. DOI: <https://doi.org/10.1016/j.neuron.2011.05.041>, PMID: 21791291
- Buhl DL**, Buzsáki G. 2005. Developmental emergence of hippocampal fast-field "ripple" oscillations in the behaving rat pups. *Neuroscience* **134**:1423–1430. DOI: <https://doi.org/10.1016/j.neuroscience.2005.05.030>, PMID: 16039793
- Buzsáki G**. 2015. Hippocampal sharp wave-ripple: A cognitive biomarker for episodic memory and planning. *Hippocampus* **25**:1073–1188. DOI: <https://doi.org/10.1002/hipo.22488>, PMID: 26135716
- Cichon NB**, Denker M, Grün S, Hanganu-Opatz IL. 2014. Unsupervised classification of neocortical activity patterns in neonatal and pre-juvenile rodents. *Frontiers in Neural Circuits* **8**:50. DOI: <https://doi.org/10.3389/fncir.2014.00050>, PMID: 24904296
- Cirelli C**, Tononi G. 2015. Cortical development, electroencephalogram rhythms, and the sleep/wake cycle. *Biological Psychiatry* **77**:1071–1078. DOI: <https://doi.org/10.1016/j.biopsych.2014.12.017>, PMID: 25680672
- Colgin LL**. 2011. Oscillations and hippocampal-prefrontal synchrony. *Current Opinion in Neurobiology* **21**:467–474. DOI: <https://doi.org/10.1016/j.conb.2011.04.006>, PMID: 21571522
- Colgin LL**. 2016. Rhythms of the hippocampal network. *Nature Reviews Neuroscience* **17**:239–249. DOI: <https://doi.org/10.1038/nrn.2016.21>, PMID: 26961163
- Dong HW**, Swanson LW, Chen L, Fanselow MS, Toga AW. 2009. Genomic-anatomic evidence for distinct functional domains in hippocampal field CA1. *PNAS* **106**:11794–11799. DOI: <https://doi.org/10.1073/pnas.0812608106>, PMID: 19561297
- Dupont E**, Hanganu IL, Kilb W, Hirsch S, Luhmann HJ. 2006. Rapid developmental switch in the mechanisms driving early cortical columnar networks. *Nature* **439**:79–83. DOI: <https://doi.org/10.1038/nature04264>, PMID: 16327778
- Eichenbaum H**. 2017. Prefrontal-hippocampal interactions in episodic memory. *Nature Reviews Neuroscience* **18**:547–558. DOI: <https://doi.org/10.1038/nrn.2017.74>, PMID: 28655882
- Fanselow MS**, Dong HW. 2010. Are the dorsal and ventral hippocampus functionally distinct structures? *Neuron* **65**:7–19. DOI: <https://doi.org/10.1016/j.neuron.2009.11.031>, PMID: 20152109
- Geisler C**, Robbe D, Zugaro M, Sirota A, Buzsáki G. 2007. Hippocampal place cell assemblies are speed-controlled oscillators. *PNAS* **104**:8149–8154. DOI: <https://doi.org/10.1073/pnas.0610121104>, PMID: 17470808
- Granger CWJ**. 1980. Testing for causality. *Journal of Economic Dynamics and Control* **2**:329–352. DOI: [https://doi.org/10.1016/0165-1889\(80\)90069-X](https://doi.org/10.1016/0165-1889(80)90069-X)
- Hallock HL**, Wang A, Griffin AL. 2016. Ventral midline thalamus is critical for hippocampal-prefrontal synchrony and spatial working memory. *Journal of Neuroscience* **36**:8372–8389. DOI: <https://doi.org/10.1523/JNEUROSCI.0991-16.2016>, PMID: 27511010
- Hanganu IL**, Ben-Ari Y, Khazipov R. 2006. Retinal waves trigger spindle bursts in the neonatal rat visual cortex. *Journal of Neuroscience* **26**:6728–6736. DOI: <https://doi.org/10.1523/JNEUROSCI.0752-06.2006>, PMID: 16793880
- Hanganu-Opatz IL**. 2010. Between molecules and experience: role of early patterns of coordinated activity for the development of cortical maps and sensory abilities. *Brain Research Reviews* **64**:160–176. DOI: <https://doi.org/10.1016/j.brainresrev.2010.03.005>, PMID: 20381527
- Hartung H**, Brockmann MD, Pöschel B, De Feo V, Hanganu-Opatz IL. 2016. Thalamic and entorhinal network activity differently modulates the functional development of prefrontal-hippocampal interactions. *The Journal of Neuroscience* **36**:3676–3690. DOI: <https://doi.org/10.1523/JNEUROSCI.3232-15.2016>, PMID: 27030754
- Hoerder-Suabedissen A**, Molnár Z. 2015. Development, evolution and pathology of neocortical subplate neurons. *Nature Reviews Neuroscience* **16**:133–146. DOI: <https://doi.org/10.1038/nrn3915>, PMID: 25697157
- Honeycutt JA**, Keary Iii KM, Kania VM, Chrobak JJ. 2016. Developmental age differentially mediates the calcium-binding protein parvalbumin in the rat: Evidence for a selective decrease in hippocampal parvalbumin cell counts. *Developmental Neuroscience* **38**:105–114. DOI: <https://doi.org/10.1159/000444447>, PMID: 27002731
- Hu H**, Vervaeke K, Storm JF. 2002. Two forms of electrical resonance at theta frequencies, generated by M-current, h-current and persistent Na⁺ current in rat hippocampal pyramidal cells. *The Journal of Physiology* **545**:783–805. DOI: <https://doi.org/10.1113/jphysiol.2002.029249>, PMID: 12482886
- Hubel DH**, Wiesel TN, LeVay S. 1977. Plasticity of ocular dominance columns in monkey striate cortex. *Philosophical Transactions of the Royal Society B: Biological Sciences* **278**:377–409. DOI: <https://doi.org/10.1098/rstb.1977.0050>, PMID: 19791

- Huberman AD**, Speer CM, Chapman B. 2006. Spontaneous retinal activity mediates development of ocular dominance columns and binocular receptive fields in v1. *Neuron* **52**:247–254. DOI: <https://doi.org/10.1016/j.neuron.2006.07.028>, PMID: 17046688
- Jay TM**, Witter MP. 1991. Distribution of hippocampal CA1 and subicular efferents in the prefrontal cortex of the rat studied by means of anterograde transport of Phaseolus vulgaris-leucoagglutinin. *The Journal of Comparative Neurology* **313**:574–586. DOI: <https://doi.org/10.1002/cne.903130404>, PMID: 1783682
- Khazipov R**, Minlebaev M, Valeeva G. 2013. Early gamma oscillations. *Neuroscience* **250**:240–252. DOI: <https://doi.org/10.1016/j.neuroscience.2013.07.019>, PMID: 23872391
- Krüger HS**, Brockmann MD, Salamon J, Ittrich H, Hanganu-Opatz IL. 2012. Neonatal hippocampal lesion alters the functional maturation of the prefrontal cortex and the early cognitive development in pre-juvenile rats. *Neurobiology of Learning and Memory* **97**:470–481. DOI: <https://doi.org/10.1016/j.nlm.2012.04.001>, PMID: 22521798
- Lindemann C**, Ahlbeck J, Bitzenhofer SH, Hanganu-Opatz IL. 2016. Spindle activity orchestrates plasticity during development and sleep. *Neural Plasticity* **2016**:1–14. DOI: <https://doi.org/10.1155/2016/5787423>, PMID: 27293903
- Luhmann HJ**, Khazipov R. 2018. Neuronal activity patterns in the developing barrel cortex. *Neuroscience* **368**. DOI: <https://doi.org/10.1016/j.neuroscience.2017.05.025>, PMID: 28528963
- Minlebaev M**, Ben-Ari Y, Khazipov R. 2009. NMDA receptors pattern early activity in the developing barrel cortex in vivo. *Cerebral Cortex* **19**:688–696. DOI: <https://doi.org/10.1093/cercor/bhn115>, PMID: 18663251
- Minlebaev M**, Colonnese M, Tsintsadze T, Sirota A, Khazipov R. 2011. Early γ oscillations synchronize developing thalamus and cortex. *Science* **334**:226–229. DOI: <https://doi.org/10.1126/science.1210574>, PMID: 21998388
- Moser MB**, Moser EI, Forrest E, Andersen P, Morris RG. 1995. Spatial learning with a minislab in the dorsal hippocampus. *PNAS* **92**:9697–9701. DOI: <https://doi.org/10.1073/pnas.92.21.9697>, PMID: 7568200
- Moser EI**, Krobet KA, Moser MB, Morris RG. 1998. Impaired spatial learning after saturation of long-term potentiation. *Science* **281**:2038–2042. DOI: <https://doi.org/10.1126/science.281.5385.2038>, PMID: 9748165
- Niwa M**, Kamiya A, Murai R, Kubo K, Gruber AJ, Tomita K, Lu L, Tomisato S, Jaaro-Peled H, Seshadri S, Hiyama H, Huang B, Kohda K, Noda Y, O'Donnell P, Nakajima K, Sawa A, Nabeshima T. 2010. Knockdown of DISC1 by in utero gene transfer disturbs postnatal dopaminergic maturation in the frontal cortex and leads to adult behavioral deficits. *Neuron* **65**:480–489. DOI: <https://doi.org/10.1016/j.neuron.2010.01.019>, PMID: 20188653
- Nolte G**, Bai O, Wheaton L, Mari Z, Vorbach S, Hallett M. 2004. Identifying true brain interaction from EEG data using the imaginary part of coherence. *Clinical Neurophysiology* **115**:2292–2307. DOI: <https://doi.org/10.1016/j.clinph.2004.04.029>, PMID: 15351371
- O'Keefe J**, Nadel L. 1978. *The Hippocampus as a Cognitive Map*. New York: Oxford University Press.
- O'Keefe J**, Recce ML. 1993. Phase relationship between hippocampal place units and the EEG theta rhythm. *Hippocampus* **3**:317–330. DOI: <https://doi.org/10.1002/hipo.450030307>, PMID: 8353611
- Patel J**, Schomburg EW, Berényi A, Fujisawa S, Buzsáki G. 2013. Local generation and propagation of ripples along the septotemporal axis of the hippocampus. *The Journal of Neuroscience* **33**:17029–17041. DOI: <https://doi.org/10.1523/JNEUROSCI.2036-13.2013>, PMID: 24155307
- Pitkänen A**, Pikkarainen M, Nurminen N, Ylinen A. 2000. Reciprocal connections between the amygdala and the hippocampal formation, perirhinal cortex, and postrhinal cortex in rat. A review. *Annals of the New York Academy of Sciences* **911**:369–391. DOI: <https://doi.org/10.1111/j.1749-6632.2000.tb06738.x>, PMID: 10911886
- Place R**, Farovik A, Brockmann M, Eichenbaum H. 2016. Bidirectional prefrontal-hippocampal interactions support context-guided memory. *Nature Neuroscience* **19**:992–994. DOI: <https://doi.org/10.1038/nn.4327>, PMID: 27322417
- Rodrigues PL**, Baccala LA. 2016. Statistically significant time-varying neural connectivity estimation using generalized partial directed coherence. *Conference proceedings : ... Annual International Conference of the IEEE Engineering in Medicine and Biology Society. IEEE Engineering in Medicine and Biology Society. Annual Conference* **2016**:5493–5496. DOI: <https://doi.org/10.1109/EMBC.2016.7591970>, PMID: 28269501
- Royer S**, Sirota A, Patel J, Buzsáki G. 2010. Distinct representations and theta dynamics in dorsal and ventral hippocampus. *Journal of Neuroscience* **30**:1777–1787. DOI: <https://doi.org/10.1523/JNEUROSCI.4681-09.2010>, PMID: 20130187
- Seelke AM**, Blumberg MS. 2010. Developmental appearance and disappearance of cortical events and oscillations in infant rats. *Brain Research* **1324**:34–42. DOI: <https://doi.org/10.1016/j.brainres.2010.01.088>, PMID: 20138849
- Shen J**, Colonnese MT. 2016. Development of Activity in the Mouse Visual Cortex. *Journal of Neuroscience* **36**:12259–12275. DOI: <https://doi.org/10.1523/JNEUROSCI.1903-16.2016>, PMID: 27903733
- Siapas AG**, Wilson MA. 1998. Coordinated interactions between hippocampal ripples and cortical spindles during slow-wave sleep. *Neuron* **21**:1123–1128. DOI: [https://doi.org/10.1016/S0896-6273\(00\)80629-7](https://doi.org/10.1016/S0896-6273(00)80629-7), PMID: 9856467
- Siapas AG**, Lubenov EV, Wilson MA. 2005. Prefrontal phase locking to hippocampal theta oscillations. *Neuron* **46**:141–151. DOI: <https://doi.org/10.1016/j.neuron.2005.02.028>, PMID: 15820700
- Sigurdsson T**, Stark KL, Karayiorgou M, Gogos JA, Gordon JA. 2010. Impaired hippocampal-prefrontal synchrony in a genetic mouse model of schizophrenia. *Nature* **464**:763–767. DOI: <https://doi.org/10.1038/nature08855>, PMID: 20360742
- Sirota A**, Montgomery S, Fujisawa S, Isomura Y, Zugaro M, Buzsáki G. 2008. Entrainment of neocortical neurons and gamma oscillations by the hippocampal theta rhythm. *Neuron* **60**:683–697. DOI: <https://doi.org/10.1016/j.neuron.2008.09.014>, PMID: 19038224

- Spellman T**, Rigotti M, Ahmari SE, Fusi S, Gogos JA, Gordon JA. 2015. Hippocampal-prefrontal input supports spatial encoding in working memory. *Nature* **522**:309–314. DOI: <https://doi.org/10.1038/nature14445>, PMID: 26053122
- Stark E**, Eichler R, Roux L, Fujisawa S, Rotstein HG, Buzsáki G. 2013. Inhibition-induced theta resonance in cortical circuits. *Neuron* **80**:1263–1276. DOI: <https://doi.org/10.1016/j.neuron.2013.09.033>, PMID: 24314731
- Stewart M**, Fox SE. 1990. Do septal neurons pace the hippocampal theta rhythm? *Trends in Neurosciences* **13**: 163–169. DOI: [https://doi.org/10.1016/0166-2236\(90\)90040-H](https://doi.org/10.1016/0166-2236(90)90040-H), PMID: 1693232
- Strange BA**, Witter MP, Lein ES, Moser EI. 2014. Functional organization of the hippocampal longitudinal axis. *Nature Reviews Neuroscience* **15**:655–669. DOI: <https://doi.org/10.1038/nrn3785>, PMID: 25234264
- Stujenske JM**, Spellman T, Gordon JA. 2015. Modeling the spatiotemporal dynamics of light and heat propagation for in vivo optogenetics. *Cell Reports* **12**:525–534. DOI: <https://doi.org/10.1016/j.celrep.2015.06.036>, PMID: 26166563
- Swanson LW**. 1981. A direct projection from Ammon's horn to prefrontal cortex in the rat. *Brain Research* **217**: 150–154. DOI: [https://doi.org/10.1016/0006-8993\(81\)90192-X](https://doi.org/10.1016/0006-8993(81)90192-X), PMID: 7260612
- Szczurkowska J**, Cwetsch AW, dal Maschio M, Ghezzi D, Ratto GM, Cancedda L. 2016. Targeted in vivo genetic manipulation of the mouse or rat brain by in utero electroporation with a triple-electrode probe. *Nature Protocols* **11**:399–412. DOI: <https://doi.org/10.1038/nprot.2016.014>, PMID: 26844428
- Tabata H**, Nakajima K. 2001. Efficient in utero gene transfer system to the developing mouse brain using electroporation: visualization of neuronal migration in the developing cortex. *Neuroscience* **103**:865–872. DOI: [https://doi.org/10.1016/S0306-4522\(01\)00016-1](https://doi.org/10.1016/S0306-4522(01)00016-1), PMID: 11301197
- Taxidis J**, Coomber B, Mason R, Owen M. 2010. Assessing cortico-hippocampal functional connectivity under anesthesia and kainic acid using generalized partial directed coherence. *Biological Cybernetics* **102**:327–340. DOI: <https://doi.org/10.1007/s00422-010-0370-1>, PMID: 20204395
- Thompson CL**, Pathak SD, Jeromin A, Ng LL, MacPherson CR, Mortrud MT, Cusick A, Riley ZL, Sunkin SM, Bernard A, Puchalski RB, Gage FH, Jones AR, Bajic VB, Hawrylycz MJ, Lein ES. 2008. Genomic anatomy of the hippocampus. *Neuron* **60**:1010–1021. DOI: <https://doi.org/10.1016/j.neuron.2008.12.008>, PMID: 19109908
- Tolner EA**, Sheikh A, Yukin AY, Kaila K, Kanold PO. 2012. Subplate neurons promote spindle bursts and thalamocortical patterning in the neonatal rat somatosensory cortex. *Journal of Neuroscience* **32**:692–702. DOI: <https://doi.org/10.1523/JNEUROSCI.1538-11.2012>, PMID: 22238105
- Vertes RP**, Hoover WB, Szigeti-Buck K, Leranath C. 2007. Nucleus reuniens of the midline thalamus: link between the medial prefrontal cortex and the hippocampus. *Brain Research Bulletin* **71**:601–609. DOI: <https://doi.org/10.1016/j.brainresbull.2006.12.002>, PMID: 17292803
- Wirt RA**, Hyman JM. 2017. Integrating Spatial Working Memory and Remote Memory: Interactions between the Medial Prefrontal Cortex and Hippocampus. *Brain Sciences* **7**:43. DOI: <https://doi.org/10.3390/brainsci7040043>, PMID: 28420200
- Witter MP**, Van Hoesen GW, Amaral DG. 1989. Topographical organization of the entorhinal projection to the dentate gyrus of the monkey. *Journal of Neuroscience* **9**:216–228. PMID: 2913203
- Witter MP**, Amaral DG. 2004. Hippocampal Formation. In: *The Rat Nervous System*. Elsevier Inc. p. 635–704. DOI: <https://doi.org/10.1016/B978-012547638-6/50022-5>
- Xu HP**, Furman M, Mineur YS, Chen H, King SL, Zenisek D, Zhou ZJ, Butts DA, Tian N, Picciotto MR, Crair MC. 2011. An instructive role for patterned spontaneous retinal activity in mouse visual map development. *Neuron* **70**:1115–1127. DOI: <https://doi.org/10.1016/j.neuron.2011.04.028>, PMID: 21689598
- Xu W**, Südhof TC. 2013. A neural circuit for memory specificity and generalization. *Science* **339**:1290–1295. DOI: <https://doi.org/10.1126/science.1229534>, PMID: 23493706
- Yang JW**, Reyes-Puerta V, Kilb W, Luhmann HJ. 2016. Spindle bursts in neonatal rat cerebral cortex. *Neural Plasticity* **2016**:1–11. DOI: <https://doi.org/10.1155/2016/3467832>, PMID: 27034844
- Yasuda M**, Johnson-Venkatesh EM, Zhang H, Parent JM, Sutton MA, Umemori H. 2011. Multiple forms of activity-dependent competition refine hippocampal circuits in vivo. *Neuron* **70**:1128–1142. DOI: <https://doi.org/10.1016/j.neuron.2011.04.027>, PMID: 21689599
- Ye X**, Kapeller-Libermann D, Travaglia A, Inda MC, Alberini CM. 2017. Direct dorsal hippocampal-pretectal cortex connections strengthen fear memories. *Nature Neuroscience* **20**:52–61. DOI: <https://doi.org/10.1038/nn.4443>, PMID: 27869801
- Yuste R**, Nelson DA, Rubin WW, Katz LC. 1995. Neuronal domains in developing neocortex: mechanisms of coactivation. *Neuron* **14**:7–17. DOI: [https://doi.org/10.1016/0896-6273\(95\)90236-8](https://doi.org/10.1016/0896-6273(95)90236-8), PMID: 7826643
- Zhang L**, Spigelman I, Carlen PL. 1990. Whole-cell patch study of GABAergic inhibition in CA1 neurons of immature rat hippocampal slices. *Developmental Brain Research* **56**:127–130. DOI: [https://doi.org/10.1016/0165-3806\(90\)90171-T](https://doi.org/10.1016/0165-3806(90)90171-T), PMID: 2279324

4.2 Article 2

Knock-down of hippocampal DISC1 in immune-challenged mice impairs the prefrontal–hippocampal coupling and the cognitive performance throughout development

Xi Xia Xu^{1*}, **Lingzhen Song**^{1*} and Ileana L. Hanganu-Opatz¹

¹ Institute of Developmental Neurophysiology, Center for Molecular Neurobiology, University Medical Center Hamburg-Eppendorf, 20251 Hamburg, Germany

* These authors contributed equally to this work.

Cerebral Cortex, February 2021, 31: 1240–1258

Personal contribution

I carried out part of *in vivo* electrophysiology and behavior experiments. I assisted with formal analysis. I discussed, reviewed and edited the manuscript.

ORIGINAL ARTICLE

Knock-Down of Hippocampal DISC1 in Immune-Challenged Mice Impairs the Prefrontal–Hippocampal Coupling and the Cognitive Performance Throughout Development

Xi Xia Xu, Lingzhen Song and Ileana L. Hanganu-Opatz

Institute of Developmental Neurophysiology, Center for Molecular Neurobiology, University Medical Center Hamburg-Eppendorf, 20251 Hamburg, Germany

Address correspondence to Ileana L. Hanganu-Opatz, Institute of Developmental Neurophysiology, Center for Molecular Neurobiology, University Medical Center Hamburg-Eppendorf, Falkenried 94, 20251 Hamburg, Germany. Email: hangop@zmnh.uni-hamburg.de or Xi Xia Xu, Institute of Developmental Neurophysiology, Center for Molecular Neurobiology, University Medical Center Hamburg-Eppendorf, Falkenried 94, 20251 Hamburg, Germany. Email: xi Xia Xu@zmnh.uni-hamburg.de.

Xi Xia Xu and Lingzhen Song have contributed equally to this work

Abstract

Disrupted-in-schizophrenia 1 (DISC1) gene represents an intracellular hub of developmental processes. When combined with early environmental stressors, such as maternal immune activation, but not in the absence of thereof, whole-brain DISC1 knock-down leads to memory and executive deficits as result of impaired prefrontal–hippocampal communication throughout development. While synaptic dysfunction in neonatal prefrontal cortex (PFC) has been recently identified as one source of abnormal long-range coupling, the contribution of hippocampus (HP) is still unknown. Here, we aim to fill this knowledge gap by combining *in vivo* electrophysiology and optogenetics with morphological and behavioral assessment of immune-challenged mice with DISC1 knock-down either in the whole brain (GE) or restricted to pyramidal neurons in hippocampal CA1 area (G_{HPE}). We found abnormal network activity, sharp-waves, and neuronal firing in CA1 that complement the deficits in upper layer of PFC. Moreover, optogenetic activating CA1 pyramidal neurons fails to activate the prefrontal local circuits. These deficits that persist till prejuvenile age relate to dendrite sparsification and loss of spines of CA1 pyramidal neurons. As a long-term consequence, DISC1 knock-down in HP leads to poorer recognition memory at prejuvenile age. Thus, DISC1-controlled developmental processes in HP in immune-challenged mice are critical for circuit function and cognitive behavior.

Key words: development, DISC1, hippocampal maturation, optogenetics, prefrontal–hippocampal synchrony

Introduction

Highly dynamic processes control the wiring of neural circuits during development. At its end, reliable communication between brain areas accounts for the complex behavioral abilities of an adult. For example, the coactivation of prefrontal and hippocampal networks in theta-gamma oscillatory rhythms is critical for the precise information flow in mnemonic and executive tasks (Siapas et al. 2005; Spellman et al. 2015; Backus et al. 2016; Eichenbaum 2017). This prefrontal-hippocampal coupling emerges early in life, and the unidirectional drive from the CA1 pyramidal neurons boosts the initial entrainment of local circuits across prefrontal layers (Brockmann et al. 2011; Bitzenhofer et al. 2017b; Ahlbeck et al. 2018). The long-range coupling during development has been proposed to critically contribute to the adult function and cognitive abilities. On the flip side, disease-related dysfunction and poor behavioral performance might result from developmental miswiring (Chini et al. 2020).

The maturation of connectivity and functional coupling within the brain is controlled by numerous cell autonomous processes as well as extracellular and environmental factors. Disrupted-in-schizophrenia 1 (DISC1) is an intracellular scaffold protein that has been identified as an intracellular hub of developmental processes, in particular synapse regulation (Narayan et al. 2013). Despite its name, DISC1 is unlikely to be a “genetic” factor causing schizophrenia (Sullivan et al. 2012; Ripke et al. 2013). Instead, DISC1 has been proven to illustrate the relevance of abnormal development for multiple mental conditions, because it orchestrates molecular cascades hypothesized to underlie disease-relevant physiological and behavioral deficits (Cuthbert and Insel 2013). Mouse models mimicking DISC1 dysfunction have impaired memory and attention as results of disrupted prefrontal-hippocampal circuits (Koike et al. 2006; Niwa et al. 2010; Kvalo et al. 2011; Saito et al. 2016; Crabtree et al. 2017). These deficits are more prominent when environmental stressors, such as maternal immune activation (MIA) additionally disrupt the *Disc1* locus (Cash-Padgett et al. 2013a; Lipina et al. 2013). This might be due to the fact that mutated DISC1 modulates the basal or MIA-induced cytokine production by interfering with glycogen synthase kinase-3 (Beurel et al. 2010).

Since DISC1 controls the developmental molecular cascades, it is likely that its dysfunction decisively contributes to early miswiring. Indeed, recent findings revealed that abnormal DISC1 expression perturbs the maturation of prefrontal-hippocampal coupling (Hartung et al. 2016; Oberlander et al. 2019; Xu et al. 2019; Chini et al. 2020). Immune challenged mice with a whole-brain truncated form of DISC1 (dual-hit GE mice) have disorganized oscillatory activity as well as weaker coupling and directed interactions between prefrontal cortex (PFC) and hippocampus (HP) at neonatal age. In contrast, the activity patterns and communication within prefrontal-hippocampal networks as well as the early cognitive abilities were largely unaffected in single-hit genetic (G) (only DISC1 knock-down) or environmental (E) (only MIA) mouse models (Hartung et al. 2016; Oberlander et al. 2019).

The early dysfunction of dual-hit GE mice might result from abnormal activity in either one or both brain areas or from disrupted projections from HP to PFC. Recently, we identified transient neonatal synaptic deficits of prefrontal layer 2/3 pyramidal neurons as one mechanism underlying the abnormal prefrontal-hippocampal communication throughout development (Xu et al. 2019; Chini et al. 2020). However, it is

unknown whether developmental dysfunction in HP and/or abnormal prefrontal-hippocampal connectivity contributes to the disrupted prefrontal-hippocampal communication. Here, we address this open question by using in utero electroporation (IUE) to knock down DISC1 in CA1 pyramidal neurons of intermediate/ventral HP (i/vHP) during perinatal development in mice exposed to MIA (dual-hit $G_{HP}E$ mice). We combined in vivo electrophysiology with optogenetics to provide direct evidence for the causal contribution of hippocampal pyramidal neurons to the deficits of prefrontal-hippocampal coupling in $G_{HP}E$ mice throughout development.

Materials and Methods

All experiments were performed in compliance with the German laws and the guidelines of the European Community for the use of animals in research and were approved by the local ethical committee (015/17, 015/18). Timed-pregnant C57BL/6J mice from the animal facility of the University Medical Center Hamburg-Eppendorf were used. The day of vaginal plug detection was defined as gestational day(G) 0.5, whereas the day of birth was defined as postnatal day(P) 0.

Experimental Design

Multisite extracellular recordings and behavioral testing were performed on pups of both sexes during neonatal development (i.e., P8–P10) as well as during prejuvenile development (i.e., P16–P23). None of the investigated parameters differed between males and females, thus, data for both sexes were pooled. In this study, we applied IUE with short-hairpin RNA (shRNA) to DISC1 (5'-GGCAAACACTGTGAAGTGC-3') under H1 promoter-driven pSuper plasmid to knock down the DISC1 in CA1 of i/vHP. A scrambled target sequence without homology to any known messenger RNA (5'-ATCTCGCTTGGGCGAGAGT-3') was used as control shRNA. Two genetically engineered mutant mouse models were investigated. First, heterozygous genetically engineered mutant DISC1 mice carrying a *Disc1* allele (*Disc1*Tm1Kara) on a C57BL/6J background were used. Due to two termination codons and a premature polyadenylation site, the allele produces a truncated transcript (Kvalo et al. 2008). Genotypes were determined using genomic DNA and following primer sequences: forward primer 5'-TAGCCACTCTCATTGTCAGC-3', reverse primer 5'-CCTCATCCCTTCCACTCAGC-3'. DISC1 whole-brain knock-down mice were transfected by IUE with control shRNA+ pAAVCAG-tDimer2 or control shRNA+ pAAV-CAG-ChR2(E123T/T159C)-2A-tDimer2 at G15.5. Control shRNA had no effects on the network activity and prefrontal-hippocampal coupling at neonatal and prejuvenile ages. The resulting offspring mimicking the dual genetic-environmental etiology of mental disorders were classified in GE mice (whole-brain DISC1 knock-down + MIA). Second, C57BL/6J mice with DISC1 knock-down confined to HP were engineered through transfection with DISC1 shRNA. Mice were transfected by IUE with DISC1 shRNA+ pAAVCAG-tDimer2 or DISC1 shRNA+ pAAV-CAG-ChR2(E123T/T159C)-2A-tDimer2 at G15.5. The resulting offspring mimicking the dual genetic-environmental etiology of mental disorders were classified in $G_{HP}E$ mice (hippocampal DISC1 knock-down + MIA). Both two mouse models were challenged by MIA, using the viral mimetic polyinosinic:polycytidylic acid (poly I:C, 5 mg/kg) injected intravenously (i.v.) into the pregnant dams at gestational day G9.5. The offspring of wild-type C57BL/6J

dams injected at G9.5 with saline (0.9%, i.v.) were transfected with control shRNA+pAAV-CAG-tDimer2 or control shRNA+pAAV-CAG-ChR2(E123T/T159C)-2A-tDimer2 and were classified in control mice (CON).

In Utero Electroporation

Starting 1 day before and until 2 days after surgery, timed-pregnant C57BL/6J mice received on a daily basis additional wet food supplemented with 2–4 drops Metacam (0.5 mg/ml, Boehringer-Ingelheim, Germany). At G15.5, pregnant mice were injected subcutaneously with buprenorphine (0.05 mg/kg body weight) 30 min before surgery. The surgery was performed on a heating blanket and toe pinch and breathing were monitored throughout. Under isoflurane anesthesia (induction: 5%, maintenance: 3.5%), the eyes of the dam were covered with eye ointment to prevent damage before the uterine horns were exposed and moistened with warm sterile phosphate buffered saline (PBS, 37°C). Solution containing 1.25 µg/µL DNA [pAAV-CAG-ChR2(E123T/T159C)-2A-tDimer2, or pAAV-CAG-tDimer2, or shRNA to DISC1 together with pAAV-CAG-tDimer2 (molar ratio = 3:1)] and 0.1% fast green dye at a volume of 0.75–1.25 µL were injected into the right lateral ventricle of individual embryos using pulled borosilicate glass capillaries with a sharp and long tip. Plasmid DNA was purified with NucleoBond (Macherey-Nagel). The 2A encodes for a ribosomal skip sentence, splitting the fluorescent protein tDimer2 from the opsin during gene translation. To target i/vHP, a tri-polar approach was used (Szczyrkowska et al. 2016). Each embryo within the uterus was placed between the electroporation tweezer-type paddles (5 mm diameter, both positive poles, Protech) that were oriented at 90° leftward angle from the midline and a 0° angle downward from anterior to posterior. A third custom build negative pole was positioned on top of the head roughly between the eyes. Electrode pulses (30 V, 50 ms) were applied six times at intervals of 950 ms controlled by an electroporator (CU21EX, BEX). By these means, neural precursor cells from the subventricular zone, which radially migrate into the i/vHP CA1 area, were transfected. The expression was confined to HP and no neighboring neocortical areas were transfected. Uterine horns were placed back into the abdominal cavity after electroporation. The abdominal cavity was filled with warm sterile PBS (37°C) and abdominal muscles and skin were sutured individually with absorbable and nonabsorbable suture thread, respectively. After recovery, pregnant mice were returned to their home cages, which were half placed on a heating blanket for 2 days after surgery.

Surgery for In Vivo Electrophysiological Recordings and Light Stimulation

For neonatal (P8–10) recordings in nonanesthetized state, 0.5% bupivacain/1% lidocaine was locally applied on the neck muscles. For prejuvenile (P20–23) recordings under anesthesia, mice were injected intraperitoneally (i.p.) with urethane (1 mg/g body weight; Sigma-Aldrich) prior to surgery. For both age groups, under isoflurane anesthesia (induction: 5%, maintenance: 2.5%), the head of the pup was fixed into a stereotaxic apparatus using two plastic bars mounted on the nasal and occipital bones with dental cement. The bone above the PFC (0.5 mm anterior to bregma, 0.1–0.5 mm right to the midline), HP (3.5 mm posterior to bregma, 3.5 mm right to the midline) was carefully removed by drilling a hole of <0.5 mm in diameter. After a 10 min recovery period on a heating blanket, mouse was placed into the setup

for electrophysiological recording. Throughout the surgery and recording session the mouse was positioned on a heating pad with the temperature kept at 37°C.

Electrophysiological Recordings

A four-shank electrode (NeuroNexus) containing 4 x 4 recording sites (0.4–0.8 MΩ impedance, 100 µm spacing, 125 µm inter-shank spacing) was inserted into the prelimbic (PL) subdivision of PFC. A one-shank optoelectrode (NeuroNexus) containing 1 x 16 recordings sites (0.4–0.8 MΩ impedance, 50 µm spacing) aligned with an optical fiber (105 mm diameter) ending 200 µm above the top recording site was inserted into CA1 area. A silver wire was inserted into the cerebellum and served as ground and reference electrode. Extracellular signals were band-pass filtered (0.1–9000 Hz) and digitized (32 kHz) with a multichannel extracellular amplifier (Digital Lynx SX; Neuralynx) and the Cheetah acquisition software (Neuralynx). Spontaneous (i.e., not induced by light stimulation) activity was recorded for 20 min at the beginning of each recording session as baseline activity. The position of recording electrodes in the PL and CA1 area of i/vHP was confirmed post mortem. Wide field fluorescence images were acquired to reconstruct the recording electrode position in brain slices of electrophysiologically investigated pups and to localize tDimer2 expression in pups after IUE. Only pups with correct electrode and transfection position were considered for further analysis. In PL, the most medial shank was inserted to target layer 2/3, whereas the most lateral shank was located into layer 5/6. For the analysis of hippocampal local field potential (LFP), the recording site located in the pyramidal layer, where sharp waves (SPWs) reverse (Bitzenhofer and Hanganu-Opatz 2014) was selected to minimize any nonstationary effects of large amplitude events. For the analysis of hippocampal firing, two channels above and two channels below the site used for LFP analysis were additionally considered.

Light Stimulation

Pulsatile (laser on–off, 3 ms-long, 8 Hz) or ramp (linearly increasing power, 3 s-long) light stimulations were performed with an arduino uno (Arduino) controlled diode laser (473 nm; Omicron). Laser power was adjusted to trigger neuronal spiking in response to >25% of 3 ms-long light pulses at 8 Hz. Resulting light power was in the range of 20–40 mW/mm² at the fiber tip.

Behavioral Experiments

The exploratory behavior and recognition memory of CON, G_{HP}E, and GE mice were tested at prejuvenile age (P16–20) using previously established experimental protocols (Kruger et al. 2012). Briefly, all behavioral tests were conducted in a custom-made circular white arena, the size of which (D: 34 cm, H: 30 cm) maximized exploratory behavior, while minimizing incidental contact with testing objects (Heyser and Ferris 2013). The objects used for testing of novelty recognition were six differently shaped, textured and colored, easy to clean items that were provided with magnets to fix them to the bottom of the arena. Object sizes (H: 3 cm, diameter: 1.5–3 cm) were smaller than twice the size of the mouse and did not resemble living stimuli (no eye spots, predator shape). The objects were positioned at 10 cm from the borders and 8 cm from the center of the arena. After every trial the objects and arena were cleaned with 0.1% acetic acid to remove all odors. A black and white CCD camera (VIDEOR TECHNICAL E. Hartig GmbH) was mounted 100 cm above the arena and connected to a PC via PCI interface

serving as frame grabber for video tracking software (Video Mot2 software, TSE Systems GmbH).

Exploratory Behavior in the Open Field

Mice (P15) were habituated to the arena by freely exploring the arena during two 10-min sessions 1 day before the OF task. The next day, mice (P16) were allowed to freely explore the testing arena for 10 min. Additionally, the floor area of the arena was digitally subdivided in 8 zones (4 center zones and 4 border zones) using the zone monitor mode of the VideoMot 2 analysis software (VideoMot 2, TSE Systems GmbH). The time spent by pups in center and border zones, as well as the running distance and velocity were quantified.

Novelty Recognition Paradigms

All protocols for assessing item recognition memory in P17 mice consisted of familiarization and testing trials (Ennaceur and Delacour 1988). In the novel object recognition (NOR) task, during the familiarization trial each mouse was placed into the arena containing two identical objects and released against the center of the opposite wall with the back to the objects. After 10 min of free exploration of objects, the mouse was returned to a temporary holding cage. Subsequently, the test trial was performed after a delay of 5 min postfamiliarization. The mice were allowed to investigate one familiar and one novel object with a different shape and texture for 5 min. Since some mice lost interest to achieve the tasks even before the end of investigation time, object interaction during the first 3 min was analyzed and compared between the groups. Discrimination ratio was calculated as (time spent interacting with novel object – time spent interacting with the familiar object)/(time spent interacting with novel object + time spent interacting with the familiar object).

In the recency recognition (RR) task, tested at P19–20, mice experienced two 10 min-long familiarization trials with two different sets of identical objects that were separated by a delay of 30 min. The second familiarization trial was followed after 5 min by a test trial in which one object used in the first and one object used in the second more recent familiarization trial were placed in the arena at the same positions as during the familiarization trials. Object interaction during the first 3 min was analyzed and compared between the groups. All trials were video-tracked and the analysis was performed using the Video Mot2 analysis software. The object recognition module of the software was used and a three-point tracking method identified the head, the rear end and the center of gravity of the mouse. Digitally, a circular zone of 1.5 cm was created around each object and every entry of the head point into this area was considered as object interaction. Climbing or sitting on the object, mirrored by the presence of both head and center of gravity points within the circular zone, were not counted as interactions. Discrimination ratios were calculated as (time spent interacting with more recent object – time spent interacting with less recent object)/(time spent interacting with more recent object + time spent interacting with less recent object).

Histology and Immunohistochemistry

Histological procedures were performed as previously described (Bitzenhofer et al. 2017b; Oberlander et al. 2019; Xu et al. 2019). Briefly, P8–10 and P20–23 mice were anesthetized with 10% ketamine (aniMedica)/2% xylazine (WDT) in 0.9% NaCl solution (10 µg/g body weight, i.p.) and transcardially perfused

with Histofix (Carl Roth) containing 4% paraformaldehyde. Brains were postfixed in Histofix for 24 h and sectioned coronally at 50 µm (immunohistochemistry) or 100 µm (Sholl and spine analysis). Free-floating slices were permeabilized and blocked with PBS containing 0.8% Triton X 100 (Sigma-Aldrich), 5% normal bovine serum (Jackson Immuno Research) and 0.05% sodium azide. Subsequently, slices were incubated with mouse monoclonal Alexa Fluor-488 conjugated antibody against NeuN (1:200, MAB377X, Merck Millipore) or the rabbit polyclonal primary antibody against DISC1 (1:250, 40–6800, Thermo Fisher Scientific), followed by 2 h incubation with Alexa Fluor-488 goat anti-rabbit IgG secondary antibody (1:500, A11008, Merck Millipore). Slices were transferred to glass slides and covered with Fluoromount (Sigma-Aldrich). Wide-field fluorescence images were acquired to reconstruct the recording electrode position and the location of tDimer2 expression. High-magnification images were acquired by confocal microscopy (DM IRBE, Leica) to quantify DISC1 expression. For this, the fluorescence intensity of DISC1 in tDimer2-positive neurons was calculated. All images were similarly processed and analyzed using ImageJ software.

Neuronal Morphological Analysis

Microscopic stacks were examined on a confocal microscopy (DM IRBE, Leica Microsystems, Zeiss LSN700). Stacks were acquired as 2048 × 2048 pixel images (pixel size, 78 nm; Z-step, 500 nm). Sholl analysis and spine density quantification were carried out in the ImageJ environment. For Sholl analysis, images were binarized (auto threshold) and dendrites were traced using the semiautomated plugin *Simple Neurite Tracer*. The traced dendritic tree was analyzed with the plugin *Sholl Analysis*, after the geometric center was identified using the *blow/lasso* tool. For spine density quantification, the length (line) and number of spines (point picker) on the dendrite of interest (apical, basal, proximal oblique, or secondary apical) were quantified.

Data Analysis

Data were imported and analyzed offline using custom-written tools in MATLAB software version 7.7 (Mathworks). The data were processed as following: (i) band-pass filtered (500–5000 Hz) to detect multiple-unit activity (MUA) as negative deflections exceeding five times the standard deviation of the filtered signals and (ii) low-pass filtered (<1500 Hz) using a third-order Butterworth filter before downsampling to 1000 Hz to analyze the LFP. All filtering procedures were performed in a phase-preserving manner. The position of Dil-stained recording electrodes in PL (most medial shank confined to layer 2/3, most temporal shank confined to layer 5/6) and CA1 was confirmed post-mortem by histological evaluation. Additionally, electrophysiological features (i.e., reversal of LFP and high MUA frequency over stratum pyramidale of CA1) were used for confirmation of the exact recording position in HP.

Detection of neonatal oscillatory activity. Discontinuous oscillatory events were detected using a previously developed unsupervised algorithm (Cichon et al. 2014) and confirmed by visual inspection. Briefly, deflections of the root-mean-square of band-pass (3–100 Hz) filtered signals exceeding a variance-depending threshold were assigned as network oscillations. The threshold was determined by a Gaussian fit to the values ranging from 0 to the global maximum of the root-mean-square histogram. Only oscillatory events > 1 s were considered for further analysis.

Time–frequency plots were calculated by transforming the data using the Morlet continuous wavelet.

Power Spectral Density

For power spectral density analysis, 1 s-long windows of network oscillations were concatenated and the power was calculated using Welch's method with nonoverlapping windows. For optical stimulation, we compared the average power during the 1.5 s-long time window preceding the stimulation to the last 1.5 s-long time window of light-evoked activity.

Single Unit Activity

Single unit activity (SUA) was detected and clustered using *klusta* (Rossant et al. 2016) and manually curated using *phy* (<https://github.com/cortex-lab/phy>). Data were imported and analyzed using custom-written tools in the MATLAB.

Firing Rate

The firing rate was computed by dividing the total number of spikes by the duration of the analyzed time window.

Interspike Interval

ISI was calculated at 1 ms resolution in the range of 10–200 ms.

Spike-Triggered LFP Power

Excitatory inputs arriving from a presynaptic cell generate excitatory postsynaptic potentials (EPSPs) in the postsynaptic cell. The spike-triggered LFP power was calculated to estimate the effects of the EPSPs on the LFP. Spike-triggered LFP spectra were calculated as

$$(\text{Power}_{\text{spike}} - \text{Power}_{\text{baseline}}) / \text{Power}_{\text{baseline}}$$

where the spike-triggered power spectrum ($\text{Power}_{\text{spike}}$) was calculated using Welch's method for a 200 ms-long time window centered on each spike, and the power spectrum of baseline LFP ($\text{Power}_{\text{baseline}}$) was averaged for two time windows, 100–300 ms and 200–400 ms before each spike.

Detection of SPWs in HP

The filtered signal (1–300 Hz) was subtracted from the signal recorded 100 μm above and 100 μm below stratum pyramidale. SPWs were detected as peaks above five times the standard deviation of the subtracted signal.

Phase Locking Value

Phase locking value (PLV) is developed to analyze the strength of phase synchronization. The analytic phase has a clear meaning only at a narrow frequency band. Therefore, the signal was first filtered into a narrow frequency band (bandwidth = 1 Hz, step = 1 Hz, for example 1–2 Hz, 2–3 Hz, ..., 49–50 Hz) in a phase preserving manner. Then, Hilbert transform was applied to extract the phase of the two signals. PLV was defined as following,

$$\text{PLV} = |\text{mean}(\exp(i * \Delta\phi_t))|$$

with $\Delta\phi_t$ stands for phase difference between the two signals at time point t . The value of PLV ranged between 0 (no synchrony) and 1 (max synchrony).

Spectral Coherence

Coherence was calculated using the coherency method. Briefly, the coherence was calculated (using Matlab build-in functions *cpsd.m* and *pwelch.m*) by cross-spectral density between the two signals and normalized by the power spectral density of each. The computation of the coherence C over frequency (f) for the power spectral density P of signal X and Y was performed according to the formula:

$$C_{XY}(f) = \left| \left(\frac{P_{XY}(f)}{\sqrt{P_{XX}(f)P_{YY}(f)}} \right) \right|$$

Directionality Methods

To investigate the directionality of functional connectivity between PFC and HP, generalized partial directed coherence (gPDC) was used. gPDC is based on linear Granger causality measure in the frequency domain. The method attempts to describe the causal relationship between multivariate time series based on the decomposition of multivariate partial coherence computed from multivariate autoregressive models. The LFP signal was divided into 1 s-long segments containing the oscillatory activity. After de-noising using MATLAB wavelet toolbox, gPDC was calculated using a previously described algorithm (Baccala and Sameshima 2001; Baccala et al. 2007).

Estimation of Light Propagation

The spatial pattern of light propagation in vivo was estimated using a previously developed model (Stujenske et al. 2015) based on Monte Carlo simulation (probe parameters: light fiber diameter: 50 μm , numerical aperture: 0.22, light parameters: 594 nm, 0.6 mW).

Pearson's correlation

For correlation between gPDC and NOR/RR, we computed Pearson's correlation using *corrplot.m* in MATLAB.

Generalized Linear Model

GLM was performed to predict the animals' behavioral performance in NOR and RR tasks by gPDC. Group comparisons were performed with GLM by including the factor of group as predictor variable.

Statistical Analysis

Statistical analyses were performed in MATLAB environment. Significant differences were detected by paired t-test or one-way ANOVA followed by Bonferroni-corrected post hoc analysis. For Sholl analysis, one-way repeated-measures ANOVA was used. Investigators were blinded to the group allocation when Sholl and spine analyses were performed. Data are presented as mean \pm sem. Significance levels of $P < 0.05$ (*), $P < 0.01$ (**), or $P < 0.001$ (***) were tested. Statistical parameters can be found in the main text, tables, and/or in the figure legends.

Results

Whole-Brain DISC1 Knock-Down in Immune-Challenged Mice Perturbs the Patterns of Network and Spiking Activity in Neonatal Intermediate/Ventral HP

Developing prefrontal–hippocampal circuits have been shown to be highly sensitive to the detrimental impact of combined

genetic defects and environmental stressors, whereas single-hit that have been previously characterized in detail at neonatal and juvenile age had no abnormal phenotype (Hartung et al. 2016; Oberlander et al. 2019). These results contrast with the prominent effects of DISC1- and MIA-only in adult mice that have network dysfunction and cognitive deficits (Kvajo et al. 2008, 2011; Abazyan et al. 2010; Cash-Padgett and Jaaro-Peled 2013b; Lipina et al. 2013; Sauer et al. 2015).

The mechanisms of abnormal long-range communication and wiring in dual-hit mice are still largely unknown. One possibility is that the maturation of PFC is impaired and therefore, the excitatory drive from the HP does not succeed to entrain the local circuits in beta-gamma frequencies. Indeed, we recently proved that this is a mechanism of developmental dysfunction (Xu et al. 2019; Chini et al. 2020). A second mechanism might be that the hippocampal driving force is decreased as result of abnormal function of developing hippocampal circuits in dual-hit mice.

To test the second hypothesis, we firstly characterized in detail the hippocampal patterns of network and firing activity in immune-challenged mice with whole-brain DISC1 knock-down. For this, we performed extracellular recordings of LFP and MUA from the CA1 area of *i/vHP* of awake P8–10 CON ($n = 22$) and GE ($n = 19$) mice (Fig. 1A). As previously reported (Brockmann et al. 2011), discontinuous spindle-shaped oscillations with frequency components peaking in theta band (4–12 Hz) intermixed with irregular low amplitude beta-gamma band components (12–50 Hz) are the dominant pattern of network activity in the CA1 area of both mouse groups (Fig. 1B). However, their properties significantly differed between CON and GE mice, conferring a highly fragmented appearance of hippocampal oscillations in GE mice (Fig. 1C,D). Their duration of oscillatory events was significantly shorter in GE mice (CON: 4.46 ± 0.24 s, GE: 3.38 ± 0.18 s, $F(1,39) = 13.31$, $P = 7.7 \times 10^{-4}$, one-way ANOVA) at a comparable occurrence (CON: 8.7 ± 0.30 oscillations/min, GE: 9.47 ± 0.38 oscillations/min, $F(1,39) = 2.44$, $P = 0.126$, one-way ANOVA) (Fig. 1C). Their spectral composition (4–50 Hz) differed between groups, the GE mice having hippocampal events with weaker power when compared to CON (4–50 Hz, $F(1,39) = 4.29$, $P = 0.045$, one-way ANOVA) (Fig. 1D). The overall firing of single neurons in the hippocampal CA1 area of CON and GE was similar both in its rate (log of firing rate, CON: -0.53 ± 0.29 ; GE: -0.48 ± 0.39 ; $F(1,39) = 0.009$, $P = 0.924$, one-way ANOVA) and temporal organization (i.e., preferred interspike interval [ISI] of 125 ms, corresponding to 8 Hz) (Fig. 1E,F).

Besides spindle-shaped oscillations, prominent SPWs reversing across the pyramidal layer have been recorded in the neonatal CA1 area of CON and GE mice (Fig. 1G). They were accompanied by ripples (100–250 Hz) and prominent firing. GE mice had fewer SPWs (0.36 ± 0.02 Hz, $F(1,39) = 4.38$, $P = 0.043$, one-way ANOVA) when compared with CON mice (0.41 ± 0.02 Hz) (Fig. 1H). The SPW-related spiking also decreased (CON: 0.76 ± 0.08 Hz, GE: 0.47 ± 0.09 , $F(1,37) = 6.02$, $P = 0.019$, one-way ANOVA) (Fig. 1I,J). The rather moderate perturbation of theta oscillations, which have been shown to mainly originate outside CA1 area (Buzsaki 2002; Janiesch et al. 2011), and the prominent deficits of locally generated SPWs and related spiking suggest that the *i/vHP* is compromised in GE mice. Analysis of the position and density of pyramidal neurons suggests that delayed migration of these neurons and correspondingly, perturbed wiring of local circuits, account for the hippocampal dysfunction (Fig. 1K).

These data indicate that neonatal HP is impaired in dual-hit genetic-environmental models of disease.

DISC1 Knock-Down in Hippocampal Pyramidal Neurons Disturbs the Prefrontal Oscillatory Activity and Prefrontal–Hippocampal Coupling of Neonatal Immune-Challenged Mice

When brain-wide expressed, genetic abnormalities, such as DISC1 knock-down in immune-challenged mice may affect many-fold the communication between limbic areas. To selectively pinpoint their role for hippocampal function, we generated $G_{HP}E$ mice in which the DISC1 knock-down was restricted to a lineage of pyramidal neurons in hippocampal CA1 area. For this, we expressed a DISC1 targeting shRNA in the CA1 of the *i/vHP* by using IUE protocols previously described (Ahlbeck et al. 2018). CON and GE mice received a scrambled/control shRNA instead (Fig. 2A). The immune challenge in $G_{HP}E$ and GE mice, which has been identified as critical cofactor of impairment (Hartung et al. 2016; Oberlander et al. 2019), was mimicked by MIA with the viral mimetic poly I:C injected at gestational day 9.5. In contrast, CON mice received saline injections at the same age. Staining for NeuN showed that a similar fraction of neurons was transfected in CON ($21.89 \pm 0.02\%$; $n = 6$), $G_{HP}E$ ($20.80 \pm 0.01\%$; $n = 6$) and GE mice ($20.59 \pm 0.02\%$; $n = 6$) (Fig. 2B). The shape of tDimer2-positive neurons and the orientation of primary dendrites confirmed previous findings (Ahlbeck et al. 2018) that the transfection was restricted to cell lineages of pyramidal neurons. In $G_{HP}E$, DISC1 was efficiently suppressed by shRNA (Fig. 2C). The relative DISC1 intensity in CA1 area was significantly weaker ($F(1,142) = 321.51$, $P = 1.06 \times 10^{-10}$, one-way ANOVA) in neonatal $G_{HP}E$ (40.98 ± 2.56) when compared with CON (101.74 ± 2.14) mice (Fig. 2C).

To monitor the effects of DISC1 knock-down in the *i/vHP*, we performed extracellular recordings of LFP and MUA from HP of P8–P10 awake CON ($n = 22$), $G_{HP}E$ ($n = 15$), and GE mice ($n = 19$). Similar to GE mice, $G_{HP}E$ mice showed disorganized oscillatory activity in CA1 area with decreased duration and theta-beta band power (4–50 Hz) but unchanged occurrence of spindle-shaped oscillations (Table 1, Fig. 2D,E). HP-confined DISC1 knock-down caused reduced SPWs occurrence and SPW-related neuronal firing, similarly to the deficits described for GE mice (Table 1, Fig. 2F,G).

In light of these findings, the question arises, whether the hippocampal dysfunction in $G_{HP}E$ mice is sufficient to affect downstream brain areas with normal DISC1 expression, such as PL. To answer this question, we performed extracellular recordings of LFP and MUA from PL of P8–P10 awake CON ($n = 22$), $G_{HP}E$ ($n = 15$), and GE mice ($n = 19$) using four shanks recording electrodes spanning the prelimbic layers 2/3 and 5/6 (Fig. 2H). In line with previous investigations (Hartung et al. 2016; Chini et al. 2020), the PL of all investigated mice showed discontinuous spindle-shaped oscillations with frequencies ranging from theta to beta-low gamma range (20–40 Hz). While the occurrence of these events was similar across the three groups, their duration and power were decreased in GE and $G_{HP}E$ mice when compared with CON mice (Table 1, Fig. 2I,J). As previously reported (Chini et al. 2020), brain-wide DISC1 knock-down in combination with MIA significantly lowered the neuronal firing in prelimbic layer 2/3. In contrast, $G_{HP}E$ mice showed normal firing in both layers 2/3 and 5/6 (Table 1, Fig. 2K) that might result from the sparse hippocampal innervation targeting the PFC. The decreased network entrainment and unchanged firing in PL of $G_{HP}E$ mice suggest that the local prelimbic circuits are indirectly impaired, most likely through a weaker drive from HP, which at this age is the main source of PL activation (Brockmann et al. 2011; Ahlbeck

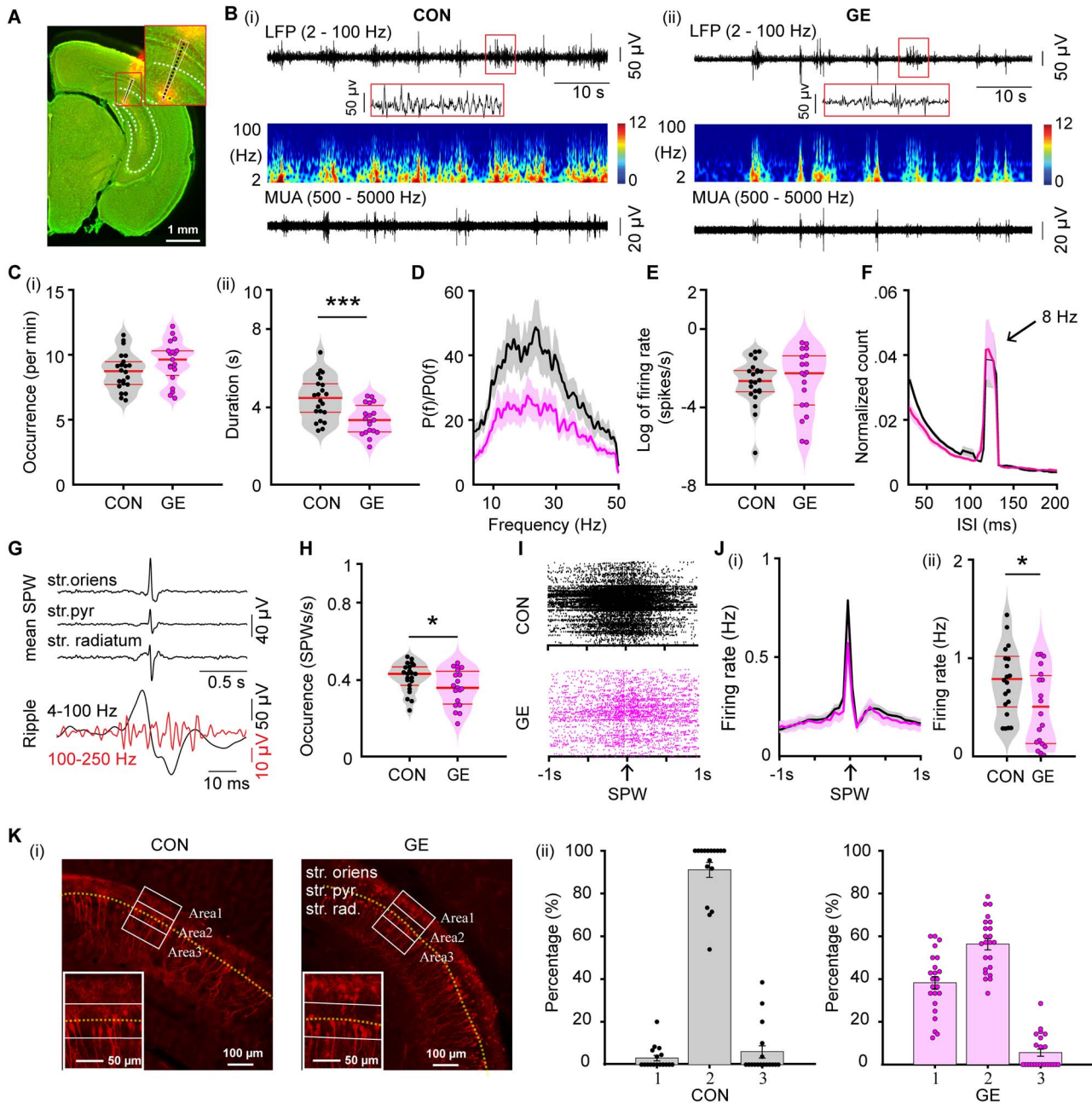


Figure 1. Patterns of network activity and neuronal firing in the CA1 area of *i/vHP* from neonatal GE mice. (A) Digital photomontage reconstructing the location of the Dil-labeled 1×16 -site recording electrode (orange) in a $100 \mu\text{m}$ -thick coronal section containing the CA1 from a P9 mouse. Inset, the position of recording sites (black dots) over the pyramidal layers displayed at higher magnification. (B) Extracellular LFP recordings of discontinuous oscillatory activity in the CA1 area from a P9 CON (i) and a P9 GE (ii) mouse displayed after bandpass (2–100 Hz) filtering (top) and the corresponding MUA after bandpass (500–5000 Hz) filtering (bottom). Traces are accompanied by the color-coded wavelet spectra of the LFP at identical time scale. (C) Violin plots displaying the occurrence (i) and the duration (ii) of hippocampal oscillatory activity recorded in CON and GE mice. (D) Averaged power spectra $P(f)$ of discontinuous oscillatory activity normalized to the baseline power $P0(f)$ of time windows lacking oscillatory activity in CON (black) and GE (red) mice. (E) Violin plots displaying the firing activity of CA1 neurons in CON and GE mice. (F) Histograms of ISI for CON (black) and GE (red) mice. Note the prominent ISI peak at ~ 125 ms interval, which corresponds to ~ 8 Hz. (G) Characteristic SPWs and ripple events recorded in the CA1 area. (H) Violin plots displaying the occurrence of SPWs in CON and GE mice. (I) Examples of spike trains from CA1 neurons aligned to SPWs in CON and GE mice. (J) Histograms of spiking activity aligned to SPWs (i) and violin plots displaying peak firing rate at SPWs (ii) in CON (black) and GE (red) mice. (K) (i) Photomicrographs depicting tDimer2-expressing pyramidal neurons (red dots) in the CA1 area of a P9 CON mouse and a P9 GE mouse. The yellow dotted line indicates the pyramidal layer of CA1. The three white blocks with width of $80 \mu\text{m}$ and length of $200 \mu\text{m}$ centered on the pyramidal layers correspond to the regions of interest for the quantification of tDimer2-transfected neurons. Inset, the tDimer2-expressing cells over the pyramidal layers displayed at higher magnification. (ii) Bar diagram of the distribution of the tDimer2-transfected neurons in the three blocks defined in (i) in CON and GE mice. Single data points are represented as dots. Single data points are represented as dots and the red horizontal bars in violin plots correspond to the median and the 25th and 75th percentiles. * $P < 0.05$, *** $P < 0.001$.

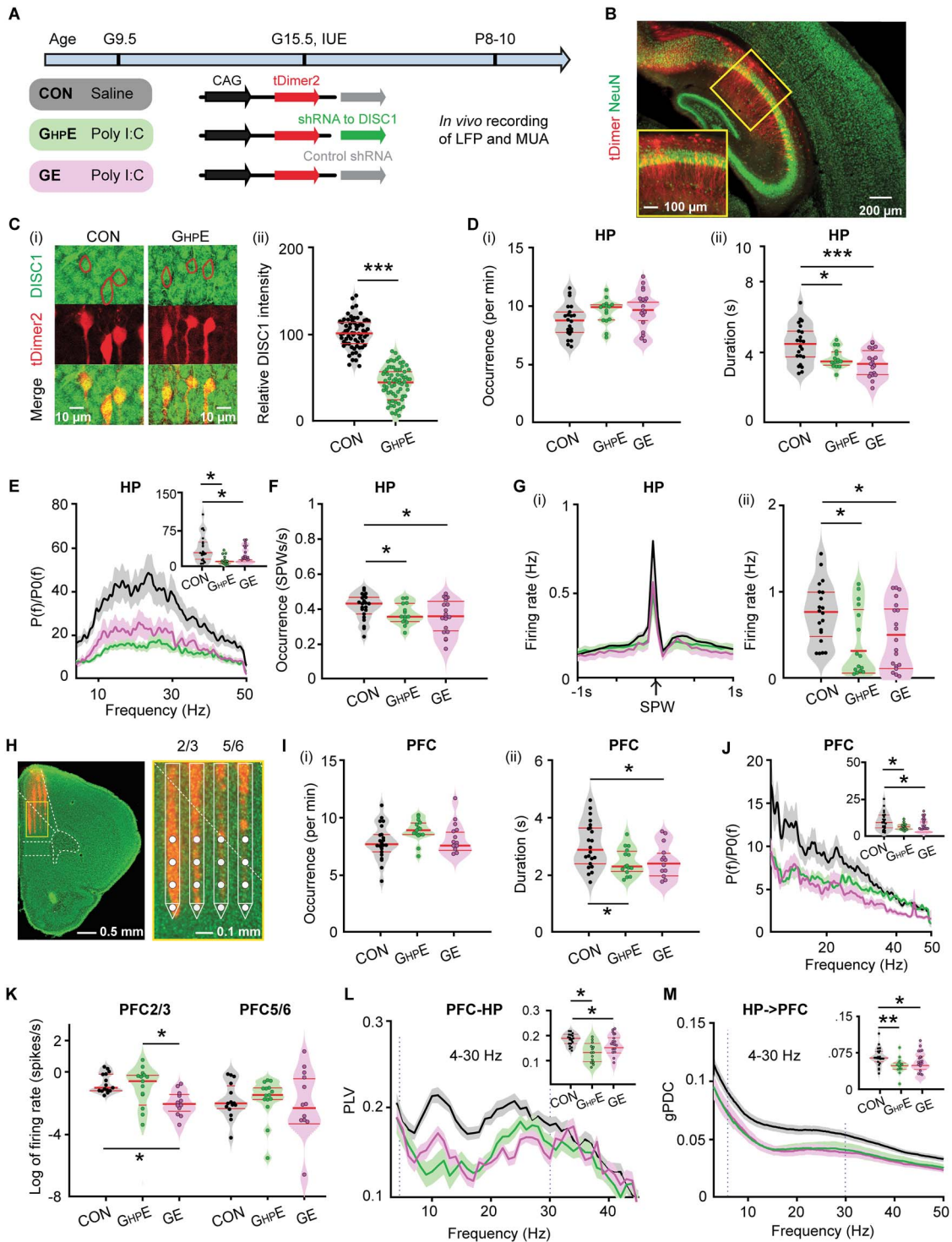


Figure 2. Patterns of network activity and neuronal firing in HP and PFC from neonatal immune challenged mice with HP-confined DISC1 suppression. (A) Timeline of experimental protocol and description of the three investigated groups of mice: CON mice, immune-challenged mice with suppression of DISC1 confined to HP (G_{HP}E), and immune-challenged mice with brain-wide DISC1 knock-down (GE). For each group the constructs used for IUE to target hippocampal CA1 pyramidal neurons is specified. (B) Photomicrographs depicting tDimer2-expressing pyramidal neurons (red) in the CA1 area when stained for NeuN (green) from a P9 mouse. Inset, photograph displaying the tDimer2-expressing cells at a higher magnification. (C) (i) Photographs displaying the DISC1 immunoreactivity (green) in relationship with the tDimer2-expression (red) in the CA1 area of i/vHP from P9 G_{HP}E and CON mice. (ii) Violin plots displaying the relative DISC1 immunoreactivity averaged for G_{HP}E and CON mice at P8-P10. (D) Violin plots displaying the occurrence (i) and the duration (ii) of hippocampal oscillatory activity recorded in CON, G_{HP}E and GE mice. (E) Averaged power spectra $P(f)$ of discontinuous oscillatory activity normalized to the baseline power $P(0f)$ of time windows lacking oscillatory activity in CON (black), G_{HP}E (green), and GE (magenta) mice. Inset, violin plots displaying the relative power averaged for 4–50 Hz in CON, G_{HP}E, and GE mice. (F) Violin plots displaying the occurrence of SPWs in the CA1 area of CON, G_{HP}E, and GE mice. (G) Histograms of spiking activity aligned to SPWs (i) and violin plots displaying the peak SPW-related firing in CON (black), G_{HP}E (green), and GE (magenta) mice (ii). (H) Left, digital photomontage reconstructing the location of the Dil-labeled 4 × 4-site recording electrode

et al. 2018). To test this hypothesis, we firstly assessed the synchrony between PL and HP in CON ($n = 22$), $G_{HP}E$ ($n = 15$), and GE mice ($n = 19$) by calculating PLV that, relying on oscillatory phase information, are not biased by different amplitudes of activity in PFC and HP. In line with previous data (Hartung et al. 2016; Xu et al. 2019), a tight theta–beta band (4–30 Hz) coupling of spindle-bursts between PL and HP has been detected in neonatal CON mice. In contrast, the PLV was significantly lower in $G_{HP}E$ and GE mice ($F(2, 51) = 4.20$, $P = 0.021$, one-way ANOVA) (Table 1, Fig. 2L). The directionality of interactions between PL and HP was also affected by both brain-wide and HP-confined DISC1 knock-down in immune-challenged mice. Calculation of gPDC, a measure that reflects the directionality of network interactions in different frequency bands, confirmed the prominent drive from HP to PL. In both GE and $G_{HP}E$, this drive decreased within 4–30 Hz frequencies (Table 1, Fig. 2M). These results give first evidence that the suppression of DISC1 restricted to HP has detrimental effects on the function of downstream PL. This dysfunction is the result of combined genetic and environmental stressors, since neither DISC- nor MIA-only causes major impairment of prefrontal–hippocampal circuits at neonatal age (Hartung et al. 2016; Oberlander et al. 2019).

Hippocampal Dysfunction Through DISC1 Suppression is Sufficient to Reduce the Oscillatory Entrainment of PL and Prelimbic-Hippocampal Coupling in Neonatal Immune-Challenged Mice

To add causal evidence to the hypothesis that the hippocampal dysfunction is critical for the abnormal coupling between PL and HP, we selectively transfected the hippocampal pyramidal neurons in CON, $G_{HP}E$ and GE mice with a highly efficient fast-kinetics double mutant Chr2E123T/T159C (ET/TC) (Berndt et al. 2011) and the red fluorescent protein tDimer2 by IUE (Fig. 3A). For $G_{HP}E$ mice, constructs coding for Chr2E123T/T159C (ET/TC) were transfected together with shRNA to DISC1. For targeting i/vHP, a previously developed protocol for IUE using three paddles was used (Szczyrkowska et al. 2016; Ahlbeck et al. 2018). This method enables stable area and cell type-specific transfection of hippocampal neurons already prenatally without the need of cell-type specific promoters of a sufficiently small size (Baumgart and Grebe 2015; Szczyrkowska et al. 2016) (Fig. 3Bi). The expression rate and distribution of tDimer2-positive neurons within the iso-contour lines for light power of 1 mW/mm² were similar in CON ($0.134 \pm 0.009/1000 \mu\text{m}^2$, $n = 16$), $G_{HP}E$ ($0.127 \pm 0.008/1000 \mu\text{m}^2$, $n = 15$) and GE ($0.126 \pm 0.010/1000 \mu\text{m}^2$, $n = 18$) ($F(2, 46) = 0.224$, $P = 0.800$, one-way ANOVA) (Fig. 3Bii). As previously shown, the transfection procedure had no effects on the overall development of mice (weight, somatic development, reflexes) (Ahlbeck et al. 2018).

First, we assessed the efficiency of light stimulation in evoking action potentials in hippocampal pyramidal neurons in vivo.

For this, we stimulated the i/vHP with pulsed blue light (473 nm, 20–40 mW/mm²) at 8 Hz, since this frequency has been shown to optimally drive the PL (Ahlbeck et al. 2018). The used light power did not cause local tissue heating that might interfere with neuronal spiking (Stujenske et al. 2015; Bitzenhofer et al. 2017a). In all three mouse groups, light stimulation induced precisely timed firing (latency < 10 ms) of CA1 neurons (Fig. 3C).

Second, to investigate the effects of hippocampal activation on downstream prefrontal circuits, we performed extracellular recordings of LFP in the PL during pulsed light stimulation of CA1 area in CON ($n = 15$), $G_{HP}E$ ($n = 18$), and GE ($n = 15$) mice (Fig. 3D). In CON mice, the light-induced hippocampal firing significantly augmented the prefrontal oscillatory activity in all frequency bands, as reflected by the higher power during stimulation when compared with the time window before the train of pulses (Table 2, Fig. 3D). In contrast, the light-induced hippocampal firing failed to boost the prefrontal oscillatory activity in $G_{HP}E$ and GE mice (Fig. 3D).

The weaker hippocampal drive to PL in $G_{HP}E$ mice might result from abnormal network entrainment of the i/vHP. To test this hypothesis, we applied ramp stimulations that, in contrast to light pulses, trigger more physiological firing and do not induce power contamination by repetitive and large voltage deflections (Bitzenhofer et al. 2017a). Ramp stimulation (3 s duration) of CA1 neurons led to sustained increase of spike discharge and augmented theta–beta oscillatory power in the HP of CON mice (Table 2, Fig. 3E). These effects were absent in GE and $G_{HP}E$ mice. Moreover, despite similar hippocampal firing responsiveness to light stimuli, the ability of CA1 neurons contributing to network oscillations in beta–gamma frequencies (20–40 Hz) dramatically decreased in GE and $G_{HP}E$ mice as shown by the weaker spike-triggered LFP relative power (Table 2, Fig. 3G).

Consistent with the excitatory drive from HP to PL during neonatal development, ramp stimulation-induced CA1 firing was relayed to PL and caused augmentation of prefrontal firing across layers in all investigated mouse groups (Fig. 3H). Since the axonal projections of CA1 neurons target prefrontal layer 5/6 neurons, the firing increase in these layers was stronger than in the layer 2/3 (2.97 ± 0.31 vs. 1.52 ± 0.25 , $F(1, 16) = 14.75$, $P = 0.0014$, one-way ANOVA), yet lacked temporal coordination in all mice (see Supplementary Fig. 1Ai,ii). In contrast, the firing within prefrontal layer 2/3 in CON induced by ramp stimulation of CA1 pyramidal neurons had a preferred ISI of ~60 ms, equivalent to a population firing at 16.7 Hz (Fig. 3Ii). Correspondingly, the HP spike-triggered prefrontal layer 2/3 LFP relative power peaked at similar frequencies (Fig. 3Iii). These peaks were absent in GE and $G_{HP}E$ mice, reflecting abnormal entrainment of prefrontal circuits. Significant power peak of spike-triggered LFP in prefrontal layer 5/6 was detected in none of the three groups (see Supplementary Fig. 1Aiii). Moreover, ramp-induced activation of CA1 pyramidal neurons boosted the synchrony between PL and HP in CON mice in a frequency-specific manner (peak at

(orange) in a 100 μm -thick coronal section containing the PFC from a P9 mouse. Right, the position of recording sites (white dots) over the prefrontal layers displayed at higher magnification. (I) Violin plots displaying the occurrence (i) and the duration (ii) of prefrontal oscillatory activity recorded in CON, $G_{HP}E$, and GE mice. (J) Averaged power spectra $P(f)$ of discontinuous oscillatory activity normalized to the baseline power $P_0(f)$ of time windows lacking oscillatory activity in CON (black), $G_{HP}E$ (green), and GE (magenta) mice. Inset, violin plots displaying the relative power averaged for 4–50 Hz in CON, $G_{HP}E$ and GE mice. (K) Violin plots displaying the neuronal firing in prefrontal layer 2/3 and layer 5/6 of CON, $G_{HP}E$, and GE mice. Each dot stands for one slice (3–4 slices per mouse). (L) Line plots of mean PLV for oscillatory activity simultaneously recorded in PFC and HP of in CON (black), $G_{HP}E$ (green), and GE (magenta) mice. Inset, violin plots displaying the PLV when averaged for 4–30 Hz. (M) Line plots of mean gPDC in relationship to frequency for HP→PFC in CON (black), $G_{HP}E$ (green), and GE (magenta) mice. Inset, violin plots displaying gPDC when averaged for 4–30 Hz in CON, $G_{HP}E$, and GE mice. Single data points are represented as dots and the red horizontal bars in violin plots correspond to the median and the 25th and 75th percentiles. * $P < 0.05$, ** $P < 0.01$, *** $P < 0.001$.

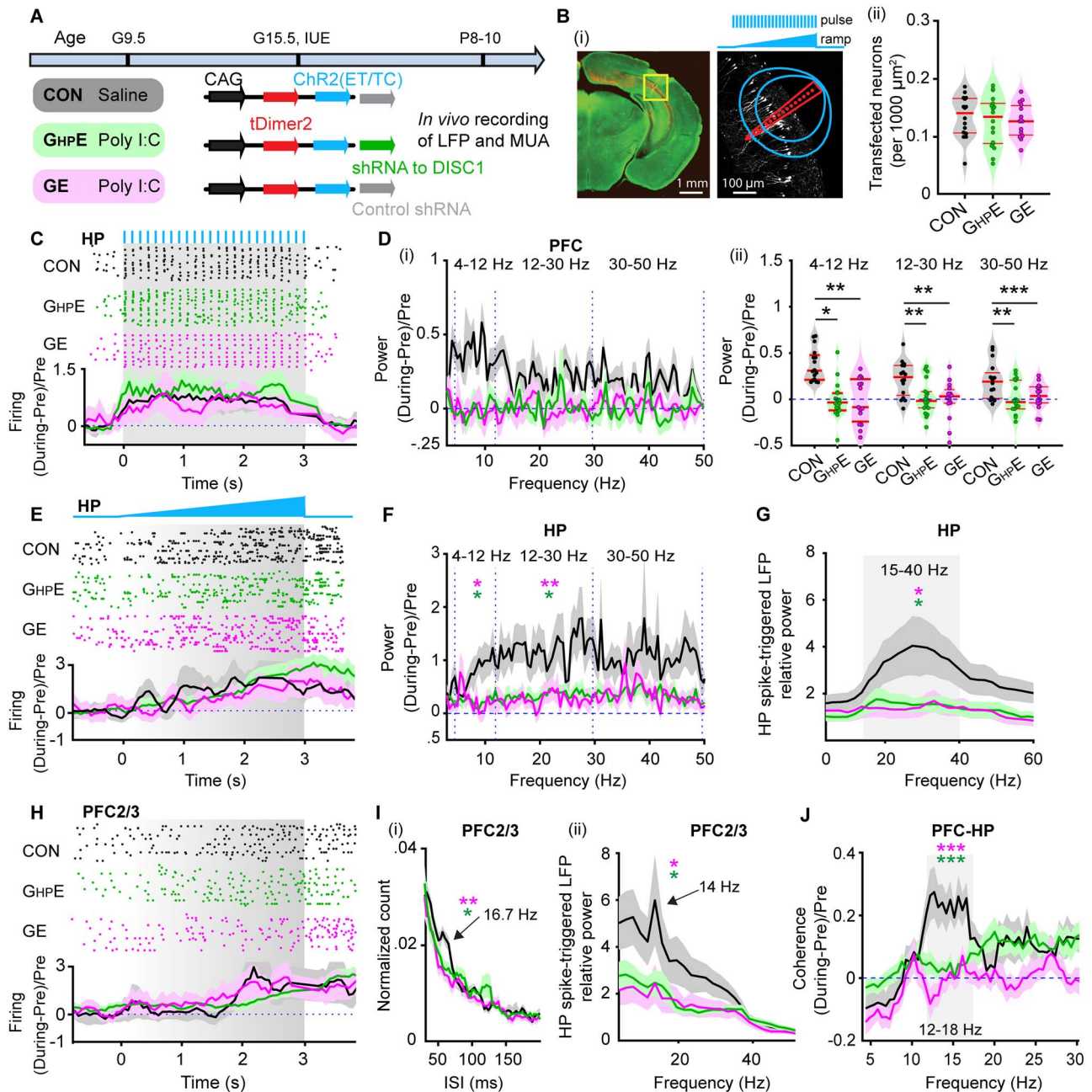


Figure 3. Light-induced activation of *i/vHP* and prefrontal-hippocampal coupling in immune challenged mice with whole-brain and HP-confined *DISC1* suppression. (A) Timeline of experimental protocol and description of the three investigated groups of mice: CON, $G_{HP}E$, and GE. For each group, the constructs used for IUE to target hippocampal CA1 pyramidal neurons is specified. (B) (i) Left, ChR2(ET/TC)-tDimer2-expressing cells (red) in a 50 μm -thick Nissl-stained (green) coronal section including CA1 area from a P9 mouse. Right, recording sites together with transfected neurons (white dots). Green lines correspond to the iso-contour lines for light power of 1 and 10 mW/mm^2 , respectively. 3 s-long pulse (8 Hz) and ramp stimulation are applied to activate hippocampal pyramidal neurons. (ii) Violin plots displaying the number of transfected neurons within the iso-contour lines for light power of 1 mW/mm^2 . (C) Top, representative raster plot of hippocampal SUA in response to 8 Hz pulse stimulation (3 ms-long pulse, 473 nm) in the CA1 area of P9 CON, $G_{HP}E$, and GE mice. Bottom, Histograms of hippocampal firing activity during 8 Hz pulse stimulation normalized to the activity before stimulation in CON (black), $G_{HP}E$ (blue), and GE (red) mice. (D) (i) Power of prefrontal oscillatory activity during pulse stimulation of CA1 pyramidal neurons normalized to the activity before stimulation in CON (black), $G_{HP}E$ (green), and GE (magenta) mice. (ii) Violin plots displaying the oscillatory power averaged for different frequency bands (4–12 Hz, 12–30 Hz, 30–50 Hz) in response to pulse stimulation for all investigated mice. (E) Top, representative raster plot of hippocampal spiking in response to ramp stimulation (3 s duration, 473 nm) in HP of CON, $G_{HP}E$, and GE mice. Bottom, Histograms of hippocampal firing activity during ramp stimulation normalized to the activity before stimulation in CON (black), $G_{HP}E$ (green), and GE (magenta) mice. (F) Power of hippocampal oscillatory activity during ramp stimulation of CA1 pyramidal neurons normalized to the activity before stimulation in CON (black), $G_{HP}E$ (green), and GE (magenta) mice. (G) Line plots of frequency-dependent relative power of spike-triggered LFP in HP of CON (black), $G_{HP}E$ (green), and GE (magenta) mice. (H) Top, representative raster plot of prefrontal spiking in response to ramp stimulation (3 s duration, 473 nm) in PFC2/3 of CON, $G_{HP}E$, and GE mice. Bottom, Histograms of prefrontal firing activity during ramp stimulation normalized to the activity before stimulation in CON (black), $G_{HP}E$ (green), and GE (magenta) mice. (I) (i) Histograms of ISI for layer 2/3 prefrontal neurons during ramp stimulation of hippocampal CA1 pyramidal neurons for CON (black), $G_{HP}E$ (green), and GE (magenta) mice. Note the prominent ISI peak at ~ 16.7 Hz. (ii) Line plots of frequency-dependent relative power of hippocampal spike-triggered LFP in prefrontal layer 2/3 of CON (black), $G_{HP}E$ (green), and GE (magenta) mice. (J) Coherence of prefrontal firing activity during ramp stimulation.

12–18 Hz), yet it did not induce a coherence increase in mice with whole-brain DISC1 suppression (Table 1, Fig. 3J). Even when the DISC1 suppression is confined to HP, the coherence did not significantly increase during ramp stimulus and augmented mainly after it, most likely as result of nonspecific network boosting.

Besides the reduced efficient activation of CA1 pyramidal neurons, abnormal connectivity might lead to dysfunction within prefrontal–hippocampal circuits in neonatal $G_{HP}E$ and GE mice. To test this hypothesis, we examined the evoked response in PFC by pulsed light stimulation of HP (see Supplementary Fig. 1B). In line with the larger density of hippocampal projections targeting prelimbic layer 5/6 than layer 2/3 neurons (Parent et al. 2010; Padilla-Coreano et al. 2016), the evoked response in layer 5/6 was stronger than in the layer 2/3 (see Supplementary Fig. 1Bi). Pulsed light stimulation in HP ensured that the activation of hippocampal neurons was timed. The delay of evoked responses in prelimbic layer 2/3 was significantly longer in $G_{HP}E$ (24.20 ± 0.79 ms, $P = 0.0029$) and GE (27.11 ± 1.65 ms, $P = 0.0008$) mice compared with CON (20.41 ± 0.18 ms, $F(2, 38) = 5.37$, $P = 0.008$, one-way ANOVA) mice (see Supplementary Fig. 1Bii). This result suggests that the connectivity between PFC and HP in $G_{HP}E$ and GE mice is impaired. Of note, no significant differences of the delay were observed for evoked responses in layer 5/6 of PFC in all three groups (see Supplementary Fig. 1Biii).

Taken together, these results indicate that hippocampal DISC1 suppression in combination with MIA lead to CA1 dysfunction that, on its turn, causes abnormal coupling within neonatal prefrontal–hippocampal networks.

DISC1 Knock-Down Causes Major Morphological and Synaptic Deficits of Pyramidal Neurons in CA1 Area

The abnormal firing and oscillatory entrainment of HP and consequently, the weaker prelimbic–hippocampal coupling in GE and $G_{HP}E$ mice might relate to abnormal morphology and connectivity of CA1 pyramidal neurons. To test this hypothesis, we undertook a detailed histological examination of the cytoarchitecture of tDimer-labeled hippocampal pyramidal neurons of P10 CON, $G_{HP}E$ and GE mice ($n = 17$ – 19 neurons from three mice in each group). The complexity of dendritic branching was assessed by Sholl analysis of three-dimensionally reconstructed hippocampal pyramidal neurons. When compared with CON mice, both $G_{HP}E$ and GE mice showed a highly significant reduction of dendritic branching of hippocampal pyramidal neurons (condition effect, $P < 1 \times 10^{-9}$) (Fig. 4A). These deficits were particularly prominent within a radius of 20–150 μ m from the cell soma center. Next, we examined the spine density along the dendrites of hippocampal pyramidal neurons. In $G_{HP}E$ and GE mice, the density of dendritic spines was significantly lower when compared with CON mice (Fig. 4B,C). The magnitude of reduction was similar for basal dendrites ($F(2, 49) = 10.21$, $P = 1.96 \times 10^{-4}$, one-way ANOVA), proximal oblique dendrites ($F(2, 50) = 9.31$, $P = 3.66 \times 10^{-4}$, one-way ANOVA), and secondary apical dendrites ($F(2, 48) = 8.14$, $P = 9.03 \times 10^{-4}$, one-way ANOVA). Thus, CA1 pyramidal neurons in $G_{HP}E$ and GE mice show simplified dendritic arborization and decreased spine density. As a

consequence, the hippocampal activity, especially the excitability of individual neurons and the locally generated SPWs, might be perturbed and the coupling with downstream prelimbic neurons, diminished.

Hippocampal DISC1 Knock-Down in Immune-Challenged Mice Causes Neuronal and Network Deficits as well as Cognitive Impairment at Prejuvenile Age

To test the long-term consequences of hippocampal dysfunction and abnormal prefrontal–hippocampal coupling, we investigated CON, GE, and $G_{HP}E$ mice at prejuvenile age (P20–P23) (Fig. 5A).

The DISC1 suppression persisted, yet at a lower magnitude, until this age, as revealed by the significantly ($F(1,146) = 25.323$, $P = 4.85 \times 10^{-7}$, one-way ANOVA) lower DISC1 expression in $G_{HP}E$ ($n = 73$ neurons) when compared with CON ($n = 75$ neurons) mice (Fig. 5B). Of note, CA1 pyramidal neurons seem to respond to IUE shRNA suppression differently compared with prelimbic neurons, where the DISC1 knock-down was temporally restricted to the neonatal period (Xu et al. 2019).

First, we performed multisite extracellular recordings of LFP from PL and hippocampal CA1 area of urethane-anesthetized P20–23 CON ($n = 12$), $G_{HP}E$ ($n = 9$), and GE ($n = 15$) mice. All investigated mice showed continuous large-amplitude slow rhythms that were superimposed with oscillatory activity in theta (4–12 Hz) and gamma (30–100 Hz) frequencies. These patterns of network activity correspond to the sleep-like rhythms mimicked by urethane anesthesia (Wolansky et al. 2006; Clement et al. 2008). While the impairment of neuronal firing, SPW, and network oscillations was less pronounced at prejuvenile age when compared with the deficits at neonatal age, the directed interactions between PFC and HP were still compromised (Fig. 5C). Both GE (0.123 ± 0.003 , $P = 0.016$, ANOVA followed by Bonferroni-corrected post hoc test) and $G_{HP}E$ (0.127 ± 0.004 , $P = 0.002$, ANOVA followed by Bonferroni-corrected post hoc test) mice had smaller gPDC peaks within theta band (4–8 Hz) and thus, weaker drive from HP to PFC, when compared with CON mice (0.147 ± 0.007) mice. Light stimulation of Chr2(ET/TC)-expressing CA1 neurons augmented the power of network oscillations in theta–beta range for CON (theta: 0.404 ± 0.096 ; beta: 0.283 ± 0.061), but not GE and $G_{HP}E$ mice (Fig. 5Di). Mirroring the weaker hippocampal drive, the light stimulation of HP augmented the power of prefrontal oscillations in theta (0.373 ± 0.094) and beta (0.269 ± 0.052) range only in CON, whereas the increase was smaller, if any, for GE (4–12 Hz: 0.061 ± 0.0750 , $P = 0.0009$; 12–30 Hz: 0.0640 ± 0.048 , $P = 0.0009$, one-way ANOVA followed by Bonferroni-corrected post hoc test) and $G_{HP}E$ (4–12 Hz: 0.160 ± 0.044 , $P = 0.007$; 12–30 Hz: 0.144 ± 0.040 , $P = 0.003$, one-way ANOVA followed by Bonferroni-corrected post hoc test) mice (Fig. 5Dii). Similar to neonatal age, these functional deficits were related to abnormal morphology and connectivity of CA1 neurons. Detailed histological examination of the cytoarchitecture revealed that at P20 the dendritic branching of hippocampal pyramidal neurons in GE and $G_{HP}E$ mice was still significantly reduced when compared with CON ($n = 17$ – 19 neurons from three mice in each group)

Line plots of coherence between PFC and HP during ramp stimulation of hippocampal CA1 pyramidal neurons normalized to coherence values before stimulation. Single data points are represented as dots and the red horizontal bars in violin plots correspond to the median and the 25th and 75th percentiles. * $P < 0.05$, ** $P < 0.01$, *** $P < 0.001$. Magenta stars correspond to the comparison between GE and CON mice. Green stars correspond to the comparison between $G_{HP}E$ and CON mice.

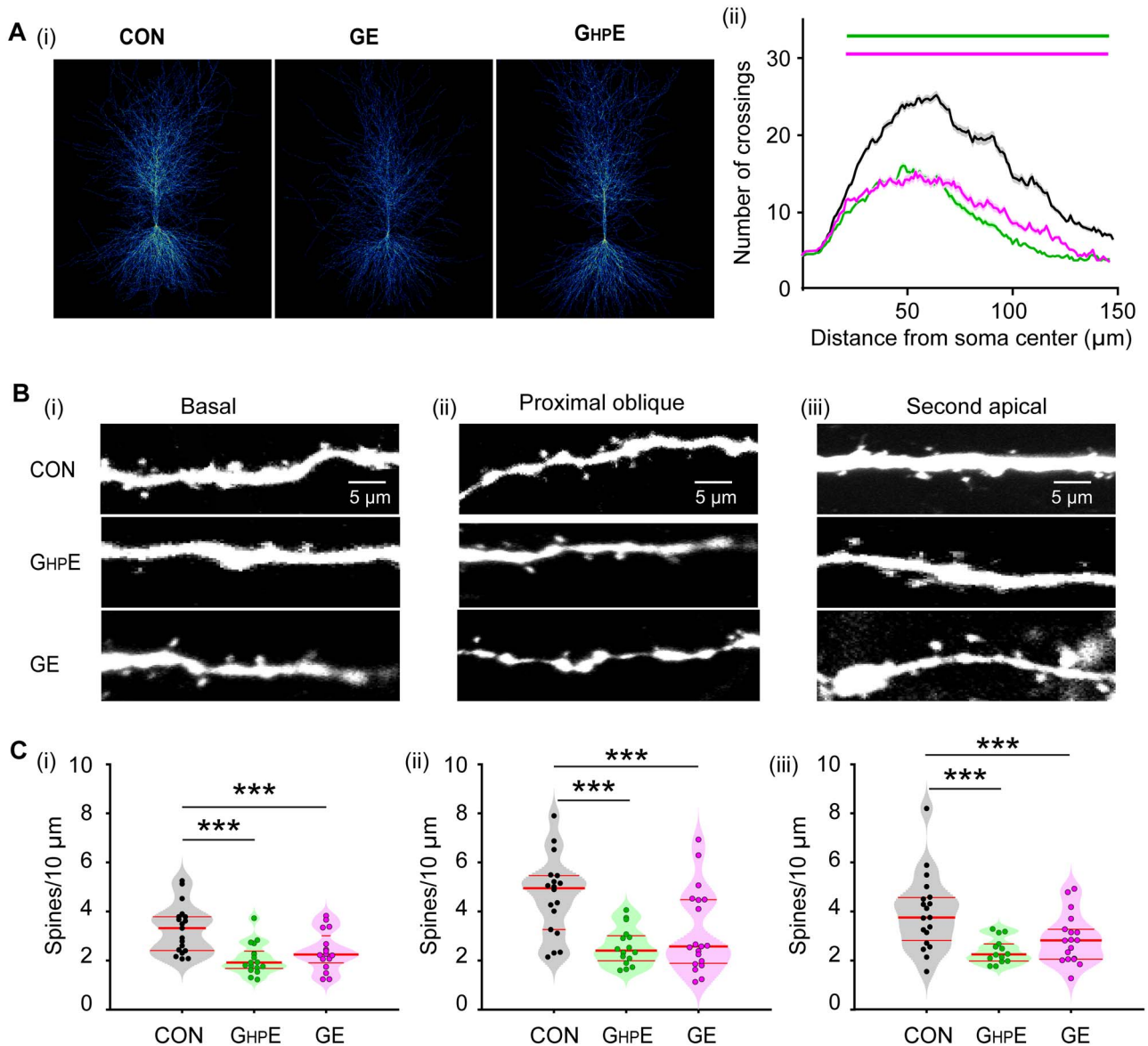


Figure 4. Morphology of hippocampal pyramidal neurons in neonatal $G_{HP}E$ and GE mice. (A) (i) Heatmap displaying an overlay of all traced dendrites of transfected CA1 pyramidal neurons in CON, $G_{HP}E$, and GE mice. (ii) Graph displaying the average number of dendritic intersections within a 150 μm radius from the soma center of CA1 pyramidal neurons in CON (black, $n = 21$ neurons from three mice), $G_{HP}E$ (blue, $n = 21$ neurons from three mice) and GE (red, $n = 21$ neurons from three mice) mice. Green and magenta bars indicate significant difference ($***P < 0.001$) between CON and $G_{HP}E$ mice and between CON and GE mice, respectively. (B) Photograph displaying representative basal (i), proximal oblique (ii) and second apical dendrites (iii) of CA1 pyramidal neurons from a P9 CON, a P9 $G_{HP}E$, and a P9 GE mouse. (C) Violin plots displaying the spine density on basal (i), proximal oblique (ii), and second apical dendrites (iii) of CA1 pyramidal neurons from CON (20 neurons from three mice), $G_{HP}E$ (20 neurons from three mice), and GE (21 neurons from three mice) mice. Single data points are represented as dots and the red horizontal bars in violin plots correspond to the median and the 25th and 75th percentiles. $***P < 0.001$.

mice (condition effect, $P = 7.30 \times 10^{-9}$) (Fig. 5E). These deficits were particularly prominent within a radius of 40–150 μm from the cell soma center. The sparsification of dendritic projections was accompanied by lower density of the dendritic spines in $G_{HP}E$ and GE mice when compared with CON mice (Fig. 5F). The magnitude of density reduction was similar for basal dendrites ($F(2, 52) = 46.36$, $P = 2.77 \times 10^{-12}$, one-way ANOVA), proximal oblique dendrites ($F(2, 54) = 31.81$, $P = 7.44 \times 10^{-10}$, one-way ANOVA), and secondary apical dendrites ($F(2, 53) = 20.22$, $P = 2.97 \times 10^{-7}$, one-way ANOVA).

Taken together, these data show that the prefrontal–hippocampal dysfunction resulting from synaptic and projection deficits of CA1 pyramidal neurons in GE and $G_{HP}E$ mice persists until prejuvenile age.

The developmental prefrontal–hippocampal dysfunction as result of hippocampal DISC1 suppression in immune-challenged mice might cause behavioral disabilities. Already at juvenile age, rodents have reliable novelty detection and recognition memory that rely on the mouse’s intrinsic exploratory drive and require no prior training or deprivation (Kruger

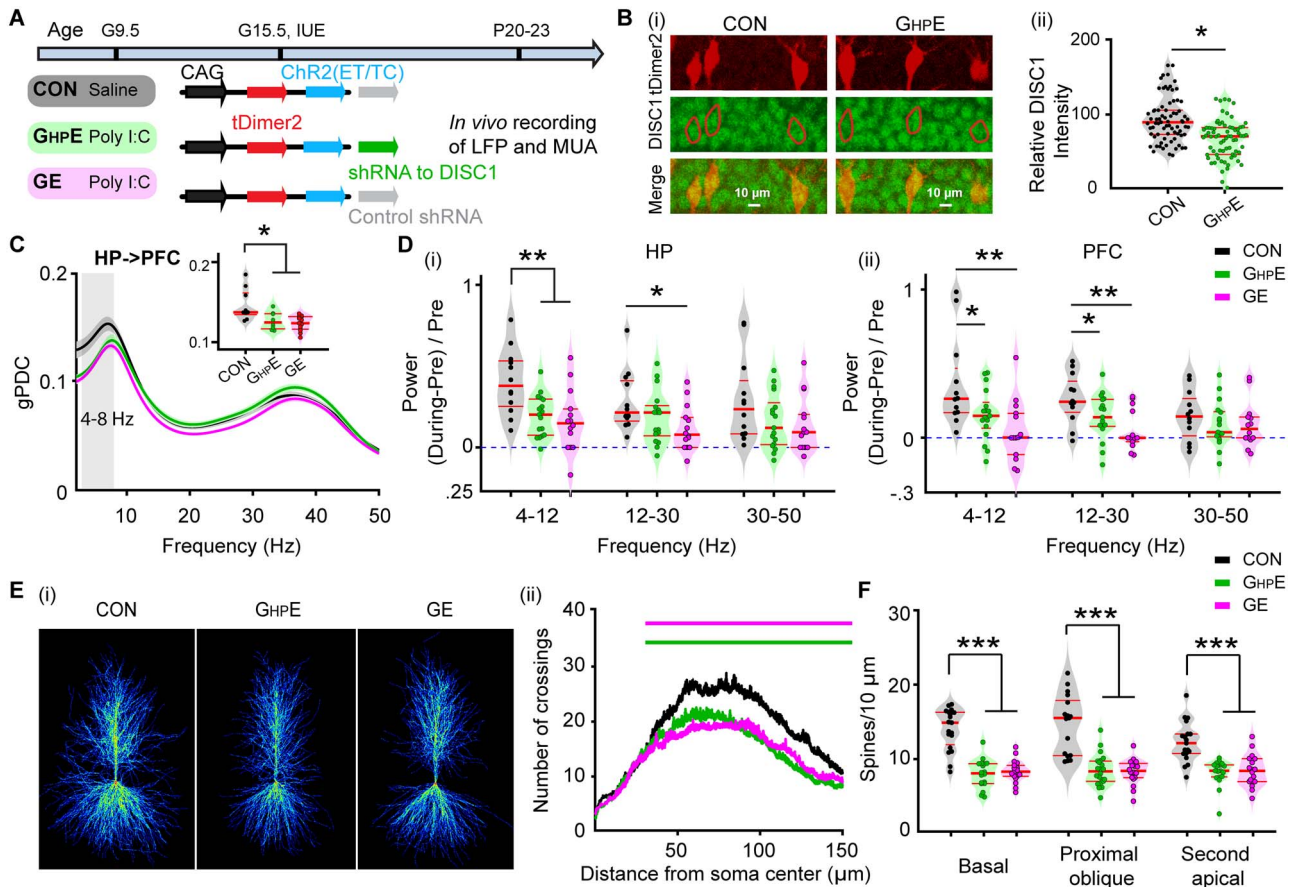


Figure 5. Patterns of prejuvenile network and neuronal firing in the CA1 area of *i/vHP* of immune challenged mice with whole-brain or HP-confined DISC1 suppression. (A) Timeline of experimental protocol and description of the three investigated groups of mice: CON, $G_{HP}E$, and GE. For each group the constructs used for IUE to target hippocampal CA1 pyramidal neurons is specified. (B) (i) Photographs displaying the DISC1 immunoreactivity (green) in relationship with the tDimer2-expression (red) in the CA1 area of *i/vHP* of P21 $G_{HP}E$ and CON mice. (ii) Violin plots displaying the relative DISC1 immunoreactivity averaged for $G_{HP}E$ and CON mice at P20–P23. (C) Line plots of mean gPDC in relationship to frequency for HP→PFC in CON (black), $G_{HP}E$ (green) and GE (magenta) mice. Inset, violin plots displaying gPDC when averaged for 4–8 Hz in CON, $G_{HP}E$, and GE mice. (D) Violin plots displaying the hippocampal (i) and prefrontal (ii) oscillatory power averaged for different frequency bands (4–12 Hz, 12–30 Hz, 30–50 Hz) in response to ramp stimulation in HP for all investigated mice. (E) (i) Heatmap displaying an overlay of all traced dendrites of transfected CA1 pyramidal neurons in CON, $G_{HP}E$, and GE mice. (ii) Graph displaying the average number of dendritic intersections within a 150 μ m radius from the soma center of CA1 pyramidal neurons in CON (black, $n = 21$ neurons from three mice), $G_{HP}E$ (blue, $n = 21$ neurons from three mice) and GE (red, $n = 21$ neurons from three mice) mice. Green and magenta bars indicate significant difference ($***P < 0.001$) between CON and $G_{HP}E$ mice and between CON and GE mice, respectively. (F) Violin plots displaying the spine density on basal, proximal oblique, and second apical dendrites of CA1 pyramidal neurons from CON, $G_{HP}E$, and GE mice. Single data points are represented as dots and the red horizontal bars in violin plots correspond to the median and the 25th and 75th percentiles. * $P < 0.05$, ** $P < 0.01$, *** $P < 0.001$.

et al. 2012). These abilities have been shown to involve communication within a circuit centered on PFC and HP (Warburton and Brown 2015). Both GE mice and immune-challenged mice with DISC1 suppression confined to PFC have been reported to have poor recognition memory (Hartung et al. 2016; Xu et al. 2019). To identify the consequences of perinatal HP-restricted DISC1 knock-down on cognitive abilities, we tested NOR and RR in CON ($n = 11$), $G_{HP}E$ ($n = 13$), and GE ($n = 12$) mice using a custom-designed arena (Fig. 6A) and previously established protocols (Fig. 6Bi and Ci). During the familiarization trials of these tests, all mice spent equal time investigating the two objects placed in the arena. During the NOR test trial protocols, CON mice spent significantly ($P = 2.38 \times 10^{-5}$, paired t-test) longer time interacting with the novel object ($79.12 \pm 4.49\%$) than with the familiar one ($20.88 \pm 4.49\%$) (Fig. 6Bii). In line with previous results, GE mice did not show a preference for the novel object (familiar: $47.46 \pm 7.90\%$; novel: $52.54 \pm 7.90\%$, $P = 0.372$, paired t-test) (Fig. 6Bii). Similarly, prejuvenile $G_{HP}E$

mice also did not show a preference for the novel object during test trial (familiar: $39.23 \pm 1.29\%$; novel: $60.77 \pm 2.19\%$, $P = 0.07$, paired t-test) (Fig. 6Bii). Correspondingly, the discrimination ratio between the familiar and the novel object significantly decreased in GE (0.0501 ± 0.158 , $P = 0.02$, one-way ANOVA followed by Bonferroni-corrected post hoc test) and $G_{HP}E$ mice (-0.215 ± 0.142 , $P = 0.02$, one-way ANOVA followed by Bonferroni-corrected post hoc test) compared with CON mice (0.582 ± 0.090) (Fig. 6Biii).

During RR task, mice process temporal information by recognizing the object with which they most recently interacted. The CON mice spent more time with the object they explored during the first familiarization trial and less time with the more recent object from the second familiarization trial (old: $67.52 \pm 4.72\%$, recent: $32.48 \pm 4.72\%$, $P = 0.0015$, paired t-test) (Fig. 6Cii). Both $G_{HP}E$ and GE mice did not show a preference for the object in the first familiarization trial and spent equal time with both objects (GE, old: $50.88 \pm 3.92\%$, recent: $49.12 \pm 3.92\%$, $P = 0.409$, paired

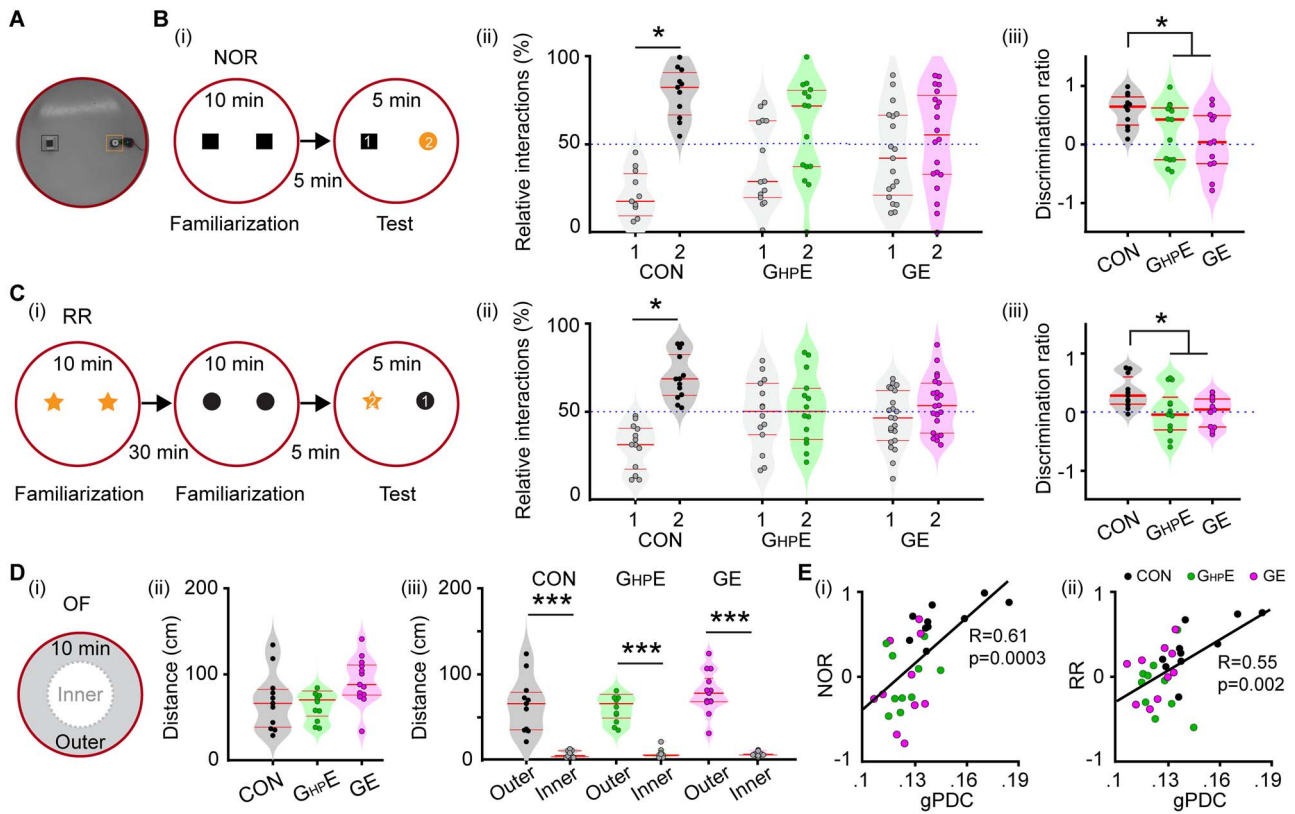


Figure 6. Novelty recognition of immune challenged mice with whole-brain and HP-confined *DISC1* suppression. (A) Photograph of the arena used for NOR and RR tasks. (B) (i) Schematic diagrams of the protocol for NOR task. (ii) Violin plots displaying the relative interaction time spent by CON, $G_{HP}E$, and GE mice with the objects during the NOR test trial. The dotted line indicates chance level. (iii) Violin plots displaying the NOR discrimination ratio when averaged for CON, $G_{HP}E$ and GE mice. (C) (i) Schematic diagrams of the protocol for RR task. (ii) Violin plots displaying the relative interaction time spent by CON, $G_{HP}E$, and GE mice with the objects during the RR test trial. The dotted line indicates chance level. (iii) Violin plots displaying the RR discrimination ratio when averaged for CON, $G_{HP}E$, and GE mice. (D) (i) Schematic diagrams of the protocol for OF task. (ii) Violin plots displaying the distance covered in 10 min by CON, $G_{HP}E$, and GE mice during the OF task. (iii) Violin plots displaying the distance covered in the outer circle and the inner circle by CON, $G_{HP}E$, and GE mice during OF task. (E) (i) The Pearson's correlation between gPDC and discrimination ratio in NOR task. (ii) Same as (i) for Pearson's correlation between gPDC and RR. Single data points are represented as dots and the red horizontal bars in violin plots represent the median and the 25th and 75th percentiles. * $P < 0.05$, *** $P < 0.001$.

t-test; $G_{HP}E$, old: $50.86 \pm 5.93\%$, recent: $49.14 \pm 5.93\%$, $P = 0.441$, paired t-test (Fig. 6Cii). Correspondingly, the discrimination ratio significantly decreased in GE (0.001 ± 0.075 , $P = 0.04$, one-way ANOVA followed by Bonferroni-corrected post hoc test) and $G_{HP}E$ (-0.0053 ± 0.1133 , $P = 0.03$, one-way ANOVA followed by Bonferroni-corrected post hoc test) compared with the values for CON mice (0.335 ± 0.087) (Fig. 6Ciii).

The poor performance in NOR and RR tasks may result from poor motor abilities and/or enhanced anxiety when interacting with the objects. To test this hypothesis, we analyzed the exploratory behavior of P16 mice from all three groups during OF task (Fig. 6Di). The distance covered in 10 min was similar in all groups (CON: 69.176 ± 10.70 cm; GE: 77.41 ± 12.11 cm; $G_{HP}E$: 92.25 ± 7.86 cm, $F(2, 33) = 1.437$, $P = 0.252$, one-way ANOVA) (Fig. 6Dii). Moreover, the distance covered in the outer circle was much larger than in the inner circle of the arena (CON: 64.67 ± 10.18 cm vs. 4.50 ± 1.18 cm; GE: 72.62 ± 10.81 cm vs. 4.78 ± 1.51 cm; $G_{HP}E$: 79.23 ± 7.00 cm vs. 5.02 ± 0.73 cm) (Fig. 6Diii). During the sample trial of NOR task, mice from all groups covered a similar distance as well (see Supplementary Fig. 2). These results indicate that exploratory and anxiety

abilities were similar in CON, $G_{HP}E$, and GE mice and thus, did not affect the recognition memory in NOR and RR tasks.

To better link the behavioral deficits in GE and $G_{HP}E$ mice with the abnormal prefrontal-hippocampal coupling, we performed the Pearson's correlation between gPDC and discrimination ratio in NOR and RR task (Fig. 6E). There was strong positive correlation between gPDC and NOR ($R = 0.61$, $P = 0.0003$, Pearson's correlation) and between gPDC and RR ($R = 0.55$, $P = 0.002$, Pearson's correlation). Given the prior group differences, a generalized linear model (GLM) with group comparisons was used to predict the animals' behavioral performance in NOR and RR tasks by the factor of prefrontal-hippocampal coupling measured with gPDC. Group comparisons were performed with GLM by including the factor of group as predictor variable. Significant positive correlation was found in gPDC-NOR ($R = 11.23$, $P = 0.027$) with significant group effect ($P = 0.014$). There was also a significant positive correlation in gPDC-RR ($R = 11.14$, $P = 0.011$), yet without significant group effect ($P = 0.75$). These results confirmed that abnormal prefrontal-hippocampal coupling as results of HP-restricted *DISC1* suppression in immune challenged mice correlates to the poorer recognition memory at prejuvenile age.

Table 1 Prefrontal-hippocampal activity patterns and coupling in CON, G_{HP}E, and GE mice

		CON	G _{HP} E	GE	F value
HP	Spindle bursts				
	Occurrence (per min)	8.73 ± 0.31	9.52 ± 0.29	9.47 ± 0.38	F(2,53) = 1.94 P = 0.15
	Duration (s)	4.46 ± 0.24	3.67 ± 0.15 *P = 0.021	3.38 ± 0.18 **P = 0.0005	F(2,53) = 8.72 P = 0.0005
SPWs	Power (4–50 Hz)	30.63 ± 4.93	12.37 ± 1.72 *P = 0.034	18.23 ± 3.32 *P = 0.05	F(2,53) = 5.87 P = 0.005
	Occurrence (Hz)	0.41 ± 0.02	0.37 ± 0.02 *P = 0.034	0.36 ± 0.02 *P = 0.024	F(2,52) = 2.73 P = 0.05
	SWP-Spike	0.76 ± 0.08	0.40 ± 0.11 *P = 0.019	0.47 ± 0.09 *P = 0.05	F(2,51) = 4.74 P = 0.013
PL	Occurrence (per min)	7.88 ± 0.33	8.87 ± 0.26	8.07 ± 0.39	F(2,47) = 2.60 P = 0.09
	Duration (s)	3.05 ± 0.17	2.47 ± 0.13 *P = 0.030	2.41 ± 0.17 *P = 0.021	F(2,47) = 5.29 P = 0.008
	Power (4–50 Hz)	10.12 ± 1.31	6.41 ± 0.60 *P = 0.049	6.33 ± 0.94 *P = 0.029	F(2,53) = 4.49 P = 0.016
MUA	Layer2/3 (log)	-0.71 ± 0.16	-0.45 ± 0.21	-1.96 ± 0.24 *P = 0.030	F(2,39) = 3.55 P = 0.038
	Layer5/6 (log)	-3.06 ± 0.30	-2.18 ± 0.35	-3.36 ± 0.61	F(2,39) = 2.35 P = 0.108
	PIV (4–30 Hz)	0.19 ± 0.01	0.15 ± 0.02 *P = 0.037	0.15 ± 0.01 *P = 0.049	F(2,51) = 4.20 P = 0.021
	gPDC (4–30 Hz)	0.068 ± 0.004	0.050 ± 0.004 *P = 0.014	0.053 ± 0.005 *P = 0.036	F(2,53) = 5.26 P = 0.008

Data are shown as mean ± SEM. Significance was assessed using one-way ANOVA test followed by Bonferroni-corrected post hoc test and the listed P values correspond to comparisons between CON and G_{HP}E mice, CON and GE mice. *P < 0.05, **P < 0.01.

Table 2 Prefrontal-hippocampal activity patterns and coupling induced by activating CA1

		CON	G _{HP} E	GE	F values
Activating HP by pulses stimulation					
	4–12 Hz	0.234 ± 0.049	0.059 ± 0.042 *P = 0.016	0.023 ± 0.047 **P = 0.005	F(2,45) = 6.47 P = 0.0034
	12–30 Hz	0.210 ± 0.049	0.045 ± 0.032 **P = 0.0096	-0.007 ± 0.039 **P = 0.0011	F(2,45) = 8.21 P = 0.0009
PFC	Power (During-pre)/pre	0.184 ± 0.035	0.051 ± 0.027 **P = 0.007	0.004 ± 0.030 ***P = 0.0004	F(2,45) = 9.38 P = 0.0004
	30–45 Hz				
	Activating HP by ramp stimulation				
HP	4–12 Hz	0.186 ± 0.045	0.070 ± 0.031 *P = 0.011	0.026 ± 0.050 *P = 0.024	F(2,45) = 3.98 P = 0.026
	12–30 Hz	0.267 ± 0.051	0.091 ± 0.043 *P = 0.018	0.046 ± 0.043 **P = 0.004	F(2,45) = 6.62 P = 0.003
	30–45 Hz	0.224 ± 0.054	0.102 ± 0.046	0.089 ± 0.049	F(2,45) = 2.34 P = 0.108
PFC2/3	Spike-triggered LFP	3.08 ± 0.59	1.43 ± 0.27 *P = 0.018	1.42 ± 0.40 *P = 0.021	F(2,43) = 5.26 P = 0.009
	15–40 Hz				
PFC-HP	Firing interval	0.020 ± 0.001	0.015 ± 0.002 *P = 0.04	0.014 ± 0.002 **P = 0.005	F(2,39) = 6.37 P = 0.004
	HP spike-triggered LFP	7.06 ± 2.19	3.03 ± 0.72 *P = 0.044	2.90 ± 0.88 *P = 0.042	F(2,45) = 3.22 P = 0.049
PFC-HP	Coherence	0.220 ± 0.044	0.041 ± 0.023 ***P = 0.0003	-0.004 ± 0.024 ***P = 0.00001	F(2,41) = 15.33 P = 0.000001
	12–18 Hz				

Data are shown as mean ± SEM. Significance was assessed using one-way ANOVA test followed by Bonferroni-corrected post hoc test and the listed P values correspond to comparisons between CON and G_{HP}E mice, CON and GE mice. *P < 0.05, **P < 0.01, ***P < 0.001.

Discussion

Developmental miswiring of the brain has been hypothesized to account for cognitive impairment in mental disorders. Previous studies provided first experimental evidence that the communication between PFC and HP, the core of a complex network underlying mnemonic and executive processing, is substantially impaired in mouse models of disease already at neonatal age (Hartung et al. 2016; Oberlander et al. 2019). The mechanisms causing diminished communication within prefrontal-hippocampal networks during development remain largely unknown. We recently identified spine loss and sparsification of dendritic projections in layer 2/3 pyramidal neurons of neonatal PFC as one mechanism of disorganized network activity and reduced coupling with HP (Xu et al. 2019; Chini et al. 2020). These findings were consistent with the previous data from adult mice, which demonstrated that specific prefrontal DISC1 knock-down induced abnormal neuronal development and cognitive behaviors (Niwa et al. 2010; Saito et al. 2016). It is still unclear whether hippocampal dysfunction contributes to the early miswiring as well. Here, we combine electrophysiology and optogenetics *in vivo* with neuroanatomy and behavioral testing of immune challenged mice with either brain-wide or HP-confined suppression of DISC1. We provide evidence that (i) highly fragmented oscillatory activity with reduced power, fewer SPWs and decreased SPW-related firing of CA1 neurons in the i/vHP are present in both GE and G_{HP}E mice; (ii) confinement of DISC1 knock-down to HP of immune challenged mice causes weaker hippocampal drive to PFC and consequently, abnormal prefrontal network activity, despite unaffected firing rates over cortical layers; (iii) HP-confined or brain-wide DISC1 suppression similarly impairs the morphology of CA1 neurons, reducing the dendritic branching and the density of spines; (iv) the morphological and functional deficits in the HP of GE and G_{HP}E mice persist until prejuvenile age leading to cognitive impairment and long-lasting disruption of underlying prefrontal-hippocampal communication.

The severe morphological and functional impairment of the developing HP when DISC1 is suppressed goes in line with previous studies that identified this gene as a hub of maturational processes (Miyoshi et al. 2003; Duan et al. 2007). Especially DISC1 knock-down in HP has been associated with long-lasting deficits and behavioral impairment related to mental disorders (Callcott et al. 2005; Meyer and Morris 2008). DISC1 controls neurite growth, neuronal migration, and differentiation as well as axon targeting (Niwa et al. 2010; Narayan et al. 2013; Saito et al. 2016). In line with this function, the hippocampal structure and neuronal distribution across layers in the i/vHP was disturbed in GE mice when compared with controls. This result was consistent with the previous report by Tomita et al. (2011), which showed that knockdown of DISC1 in the HP of developing mouse resulted in impaired migration of dorsal CA1 pyramidal neurons. Intriguingly, it was also reported that HP-confined DISC1 suppression did not perturb the migration of CA1 pyramidal neurons in the dorsal HP but hindered the migration of dentate gyrus granule cells (Meyer and Morris 2009). The arborization and synaptic interactions of CA1 pyramidal neurons seem to be profoundly altered. The sparsification of their dendritic branching and the low number of spines document major developmental deficits of CA1 neurons when DISC1 was locally suppressed. These might result from disorganized microtubule-associated dynein motor complex (Ozeki et al. 2003; Kamiya et al. 2005). Moreover, lower density of axonal projections might link HP to PFC, as

previously observed from GE mice. The abnormal morphology is likely to underlie the early dysfunction of activity patterns generated within CA1 (e.g., SPWs, beta-gamma oscillations) and the diminishment of excitatory drive to PFC.

Suppression of DISC1 decreased the occurrence of SPWs and the SPW-related neuronal firing. While SPWs have been extensively characterized in the adult HP (Buzsaki 1986), their underlying mechanisms during development are still largely unknown. SPWs emerge early in life (Nowack et al. 1989; Brockmann et al. 2011; Valeeva et al. 2019). Similar to adult one, the neonatal SPWs seem to be generated within HP following population bursts in CA3 area. They correlate with increased firing rate of hippocampal neurons. The decreased SPWs occurrence and related neuronal discharge indicate that DISC1 suppression might cause miswiring within HP and abnormal coupling between CA1 and CA3. Accordingly, both pulse and ramp stimuli induced hippocampal firing. However, the power of spike-triggered LFP in CA1 dramatically decreased in GE and G_{HP}E mice, reflecting a weaker entrainment of local circuits in HP triggered by neuronal firing. Correspondingly, the power of oscillations in beta and gamma frequency range decreased in GE and G_{HP}E mice as well. In contrast, the theta bursts were less affected, their occurrence being similar across all investigated mice. This might be due to the fact that theta bursts have a multiple mostly extra-hippocampal origin with the septum as one main generator (Janiesch et al. 2011). At adulthood, the SPW-ripple events were still perturbed in different strains with suppressed DISC1, yet their occurrence was higher when compared with controls due to dysfunction of parvalbumin-positive interneurons (Altimus et al. 2015). We propose that the abnormal maturation of hippocampal circuits might have detrimental effects on the interneuron function and cause overcompensation resulting in hippocampal hyperexcitability.

Several lines of evidence show that DISC1 suppression perturbs not only the hippocampal activity and oscillatory entrainment but also the prefrontal activity and the communication within prefrontal-hippocampal networks. First, even when confined to HP, DISC1 suppression led to disorganized prefrontal activity with weaker power. In contrast, the overall firing of neurons in the PL remained unaffected. In contrast, when the DISC1 suppression was restricted to PFC, the firing of these neurons was dramatically decreased (Xu et al. 2019). Second, the timing of prelimbic firing in G_{HP}E mice was disturbed by the HP-confined DISC1 suppression, the characteristic beta band peak of firing interval and HP-spike triggered LFP power in layer 2/3 of PFC being absent in these mice. Third, the synchrony over a wide frequency range and the directionality of prefrontal-hippocampal interactions diminished in GE and G_{HP}E mice when compared with controls. Moreover, during ramp light stimulation the coherence of prefrontal-hippocampal interactions within beta-frequency range was significantly decreased in both GE and G_{HP}E mice, reflecting the weaker excitatory drive from the HP to PFC.

We propose that two mechanisms contribute to the abnormal prefrontal-hippocampal communication of GE and G_{HP}E. On the one hand, due to synaptic deficits and the sparsification of dendritic branching, the CA1 pyramidal neurons lose to a large extent the ability to fire in an oscillatory phase-coordinated manner. Consequently, the excitatory drive reaching mainly layer 5/6 of PFC (Parent et al. 2010; Padilla-Coreano et al. 2016) decreases and the boosting of intracortical connectivity resulting in beta entrainment within layer 2/3 is weaker. On the other hand, the sparsification of axonal projections might cause less

dense connections to the PFC. Whether the glutamate release of the hippocampal terminals targeting the PFC is also impaired remains to be elucidated.

In contrast to the DISC1 suppression confined to the pyramidal neurons in PFC, the DISC1 suppression in HP is not transient during development but persisted until prejuvenile age. These differences across areas might result from different regulation of Disc1 gene by external cues. Over 50 proteins interact with DISC1 controlling different maturational processes (Camargo et al. 2007; Ye et al. 2017). Despite similar DISC1 knock-down by shRNA, these interactions may lead to major differences across brain regions and over time. The interference of DISC1 with immune-relevant signaling pathways is of particular relevance (Beurel et al. 2010). The structural and functional deficits caused by the combination of DISC1 suppression with MIA are by far more pronounced than the effects induced by either of the two factors. They persist throughout the life span, leading to altered social and cognitive behavior (Abazyan et al. 2010; Ibi et al. 2010; Lipina et al. 2013). In the present study, we identified morphological and functional deficits within prefrontal-hippocampal networks of G_{HP}E mice until prejuvenile age. This abnormal communication between the two brain areas throughout the development relates to impaired prejuvenile cognitive performance, which requires the prefrontal-hippocampal activation (Barker and Warburton 2011). The ability to recognize new objects and their recency was absent in GE and G_{HP}E mice.

While comprehensive genome-wide association studies showed that DISC1 is unlikely to be a “genetic” factor causing schizophrenia (Schizophrenia Working Group of the Psychiatric Genomics Consortium 2014; Sullivan et al. 2012; Ripke et al. 2013), a wealth of data documented its relevance for psychiatric conditions (Tomoda et al. 2016, 2017; Trossbach et al. 2016; Kakuda et al. 2019; Sawa 2019). Orchestrating molecular cascades hypothesized to underlie disease-relevant physiological and behavioral abnormalities (Cuthbert and Insel 2013). DISC1 points out the contribution of abnormal development for multiple mental conditions. The present results provide first insight into the mechanisms by which DISC1 suppression interferes with the circuit function and cognitive abilities. They show that besides prefrontal deficits of layer 2/3 pyramidal neurons, the dysfunction of hippocampal CA1 neurons unable to drive the down-stream PFC during early development causes impaired prefrontal-hippocampal communication that relates to poor cognitive performance. HP plays a key role for memory deficits in mental disorders (Chen et al. 2018). Impairment of hippocampal recruitment during memory tasks has been described for schizophrenia patients and high-risks subjects (Di Giorgio et al. 2013; Rasetti et al. 2014). We provide experimental evidence that developmental miswiring in HP might cause cognitive deficits at adulthood and disrupt the prefrontal-hippocampal coupling. Weaker coactivation of PFC and HP has been identified in schizophrenia patients during cognitive tasks (Meyer-Lindenberg et al. 2001). Thus, the present study supports the neurodevelopmental origin of schizophrenia and highlights the hub function of HP during early maturation for the functional and cognitive deficits at adulthood.

Supplementary Material

Supplementary material can be found at *Cerebral Cortex* online.

Funding

European Research Council (ERC-2015-CoG 681577 to I.L.H.-O.) and the German Research Foundation (SPP 1665, SFB 936 B5 to I.L.H.-O.). I.L. H.-O. is funding member of FENS Kavli Network of Excellence.

Notes

We thank Dr Joseph Gogos for providing the DISC1 mice and Dr A. Sawa for providing short-hairpin RNA (shRNA) to DISC1. We also thank A. Marquardt, C. Tietze, A. Dahlmann and P. Putthoff for excellent technical assistance. *Conflict of Interest*: The authors declare no competing financial interests. I.L.H.-O., X.X. designed the experiments, X.X., L.S. carried out the experiments, X.X. analyzed the data, I.L.H.-O. and X.X. interpreted the data and wrote the paper. All authors discussed and commented on the manuscript.

References

- Abazyan B, Nomura J, Kannan G, Ishizuka K, Tamashiro KL, Nucifora F, Pogorelov V, Ladenheim B, Yang C, Krasnova IN, et al. 2010. Prenatal interaction of mutant DISC1 and immune activation produces adult psychopathology. *Biol Psychiatry*. 68:1172–1181.
- Ahlbeck J, Song L, Chini M, Bitzenhofer SH, Hanganu-Opatz IL. 2018. Glutamatergic drive along the septo-temporal axis of hippocampus boosts prelimbic oscillations in the neonatal mouse. *Elife*. 7:e33158.
- Altimus C, Harrold J, Jaaro-Peled H, Sawa A, Foster DJ. 2015. Disordered ripples are a common feature of genetically distinct mouse models relevant to schizophrenia. *Mol Neuropsychiatry*. 1:52–59.
- Baccala LA, Sameshima K. 2001. Partial directed coherence: a new concept in neural structure determination. *Biol Cybern*. 84:463–474.
- Baccala LA, Sameshima K, Takahashi DY. 2007. *Generalized partial directed coherence*. In: 2007 15th International Conference on Digital Signal Processing: 163–166.
- Backus AR, Schoffelen JM, Szebenyi S, Hanslmayr S, Doeller CF. 2016. Hippocampal-prefrontal theta oscillations support memory integration. *Curr Biol*. 26:450–457.
- Barker GR, Warburton EC. 2011. When is the hippocampus involved in recognition memory? *J Neurosci*. 31:10721–10731.
- Baumgart J, Grebe N. 2015. C57BL/6-specific conditions for efficient in utero electroporation of the central nervous system. *J Neurosci Methods*. 240:116–124.
- Berndt A, Schoenenberger P, Mattis J, Tye KM, Deisseroth K, Hegemann P, Oertner TG. 2011. High-efficiency channel-rhodopsins for fast neuronal stimulation at low light levels. *PNAS*. 108:7595–7600.
- Beurel E, Michalek SM, Jope RS. 2010. Innate and adaptive immune responses regulated by glycogen synthase kinase-3 (GSK3). *Trends Immunol*. 31:24–31.
- Bitzenhofer SH, Hanganu-Opatz IL. 2014. Oscillatory coupling within neonatal prefrontal-hippocampal networks is independent of selective removal of GABAergic neurons in the hippocampus. *Neuropharmacology*. 77:57–67.
- Bitzenhofer SH, Ahlbeck J, Hanganu-Opatz IL. 2017a. Methodological approach for optogenetic manipulation of neonatal neuronal networks. *Front Cell Neurosci*. 11:239.

- Bitzenhofer SH, Ahlbeck J, Wolff A, Wiegert JS, Gee CE, Oertner TG, Hanganu-Opatz IL. 2017b. Layer-specific optogenetic activation of pyramidal neurons causes beta-gamma entrainment of neonatal networks. *Nat Commun.* 8:14563.
- Brockmann MD, Poschel B, Cichon N, Hanganu-Opatz IL. 2011. Coupled oscillations mediate directed interactions between prefrontal cortex and hippocampus of the neonatal rat. *Neuron.* 71:332–347.
- Buzsaki G. 1986. Hippocampal sharp waves - their origin and significance. *Brain Res.* 398:242–252.
- Buzsaki G. 2002. Theta oscillations in the hippocampus. *Neuron.* 33:325–340.
- Cash-Padgett T, Jaaro-Peled H. 2013a. DISC1 mouse models as a tool to decipher gene-environment interactions in psychiatric disorders. *Front Behav Neurosci.* 7:113.
- Callicott JH, Straub RE, Pezawas L, Egan MF, Mattay VS, Hariri AR, Verchinski BA, Meyer-Lindenberg A, Balkissoon R, Kolachana B, et al. 2005. Variation in DISC1 affects hippocampal structure and function and increases risk for schizophrenia. *PNAS.* 102:8627–8632.
- Camargo LM, Collura V, Rain JC, Mizuguchi K, Hermjakob H, Kerrien S, Bonnert TP, Whiting PJ, Brandon NJ. 2007. Disrupted in schizophrenia 1 interactome: evidence for the close connectivity of risk genes and a potential synaptic basis for schizophrenia. *Mol Psychiatry.* 12:74–86.
- Cash-Padgett T, Jaaro-Peled H. 2013b. DISC1 mouse models as a tool to decipher gene-environment interactions in psychiatric disorders. *Front Behav Neurosci.* 7:113.
- Chen LW, Sun D, Davis SL, Haswell CC, Dennis EL, Swanson CA, Whelan CD, Gutman B, Jahanshad N, Iglesias JE, et al. 2018. Smaller hippocampal CA1 subfield volume in posttraumatic stress disorder. *Depress Anxiety.* 35:1018–1029.
- Chini M, Popplau JA, Lindemann C, Carol-Perdiguer L, Hnida M, Oberlander V, Xu X, Ahlbeck J, Bitzenhofer SH, Mulert C, et al. 2020. Resolving and rescuing developmental miswiring in a mouse model of cognitive impairment. *Neuron.* 105 e67:60–74.
- Cichon NB, Denker M, Grun S, Hanganu-Opatz IL. 2014. Unsupervised classification of neocortical activity patterns in neonatal and pre-juvenile rodents. *Front Neural Circuits.* 8:50.
- Clement EA, Richard A, Thwaites M, Ailon J, Peters S, Dickson CT. 2008. Cyclic and sleep-like spontaneous alternations of brain state under urethane anaesthesia. *PLoS One.* 3:e2004.
- Crabtree GW, Sun Z, Kvajo M, Broek JA, Fenelon K, McKellar H, Xiao L, Xu B, Bahn S, O'Donnell JM, et al. 2017. Alteration of neuronal excitability and short-term synaptic plasticity in the prefrontal cortex of a mouse model of mental illness. *J Neurosci.* 37:4158–4180.
- Cuthbert BN, Insel TR. 2013. Toward the future of psychiatric diagnosis: the seven pillars of RDoC. *BMC Med.* 11:126.
- Di Giorgio A, Gelao B, Caforio G, Romano R, Andriola I, D'Ambrosio E, Papazacharias A, Elifani F, Bianco LL, Taurisano P, et al. 2013. Evidence that hippocampal-parahippocampal dysfunction is related to genetic risk for schizophrenia. *Psychol Med.* 43:1661–1671.
- Duan X, Chang JH, Ge S, Faulkner RL, Kim JY, Kitabatake Y, Liu XB, Yang CH, Jordan JD, Ma DK, et al. 2007. Disrupted-in-schizophrenia 1 regulates integration of newly generated neurons in the adult brain. *Cell.* 130:1146–1158.
- Eichenbaum H. 2017. Prefrontal-hippocampal interactions in episodic memory. *Nat Rev Neurosci.* 18:547–558.
- Ennaceur A, Delacour J. 1988. A new one-trial test for neurobiological studies of memory in rats. 1: Behavioral data. *Behav Brain Res.* 31:47–59.
- Hartung H, Cichon N, De Feo V, Riemann S, Schildt S, Lindemann C, Mulert C, Gogos JA, Hanganu-Opatz IL. 2016. From shortage to surge: a developmental switch in hippocampal-prefrontal coupling in a gene-environment model of neuropsychiatric disorders. *Cereb Cortex.* 26:4265–4281.
- Heyser CJ, Ferris JS. 2013. Object exploration in the developing rat: methodological considerations. *Dev Psychobiol.* 55:373–381.
- Ibi D, Nagai T, Koike H, Kitahara Y, Mizoguchi H, Niwa M, Jaaro-Peled H, Nitta A, Yoneda Y, Nabeshima T, et al. 2010. Combined effect of neonatal immune activation and mutant DISC1 on phenotypic changes in adulthood. *Behav Brain Res.* 206:32–37.
- Janiesch PC, Kruger HS, Poschel B, Hanganu-Opatz IL. 2011. Cholinergic control in developing prefrontal-hippocampal networks. *J Neurosci.* 31:17955–17970.
- Kakuda K, Niwa A, Honda R, Yamaguchi KI, Tomita H, Nojebuzzaman M, Hara A, Goto Y, Osawa M, Kuwata K. 2019. A DISC1 point mutation promotes oligomerization and impairs information processing in a mouse model of schizophrenia. *J Biochem.* 165:369–378.
- Kamiya A, Kubo K, Tomoda T, Takaki M, Youn R, Ozeki Y, Sawamura N, Park U, Kudo C, Okawa M, et al. 2005. A schizophrenia-associated mutation of DISC1 perturbs cerebral cortex development. *Nat Cell Biol.* 7:1167–1178.
- Koike H, Arguello PA, Kvajo M, Karayiorgou M, Gogos JA. 2006. Disc1 is mutated in the 129S6/SvEv strain and modulates working memory in mice. *PNAS.* 103:3693–3697.
- Kruger HS, Brockmann MD, Salamon J, Itrich H, Hanganu-Opatz IL. 2012. Neonatal hippocampal lesion alters the functional maturation of the prefrontal cortex and the early cognitive development in pre-juvenile rats. *Neurobiol Learn Mem.* 97:470–481.
- Kvajo M, McKellar H, Arguello PA, Drew LJ, Moore H, MacDermott AB, Karayiorgou M, Gogos JA. 2008. A mutation in mouse Disc1 that models a schizophrenia risk allele leads to specific alterations in neuronal architecture and cognition. *PNAS.* 105:7076–7081.
- Kvajo M, McKellar H, Drew LJ, Lepagnol-Bestel AM, Xiao L, Levy RJ, Blazeski R, Arguello PA, Lacefield CO, Mason CA, et al. 2011. Altered axonal targeting and short-term plasticity in the hippocampus of Disc1 mutant mice. *PNAS.* 108:1349–1358.
- Lipina TV, Zai C, Hlousek D, Roder JC, Wong AH. 2013. Maternal immune activation during gestation interacts with Disc1 point mutation to exacerbate schizophrenia-related behaviors in mice. *J Neurosci.* 33:7654–7666.
- Meyer-Lindenberg A, Poline JB, Kohn PD, Holt JL, Egan MF, Weinberger DR, Berman KF. 2001. Evidence for abnormal cortical functional connectivity during working memory in schizophrenia. *Am J Psychiatry.* 158:1809–1817.
- Meyer KD, Morris JA. 2008. Immunohistochemical analysis of Disc1 expression in the developing and adult hippocampus. *Gene Expr Patterns.* 8:494–501.
- Meyer KD, Morris JA. 2009. Disc1 regulates granule cell migration in the developing hippocampus. *Hum Mol Genet.* 18:3286–3297.
- Miyoshi K, Honda A, Baba K, Taniguchi M, Oono K, Fujita T, Kuroda S, Katayama T, Tohyama M. 2003. Disrupted-in-schizophrenia 1, a candidate gene for schizophrenia, participates in neurite outgrowth. *Mol Psychiatry.* 8:685–694.
- Narayan S, Nakajima K, Sawa A. 2013. DISC1: a key lead in studying cortical development and associated brain disorders. *Neuroscientist.* 19:451–464.

- Niwa M, Kamiya A, Murai R, Kubo K, Gruber AJ, Tomita K, Lu L, Tomisato S, Jaaro-Peled H, Seshadri S, et al. 2010. Knock-down of DISC1 by in utero gene transfer disturbs postnatal dopaminergic maturation in the frontal cortex and leads to adult behavioral deficits. *Neuron*. 65:480–489.
- Nowack WJ, Janati A, Angtuaco T. 1989. Positive temporal sharp waves in neonatal EEG. *Clin Electroencephalogr*. 20:196–201.
- Oberlander VC, Xu X, Chini M, Hanganu-Opatz IL. 2019. Developmental dysfunction of prefrontal-hippocampal networks in mouse models of mental illness. *Eur J Neurosci*. 50:3072–3084.
- Ozeki Y, Tomoda T, Kleiderlein J, Kamiya A, Bord L, Fujii K, Okawa M, Yamada N, Hatten ME, Snyder SH, et al. 2003. Disrupted-in-Schizophrenia-1 (DISC-1): mutant truncation prevents binding to NudE-like (NUDEL) and inhibits neurite outgrowth. *PNAS*. 100:289–294.
- Padilla-Coreano N, Bolkan SS, Pierce GM, Blackman DR, Hardin WD, Garcia-Garcia AL, Spellman TJ, Gordon JA. 2016. Direct ventral hippocampal-prefrontal input is required for anxiety-related neural activity and behavior. *Neuron*. 89:857–866.
- Parent MA, Wang L, Su J, Netoff T, Yuan LL. 2010. Identification of the hippocampal input to medial prefrontal cortex in vitro. *Cereb Cortex*. 20:393–403.
- Rasetti R, Mattay VS, White MG, Sambataro F, Podell JE, Zolnick B, Chen Q, Berman KF, Callicott JH, Weinberger DR. 2014. Altered hippocampal-parahippocampal function during stimulus encoding: a potential indicator of genetic liability for schizophrenia. *JAMA Psychiatry*. 71:236–247.
- Ripke S, O'Dushlaine C, Chambert K, Moran JL, Kähler AK, Akterin S, Bergen SE, Collins AL, Crowley JJ, Fromer M, et al. 2013. Genome-wide association analysis identifies 13 new risk loci for schizophrenia. *Nat Genet*. 45:1150–1159.
- Rossant C, Kadir SN, Goodman DFM, Schulman J, Hunter MLD, Saleem AB, Grosmark A, Belluscio M, Denfield GH, Ecker AS, et al. 2016. Spike sorting for large, dense electrode arrays. *Nat Neurosci*. 19:634–641.
- Saito A, Taniguchi Y, Rannals MD, Merfeld EB, Ballinger MD, Koga M, Ohtani Y, Gurley DA, Sedlak TW, Cross A, et al. 2016. Early postnatal GABAA receptor modulation reverses deficits in neuronal maturation in a conditional neurodevelopmental mouse model of DISC1. *Mol Psychiatry*. 21:1449–1459.
- Sauer JF, Struber M, Bartos M. 2015. Impaired fast-spiking interneuron function in a genetic mouse model of depression. *Elife*. 4:e04979.
- Sawa A. 2019. DISC1 and its protein interactomes for mental function. *Biol Psychiatry*. 85:283–284.
- Siapas AG, Lubenov EV, Wilson MA. 2005. Prefrontal phase locking to hippocampal theta oscillations. *Neuron*. 46:141–151.
- Spellman T, Rigotti M, Ahmari SE, Fusi S, Gogos JA, Gordon JA. 2015. Hippocampal-prefrontal input supports spatial encoding in working memory. *Nature*. 522:309–314.
- Stujenske JM, Spellman T, Gordon JA. 2015. Modeling the spatiotemporal dynamics of light and heat propagation for in vivo optogenetics. *Cell Rep*. 12:525–534.
- Sullivan PF, Daly MJ, O'Donovan M. 2012. Genetic architectures of psychiatric disorders: the emerging picture and its implications. *Nat Rev Genet*. 13:537–551.
- Szczurkowska J, Cwetsch AW, dal Maschio M, Ghezzi D, Ratto GM, Cancedda L. 2016. Targeted in vivo genetic manipulation of the mouse or rat brain by in utero electroporation with a triple-electrode probe. *Nat Protoc*. 11:399–412.
- Tomita K, Kubo K, Ishii K, Nakajima K. 2011. Disrupted-in-Schizophrenia-1 (Disc1) is necessary for migration of the pyramidal neurons during mouse hippocampal development. *Hum Mol Genet*. 20:2834–2845.
- Tomoda T, Hikida T, Sakurai T. 2017. Role of DISC1 in neuronal trafficking and its implication in neuropsychiatric manifestation and Neurotherapeutics. *Neurotherapeutics*. 14:623–629.
- Tomoda T, Sumitomo A, Jaaro-Peled H, Sawa A. 2016. Utility and validity of DISC1 mouse models in biological psychiatry. *Neuroscience*. 321:99–107.
- Trossbach SV, Bader V, Hecher L, Pum ME, Masoud ST, Prikulis I, Schäble S, de Souza Silva MA, Su P, Boulat B, et al. 2016. Misassembly of full-length disrupted-in-schizophrenia 1 protein is linked to altered dopamine homeostasis and behavioral deficits. *Mol Psychiatry*. 21:1561–1572.
- Valeeva G, Nasretdinov A, Rychkova V, Khazipov R. 2019. Bilateral synchronization of hippocampal early sharp waves in neonatal rats. *Front Cell Neurosci*. 13:29.
- Warburton EC, Brown MW. 2015. Neural circuitry for rat recognition memory. *Behav Brain Res*. 285:131–139.
- Wolansky T, Clement EA, Peters SR, Palczak MA, Dickson CT. 2006. Hippocampal slow oscillation: a novel EEG state and its coordination with ongoing neocortical activity. *J Neurosci*. 26:6213–6229.
- Xu X, Chini M, Bitzenhofer SH, Hanganu-Opatz IL. 2019. Transient knock-down of prefrontal DISC1 in immune-challenged mice causes abnormal long-range coupling and cognitive dysfunction throughout development. *J Neurosci*. 39:1222–1235.
- Ye F, Kang E, Yu C, Qian X, Jacob F, Yu C, Mao M, Poon RYC, Kim J, Song H, et al. 2017. DISC1 regulates neurogenesis via modulating kinetochore attachment of Ndel1/Nde1 during mitosis. *Neuron*. 96:1041–1054e1045.

4.3 Article 3

Sparser and less efficient projections from hippocampus to prefrontal cortex account for developmental network dysfunction in a mouse model with schizophrenia-like etiology

Lingzhen Song^{1*}, Xiaxia Xu^{1*}, Peggy Putthoff¹, David Fleck², Marc Spehr², Ileana L. Hanganu-Opatz¹

¹ Institute of Developmental Neurophysiology, Center for Molecular Neurobiology, University Medical Center Hamburg-Eppendorf, 20251 Hamburg, Germany

² Department of Chemosensation, Institute for Biology II, RWTH Aachen University, 52074 Aachen, Germany

* These authors contributed equally to this work.

The Journal of Neuroscience, (2021). Revision.

Personal contribution

I designed part of the project. I carried out *in vivo* electrophysiology and *in vitro* electrophysiology experiments. I carried out histological investigations and image analysis. I carried out the formal analysis and data curation. I wrote the original draft, reviewed and edited the manuscript.

Sparser and less efficient projections from hippocampus to prefrontal cortex account for developmental network dysfunction in a mouse model with schizophrenia-like etiology

Lingzhen Song^{1#}, Xiaxia Xu^{1#}, Peggy Putthoff¹, David Fleck², Marc Spehr² and Ileana L. Hanganu-Opatz^{1,*}

¹Institute of Developmental Neurophysiology, Center for Molecular Neurobiology, University Medical Center Hamburg-Eppendorf, 20251 Hamburg, Germany

²Department of Chemosensation, Institute for Biology II, RWTH Aachen University, 52074 Aachen, Germany

#equal contribution

Running title: Less-efficient connectivity in a schizophrenia model

*Corresponding authors: Ileana L. Hanganu-Opatz
hangop@zmnh.uni-hamburg.de

Figures: 8

Tables: 4

Multimedia: 1

Number of pages: 47

Number of words in Abstract: 215

Number of words in Introduction: 604

Number of words in Discussion: 1299

Competing financial interest

The authors declare no competing financial interests.

Acknowledgements

We thank Dr. Joseph Gogos for providing the DISC1 mice. We also thank A. Marquardt and A. Dahlmann for excellent technical assistance. This work was funded by grants from the European Research Council (ERC-2015-CoG 681577 to I.L.H.-O.), German Research Foundation (Ha4466/11-1, SPP 1665, SFB 936 B5 to I.L.H.-O, 368482240/GRK2416, 302153259, 378028035 to M.S.) and Landesforschungsförderung Hamburg (LFF73 and LFF76 to I.L. H.-O.).

Abstract

Precise information flow from the hippocampus (HP) to prefrontal cortex (PFC) critically controls the cognitive processing and, on the flip side, is selectively impaired in mental illness. Prefrontal-hippocampal coupling emerges early in life and, already at this age, is weaker in animal models mimicking the genetic and environmental etiology (GE) of schizophrenia. While this impairment relates to local miswiring in PFC and HP, it is unknown whether abnormal connectivity between both brain areas additionally contributes. Here, we combine *in vivo* electrophysiology and optogenetics with in-depth tracing of projections to monitor the morphology and function of hippocampal afferents in the PFC of control and GE mice throughout development. We show that projections from the hippocampal CA1 area preferentially target layer 5/6 pyramidal neurons and interneurons, and less layer 2/3 neurons of prelimbic (PL) subdivision of PFC. In neonatal GE mice, sparser axonal projections from CA1 pyramidal neurons with abnormal excitability reach the PL. Their ability to entrain layer 5/6 firing and oscillatory activity is decreased. These structural and functional deficits of hippocampal-prelimbic connectivity persist, yet are less prominent in pre-juvenile GE mice. Thus, besides local dysfunction of HP and PL, sparser and less efficient connectivity between the two brain areas is present in GE mice throughout development and might cause lifelong miswiring and ultimately, cognitive disruption.

Keywords: development, prefrontal cortex, hippocampus, network oscillations, axonal projections, schizophrenia, neuronal firing

Significance Statement

Poor cognitive performance in mental disorders comes along with prefrontal-hippocampal dysfunction. Recent data from mice that mimic the genetic and environmental etiology of schizophrenia identified the origin of deficits during early development, when the local circuits in both areas are compromised. Here, we show that sparser and less efficient innervation as well as cellular dysfunction is the substrate of the weaker excitatory drive from hippocampus to prefrontal cortex as well as of poorer oscillatory coupling between the two brain areas in

these mice. While the structural and functional connectivity deficits persist during the entire development, their magnitude decreases with age. The results add experimental evidence for the developmental miswiring hypothesis of schizophrenia.

Introduction

The brain circuitry accounting for memory and executive abilities in mammals is highly complex and extends over cortical and subcortical areas, yet two brain areas, the hippocampus (HP) and prefrontal cortex (PFC), are considered as being its core (Bahner and Meyer-Lindenberg, 2017). Both areas are involved in memory processing: the HP controls memory consolidation, whereas the PFC suppresses competing memories and allows context-appropriate memories (Spellman et al., 2015; Eichenbaum, 2017). The HP and PFC tightly interact to achieve these tasks (Miller and Cohen, 2001) via direct monosynaptic as well as indirect polysynaptic projections (Jay et al., 1989; Dolleman-Van Der Weel and Witter, 1996; Vertes, 2006). The highly efficient communication relevant for memory processing is mediated by oscillatory synchrony of neural activity in the two brain areas (Siapas et al., 2005; Backus et al., 2016; Alemany-Gonzalez et al., 2020). On the flip side, abnormal episodic memory, as one trait of a broader pattern of deficits in higher cognitive functions, has been reported for schizophrenia (Guo et al., 2019). The cognitive impairment significantly contributes to disability and represents a major burden for patients because is generally treatment refractory (Bora et al., 2010). Poor cognitive performance relates to reduced prefrontal-hippocampal connectivity in both schizophrenia patients, prodromal and high-risk subjects as well as mouse models of disease (Friston and Frith, 1995; Meyer-Lindenberg et al., 2001; Sigurdsson et al., 2010; Greenland-White et al., 2017). In line with the neurodevelopmental origin of schizophrenia, it has been hypothesized that, while the behavioral symptoms are firstly detectable at adolescence-young adulthood, the underlying network is compromised at a much earlier stage (Owen et al., 2016).

Experimental confirmation of this hypothesis in human subjects faces major technical and ethical limitations. Therefore, animal models, despite being able to mimic only some disease features (e.g. etiology, neurochemical deficits, behavioral symptoms), are instrumental for uncovering the mechanisms of schizophrenia-related dysfunction (Sigurdsson, 2016; Diamantopoulou and Gogos, 2019). Genetic models, such as mice modeling 22q11.2 microdeletions identified in patients (McDonald-McGinn et al., 2015) as well as models

combining genetic deficits and environmental stressors related to higher disease risk (dual-hit genetic-environmental (GE) models) (Kannan et al., 2013) show cognitive impairment and abnormal communication within prefrontal-hippocampal circuits (Sigurdsson et al., 2010). We previously showed that these deficits emerge already early in life, at a developmental stage corresponding to neonatal period in mice (first postnatal week) and third gestational trimester in humans (Clancy et al., 2001). Dual-hit GE mice mimicking both the genetic (mutation of the intracellular hub of developmental processes Disrupted-In-Schizophrenia 1 (DISC1) gene) (Brandon and Sawa, 2011) and the environmental (challenge by maternal immune activation (MIA)) background that has been related to mental illness, have abnormal patterns of early electrical activity both in PFC and HP (Hartung et al., 2016; Xu et al., 2019; Chini et al., 2020; Xu et al., 2021). Additionally, prefrontal-hippocampal coupling through synchrony of oscillatory activity as well as directed HP-to-PFC interactions is diminished. Three mechanisms might cause these early deficits: (i) local disruption of prefrontal circuits, (ii) local disruption of hippocampal circuits, and/or (iii) abnormal long-range communication between PFC and HP. We previously confirmed the first two mechanisms and reported that (i) layer 2/3 pyramidal neurons in PFC experienced excessive microglia-induced synaptic pruning leading to impaired beta-gamma oscillations (Chini et al., 2020) and (ii) the sharp-waves, firing, and network activity in hippocampal CA1 area are decreased in GE mice (Xu et al., 2021). Here, we address the third hypothesis and investigate the long-range connectivity between HP and PFC throughout development in dual-hit GE mice. We show that both structural and functional deficits of hippocampal innervation of PFC compromise the communication between the two brain areas.

Materials and Methods

Animals

All experiments were performed in compliance with the German laws and the guidelines of the European Community for the use of animals in research and were approved by the local ethical committee (G17/015, N18/015). Timed-pregnant mice from the animal facility of the University Medical Center Hamburg-Eppendorf were housed individually at a 12 h light/12 h dark cycle

and were given access to water and food ad libitum. The day of vaginal plug detection was considered embryonic day (E) 0.5, the day of birth was considered postnatal day (P) 0. The heterozygous offspring carrying a DISC1 allele (DISC1^{Tm1Kara}) on a C57BL/6J background, whose dams were injected at E9.5 with the viral mimetic polyinosinic-polycytidylic acid (poly I:C, 4 mg/kg, i.p.), were classified as dual-hit genetic-environmental (GE) mice (Hartung et al., 2016). Pups born from homozygous Disc1^{Tm1Kara} dams and wildtype males, and pups born from wildtype dams and homozygous Disc1^{Tm1Kara} males were pooled together, as no difference between the two groups was found. Genotypes were assessed using genomic DNA (tail biopsies) and following primer sequences: forward primer 5'-TAGCCACTCTCATTGTCAGC-3' and reverse primer 5'-CCTCATCCCTTCCACTCAGC-3'. Nontreated wildtype C57BL/6J mice and the offspring of dams injected at E9 with saline (0.9%) were used as controls (CON) and combined together, as no difference between the two groups was found. All experiments were performed on pups of both sexes during neonatal development at P8–P10, as well as during pre-juvenile development at P20–P24.

Stereotaxic injections

The pups were placed in a stereotactic apparatus and kept under anesthesia with isoflurane (induction: 5%, maintenance: 2.5%) for the entire procedure. For retrograde tracing, fluorogold (FG, 2.5%, Fluorochrome, LLC, USA) was iontophoretically injected into the PFC (0.5 mm anterior to bregma, 0.3 mm right to the midline) of P7 or P21 mice. For anterograde tracing, biotinylated dextran amine (BDA, 5% in 0.125 M phosphate buffer, Thermo Fisher Scientific, USA) was iontophoretically injected in the HP (0.7 mm anterior to lambda, 2.3 mm right to the midline) of P7 or P21 mice. A glass capillary (~25 mm tip diameter) was filled with either ~1 µl FG or ~1 µl BDA by capillary forces, and a silver wire was inserted such that it was in contact with the FG or BDA solution. For both anterograde and retrograde tracing, the positive pole of the iontophoresis device was attached to the silver wire, whereas the negative one was attached to the skin of the neck. The capillary was carefully lowered into the PFC (~1.5 mm dorsal from the dura) or HP (~1.5 mm dorsal from the dura). For injections anodal current to the pipette (6 s on/off current pulses of 6 mA) was applied for 10 min.

For trans-synaptic labeling, a 0.5 μ l syringe (Hamilton Company, Reno, NV) was attached to a microsyringe pump controller (Micro4, WPI) and wheat germ agglutinin (WGA, 200 nl 4%, Vector Laboratories, Burlingame, CA) was injected at a rate of 80 μ l/min into the HP at the same coordinates as for BDA injection. For anterograde labeling of hippocampal inputs for optogenetic experiments, same procedure was used to inject AAV9-hSyn-hChR2(H134R)-EYFP (Addgene, 2.67×10^{13} GC/ μ l) into the HP (80 nl, 50 nl/min for P1 mice and 150 nl, 80 nl/min for P13-P15 mice). Following injection, the pipette or syringe was left in place for at least 5 min to allow optimal diffusion of the solution. The scalp was closed by application of tissue adhesive glue. The pups were warmed on a heating pad for 10–15 min and returned to the dam until full recovery of the motor activity. The pups were perfused 3 days later for FG and BDA stainings. The perfusion occurred 30 h after WGA injection, in line with literature and our pilot data that showed trans-synaptic transfer to the 1st order but not other downstream neurons (Phillips et al., 2019). All the WGA-positive cells were co-stained with NeuN to exclude the possibility of non-neuronal innervation (data not shown).

In utero electroporation and clearing

Timed-pregnant CON or GE mice (E15.5) were injected subcutaneously with buprenorphine (0.05 mg/kg body weight) 30 min before surgery. Surgery was performed on a heating blanket and toe pinch and breathing were monitored throughout. Under isoflurane anesthesia (induction: 5%, maintenance: 3.5%), the eyes of the dam were covered with eye ointment to prevent damage before the uterine horns were exposed and moistened with warm sterile phosphate buffered saline (PBS, 37°C). Solution containing 1.25 μ g/ μ l pAAV-CAG-tDimer2 and 0.1% fast green dye at a volume of 0.75-1.25 μ l was injected into the right lateral ventricle of individual embryos using pulled borosilicate glass capillaries with a sharp and long tip. Plasmid DNA was purified with NucleoBond (Macherey-Nagel, Germany). To target intermediate and ventral HP (i/vHP), a tri-polar approach was used (Szczyrkowska et al., 2016). Each embryo within the uterus was placed between the electroporation tweezer-type paddles (5 mm diameter, both positive poles, Protech, TX, USA) that were oriented at a 90° leftward angle from the midline and a 0° angle downward from anterior to posterior. A third custom build

negative pole was positioned on top of the head roughly between the eyes. Electrode pulses (30 V, 50 ms) were applied six times at intervals of 950 ms controlled by an electroporator (CU21EX, BEX, Japan). Uterine horns were placed back into the abdominal cavity after electroporation. The abdominal cavity was filled with warm sterile PBS (37°C) and abdominal muscles and skin were sutured individually with absorbable and non-absorbable suture thread, respectively. After recovery, pregnant mice were returned to their home cages, which were half placed on a heating blanket for two days after surgery, and received on a daily basis additional wet food supplemented with 2-4 drops Metacam (0.5 mg/ml, Boehringer-Ingelheim, Germany).

Fluorescence expression was confirmed at P2 using a portable fluorescence flashlight (Nightsea, MA, USA). At P10, pups were anesthetized with 10% ketamine (aniMedica, Germany) / 2% xylazine (WDT, Germany) in 0.9% NaCl solution (10 µg/g body weight, intraperitoneally) and transcardially perfused with Histofix (Carl Roth, Germany) containing 4% paraformaldehyde. Brain clearing was performed as previously described (Chung and Deisseroth, 2013). Brains were postfixed overnight at 4°C to maintain structural integrity in hydrogel fixation solution containing 4% acrylamide, 0.05% bis-acrylamide, 0.25% VA-044 Initiator, 4% PFA in PBS^{-/-}. To allow hydrogel polymerisation, oxygen was removed via a vacuum pump connected to a desiccator. Argon was released and removed twice to establish O₂-free conditions. After heat-triggered polymerization (37°C; 3 h), samples were extracted from hydrogel and washed in clearing solution containing 200 mM boric acid and 138 mM SDS (pH 8.5) for 24 h at room temperature (RT). Embedded brains were cleared at 37°C for 48 days. Clearing solution was changed twice each week. DRAQ5 (nuclear marker; 1:1000) was added for 2 days. Next, removal of SDS (washing (3x) in PBST (0.1% TritonX in PBS^{-/-}) at RT) terminated clearing. Imaging was performed after 24 h incubation in RIMS80 containing 80 g Nycodenz, 20 mM PS, 0.1% Tween 20, and 0.01% sodium acid. Imaging was performed with a Cleared Tissue LightSheet (Intelligent Imaging Innovations, Inc., Denver CO) dual-side illumination lightsheet microscope for whole organ imaging, equipped with a PlanNeoFluar 1.0x / 0.25NA objective. 3D stacks were acquired sequentially. A 640 nm laser was used for

excitation of DRAQ5 using a multi-line Set 43HE filter cube and a 561 nm laser for tDimer Ds-Red Filter cube. Image stacks were stitched using slidebook 6 software. Brain regions of interest were manually marked using a nuclear staining by inspecting coronal slices of the 3D dataset using Imaris 9.7. Fibers were reconstructed and fiber volume within the prelimbic cortex was calculated. The fiber volume / PL volume ratio was normalized to the transfected cell count in the lateral hippocampal region.

Electrophysiological recordings and optogenetic manipulation in vivo

Multisite extracellular recordings were performed in the prelimbic subdivision (PL) of the PFC from P8-10 or P20-P24 mice. For recordings in non-anesthetized state in P8-P10 mice, 0.5% bupivacaine / 1% lidocaine was locally applied on the neck muscles. For recordings in anesthetized state in P20-P24 mice, mice were injected intraperitoneally with urethane (1 mg/g body weight; Sigma-Aldrich) before surgery. For both groups, the surgery was performed under isoflurane anesthesia (induction: 5%; maintenance: 1.5-2%). The head of the pup was fixed into a stereotaxic apparatus using two plastic bars mounted on the nasal and occipital bones with dental cement. The bone over the PFC (0.8 mm anterior to bregma, 0.1-0.5 mm right to the midline) and the CA1 area of the intermediate HP (3.5-3.7 mm anterior to bregma, 3.5-3.8 mm right to the midline) was carefully removed by drilling holes of 0.5 mm diameter. Four-shank optoelectrodes with 4 × 4 recording sites (0.4-0.8 MΩ impedance, 0.1 mm spacing, 0.125 mm inter-shank spacing; NeuroNexus, MI, USA), aligned with optical fibers (50 μm diameter) and ending 200 μm above the top recording sites, were inserted into PL at a depth of 2.0 mm from the skull surface. One silver wire was inserted into cerebellum to serve as ground and reference electrode. Before signal acquisition, a recovery period of 15 min after electrode insertion was provided. In PL, the two medial shanks were located into layer 2/3, whereas the lateral shanks were located into layer 5/6. Extracellular signals were band-pass filtered (0.1 Hz to 5 kHz) and digitized (32 kHz) with a multichannel extracellular amplifier (Digital Lynx SX, Neurolynx) and the Cheetah acquisition software (Neurolynx).

Pulsatile (laser on-off, 5 ms, 8 Hz, 3 s) or ramp (linearly increasing power, 3 s) light stimulations *in vivo* were performed with an Arduino uno (Arduino, Italy) controlled laser system

(473 nm wavelength, Omicron, Austria), which was coupled with a 50 μm (four-shank electrodes) diameter light fiber (Thorlabs, NJ, USA). Each type of stimulation was repeated 60 times with an interval of 7 s. Laser power was measured and adjusted to the range of 0.75-2.5 mW at the fiber tip.

Electrophysiological recordings and optogenetic manipulation in vitro

For patch-clamp recordings, pups were anaesthetized with 5% isoflurane and decapitated. Brains were rapidly removed and placed in ice-cooled oxygenated (95% O_2 /5% CO_2) high-sucrose-based artificial cerebral spinal fluid (ACSF) containing (in mM): 228 sucrose, 2.5 KCl, 1 NaH_2PO_4 , 26.2 NaHCO_3 , 11 glucose and 7 MgSO_4 (310 mosmol/kg H_2O). Coronal brain slices (300 μm) were prepared using a vibratome (Leica VT 1000S). Slices were allowed to recover in oxygenated ACSF containing (in mM): 119 NaCl, 2.5 KCl, 1 NaH_2PO_4 , 26.2 NaHCO_3 , 11 glucose, 1.3 MgSO_4 (310 mOsmol/kg H_2O) at 33 °C for at least 30 min, then kept at room temperature (~22 °C) for at least another 60 min before recordings. Slices were transferred to the recording chamber and continuously perfused with oxygenated standard ACSF (2–3 mL/min) at room temperature.

Whole-cell recordings were made from neurons located in PL. The location and neuronal morphology served to identify the prelimbic layers. Two to three coronal slices were used per animal and chosen according to the coordinates relative to Bregma (AP: +1.70 to +0.7 mm). Slices were visualized using an upright microscope (BX50WI, Olympus Optical, Tokyo, Japan) and with infrared and differential interference contrast optics. All recordings were performed from pyramidal neurons that were identified according to their shape, spiking pattern, and action potential width. Borosilicate glass patch pipettes (4-8 $\text{M}\Omega$) were filled with K-gluconate-based solution containing (in mM): 130 K-gluconate, 10 HEPES, 0.5 EGTA, 4 Mg-ATP, 0.3 Na-GTP, 8 NaCl (285 mosmol/kg H_2O , pH adjusted to 7.4 with KOH) and 0.3%-0.5% biocytin for post hoc morphological identification of recorded cells. Recordings were performed with an EPC 10 amplifier and PatchMaster software v2x73.1 (HEKA Elektronik), filtered at 2.9 kHz using a Bessel filter, and sampled at 10 kHz. All potentials were corrected for the liquid junction potential of the gluconate-based electrode solution, which, according to our

measurement, was -8.65 mV. The resting membrane potential (RMP) was measured immediately after obtaining the whole-cell configuration. Unless otherwise noted, all experiments were carried out at a membrane potential of -70 mV under voltage clamp conditions. To measure the basic properties of the membrane, 600 ms long hyperpolarizing or depolarizing current pulses ranging from -100 pA to 120 pA in a 20 pA step were applied. Access resistance (R_s) was monitored under voltage-clamp conditions by analyzing capacitive transients during 5 ms-long square wave depolarizing pulses. Recordings were included only when a $G\Omega$ seal formed prior to whole-cell access with R_s of less than 30 M Ω . Cells with R_s changes $> 25\%$ were excluded from further investigation. Spontaneous excitatory postsynaptic current (EPSC) events were recorded at a holding potential of -70 mV. None of the investigated neurons showed spontaneous firing at resting membrane potential.

For optogenetic stimulation *in vitro*, 470-nm light pulses were applied with a CoolLED system (pE-2) attached to the upright microscope. Maximal light output at 470 nm was measured at 2 mW with optical power meter (Thorlabs, NJ, USA). For stimulation of hippocampal afferents targeting prelimbic neurons, light pulses (3 ms, 5 ms 10 ms, 15 s interval) were repetitively applied every 15 s for up to 10 times. For the investigation of short-term synaptic plasticity, train pulses consisted of 2 s-long light pulses at 2 Hz, 4Hz, 8 Hz repeated every 15 s for up to 5 times. The induced EPSCs and inhibitory postsynaptic current (IPSCs) were voltage-clamp recorded at -70 mV and $+10$ mV, respectively. To block AMPA/kainate receptors, 10 μ M CNQX (6-cyano-7-nitroquinoxaline-2, 3-dione) was added to the recording chamber solution.

Histology and immunohistochemistry

Briefly, P8–P10 and P20–P24 mice were anesthetized with 10% ketamine / 2% xylazine in 0.9% NaCl solution (10 μ g/g body weight, i.p.) and transcardially perfused with Histofix containing 4% PFA. Brains were postfixed with 4% PFA for 24 h and sectioned coronally at 100 μ m for reconstruction of the position of electrodes, or 50 μ m for further staining. Sections for staining were collected in three equally spaced series. To reduce the redundancy of information of

neighbor slices, only one of the series was mounted or used for subsequent staining and analysis.

For immunohistochemistry, free floating slices were permeabilized and blocked with PBS containing 0.3% Triton X-100 (Sigma Aldrich), 5% normal bovine serum (Jackson ImmunoResearch). Subsequently, slices were incubated overnight with mouse monoclonal Alexa Fluor-488-conjugated antibody against NeuN (1:100, MAB377X; Merck Millipore, MA, USA), Alexa Fluor-488-conjugated streptavidin (1:1000, Merck Millipore), or rabbit polyclonal primary antibody against GABA (1:1000, no. A2052; Sigma-Aldrich), polyclonal guinea-pig antibody against VGLUT1 (1:1000, Synaptic Systems, Germany), rabbit polyclonal primary antibody against lectin (1:1000, no. A2052; Sigma-Aldrich) followed by 2 h incubation with Alexa Fluor-568 goat anti-rabbit IgG secondary antibody (1:500, A11008; Merck Millipore), Alexa Fluor-568 goat anti-guinea pig (1:500, Molecular Probes, OR, USA), Alexa Fluor-568 donkey anti-rabbit (1:500, Life Technologies, CA, USA) and Alexa Fluor-568-conjugated streptavidin (1:1000, Merck Millipore). DAPI (1:500) was added to the second antibody for the nuclear labeling. Finally, slices were transferred to glass slides and covered with Vecta-Shield (Vector Laboratories). To avoid cross-reactivity between the anti-lectin primary antibody and other antibodies, sections were firstly incubated with anti-lectin and then underwent subsequent biotinylation and streptavidin treatment steps. Following the last wash, sections were again blocked for 2 h.

For BDA staining, sections (prepared as described above) were rinsed in PBS (0.125 M, pH 7.4–7.6) for 10 min, treated with peroxide solution (3% peroxide, 10% methanol in 0.125 M PB) for 10 min to quench any endogenous peroxidases within the tissue, and rinsed again in PB three times for 10 minutes each. Subsequently, the sections were washed in PBS containing 0.5% Triton-X and incubated with avidin biotinylated enzyme complex (Vectastain ABC kit; Vector, Burlingame, CA) at room temperature (90 min) or overnight at 4°C according to the manufacturer's instructions. After rinsing in Tris-HCl (pH 7.4), the sections were further incubated with DAB working buffer (DAB peroxidase substrate kit, Vector Laboratories, USA) at room temperature for 2–10 min. After the signal was detected, all sections were rinsed with

Tris-HCl, mounted on slides, dehydrated, cleared in xylenes, coverslipped, and viewed with brightfield microscopy. In some cases, nuclear staining was necessary to aid the delineation of brain regions.

Imaging

Wide-field fluorescence was performed to reconstruct the position of recording electrode in brain slices of investigated pups. Fluorogold-positive cells were automatically quantified using custom-written algorithms in FIJI, and confirmed manually. For DAB staining, all bright field images were obtained using a Zeiss imager M1 microscope (Zeiss, Oberkochen, Germany) with identical settings. Bright field photomicrographs were imported into FIJI and their contrast and brightness were adjusted. Axons were manually traced using FIJI. Area and layer borders were set by superimposing photomicrographs of BDA sections with another series of sections that processed for nuclear staining. For each experiment, one series of sections of hippocampus was stained with streptavidin and DAPI, injection sites in hippocampus were examined and the number of injected neurons was counted. Statistical tests were conducted on the density of axons ($\mu\text{m}/\text{mm}^2$) when normalized to the density of stained neurons in the hippocampus CA1.

Data Analysis

Electrophysiological data were imported and analyzed off line using custom-written tools in MATLAB software version 7.7 (Mathworks). Data were band-pass filtered (500–5000 Hz for spike analysis or 1–100 Hz for local field potentials (LFP)) using a third-order Butterworth filter forward and backward to preserve phase information before down-sampling to 1000 Hz to analyze LFP.

Power spectral density. For power spectral density analysis, 1 s-long windows of network oscillations were concatenated and the power was calculated using Welch's method with non-overlapping windows. For optical ramp stimulation, we compared the average power during the 1.5 s-long time window preceding the stimulation to the last 1.5 s-long time window of light-evoked activity.

Single unit activity (SUA). SUA was detected and clustered using klusta (Rossant et al., 2016) and manually curated using phy (<https://github.com/cortex-lab/phy>). Data were imported and analyzed using custom-written tools (<https://github.com/OpatzLab/HanganuOpatzToolbox>) in the MATLAB (MathWorks).

Firing rate. The firing rate was computed by dividing the total number of spikes by the duration of the analyzed time window. For optical pulsatile stimulations, modulation index (MI) of firing rate was calculated as $(\text{Firing}_{\text{during-stimulation}} - \text{Firing}_{\text{pre-stimulation}}) / (\text{Firing}_{\text{during-stimulation}} + \text{Firing}_{\text{pre-stimulation}})$.

Membrane properties. Analysis of data resulted from patch-clamp recordings was performed offline using custom-written scripts in the MATLAB. For all recorded neurons, RMP, input resistance (R_{in}), membrane time constant (τ_m), membrane capacity (C_m), R_s , action potential (AP) amplitude, halfwidth, and firing threshold were calculated. R_{in} was calculated according to Ohm's law by dividing the resulting potential changes by the amplitude of the applied current (-60 pA). τ_m was calculated by fitting a monoexponential function to the induced potential deflection. C_m was calculated by dividing τ_m by R_{in} . Firing threshold voltage was considered at the point where the depolarization speed firstly exceeded 10 mV/ms. Action potential amplitude was measured from threshold to peak, with the half-width measured at half this distance. Firing rate was calculated during a 600 ms-long depolarization of the cells by 80 pA current injection. Sag amplitude was calculated for each cell as the proportional difference between the initial voltage response (i.e. during the first 200 ms of the current pulse) and the steady state response (averaged for 100 ms) to a hyperpolarizing current pulse of -100 pA.

Synaptic activity. Synaptic events were automatically detected automatically on template parameters (Pernia-Andrade et al., 2012) and manually examined to exclude false positive events. Events were excluded if the amplitude was < 3 pA. Inter-event interval (event frequency) and event amplitude were analyzed and compared between groups. Light-evoked EPSCs (eEPSCs) were averaged over 10-20 stimuli. Their peak amplitude and onset (i.e. delay between light stimulus and time point at which the response speed exceeded 10 pA/ms) were calculated. The coefficient of variation (CV) for a given measured variable was defined as the

ratio between the standard deviation and the average value of 10-20 individual responses to light stimulation.

Statistics. Statistical analyses were performed in MATLAB environment. Data were tested for significant differences using one-way repeated-measures analysis of variance (ANOVA) followed with Bonferroni-corrected post hoc analysis. Data with non-normal distribution (only the eEPSC amplitude) were tested with the nonparametric ANOVA followed with Bonferroni-corrected post hoc analysis. Values were considered as outliers and removed when their distance from the 25th or 75th percentile exceeded 1.5 times the interquartile interval. Data are presented as mean \pm SEM. Significance levels of $p < 0.05$ (*), $p < 0.01$ (**) or $p < 0.001$ (***) were used.

Results

Anatomical characterization of hippocampal projections targeting the prelimbic cortex in control and dual-hit GE mice

To gain insight into prefrontal-hippocampal communication during development in dual-hit GE mice we first performed an in-depth structural analysis of axonal projections that link the two regions. In adult mice, our data showed that, while the prelimbic subdivision of medial PFC (PL) and hippocampus (HP) interact along multiple multi-synaptic routes, the main route of communication are dense ipsilateral monosynaptic projections from HP to PL, lacking a feedback equivalent (Jay and Witter, 1991; Cenquizca and Swanson, 2007). The developmental profile of these unidirectional projections is, however, still poorly understood.

To close this knowledge gap, we performed retrograde and anterograde staining of the hippocampal projections accompanied by path tracking during early neonatal development (Fig. 1A). First, we used the retrograde tracer Fluorogold (FG) that was iontophoretically injected into the PL of control mice (CON) ($n=4$) at postnatal day (P) 7. Three days later, we detected labeled neurons in PL (Fig. 1B), with minimal diffusion to neighboring areas, such as infralimbic cortex (IL). FG injection labeled few cells in dorsal HP (dHP), but labeled cell density augmented along the fronto-caudal axis and peaked at the level of intermediate and ventral HP (i/vHP), which is consistent with our previous results (Ahlbeck et al., 2018). FG-positive

neurons were not uniformly distributed over hippocampal areas but mainly concentrated in the deep layers of CA1 region, close to *stratum oriens* (SO) (Fig. 1B). Second, we iontophoretically injected the anterograde tracer biotinylated dextran amine (BDA) into the hippocampal CA1 region of P7 CON mice (n=8) (Fig. 1C). Three days later, BDA-labeled axonal terminals were detected in PL, accumulating in, yet not exclusively restricted to layer 5/6 (Fig. 1C). The path and distribution of hippocampal axonal streamlines terminating in PL was revealed in cleared brains (Fig. 1D, Multimedia 1). These results show that, already at neonatal age, the distribution of axonal projections over prelimbic layers resembles connectivity previously described for adult mice (Parent et al., 2010; Padilla-Coreano et al., 2016; Liu and Carter, 2018). The BDA-positive terminals had large boutons (Fig. 1E) and were vGLUT1 immunopositive (Fig. 1E), indicating that hippocampal projections targeting PL are glutamatergic. They seem to target both interneurons and pyramidal neurons, as shown by close proximity of BDA-stained axons to both GABA-positive and -negative cells (Fig. 1E). To confirm these results and identify first-order postsynaptic neurons in PL innervated by hippocampal axons, we injected the trans-synaptic marker wheat germ agglutinin (WGA) into the HP of CON mice (n=3). WGA-positive postsynaptic neurons have been identified in both layer 5/6 and layer 2/3 of PL (Fig. 1F). GABA co-staining showed that the large majority (97.9 %, 423 out of 432) of WGA-positive neurons were GABA-negative and very few targeted neurons (2.1 %, 9 out of 432) were GABA-positive (Fig. 1F). These results indicate that, already at the end of the first postnatal week, hippocampal neurons located in *stratum oriens* of CA1 area project to PL, where they mainly, but not exclusively, target pyramidal neurons.

In dual-hit GE mice (n=6), the overall pattern of hippocampal innervation in PL was similar to that identified in neonatal CON mice. However, when monitoring the density of axonal projections from i/vHP to PL major differences were detected between the two groups. Already at first glance, when investigating the cleared brains, less projections were visualized and quantified in the PL of neonatal GE mice when compared to CON mice (Fig. 2B). This was confirmed after BDA staining. Fewer projections have been detected in the deeper prelimbic layers of neonatal GE mice (n=12 slices from 9 mice) than CON mice (n=11 slices from 8 mice)

(in $\mu\text{m}^2/\text{cell}$, CON: 46.05 ± 5.88 ; GE: 18.93 ± 3.41 ; $F(1,21)=7.38$, $p=0.01$) (Fig. 2A, B). In contrast, the density of hippocampal projections in the upper layers of PL was similar (in $\mu\text{m}^2/\text{cell}$, CON: 11.31 ± 4.09 ; GE: 8.80 ± 3.65 ; $F(1,23)=0.229$, $p=0.6368$) in all investigated mice (CON: $n=12$ slices from 8 mice; GE: $n=13$ slices from 9 mice), yet these layers are not the major target of CA1 innervation and therefore, the overall density here was low (Fig. 2B). Thus, sparser connectivity from HP to PL is present in GE mice.

These connectivity deficits persisted during the entire development as shown by the results of similar BDA injections in the *i/vHP* of P21 pre-juvenile GE and CON mice (Fig. 2C). At P24, the density of hippocampal projections, especially in deeper prelimbic layers, strongly increased in all mice, yet it was still smaller (in $\mu\text{m}^2/\text{cell}$, CON layer 5/6: 153.27 ± 23.76 ; GE layer 5/6: 55.92 ± 10.88 ; $F(1,38)=12.59$, $p=0.0010$, Fig. 2D) in GE mice ($n=18$ slices from 10 mice) when compared to CON mice (CON: $n=22$ slices from 10 mice). In contrast, no differences between the groups were detected for the rather sparse innervation of prelimbic layer 2/3 (CON: $n=20$ slices from 10 mice; GE: $n=19$ slices from 10 mice; in $\mu\text{m}^2/\text{cell}$, CON: 37.33 ± 7.57 ; GE: 23.22 ± 5.48 ; $F(1,37)=2.36$, $p=0.1332$).

To answer the question whether the sparser hippocampal innervation of layer 5/6 in GE mice relates to less projecting neurons in CA1 area or cropped arborization of projections, we injected the retrograde tracer FG into PL (CON: $n=7$ slices from 3 mice, GE: $n=8$ slices from 4 mice) and quantified the density of stained hippocampal neurons (Fig. 2E, F). The density of PL-projecting neurons was significantly lower in neonatal GE mice when compared to CON (in $\times 10000/\text{mm}^2$, CON: 2.96 ± 0.50 ; GE: 1.71 ± 0.33 ; $F(1,13)=5.2843$, $p=0.0387$). In contrast, the density of retrogradely stained CA1 neurons was similar in CON (CON: $n=8$ slices from 3 mice) and GE ($n=10$ slices from 4 mice) mice at pre-juvenile age (in $\times 10000/\text{mm}^2$, CON: 2.21 ± 0.25 ; GE: 2.42 ± 0.35 , $F(1,16)=0.2303$, $p=0.6378$).

These data show that the hippocampal innervation of PL is impaired in GE mice, with fewer CA1 neurons projecting to PL at neonatal age and less arborized projections towards the end of pre-juvenile development.

Region- and age-dependent cellular dysfunction within hippocampal-prelimbic circuits of dual-hit GE mice

The structural deficits observed in dual-hit GE mice along development lead to the question whether the early neuronal function is affected as well. Abnormal cellular activity might underlie the decreased functional communication between PL and HP that has been previously reported in these mice at neonatal age (Hartung et al., 2016; Xu et al., 2019).

To test this hypothesis, we firstly monitored the membrane properties of prelimbic and hippocampal neurons in neonatal (P8-10) and pre-juvenile (P20-24) CON and GE mice. For this, we performed whole-cell patch-clamp recordings from visually-identified and biocytin-stained neurons in coronal slices including PL or i/vHP, respectively. In the PL, cells in the upper layers (i.e. layer 2 and 3) as well as deeper layers (i.e. layer 5 and 6) have been recorded. The pyramidal shape and the orientation of dendrites monitored post-mortem after biocytin staining served as criteria to unequivocally classify the investigated cells as pyramidal neurons (Fig. 3A, G). Already at neonatal age, the passive and active membrane properties of prelimbic pyramidal neurons differed between neonatal CON and GE mice (CON layer 5/6: n=33 cells, GE layer 5/6: n=20 cells, CON layer 2/3: n=27 cells, GE layer 2/3: n=14 cells). The resting membrane potential (RMP) of upper layer neurons was more depolarized, the AP amplitude smaller, and the AP halfwidth longer in GE when compared to CON mice (Table 1). All neurons fired overshooting action potentials (APs) in response to sustained depolarization by intracellular current injection (Fig. 3B). No difference in firing rate in response to depolarizing current injection was detected between CON and GE (Fig. 3C). With ongoing maturation, the cellular properties of prelimbic neurons evolved in all mice (CON layer 5/6: n=57 cells, GE layer 5/6: n=23 cells, CON layer 2/3: n=15 cells, GE layer 2/3: n=9 cells, Fig. 3D). The differences between CON and GE mice diminished with age, solely the RMP of prelimbic layer 2/3 pyramidal neurons being more hyperpolarized in pre-juvenile GE mice when compared to CON (Table 1).

Second, we performed voltage-clamp recordings at a holding potential of -70 mV from prelimbic neurons from neonatal CON and GE mice to assess their synaptic inputs (Fig. 3E,

F). Spontaneous excitatory postsynaptic currents (sEPSCs) with large amplitude and fast kinetics were recorded in prelimbic neurons from both groups. The occurrence (Fig. 3Ei) but not amplitude (Fig. 3Eii) of sEPSCs in prelimbic layer 2/3 was significantly smaller in GE mice (Table 2). The synaptic activity in both areas was comparable between groups in pre-juvenile CON and GE mice (Fig. 3F, Table 2). These data confirm previous investigations that detected prominent dysfunction within local circuits and morphological change in the upper prelimbic layers in neonatal GE mice, and less prominent changes in pre-juvenile GE mice (Chini et al., 2020).

Similar investigation of pyramidal neurons in hippocampal CA1 area showed that their passive and active membrane properties differed between neonatal CON (n=15) and GE neurons (n=10). While the RMP and membrane capacitance values were similar among groups, the input resistance was significantly smaller and the time constant shorter for CA1 neurons of GE mice (Table 1), suggesting a lower excitability of these neurons when compared to those from CON mice. This difference is supported by the bigger voltage sag recorded upon hyperpolarization in hippocampal neurons from GE mice (Fig. 3H, Table 1). The voltage sag mirrors the activation of hyperpolarization-activated cyclic nucleotide-gated (HCN) channels that is known to control the neuronal excitability (Brennan et al., 2016). The firing rate in response to sustained depolarization was similar in CON and GE mice (Fig. 3I, Table 1). Solely the AP width was higher in neurons from GE mice. At pre-juvenile age, no major differences in membrane properties and firing rate of hippocampal neurons were detected between CON and GE mice (Fig. 3J, n=12 for CON, n=9 for GE, Table 1).

These data indicate that a mild cellular dysfunction of prefrontal and hippocampal neurons is present in neonatal GE mice and diminishes with age.

Weaker efficiency of hippocampal drive to prelimbic cortex in neonatal dual-hit GE mice

To investigate whether, besides structural disruption, the functional connectivity between HP and PL is compromised in GE mice during development, we monitored the responsiveness of prelimbic neurons to the activation of hippocampal terminals.

In a first step, we focused on cellular processes assessed under *in vitro* conditions. For this, we selectively transfected pyramidal neurons in the HP of P1 CON and GE mice with ChR2 (H134R) and the fluorescent protein EYFP by micro-injections (Fig. 4Ai). Whole-cell patch-clamp recordings from pyramidal CA1 neurons in coronal slices including HP from P8-10 mice confirmed that blue light (473 nm, 3 ms) pulses reliably evoked APs (Fig. 4Aii-iii). In line with the results of morphological investigations, fluorescent axonal terminals of transfected CA1 neurons were detected in the deep and, to a lesser extent, in upper layers of PL (Fig. 4Bi). We performed voltage-clamp recordings from visually-identified prelimbic pyramidal neurons and non-pyramidal cells (i.e putatively interneurons) located in the proximity of terminals during light-stimulation of hippocampal axons (Fig. 4Bii). Single pulses of light stimulation evoked prominent excitatory postsynaptic currents (eEPSCs) in both pyramidal neurons (Fig. 4Ci) and interneurons (Fig. 4Cii), the amplitude of which augmented with increasing stimulus duration (3 ms: 24.81 ± 6.70 pA, 5 ms: 42.19 ± 9.02 pA, 10 ms: 63.6 ± 12.12 pA, $F(2,69)=8.07$, $p=0.017$, $p=0.012$, $n=24$) (Fig. 4Biii). The eEPSCs recorded from pyramidal neurons had a short latency and fast kinetics and were fully abolished when ionotropic AMPA/kainate receptor antagonists CNQX (10 μ M) was added to the extracellular solution (Fig. 4Ci). Upon depolarization, the AMPA receptor-mediated events were accompanied by a delayed di-synaptic postsynaptic current.

While light stimulation evoked robust responses in prelimbic neurons of all investigated pups (Fig. 4D), detailed analysis of examining eEPSCs properties revealed differences between CON and GE mice (Table 3). In both prelimbic layers in GE mice, less neurons responded to light stimulation of hippocampal projections (layer 5/6, 41.67%; layer 2/3, 44.44%) when compared to responding neurons in CON (layer 5/6, 82.76%, $p=0.0048$; layer 2/3, 80.76%, layer 5/6, $p=0.029$). Moreover, the eEPSC evoked in layer 5/6 neurons had not only smaller amplitude in GE vs. CON mice (63.6 ± 12.12 vs. 9.72 ± 2.41 pA, $p=0.0009$) but showed also a higher degree of variability upon stimuli as mirrored by the larger coefficient of variation (CV) (Fig. 4Ei, ii, Table 3). The kinetics of eEPSCs was also disrupted in GE mice, the events having a delayed onset (5.15 ± 0.476 vs 7.99 ± 0.762 ms, $p=0.006$) and longer rise-time (3.07

± 0.044 vs 3.60 ± 0.301 ms, $p=0.022$) (Fig. 4Eiii, iv). In contrast, the properties of light-evoked EPSCs in layer 2/3 neurons were similar for all investigated mice (Fig. 4E, Table 3). The function of hippocampal terminals in PL was further assessed by repetitive stimulation (Fig. 4Fi). All prelimbic neurons of neonatal CON and GE mice responded with a substantial depression of eEPSCs when normalized to the first event (Fig. 4Fii). However, the paired-pulse ratio (PPR), a measure of short-term plasticity (STP), for layer 5/6 neurons in GE mice significantly decreased when the stimulation was delivered at a 500 ms interval (0.67 ± 0.057 vs 0.21 ± 0.106 , $p=0.0083$) (Fig. 4G, Table 3). These results suggest that the hippocampal inputs are less efficient on prelimbic neurons in GE mice.

To directly test this hypothesis, we investigated the impact of hippocampal inputs on the oscillatory entrainment of local circuits in the PL of CON and GE mice *in vivo*. For this, multi-site extracellular recordings of local field potential (LFP) and multiunit activity (MUA) were performed in prelimbic layer 5/6 and layer 2/3 of P8-10 CON ($n=14$) and GE mice ($n=11$) before, during and after repetitive stimulation with ramp light stimuli or pulse trains (Fig. 5A, B). In line with our previous results, the used light intensity (0.75-2.5 mW) led to a temperature increase of max. 0.2 °C, which is far below the local tissue heating that might interfere with neuronal spiking (Stujenske et al., 2015; Bitzenhofer et al., 2017). Ramp stimulation (3 s) significantly augmented theta band (4-12 Hz) oscillatory power in layer 5/6 of CON but not GE mice (0.807 ± 0.121 vs. 0.218 ± 0.096 , $F(1,23)=3.365$, $p=0.039$) (Fig. 5C, Table 4). Similarly, the magnitude of LFP response to light pulse trains (5 ms-long, 8 Hz, total duration of a train 3 s) significantly differed between the two groups. Activation of hippocampal terminals in layer 5/6 by pulsed light caused a large short-delay (~ 19 ms) LFP depolarization that had a smaller amplitude in GE mice when compared to CON mice (144.9 ± 26.97 vs 67.0 ± 13.80 μV , $F(1,23)=3.396$, $p=0.024$) (Fig. 5Dii, Table 4). Moreover, the firing of prelimbic neurons changed after pulsed light stimulation (Fig. 5E). Analysis of single unit activity (SUA) revealed that a prominent augmentation (311%) of firing rate occurred ~ 13 ms after the stimulation in 72 out of 239 units ($\sim 30.1\%$) recorded in layer 5/6 of CON mice. In GE mice, only 18 out of 189 units ($\sim 9.5\%$) responded to light stimuli with a weaker (98.4%) and delayed (~ 22 ms) firing rate increase (Fig.

5E, F). Analysis of modulation index (MI) of the firing rate of all activated units showed that the activated GE neurons fired significantly less when compared to CON (0.796 ± 0.023 vs 0.615 ± 0.054 , $F(1,88)= 11.5007$, $p= 0.001$, Fig. 5Fiv). These results indicate that not only hippocampal terminals target fewer prefrontal neurons in GE, but also their efficacy in boosting the firing rate is attenuated.

In line with the weak hippocampal innervation of prelimbic upper layers (Fig. 2B, 5B), their activation with ramp light stimuli led to weak, if any, network effects in both CON ($n=13$) and GE mice ($n=10$) (Fig. 6A, B, Table 4). However, the evoked LFP response had a lower amplitude in GE mice (132.3 ± 27.6 vs. 63.0 ± 17.94 μV , $F(1,21)=3.939$, $p=0.047$) (Fig. 6C, Table 4). The firing rate and onset of light-induced firing were similar in all investigated mice (Fig. 6D). A smaller fraction of responsive units has been detected in GE (8.8%, 16 out of 181) when compared to CON (12.2%, 28 out of 230) mice (Fig. 6Ei-iii). The firing rate MI of all activated units did not differ between CON and GE (0.763 ± 0.029 vs 0.750 ± 0.040 , $F(1,42)= 0.079$, $p= 0.780$, Fig. 6Evi).

These results indicate that, especially in layer 5/6, the hippocampal innervation has a weaker power to boost the firing and oscillatory activity in the PL of GE mice.

Persistent dysfunction of hippocampal drive to prelimbic cortex in pre-juvenile dual-hit GE mice

Since previous studies showed major functional and behavioral deficits as result of abnormal prefrontal-hippocampal communication in juvenile GE mice (Xu et al., 2019; Chini et al., 2020; Xu et al., 2021), it is likely that this dysfunction persists along development. To test this hypothesis, we monitored the function of hippocampal innervation of PL in CON and GE mice at pre-juvenile age.

First, the function of hippocampal projections in PL was assessed *in vitro*. Similar to the results obtained from coronal slices including the PL from neonatal mice, light stimulation (10 ms, 473 nm) of hippocampal inputs evoked robust excitatory postsynaptic currents in prefrontal neurons from all investigated pre-juvenile mice (Fig. 7A). However, the fraction of responsive neurons was larger in CON (layer 5/6: 67.65%; layer 2/3: 57.14%) when compared to GE mice

(layer 5/6: 46.88%; layer 2/3: 31.25%) (Table 3). The light-induced synaptic inputs had a faster kinetics when compared to the currents recorded in the neonatal PL in all investigated pre-juvenile mice (Fig. 7Biii-iv, Table 3). The amplitude of the eEPSCs recorded in layer 5/6 was significant smaller in GE (Fig. 7Bi, 70.1 ± 13.74 vs 19.7 ± 4.39 pA, $p=0.0354$) and had a higher variability when compared to CON mice (Fig. 7Bii, Table 3). In contrast, the eEPSCs recorded from layer 2/3 neurons were similar in pre-juvenile CON and GE mice. Repetitive stimulation (8 Hz, 10 ms) of hippocampal inputs evoked sustained EPSCs that had different response patterns in CON and GE neurons. In contrast to the prominent depression of inputs in all neonatal neurons, a slight depression was detected for layer 2/3 neurons of GE mice, whereas the eEPSCs in layer 5/6 were either facilitated or unchanged (Fig. 7C). However, PPR for layer 2/3 decreased in GE mice and showed a clear depression over higher frequencies. Moreover, there were significant difference in the value of PPR between CON and GE when light was conducted at 125 ms interval, but not at 250 ms and 500 ms intervals (Fig. 7Dii, Table 3). This means the STP of hippocampal inputs was comparable in response to low frequency stimulation in CON and GE, but differs for high frequency stimulation. Taken together, these results indicate that the dysfunction of hippocampal innervation persists at pre-juvenile age in GE mice, yet it appears less pronounced than the deficits reported for neonatal stage.

Second, we performed multisite extracellular recording of LFP and MUA combined with the optogenetic stimulation of hippocampal terminals in pre-juvenile CON ($n=17$) and GE mice ($n=9$) *in vivo* (Fig. 8). We used similar stimulation protocols as described for neonatal animals. Ramp light stimulation of hippocampal projections targeting prelimbic layers 5/6 and 2/3 had a minor, if any, effect on the power of network oscillation in CON and GE mice (Table 4). The pulsed light evoked a strong bi-phasic LFP response (Fig. 8Ai) with comparable amplitude in all investigated mice (Fig. 8A, C, Table 4). The overall prelimbic firing was augmented upon light stimuli, yet the number of responsive units was lower in layer 5/6 of GE mice (155 out of 342, ~45.3%) when compared to CON mice (221 out of 398, ~55.5%) (Fig. 8B). The firing rate MI of all activated units did not differ between CON and GE (0.225 ± 0.023 vs 0.239 ± 0.028 , $F(1,374)= 0.1372$, $p= 0.712$, Fig. 8Cv). When the light activated the hippocampal axonal

terminals in layer 2/3, the firing rate strongly augmented in CON but much weaker in GE mice (Fig. 8D). However, the number of activated unit was comparable in the two groups of pre-juvenile mice (CON: 121 out of 327, ~38.8%; GE: 86 out of 230 units, ~37.3%). The firing rate MI of all activated units was significant lower in GE when compare to CON (0.178 ± 0.024 vs 0.121 ± 0.013 , $F(1,206)= 3.881$, $p= 0.049$, Fig. 8Dv).

Thus, the functional disruption of hippocampal drive to the PL in dual-hit GE mice persists throughout development, although the magnitude and patterns of dysfunction differ from those identified at neonatal age.

Discussion

More than 30 years ago, disturbed interactions between HP and PFC have been proposed as a core aspect of schizophrenia pathophysiology that links the neurodevelopmental miswiring and later behavioral deficits (Weinberger, 1987). The experimental evidence for abnormal prefrontal-hippocampal communication during development was, however, until recently missing. We previously capitalized on *in vivo* recording and manipulation techniques in mouse models of disease and showed that the development of local circuits in both PFC and HP are profoundly impaired when genetic and environmental stressors mimic the etiology of disease (Xu et al., 2019; Chini et al., 2020; Xu et al., 2021). Moreover, the excitatory drive from the HP to PFC has a weaker impact in these disease models (Hartung et al., 2016; Oberlander et al., 2019). In the present study, we monitor the structure and function of prefrontal-hippocampal connectivity in control and GE mice. We show that in GE mice (i) the sparser axonal projections from HP to PL act as substrate of diminished HP-PFC communication throughout postnatal development; (ii) presynaptic abnormality of hippocampal terminals and their poorer efficiency in activating the PL cause miswiring of long-range connectivity, and (iii) the deficits of hippocampal projections persist, yet at lower magnitude, until pre-juvenile age.

A wealth of studies documented the schizophrenia-characteristic dysconnectivity between HP and PFC in chronic patients, first-episode patients as well as high-risk individuals during cognitive tasks (Meyer-Lindenberg et al., 2001; Benetti et al., 2009; Wolf et al., 2009). The weaker driving force from the HP to PFC has been replicated in different animal models

of disease at adult age (Dickerson et al., 2010; Sigurdsson et al., 2010; Mukai et al., 2015). Three possible sources of disconnection have been identified. First, the excitatory drive from the HP is decreased due to cellular dysfunction and altered morphological features of CA1 pyramidal neurons. Post-mortem histology in schizophrenia patients and mouse models as well as monitoring of neuronal and network activity in HP *in vivo* and *in vitro* conformed this hypothesis (Harrison and Weinberger, 2005; Meyer-Lindenberg, 2010; Marissal et al., 2018). Second, abnormal structure and function of both prefrontal pyramidal neurons and interneurons might hamper the normal communication between HP and PFC (Benchenane et al., 2010; Mukai et al., 2015; Sauer et al., 2015; Abbas et al., 2018). Third, decreased connectivity between the two brain areas might serve as substrate of the decoupling monitored by decreased synchrony between HP and PFC (Meyer-Lindenberg et al., 2005; Cohen, 2011; Mukai et al., 2015).

In line with the neurodevelopmental hypothesis of schizophrenia, the dysconnectivity between HP and PFC emerged early in life. Since for ethical and technical reasons, data from high-risk humans are not available, animal models represent a valuable tool for investigating the prefrontal-hippocampal communication early in life. In particular, mice that mimicked the dual etiology of the disease and combine the genetic deficits with the action of environmental stressors, showed towards the end of the first postnatal week, a developmental stage corresponding to the second-third gestational trimester in humans (Clancy et al., 2001), disconnection of PFC and HP (Hartung et al., 2016; Oberlander et al., 2019). DISC1 suppression or MIA alone had no impact on the neuronal and network function at neonatal age. Similar to adults, the structure and function of PFC and HP in neonatal dual-hit GE mice were compromised and the deficits persist, yet sometimes at a lower magnitude, throughout the entire development (Xu et al., 2019; Chini et al., 2020; Xu et al., 2021). In the present study, we complemented these data with the analysis of the role of early connectivity on the prefrontal-hippocampal disconnection.

Monitoring of hippocampal projections in cleared brains revealed the sparser targeting of PFC. The role of DISC1 in dendritic and axonal development is well documented (Morris et

al., 2003; Ozeki et al., 2003; Shen et al., 2008; Kvajo et al., 2011). The abnormal long-range axonal projections from HP to PFC in GE mice might relate to the ability of DISC1 to interact with proteins that bind to microtubules and associated complexes (Morris et al., 2003; Ozeki et al., 2003; Brandon et al., 2005; Wang and Brandon, 2011), it is not surprising that. In line with the structural change, the diminishment of excitatory drive towards PFC neurons was observed. Hippocampal terminals targeted fewer prefrontal neurons in GE mice and their efficiency in boosting the firing of prefrontal neurons was much weaker.

Besides the decreased axonal density and efficiency, multiple presynaptic alterations of hippocampal inputs were found in dual-hit GE mice. The observed AP widening might lead to altered short-term synaptic plasticity by increasing the initial probability of presynaptic release and shifting the presynaptic short-term plasticity toward depression (Abbott and Regehr, 2004). Furthermore, our observation that the differences between neonatal CON and GE in short-term depression paradigms were most obvious at lower stimulation frequency (500 ms interval), than at higher stimulus frequency (125 ms interval), supports the impact of wider action potentials in the HP for neurotransmitter release in PFC. It has been shown that the presynaptic characteristics are not fixed throughout development. The depression contributes less to synaptic dynamics, whereas facilitation becomes more prominent (Reyes and Sakmann, 1999; Dittman et al., 2000). At pre-juvenile age, short-term facilitation of hippocampal terminals on prefrontal neurons was observed in CON, supporting the synaptic enhancement during development. However, in GE mice high frequency depression was observed in layer 2/3 neurons of PL. The underlying mechanisms might be a presynaptic deregulation of the synaptic vesicle recycling and the release of neurotransmitter (Flores et al., 2011; Tang et al., 2016) or postsynaptic receptor desensitization that make the target neurons less sensitive to neurotransmitter (Zucker and Regehr, 2002). From neonatal to pre-juvenile age, the response to light stimulation of hippocampal terminals becomes faster as shown by the shorter onset of eEPSCs and faster firing of prefrontal neurons. These changes are less evident in GE mice. Overall, in addition to the reduced innervation, alterations in synaptic plasticity may cumulatively impinge on the structure and function of hippocampal-prefrontal network.

The results of light stimulation in CON mice provide first insights into the mechanisms how hippocampal inputs shape the prefrontal excitation-inhibition throughout the development. At neonatal age, few neurons reduced their firing rate after pulsed light stimulation, whereas their number significantly augmented at pre-juvenile age. The decreased firing rates might arise from the feed-forward inhibition of the interneurons that are directly targeted by hippocampal terminals, or from the activation of interneurons directly connected to the light-activated pyramidal neurons. Multiple mechanisms, such as more interneurons are recruited by the hippocampal innervation, the synaptic strength on interneurons increase along with the development, or the interaction between pyramidal neurons and interneurons change with age, might underlie these observations. Our results showed the depression-to-facilitation shift of hippocampal input on layer 2/3 prelimbic neurons is disrupted in pre-juvenile GE mice. Excitation-inhibition imbalance in PL might underlie numerous neurological and behavioral abnormalities found in GE mice.

The present results add experimental evidence for the developmental miswiring of prefrontal-hippocampal networks in schizophrenia. The profound dysfunction of these networks takes place already at early stages of development. The sparse and less efficient projections from CA1 area to the PFC do not boost the prefrontal networks, causing their poor activation and entrainment in oscillatory rhythms. Together with the local synaptic deficits in both areas, the weaker connectivity causes an abnormal communication and information processing that, despite partial compensation at pre-juvenile age, might be vulnerable to environmental stressors or age-related changes of neuromodulatory systems (e.g. dopamine) (Arnsten et al., 2012; McEwen and Morrison, 2013; Klune et al., 2021). By these means, the early disconnection between PFC and HP has long-lasting impact on memory and executive processing. While these data from animal models of disease help to identify possible “hubs” of miswiring early in life, future investigations need to explore the clinical validity of developmental mechanisms of schizophrenia.

Author contributions

I.L.H.-O. and L.S. designed the experiments, L.S., X.X., and P.P. performed the experiments and analyzed the data, D.F. and M.S. carried out the Clarity imaging and analysis, I.L.H.-O. and L.S. interpreted the data and wrote the paper. All authors discussed and commented on the manuscript.

References

- Abbas AI, Sundiang MJM, Henoch B, Morton MP, Bolkan SS, Park AJ, Harris AZ, Kellendonk C, Gordon JA (2018) Somatostatin Interneurons Facilitate Hippocampal-Prefrontal Synchrony and Prefrontal Spatial Encoding. *Neuron* 100:926-939 e3.
- Abbott LF, Regehr WG (2004) Synaptic computation. *Nature* 431:796-803.
- Ahlbeck J, Song L, Chini M, Bitzenhofer SH, Hanganu-Opatz IL (2018) Glutamatergic drive along the septo-temporal axis of hippocampus boosts prelimbic oscillations in the neonatal mouse. *Elife* 7:e33158.
- Aleman-Gonzalez M, Gener T, Nebot P, Vilademunt M, Dierssen M, Puig MV (2020) Prefrontal-hippocampal functional connectivity encodes recognition memory and is impaired in intellectual disability. *PNAS* 117:11788-11798.
- Arnsten AF, Wang MJ, Paspalas CD (2012) Neuromodulation of thought: flexibilities and vulnerabilities in prefrontal cortical network synapses. *Neuron* 76:223-239.
- Backus AR, Schoffelen JM, Szebenyi S, Hanslmayr S, Doeller CF (2016) Hippocampal-Prefrontal Theta Oscillations Support Memory Integration. *Curr Biol* 26:450-457.
- Bahner F, Meyer-Lindenberg A (2017) Hippocampal-prefrontal connectivity as a translational phenotype for schizophrenia. *Eur Neuropsychopharmacol* 27:93-106.
- Benchenane K, Peyrache A, Khamassi M, Tierney PL, Gioanni Y, Battaglia FP, Wiener SI (2010) Coherent theta oscillations and reorganization of spike timing in the hippocampal-prefrontal network upon learning. *Neuron* 66:921-936.
- Benetti S, Mechelli A, Picchioni M, Broome M, Williams S, McGuire P (2009) Functional integration between the posterior hippocampus and prefrontal cortex is impaired in both first episode schizophrenia and the at risk mental state. *Brain* 132:2426-2436.
- Bitzenhofer SH, Ahlbeck J, Wolff A, Wiegert JS, Gee CE, Oertner TG, Hanganu-Opatz IL (2017) Layer-specific optogenetic activation of pyramidal neurons causes beta-gamma entrainment of neonatal networks. *Nat Commun* 8:14563.
- Bora E, Yucel M, Pantelis C (2010) Cognitive impairment in schizophrenia and affective psychoses: implications for DSM-V criteria and beyond. *Schizophr Bull* 36:36-42.

- Brandon NJ, Sawa A (2011) Linking neurodevelopmental and synaptic theories of mental illness through DISC1. *Nat Rev Neurosci* 12:707-722.
- Brandon NJ, Schurov I, Camargo LM, Handford EJ, Duran-Jimeniz B, Hunt P, Millar JK, Porteous DJ, Shearman MS, Whiting PJ (2005) Subcellular targeting of DISC1 is dependent on a domain independent from the Nudel binding site. *Mol Cell Neurosci* 28:613-624.
- Brennan GP, Baram TZ, Poolos NP (2016) Hyperpolarization-Activated Cyclic Nucleotide-Gated (HCN) Channels in Epilepsy. *Cold Spring Harb Perspect Med* 6:a022384.
- Cenquizca LA, Swanson LW (2007) Spatial organization of direct hippocampal field CA1 axonal projections to the rest of the cerebral cortex. *Brain Res Rev* 56:1-26.
- Chini M, Popplau JA, Lindemann C, Carol-Perdiguer L, Hnida M, Oberlander V, Xu X, Ahlbeck J, Bitzenhofer SH, Mulert C, Hanganu-Opatz IL (2020) Resolving and Rescuing Developmental Miswiring in a Mouse Model of Cognitive Impairment. *Neuron* 105:60-74 e7.
- Chung K, Deisseroth K (2013) CLARITY for mapping the nervous system. *Nat Methods* 10:508-513.
- Clancy B, Darlington RB, Finlay BL (2001) Translating developmental time across mammalian species. *Neuroscience* 105:7-17.
- Cohen MX (2011) Hippocampal-prefrontal connectivity predicts midfrontal oscillations and long-term memory performance. *Curr Biol* 21:1900-1905.
- Diamantopoulou A, Gogos JA (2019) Neurocognitive and Perceptual Processing in Genetic Mouse Models of Schizophrenia: Emerging Lessons. *Neuroscientist* 25:597-619.
- Dickerson DD, Wolff AR, Bilkey DK (2010) Abnormal long-range neural synchrony in a maternal immune activation animal model of schizophrenia. *J Neurosci* 30:12424-12431.
- Dittman JS, Kreitzer AC, Regehr WG (2000) Interplay between Facilitation, Depression, and Residual Calcium at Three Presynaptic Terminals. *The Journal of Neuroscience* 20:1374-1385.

- Dolleman-Van Der Weel MJ, Witter MP (1996) Projections from the nucleus reuniens thalami to the entorhinal cortex, hippocampal field CA1, and the subiculum in the rat arise from different populations of neurons. *J Comp Neurol* 364:637-650.
- Eichenbaum H (2017) Prefrontal-hippocampal interactions in episodic memory. *Nat Rev Neurosci* 18:547-558.
- Flores R, 3rd, Hirota Y, Armstrong B, Sawa A, Tomoda T (2011) DISC1 regulates synaptic vesicle transport via a lithium-sensitive pathway. *Neurosci Res* 71:71-77.
- Friston KJ, Frith CD (1995) Schizophrenia: a disconnection syndrome? *Clin Neurosci* 3(2):89-97.
- Greenland-White SE, Ragland JD, Niendam TA, Ferrer E, Carter CS (2017) Episodic memory functions in first episode psychosis and clinical high risk individuals. *Schizophr Res* 188:151-157.
- Guo JY, Ragland JD, Carter CS (2019) Memory and cognition in schizophrenia. *Mol Psychiatry* 24:633-642.
- Harrison PJ, Weinberger DR (2005) Schizophrenia genes, gene expression, and neuropathology: on the matter of their convergence. *Mol Psychiatry* 10:40–68.
- Hartung H, Cichon N, De Feo V, Riemann S, Schildt S, Lindemann C, Mulert C, Gogos JA, Hanganu-Opatz IL (2016) From Shortage to Surge: A Developmental Switch in Hippocampal-Prefrontal Coupling in a Gene-Environment Model of Neuropsychiatric Disorders. *Cereb Cortex* 26:4265-4281.
- Jay TM, Witter MP (1991) Distribution of hippocampal CA1 and subicular efferents in the prefrontal cortex of the rat studied by means of anterograde transport of Phaseolus vulgaris-leucoagglutinin. *J Comp Neurol* 313:574-586.
- Jay TM, Glowinski J, Thierry AM (1989) Selectivity of the hippocampal projection to the prelimbic area of the prefrontal cortex in the rat. *Brain Res* 505:337-340.
- Kannan G, Sawa A, Pletnikov MV (2013) Mouse models of gene-environment interactions in schizophrenia. *Neurobiol Dis* 57:5-11.

- Klune CB, Jin B, DeNardo LA (2021) Linking mPFC circuit maturation to the developmental regulation of emotional memory and cognitive flexibility. *Elife* 10:e64567.
- Kvajo M, McKellar H, Drew LJ, Lepagnol-Bestel AM, Xiao L, Levy RJ, Blazeski R, Arguello PA, Lacefield CO, Mason CA, Simonneau M, O'Donnell JM, MacDermott AB, Karayiorgou M, Gogos JA (2011) Altered axonal targeting and short-term plasticity in the hippocampus of *Disc1* mutant mice. *PNAS* 108:E1349-1358.
- Liu X, Carter AG (2018) Ventral Hippocampal Inputs Preferentially Drive Corticocortical Neurons in the Infralimbic Prefrontal Cortex. *J Neurosci* 38:7351-7363.
- Marissal T, Salazar RF, Bertollini C, Mutel S, De Roo M, Rodriguez I, Muller D, Carleton A (2018) Restoring wild-type-like CA1 network dynamics and behavior during adulthood in a mouse model of schizophrenia. *Nat Neurosci* 21:1412-1420.
- McDonald-McGinn DM, Sullivan KE, Marino B, Philip N, Swillen A, Vorstman JA, Zackai EH, Emanuel BS, Vermeesch JR, Morrow BE, Scambler PJ, Bassett AS (2015) 22q11.2 deletion syndrome. *Nat Rev Dis Primers* 1:15071.
- McEwen BS, Morrison JH (2013) The brain on stress: vulnerability and plasticity of the prefrontal cortex over the life course. *Neuron* 79:16-29.
- Meyer-Lindenberg A (2010) From maps to mechanisms through neuroimaging of schizophrenia. *Nature* 468:194-202.
- Meyer-Lindenberg A, Poline JB, Kohn PD, Holt JL, Egan MF, Weinberger DR, Berman KF (2001) Evidence for abnormal cortical functional connectivity during working memory in schizophrenia. *Am J Psychiatry* 158:1809-1817.
- Meyer-Lindenberg AS, Olsen RK, Kohn PD, Brown T, Egan MF, Weinberger DR, Berman KF (2005) Regionally specific disturbance of dorsolateral prefrontal-hippocampal functional connectivity in schizophrenia. *Arch Gen Psychiatry* 62:379-386.
- Miller EK, Cohen JD (2001) An integrative theory of prefrontal cortex function. *Annu Rev Neurosci* 24:167-202.

- Morris JA, Kandpal G, Ma L, Austin CP (2003) DISC1 (Disrupted-In-Schizophrenia 1) is a centrosome-associated protein that interacts with MAP1A, MIPT3, ATF4/5 and NUDEL: regulation and loss of interaction with mutation. *Hum Mol Genet* 12:1591-1608.
- Mukai J, Tamura M, Fenelon K, Rosen AM, Spellman TJ, Kang R, MacDermott AB, Karayiorgou M, Gordon JA, Gogos JA (2015) Molecular substrates of altered axonal growth and brain connectivity in a mouse model of schizophrenia. *Neuron* 86:680-695.
- Oberlander VC, Xu X, Chini M, Hanganu-Opatz IL (2019) Developmental dysfunction of prefrontal-hippocampal networks in mouse models of mental illness. *Eur J Neurosci* 50:3072-3084.
- Owen MJ, Sawa A, Mortensen PB (2016) Schizophrenia. *The Lancet* 388:86-97.
- Ozeki Y, Tomoda T, Kleiderlein J, Kamiya A, Bord L, Fujii K, Okawa M, Yamada N, Hatten ME, Snyder SH, Ross CA, Sawa A (2003) Disrupted-in-Schizophrenia-1 (DISC-1): mutant truncation prevents binding to NudE-like (NUDEL) and inhibits neurite outgrowth. *PNAS* 100:289-294.
- Padilla-Coreano N, Bolkan SS, Pierce GM, Blackman DR, Hardin WD, Garcia-Garcia AL, Spellman TJ, Gordon JA (2016) Direct Ventral Hippocampal-Prefrontal Input Is Required for Anxiety-Related Neural Activity and Behavior. *Neuron* 89:857-866.
- Parent MA, Wang L, Su J, Netoff T, Yuan LL (2010) Identification of the hippocampal input to medial prefrontal cortex in vitro. *Cereb Cortex* 20:393-403.
- Pernia-Andrade AJ, Goswami SP, Stickler Y, Frobe U, Schlogl A, Jonas P (2012) A deconvolution-based method with high sensitivity and temporal resolution for detection of spontaneous synaptic currents in vitro and in vivo. *Biophys J* 103:1429-1439.
- Phillips ML, Robinson HA, Pozzo-Miller L (2019) Ventral hippocampal projections to the medial prefrontal cortex regulate social memory. *Elife* 8:e44182.
- Reyes A, Sakmann B (1999) Developmental switch in the short-term modification of unitary EPSPs evoked in layer 2/3 and layer 5 pyramidal neurons of rat neocortex. *J Neurosci* 19:3827-3835.

- Rossant C, Kadir SN, Goodman DFM, Schulman J, Hunter MLD, Saleem AB, Grosmark A, Belluscio M, Denfield GH, Ecker AS, Tolias AS, Solomon S, Buzsaki G, Carandini M, Harris KD (2016) Spike sorting for large, dense electrode arrays. *Nat Neurosci* 19:634-641.
- Sauer JF, Struber M, Bartos M (2015) Impaired fast-spiking interneuron function in a genetic mouse model of depression. *Elife* 4:e04979.
- Shen S, Lang B, Nakamoto C, Zhang F, Pu J, Kuan SL, Chatzi C, He S, Mackie I, Brandon NJ, Marquis KL, Day M, Hurko O, McCaig CD, Riedel G, St Clair D (2008) Schizophrenia-related neural and behavioral phenotypes in transgenic mice expressing truncated *Disc1*. *J Neurosci* 28:10893-10904.
- Siapas AG, Lubenov EV, Wilson MA (2005) Prefrontal phase locking to hippocampal theta oscillations. *Neuron* 46:141-151.
- Sigurdsson T (2016) Neural circuit dysfunction in schizophrenia: Insights from animal models. *Neuroscience* 321:42-65.
- Sigurdsson T, Stark KL, Karayiorgou M, Gogos JA, Gordon JA (2010) Impaired hippocampal-prefrontal synchrony in a genetic mouse model of schizophrenia. *Nature* 464:763-767.
- Spellman T, Rigotti M, Ahmari SE, Fusi S, Gogos JA, Gordon JA (2015) Hippocampal-prefrontal input supports spatial encoding in working memory. *Nature* 522:309-314.
- Stujenske JM, Spellman T, Gordon JA (2015) Modeling the Spatiotemporal Dynamics of Light and Heat Propagation for In Vivo Optogenetics. *Cell Rep* 12:525-534.
- Szczurkowska J, Cwetsch AW, dal Maschio M, Ghezzi D, Ratto GM, Cancedda L (2016) Targeted in vivo genetic manipulation of the mouse or rat brain by in utero electroporation with a triple-electrode probe. *Nat Protoc* 11:399-412.
- Tang W, Thevathasan JV, Lin Q, Lim KB, Kuroda K, Kaibuchi K, Bilger M, Soong TW, Fivaz M (2016) Stimulation of Synaptic Vesicle Exocytosis by the Mental Disease Gene *DISC1* is Mediated by N-Type Voltage-Gated Calcium Channels. *Front Synaptic Neurosci* 8:15.

- Vertes RP (2006) Interactions among the medial prefrontal cortex, hippocampus and midline thalamus in emotional and cognitive processing in the rat. *Neuroscience* 142:1-20.
- Wang Q, Brandon NJ (2011) Regulation of the cytoskeleton by Disrupted-in-schizophrenia 1 (DISC1). *Mol Cell Neurosci* 48:359-364.
- Weinberger DR (1987) Implications of normal brain development for the pathogenesis of schizophrenia. *Arch Gen Psychiatry* 44:660-669.
- Wolf RC, Vasic N, Sambataro F, Hose A, Frasch K, Schmid M, Walter H (2009) Temporally anticorrelated brain networks during working memory performance reveal aberrant prefrontal and hippocampal connectivity in patients with schizophrenia. *Prog Neuropsychopharmacol Biol Psychiatry* 33:1464-1473.
- Xu X, Song L, Hanganu-Opatz IL (2021) Knock-Down of Hippocampal DISC1 in Immune-Challenged Mice Impairs the Prefrontal-Hippocampal Coupling and the Cognitive Performance Throughout Development. *Cereb Cortex* 31:1240-1258.
- Xu X, Chini M, Bitzenhofer SH, Hanganu-Opatz IL (2019) Transient Knock-Down of Prefrontal DISC1 in Immune-Challenged Mice Causes Abnormal Long-Range Coupling and Cognitive Dysfunction throughout Development. *J Neurosci* 39:1222-1235.
- Zucker RS, Regehr WG (2002) Short-term synaptic plasticity. *Annu Rev Physiol* 64:355-405.

Legends

Figure 1. Organization of hippocampal afferents targeting the prelimbic subdivision of PFC. **A**, Schematic representation of tracing protocols. Mice were injected unilaterally with the retrograde tracer FG into PL or with either the anterograde tracer BDA or the transsynaptic tracer WGA into HP. **B**, Left, fluorescent images of FG (white) injection site in the PL of 50 μm -thick coronal slice from a P10 mouse when co-stained with NeuN (green). Right, corresponding NeuN-stained coronal slices (50 μm -thick) including the dorsal HP (dHP), intermediate HP (iHP), and ventral HP (vHP) with retrogradely stained cells (white). Scale bar, 500 μm . Insets, FG-stained neurons (white) shown at higher magnification. Scale bar, 100 μm . PL: prelimbic cortex, IL: infralimbic cortex, Cg: cingulate cortex. SO: stratum oriens, SP: stratum pyramidale, SR: stratum radiatum. **C**, Left, photograph of a representative BDA injection into the i/vHP of a P10 mouse visualized by streptavidin staining (green) and co-stained with DAPI (blue) in a 50 μm -thick coronal slice. Right, bright field photographs illustrating the BDA-positive axons in the PL and IL. Dotted lines mark the borders of the two subdivisions as well the prelimbic layers. Inset, hippocampal axons targeting the PL shown at a higher magnification. **D**, 3D reconstruction of hippocampal axons (tDimer, red) into the PL (cyan surface) in a cleared P10 mouse brain. PL volume was delimited according to nuclei staining (DRAQ5; not shown). **E**, Top, orthogonal views of the Z-stack (YZ, XZ) images illustrating BDA-positive boutons (green) that colocalized with vGLUT1 (red). Bottom, confocal images displaying BDA-positive boutons (green) on GABA-positive (red) somata (arrows), and GABA-negative neurons (asterisk). **F**, Left, a representative example of WGA staining (magenta) in a 50 μm -thick coronal slice including the PFC of a P10 mouse that transsynaptically labeled neurons targeted by hippocampal axons. Dotted lines mark the borders of the two subdivisions as well the prelimbic layers. Right, photographs displaying the colocalization of WGA (magenta) and GABA (cyan) staining for GABA-positive neurons (circle). GABA-negative but WGA-positive neurons are marked by squares.

Figure 2. Developmental dynamics of hippocampal innervation of PL in neonatal and pre-juvenile dual-hit GE mice. **A**, Left, schematic illustrating the extent of the BDA injections

into the HP of CON (gray) and dual-hit GE (green) mice. Right, a representative brightfield photograph of BDA-stained neurons in the CA1 area of a 50 μm -thick coronal slice from a P10 CON mouse. **B, (i)**, Logarithmic violin plots depicting the relative space occupancy of hippocampal fibers within PL, normalized to the number of transfected neurons in i/vHP. **(ii)**, Violin plots of the normalized density of hippocampal terminals in layer 2/3 and layer 5/6 of PL averaged for all investigated neonatal CON and GE mice. **C**, Same as **A**, for pre-juvenile mice. **D**, Violin plots of the normalized density of hippocampal terminals in layer 2/3 and layer 5/6 of PL of pre-juvenile CON and GE mice. **E**, Photograph of FG-labeled neurons (white) in the CA1 area of i/vHP in a 50 μm -thick NeuN-stained (green) coronal slice from a P10 CON and a P10 GE mouse, respectively. **F**, Violin plots of the normalized density of PL-projecting neurons in the hippocampal CA1 area averaged for all investigated neonatal (left) and pre-juvenile (right) CON and GE mice. Single data points are represented as dots and the red horizontal bars in violin plots correspond to the median and the 25th and 75th percentiles. * $p < 0.05$, ** $p < 0.01$, *** $p < 0.001$.

Figure 3. Passive and active membrane properties as well as synaptic inputs of prelimbic and hippocampal neurons from neonatal and pre-juvenile CON and GE mice *in vitro*. **A**, Confocal image showing a biocytin-filled pyramidal neuron in layer 5/6 of PL from a P10 CON mouse. **B**, Representative voltage responses to the injection of hyper- and depolarizing current pulses (holding membrane potential of -70 mV) of pyramidal neurons in layer 5/6 (light gray), layer 2/3 (dark gray) of the PL from P10 CON mice as well as for pyramidal neurons in layer 5/6 (light green), layer 2/3 (dark green) of the PL from P10 GE mice. **C**, Firing rate in relationship to current injection displayed for layer 5/6 ($n=33$) and layer 2/3 ($n=25$) neurons from neonatal CON mice as well as for layer 5/6 ($n=20$) and layer 2/3 ($n=14$) from neonatal GE mice. **D**, Same as **C**, for pre-juvenile mice ($n=28$ for CON layer 5/6, $n=15$ for CON layer 2/3, $n=20$ for GE layer 5/6, $n=12$ for GE layer 2/3). **E, (i)**, Representative traces of sEPSCs recorded from layer 2/3 pyramidal neurons from P10 CON (gray) and GE (green) mice. **(ii)**, Cumulative probability distribution of inter-event intervals (IEIs) and violin plots (inset) of sEPSCs frequencies averaged for all prefrontal neurons in CON and GE mice. **(iii)**, Same

as **(ii)** for sEPSC amplitude. **F**, Same as **E**, for pre-juvenile mice. **G**, Confocal image showing a biocytin-filled pyramidal neuron in the hippocampal CA1 area from a P10 CON mouse. SO: stratum oriens, SP: stratum pyramidale, SR: stratum radiatum. **H**, Representative voltage responses to the injection of hyper- and depolarizing current pulses (holding membrane potential of -70 mV) of CA1 pyramidal neurons from P10 CON (black) and GE (green) mice. **I**, Firing rate in relationship to current injection displayed for CA1 neurons from neonatal CON (n=15, black) and GE (n=10, green) mice. **J**, Same as **I**, for pre-juvenile CA1 neurons (n=12 for CON, n=9 for GE). Single data points are represented as dots and the red horizontal bars in violin plots correspond to the median and the 25th and 75th percentiles. *p < 0.05, **p < 0.01, ***p < 0.001.

Figure 4. Synaptic properties and plasticity of hippocampal inputs on prelimbic pyramidal neurons in neonatal CON and GE mice. **A, (i)**, Representative image showing ChR2 (H134R) (red) expression in a DAPI-stained coronal slice from a P10 CON mouse following hippocampal injection at P1. **(ii)**, Schematic of light stimulation of hippocampal CA1 neurons expressing ChR2 (H134R) (red). **(iii)**, Voltage responses of a ChR2-expressing neuron to light stimuli (470 nm, 5-10 mW/mm²) of 2-500 ms duration. **B, (i)**, Representative image showing hippocampal axons (red) in PL and IL from a P10 CON mouse following hippocampal injection at P1. **(ii)**, Schematic of light stimulation of hippocampal axons in PL. **(iii)**, Violin plots of eEPSC amplitudes evoked by light stimuli of 3, 5, 10 ms duration. Data were collected from layer 5/6 pyramidal neurons (n=24) in PL of CON mice. **C, (i)**, Left, representative current responses to light stimulation (blue bar 10 ms) of HP terminals for a putative pyramidal neuron (red, holding potential of -70 mV; gray, -40 mV, black, 10 mV). The response was abolished by bath CNQX (blue trace). Right, representative voltage response to light stimulation (blue bar 10 ms) of HP terminals for a pyramidal neuron. **(ii)**, Same as **Ci** for a putative interneuron. **D**, Average eEPSC (holding potential of -70mV) evoked by light in layer 5/6 (n=24) and layer 2/3 (n=21) neurons from neonatal CON mice as well as for pyramidal neurons in layer 5/6 (n=10) and layer 2/3 (n=8) from neonatal GE mice. Blue bar corresponds to 10 ms light stimulation. Inset, bar diagram of the percentage of responsive pyramidal

neurons in different groups. **E**, Violin plots showing the **(i)** amplitudes, **(ii)** coefficient of variation of amplitudes, **(iii)** synaptic delay and **(iv)** rise tau of eEPSCs averaged for all prefrontal neurons in CON and GE mice. **F**, **(i)**, Representative current response to pulsed light (8 Hz) (blue) of a layer 5/6 pyramidal neuron from a P10 CON mouse. **(ii)**, Plot of eEPSC amplitude (normalized to the 1st EPSC amplitude) in response to 8 Hz stimulation averaged for all prefrontal neurons in CON and GE mice. **G**, **(i)**, Representative response to light stimuli (500 ms inter-stimulus interval) of a layer 5/6 pyramidal neuron from a P10 CON mouse. **(ii)**, Plot of PPR at 125, 250, 500 ms inter-stimulus intervals averaged for all prefrontal neurons in CON and GE mice. Single data points are represented as dots and the red horizontal bars in violin plots correspond to the median and the 25th and 75th percentiles. * $p < 0.05$, ** $p < 0.01$, *** $p < 0.001$.

Figure 5. Oscillatory activity and neuronal firing in prelimbic layer 5/6 after optogenetic activation of hippocampal terminals in neonatal CON and GE mice *in vivo*. **A**, Digital photomontage reconstructing the location of a 4-shank recording electrode in a DAPI-stained 100 μm -thick coronal section (blue) with hippocampal terminals expressing ChR2 (H134R) (red) from a P9 mouse. Inset, the position of recording sites (white) over the prelimbic layers displayed at higher magnification. Blue lines correspond to the iso-contour lines of light intensity (diameter 50 μm , numerical aperture 0.22, light parameters: 473 nm, 2 mW) for 5 and 10 mW/mm^2 . **B**, Schematic of light stimulation of hippocampal terminals in layer 5/6 of PL. **C**, **(i)**, Power of oscillatory activity in layer 5/6 during ramp stimulation of hippocampal terminals in layer 5/6, normalized to the activity 1.5 s before stimulation in CON (gray) and GE (green) mice. **(ii)**, Violin plots displaying the oscillatory power averaged for different frequency bands (4–12 Hz, 12–30 Hz, 30–50 Hz) in response to ramp stimulation for all investigated CON and GE mice. **D**, **(i)**, Averaged LFP traces recorded in layer 5/6 in response to light stimulation of HP terminals (blue bars) in CON (gray) and GE (green) mice. **(ii)**, Violin plots showing the average amplitude of the maximum LFP response in layers 5/6 of CON and GE mice. **(iii)**, Violin plots showing the average delay of the maximum LFP response in layers 5/6 of CON and GE mice. **E**, **(i)**, Raster plot depicting the firing of single prelimbic cells in response to the

pulse stimulation of hippocampal terminals in layer 5/6 of CON mice. **(ii)**, Same as **(i)**, for GE mice. **(iii)**, Firing rate of all units in layer 5/6 around the pulse stimulation averaged for CON (gray) and GE (green) mice. **F, (i)**, Modulation index of spiking response of prefrontal single units to pulse stimulation in layer 5/6 of CON mice. Modulation index > 0 indicates increased firing activity, whereas values < 0 correspond to decreased firing activity. **(ii)**, Same as **(i)**, for GE mice. **(iii)**, Stacked bar plot showing the percentage of activated (red), unmodulated (white), and inhibited (blue) units after the pulse stimulation in layers 5/6 of CON and GE. **(iv)**, Violin plots showing the modulation index of firing rate of all activated units in layers 5/6 of CON and GE. Single data points are represented as dots and the red horizontal bars in violin plots correspond to the median and the 25th and 75th percentiles. *p < 0.05, **p < 0.01, ***p < 0.001.

Figure 6. Oscillatory activity and neuronal firing in prelimbic layer 2/3 after optogenetic activation of hippocampal terminals in neonatal CON and GE mice *in vivo*. **A**, Schematic of light stimulation of hippocampal axonal terminals in layer 2/3 of PL. **B, (i)**, Power of oscillatory activity in PL layer 2/3 during ramp stimulation of hippocampal terminals in layer 2/3, normalized to the activity 1.5 s before stimulation in CON (gray) and GE (green) mice. **(ii)**, Violin plots displaying the oscillatory power averaged for different frequency bands (4–12 Hz, 12–30 Hz, 30–50 Hz) in response to ramp stimulation for all investigated CON and GE mice. **C, (i)**, Averaged LFP response recorded in prelimbic layer 2/3 in response to light stimulation (blue bars) of HP terminals in CON (gray) and GE (green) mice. **(ii)**, Violin plots showing the average amplitude of the maximum LFP response evoked by light in layers 2/3 of CON and GE. **(iii)**, Violin plots showing the average delay of the maximum LFP response evoked by light in layers 2/3 of CON and GE. **D, (i)**, Raster plot depicting the firing of single prelimbic cells in response to the pulse stimulation of hippocampal terminals in layer 2/3 of CON mice. **(ii)**, Same as **(i)**, for GE mice. **(iii)**, Firing rate of all units in layer 2/3 around the pulse stimulation averaged for CON (gray) and GE (green) mice. **E, (i)**, Modulation index of spiking response of prefrontal single units to pulse stimulation in layer 2/3 of CON mice. Modulation index > 0 indicates increased firing activity, whereas values < 0 correspond to decreased firing activity. **(ii)**, Same as **(i)**, for GE mice. **(iii)**, Stacked bar plot showing the percentage of activated (red),

unmodulated (white), and inhibited (blue) units after the pulse stimulation in layers 2/3 of CON and GE. **(iv)**, Violin plots showing the modulation index of firing rate of all activated units in layers 2/3 of CON and GE. Single data points are represented as dots and the red horizontal bars in violin plots correspond to the median and the 25th and 75th percentiles. * $p < 0.05$, ** $p < 0.01$, *** $p < 0.001$.

Figure 7. Synaptic properties and plasticity of hippocampal inputs on prelimbic pyramidal neurons in pre-juvenile CON and GE mice. **A**, Averaged eEPSC (holding potential of -70mV) evoked by light in layer 5/6 (n=23) and layer 2/3 (n=15) neurons from pre-juvenile CON mice as well as in pyramidal neurons in layer 5/6 (n=12) and layer 2/3 (n=6) from pre-juvenile GE mice. Blue bar corresponds to 10 ms light stimulation. Inset, bar diagram of the percentage of responsive pyramidal neurons in different groups. **B**, Violin plots showing the **(i)** amplitudes, **(ii)** coefficient of variation of amplitudes, **(iii)** synaptic delay, and **(iv)** rise tau of eEPSCs averaged for all prefrontal neurons in CON and GE mice. **C**, Top, Representative current response to pulsed light (8 Hz) (blue) of a layer 5/6 pyramidal neuron from a P21 CON mouse. Bottom, Plot of eEPSC amplitude (normalized to the 1st EPSC amplitude) in response to 8 Hz stimulation averaged for all prefrontal neurons in CON and GE mice. **D**, **(i)**, Representative response to light stimuli (500 ms inter-stimulus interval) of a layer 5/6 pyramidal neuron from a P21 CON mouse. **(ii)**, Plot of PPR at 125, 250, 500 ms inter-stimulus intervals averaged for all prefrontal neurons in CON and GE mice. * for comparison of layer 5/6, ## for comparison of layer 2/3. Single data points are represented as dots and the red horizontal bars in violin plots correspond to the median and the 25th and 75th percentiles. * $p < 0.05$, ** $p < 0.01$, *** $p < 0.001$.

Figure 8. Oscillatory activity and neuronal firing in PL after optogenetic activation of hippocampal terminals in pre-juvenile CON and GE mice *in vivo*. **A**, **(i)**, Averaged LFP response recorded in prelimbic layer 5/6 in response to light stimulation (blue bars) of HP terminals in CON (gray) and GE (green) mice. **(ii)**, Violin plots showing the average amplitude of the maximum LFP response evoked by light in layer 5/6 of CON and GE mice. **B**, **(i)**, Raster plot depicting the firing of single prelimbic cells in response to pulse stimulation of hippocampal

terminals in layer 5/6 of CON mice. **(ii)**, Same as **(i)**, for GE mice. **(iii)**, Firing rate of all units in layer 5/6 around the pulse stimulation averaged for CON (gray) and GE (green) mice. **(iv)**, Stacked bar plot showing the percentage of activated (red), unmodulated (white), and inhibited (blue) units after pulse stimulation of prelimbic layer 5/6 of CON and GE mice. **(v)**, Violin plots showing the modulation index of firing rate of all activated units in layer 5/6 of CON and GE mice. **C**, Same as in **A**, but for the stimulation in layer 2/3 of PL. **D**, Same as in **B**, but for spike response of single prefrontal cells to pulse stimulation of hippocampal terminals in layer 2/3. Single data points are represented as dots and the red horizontal bars in violin plots correspond to the median and the 25th and 75th percentiles. * $p < 0.05$, ** $p < 0.01$, *** $p < 0.001$.

Table 1. Passive and active membrane properties of prefrontal and hippocampal neurons from neonatal and pre-juvenile CON and GE mice *in vitro*. Data are shown as mean \pm SEM. Significance was assessed using one-way analysis of variance (ANOVA) test followed by Bonferroni-corrected post hoc test and the listed p values correspond to comparisons between CON and GE mice for the neurons in same region.

Table 2. Properties of sEPSCs recorded from prefrontal neurons in CON and GE mice *in vitro*. Data are shown as mean \pm SEM. Significance was assessed using one-way analysis of variance (ANOVA) test followed by Bonferroni-corrected post hoc test. The listed p values (* $p < 0.05$) correspond to comparisons CON L5/6 vs. GE L5/6 and CON L2/3 vs. GE L2/3, whereas p values (## p) correspond to comparisons CON L5/6 vs. CON L2/3 and GE L5/6 vs. GE L2/3.

Table 3. Properties of EPSCs evoked by stimulation of hippocampal terminals *in vitro*. Data are shown as mean \pm SEM. Significance was assessed using one-way analysis of variance (ANOVA) test followed by Bonferroni-corrected post hoc test. The listed p values (* $p < 0.05$, ** $p < 0.01$) correspond to comparisons CON L5/6 vs. GE L5/6 and CON L2/3 vs. GE L2/3, whereas p values (## $p < 0.01$) correspond to comparisons CON L5/6 vs. CON L2/3 and GE L5/6 vs. GE L2/3.

Table 4. Prefrontal activity patterns induced by light stimulation of hippocampal terminals at neonatal and pre-juvenile age. Data are shown as mean \pm SEM. Significance was assessed using one-way ANOVA test followed by Bonferroni-corrected post hoc test. The listed P values correspond to comparisons CON L5/6 vs. GE L5/6 and CON L2/3 vs. GE L2/3.

Multimedia and 3D Models

Multimedia 1: Hippocampal projections to the prelimbic cortex

3D reconstruction of traced hippocampal terminals in PL from a neonatal CON mouse after tissue clearing. tDimer expression (red), nuclei staining (cyan). The PL (cyan surface) was outlined according to nuclei staining. tDimer labeled fibers were segmented and the signal was enhanced.

Table 1. Passive and active membrane properties of prefrontal and hippocampal neurons from neonatal and pre-juvenile CON and GE mice *in vitro*.

Membrane Properties	Layer 5/6			Layer 2/3			HP			
	CON	GE	p	CON	GE	p	CON	GE	p	
Neonatal (P8-P10)	R_{in} (M Ω)	401.8 \pm 19.5	427.6 \pm 35.1	0.5352	471.3 \pm 18	536.1 \pm 35.8	0.0699	490.6 \pm 43.1	372.2 \pm 22.4	0.0169
	C_m (pF)	125.1 \pm 5.6	125.6 \pm 13.9	0.9693	94.2 \pm 4.4	90.5 \pm 3.3	0.5804	112.1 \pm 11.8	107.0 \pm 10.6	0.2376
	Passive τ_m (ms)	83.9 \pm 4.3	81.4 \pm 8.0	0.7876	67.2 \pm 3.5	73.4 \pm 4.6	0.2879	51.8 \pm 4.6	39.5 \pm 4.6	0.0166
	RMP (mV)	-68.4 \pm 0.7	-67.2 \pm 0.9	0.3986	-69.8 \pm 0.9	-65.8 \pm 1.1	0.0096	-68.6 \pm 1.9	-69.8 \pm 2.0	0.2845
	Sag (%)	10.2 \pm 0.9	12.8 \pm 2.5	0.2225	4.4 \pm 0.62	4.58 \pm 0.38	0.8457	23.0 \pm 3.2	31.6 \pm 3.1	0.00003
	AP threshold (mV)	-42.4 \pm 1.3	-42.8 \pm 2.1	0.9080	-38.8 \pm 1.2	-39.1 \pm 1.3	0.8544	-41.3 \pm 1.3	-45.0 \pm 3.8	0.2204
	AP amplitude (mV)	71.5 \pm 1.3	69.4 \pm 2.2	0.8525	66.8 \pm 1.4	59.5 \pm 1.8	0.0028	78.8 \pm 2.3	79.3 \pm 1.8	0.919
	Active AP halfwidth (ms)	3.56 \pm 0.15	3.40 \pm 0.18	0.5970	2.85 \pm 0.06	3.38 \pm 0.15	0.00062	2.44 \pm 0.10	2.56 \pm 0.11	0.0042
	Rheobase (pA)	43.5 \pm 3.6	40.4 \pm 45.0	0.6716	43.1 \pm 2.9	46.6 \pm 6.8	0.5710	59.4 \pm 4.0	52.8 \pm 3.1	0.2555
	Firing rate (Hz)	12.3 \pm 0.7	11.3 \pm 1.1	0.4956	12.5 \pm 1.0	11.3 \pm 1.6	0.4945	13.8 \pm 1.1	14.1 \pm 1.7	0.8713
Pre-juvenile (P20-P24)	R_{in} (M Ω)	222.2 \pm 11.5	188.9 \pm 17.9	0.1146	235.4 \pm 13.2	237.8 \pm 9.7	0.8938	239.0 \pm 19.6	211.9 \pm 24.7	0.3703
	C_m (pF)	178.2 \pm 12.5	184.7 \pm 13.9	0.7547	131.3 \pm 9.37	115.2 \pm 8.4	0.2409	174.9 \pm 24.0	131.9 \pm 22.8	0.1997
	Passive τ_m (ms)	59.6 \pm 5.8	45.9 \pm 4.7	0.1353	46.9 \pm 3.64	44.5 \pm 2.9	0.6337	37.7 \pm 1.6	33.2 \pm 5.1	0.3286
	RMP (mV)	-69.5 \pm 0.5	-69.3 \pm 0.5	0.8084	-66.9 \pm 0.5	-69.7 \pm 0.4	0.00076	-64.9 \pm 1.1	-63.5 \pm 2.0	0.5000
	Sag (%)	16.2 \pm 1.7	18.4 \pm 2.7	0.4839	6.4 \pm 1.6	4.3 \pm 0.7	0.3337	27.3 \pm 2.0	21.1 \pm 2.8	0.0664
	AP threshold (mV)	-46.1 \pm 1.3	-48.4 \pm 2.0	0.3297	-44.5 \pm 1.2	-46.4 \pm 1.7	0.3370	-45.4 \pm 1.8	-49.3 \pm 1.9	0.1325
	AP amplitude (mV)	90.1 \pm 1.1	90.9 \pm 1.6	0.6539	88.5 \pm 1.1	86.8 \pm 1.3	0.3388	97.1 \pm 2.7	96.8 \pm 4.4	0.9528
	Active AP halfwidth (ms)	1.67 \pm 0.05	1.53 \pm 0.07	0.6839	1.79 \pm 0.06	1.65 \pm 0.07	0.1186	1.73 \pm 0.04	1.74 \pm 0.06	0.8715
	Rheobase (pA)	73.8 \pm 5.2	78.6 \pm 9.3	0.6231	85.1 \pm 6.2	89.5 \pm 7.8	0.6694	50.7 \pm 2.7	48.4 \pm 5.1	0.6444
	Firing rate (Hz)	11.4 \pm 0.8	10.2 \pm 1.3	0.4260	11.8 \pm 0.7	10.6 \pm 1.1	0.3109	15.0 \pm 1.2	15.9 \pm 1.8	0.7774

Data are shown as mean \pm SEM. Significance was assessed using one-way analysis of variance (ANOVA) test followed by Bonferroni-corrected post hoc test and the listed p values correspond to comparisons between CON and GE mice for the neurons in same region.

Table 2. Properties of sEPSCs recorded from prefrontal neurons in CON and GE mice *in vitro*.

sEPSC properties	Neonatal (P8-P10)					Pre-juvenile (P20-P24)				
	CON L5/6	GE L5/6	CON L2/3	GE L2/3	F values	CON L5/6	GE L5/6	CON L2/3	GE L2/3	F values
Frequency (Hz)	0.24 ± 0.023	0.19 ± 0.022	0.45 ± 0.037	0.31 ± 0.041	F(3, 90)=14.52 P=8.6E-08	0.93 ± 0.074	0.79 ± 0.083	1.28 ± 0.15	1.41 ± 0.18	F(3, 100)=4.86 P=0.0034
Amplitude (pA)	7.40 ± 0.22	7.45 ± 0.36	6.92 ± 0.36	7.75 ± 0.56	F(3, 90)=1.22 P=0.3074	7.97 ± 0.27	7.88 ± 0.42	7.45 ± 0.47	7.09 ± 0.53	F(3, 100)=0.72 P=0.5403

Data are shown as mean ± SEM. Significance was assessed using one-way analysis of variance (ANOVA) test followed by Bonferroni-corrected post hoc test. The listed p values (*p < 0.05) correspond to comparisons CON L5/6 vs. GE L5/6 and CON L2/3 vs. GE L2/3, whereas p values (##p < 0.01) correspond to comparisons CON L5/6 vs. CON L2/3, GE L5/6 vs. GE L2/3.

Table 3. Properties of EPSCs evoked by stimulation of hippocampal terminals *in vitro*.

Light-evoked EPSCs	Neonatal					Pre-juvenile				
	CON L5/6	GE L5/6	CON L2/3	GE L2/3	F values	CON L5/6	GE L5/6	CON L2/3	GE L2/3	F values
Response %	24/29 (82.76%)	10/24 (41.67%)	21/26 (80.76%)	8/18 (44.44%)		23/34 (67.65%)	15/32 (46.88%)	12/21 (57.14%)	6/16 (37.5%)	
Amplitude (pA)	63.6 ± 12.12 **p=0.001	9.72 ± 2.41	47.9 ± 12.00	40.97 ± 13.6	F(3, 59)=14.02 P=0.0029	70.1 ± 13.74 *p=0.0354	19.7 ± 4.39	43.0 ± 14.32	26.2 ± 15.96	F(3, 52)=9.877 P=0.0196
Coefficient of variation	0.236 ± 0.032 *p=0.016	0.421 ± 0.052	0.390 ± 0.04	0.416 ± 0.066	F(3, 59)=5.35 P=0.0026	0.34 ± 0.041 **p= 0.0005	0.60 ± 0.037	0.45 ± 0.063	0.40 ± 0.049	F(3, 52)=6.045 P=0.0012
Onset delay (ms)	5.15 ± 0.476 **p=0.006	7.99 ± 0.762	6.29 ± 0.382	7.55 ± 1.128	F(3, 59)=5.00 P=0.0037	4.41 ± 0.508	3.75 ± 0.506 ##p= 0.0044	4.89 ± 0.378	5.15 ± 0.861	F(3, 52)=5.967 P=0.0014
Tau rise (ms)	3.07 ± 0.044 *p= 0.022	3.60 ± 0.301	3.18 ± 0.093	3.06 ± 0.171	F(3, 59)=3.20 P=0.030	3.63 ± 0.212	3.20 ± 0.158	3.31 ± 0.183	3.11 ± 0.159	F(3, 52)=1.358 P=0.2651
125 ms	0.70 ± 0.056	0.48 ± 0.15	0.64± 0.09	0.63 ± 0.13	F(3, 59)=2.28 P=0.5156	1.23 ± 0.09 *p=0.037	0.94 ± 0.13	0.96 ± 0.12 *p= 0.0086	0.51 ± 0.12	F(3, 52)=17.11 P=6.70E-04
PPR 250 ms	0.72 ± 0.06	0.54 ± 0.08	0.69± 0.06	0.68 ± 0.15	F(3, 59)=3.95 P=0.2672	1.35 ± 0.08	1.19 ± 0.14	1.07 ± 0.15	0.87 ± 0.14	F(3, 52)=8.88 P=0.0310
500 ms	0.66 ± 0.056 **p= 0.0061	0.27 ± 0.104	0.70± 0.069	0.62± 0.079	F(3, 59)=11.09 P=0.0074	1.28 ± 0.111	1.23 ± 0.108	0.98 ± 0.105	1.03 ± 0.174	F(3, 52)=5.505 P=0.1384

Data are shown as mean ± SEM. Significance was assessed using one-way analysis of variance (ANOVA) test followed by Bonferroni-corrected post hoc test. The listed p values (*p< 0.05, **p< 0.01) correspond to comparisons CON L5/6 vs. GE L5/6 and CON L2/3 vs. GE L2/3, whereas p values (##p< 0.01) correspond to comparisons CON L5/6 vs. CON L2/3, GE L5/6 vs. GE L2/3.

Table 4. Prefrontal activity patterns induced by light stimulation of hippocampal terminals at neonatal and pre-juvenile age.

		Neonatal			Pre-juvenile			
		CON L5/6	GE L5/6	F values	CON L5/6	GE L5/6	F values	
Layer 5/6 stimulation	Power (Stim-pre)/pre	4-12 Hz	0.807 ± 0.121	0.218 ± 0.096	F(1,23)=3.365 P=0.039	0.071 ± 0.036	-0.02 ± 0.034	F(1,26)=1.716 P=0.190
		12-30 Hz	0.701 ± 0.141	0.216 ± 0.0562	F(1,23)=1.779 P=0.182	0.056 ± 0.027	0.042 ± 0.019	F(1,26)=0.114 P=0.735
		30-45 Hz	0.383 ± 0.062	0.151 ± 0.061	F(1,23)=2.913 P=0.0846	0.063 ± 0.043	0.079 ± 0.023	F(1,26)=0.179 P=0.673
	evoked LFP	Amplitude (μ V)	144.9 ± 26.97	67.0 ± 13.80	F(1,23)=3.396 P=0.024	70.8 ± 7.88	63.1 ± 3.43	F(1,26)=0.007 P=0.936
		Delay (ms)	19.3 ± 0.40	19.3 ± 0.89	F(1,23)=0.365 P=0.552	17.5 ± 0.41	17.1 ± 0.57	F(1,26)=0.392 P=0.537
Layer 2/3 stimulation	Power (Stim-pre)/pre	4-12 Hz	0.289 ± 0.109	0.106 ± 0.135	F(1,21)=2.314 P=0.128	0.052 ± 0.029	0.0003 ± 0.031	F(1,26)=1.517 P=0.218
		12-30 Hz	0.285 ± 0.103	0.272 ± 0.142	F(1,21)=0.314 P=0.575	0.028 ± 0.028	0.036 ± 0.021	F(1,26)=0.070 P=0.792
		30-45 Hz	0.231 ± 0.074	0.098 ± 0.066	F(1,21)=2.827 P=0.093	0.044 ± 0.031	0.036 ± 0.030	F(1,26)=0.008 P=0.930
	evoked LFP	Amplitude (μ V)	132.3 ± 27.6	63.0 ± 17.94	F(1,21)=3.939 P=0.047	58.9 ± 8.20	39.7 ± 4.83	F(1,26)=3.282 P=0.07
		Delay (ms)	19.8 ± 0.48	20.2 ± 0.68	F(1,21)=0.013 P=0.910	17.6 ± 0.32	17.2 ± 0.52	F(1,26)=0.910 P=0.350

Data are shown as mean ± SEM. Significance was assessed using one-way ANOVA test followed by Bonferroni-corrected post hoc test. The listed P values correspond to comparisons CON L5/6 vs. GE L5/6 and CON L2/3 vs. GE L2/3.

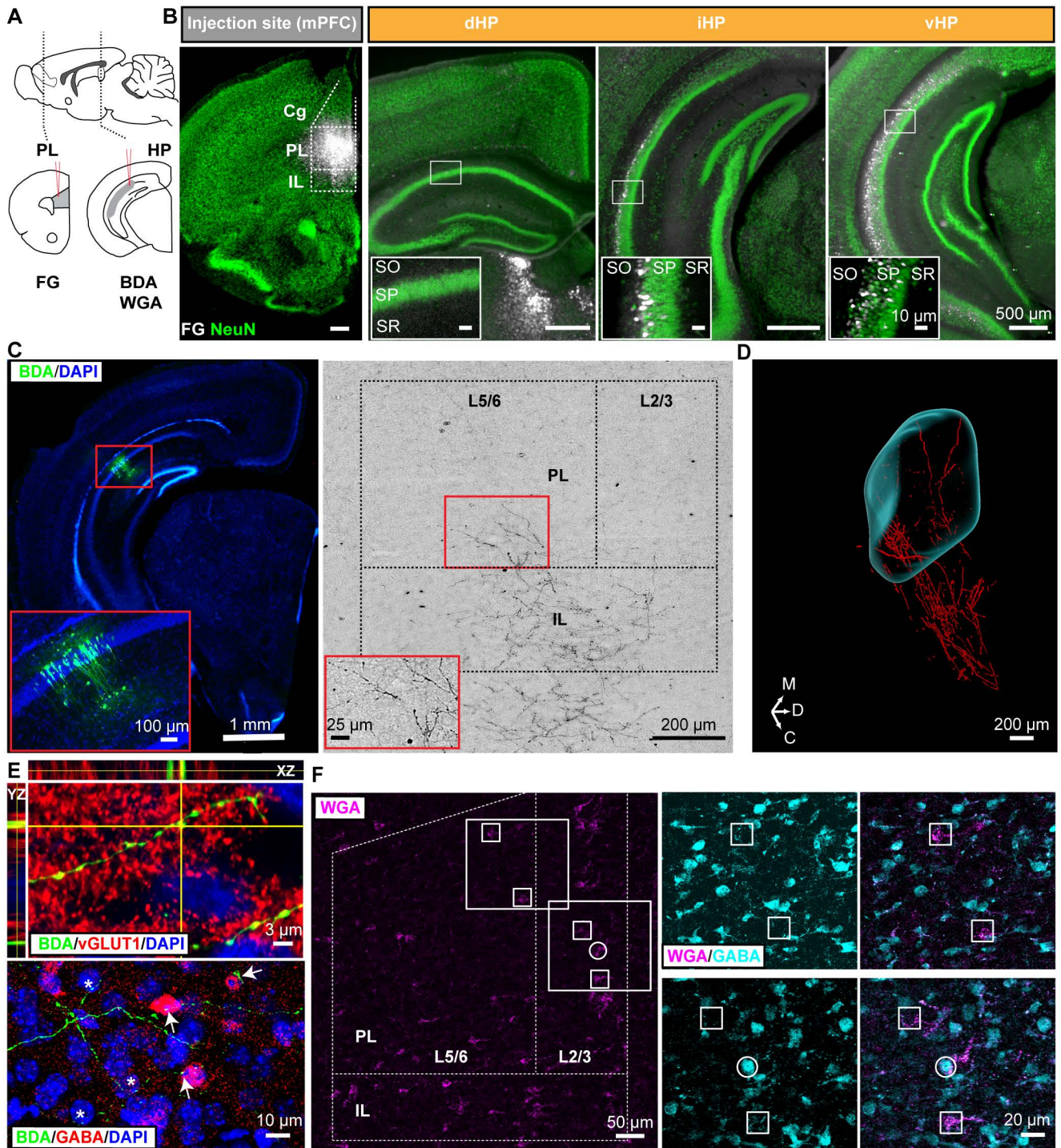


Figure 1 - Song et al.

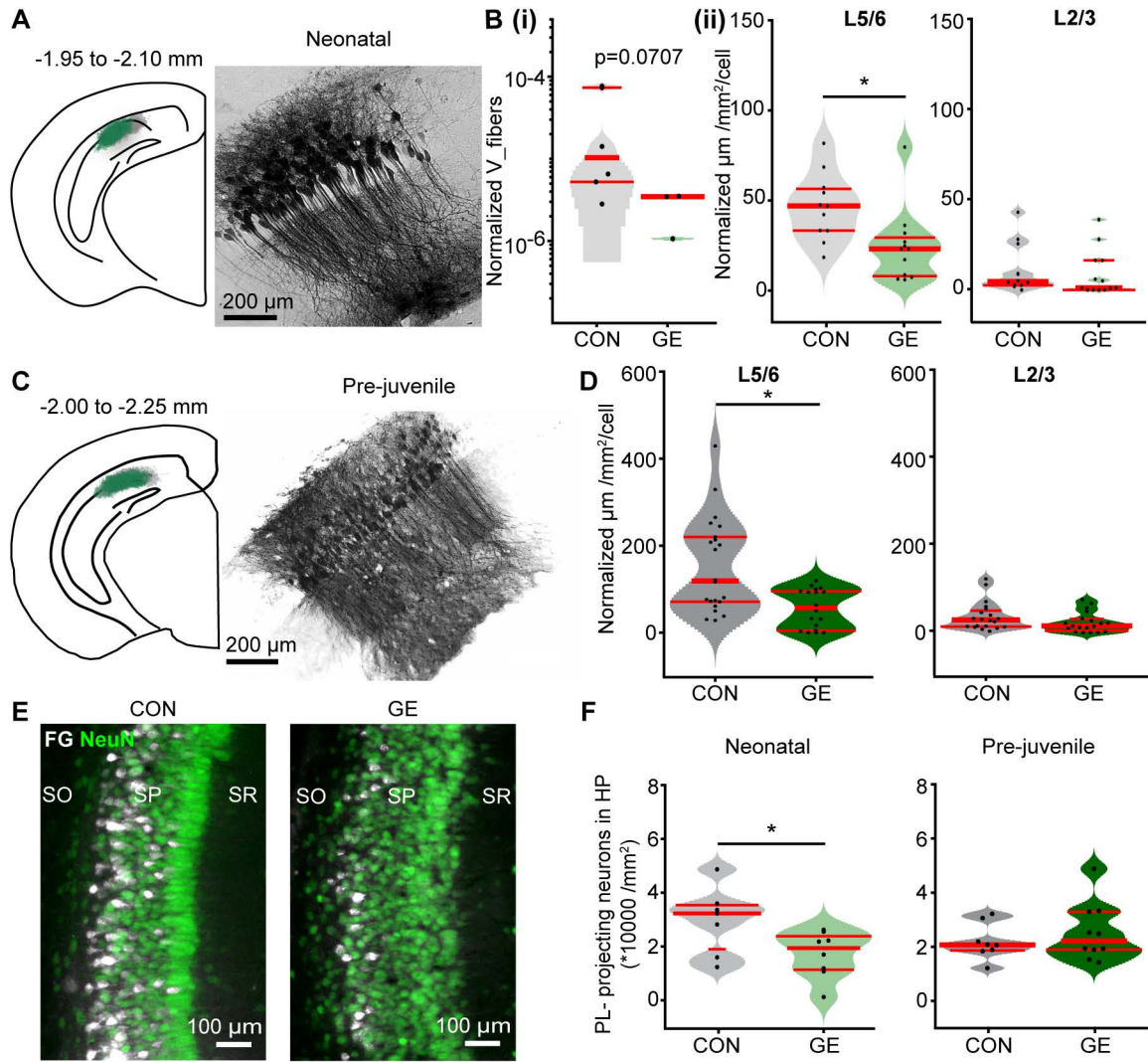


Figure 2 -Song et al.

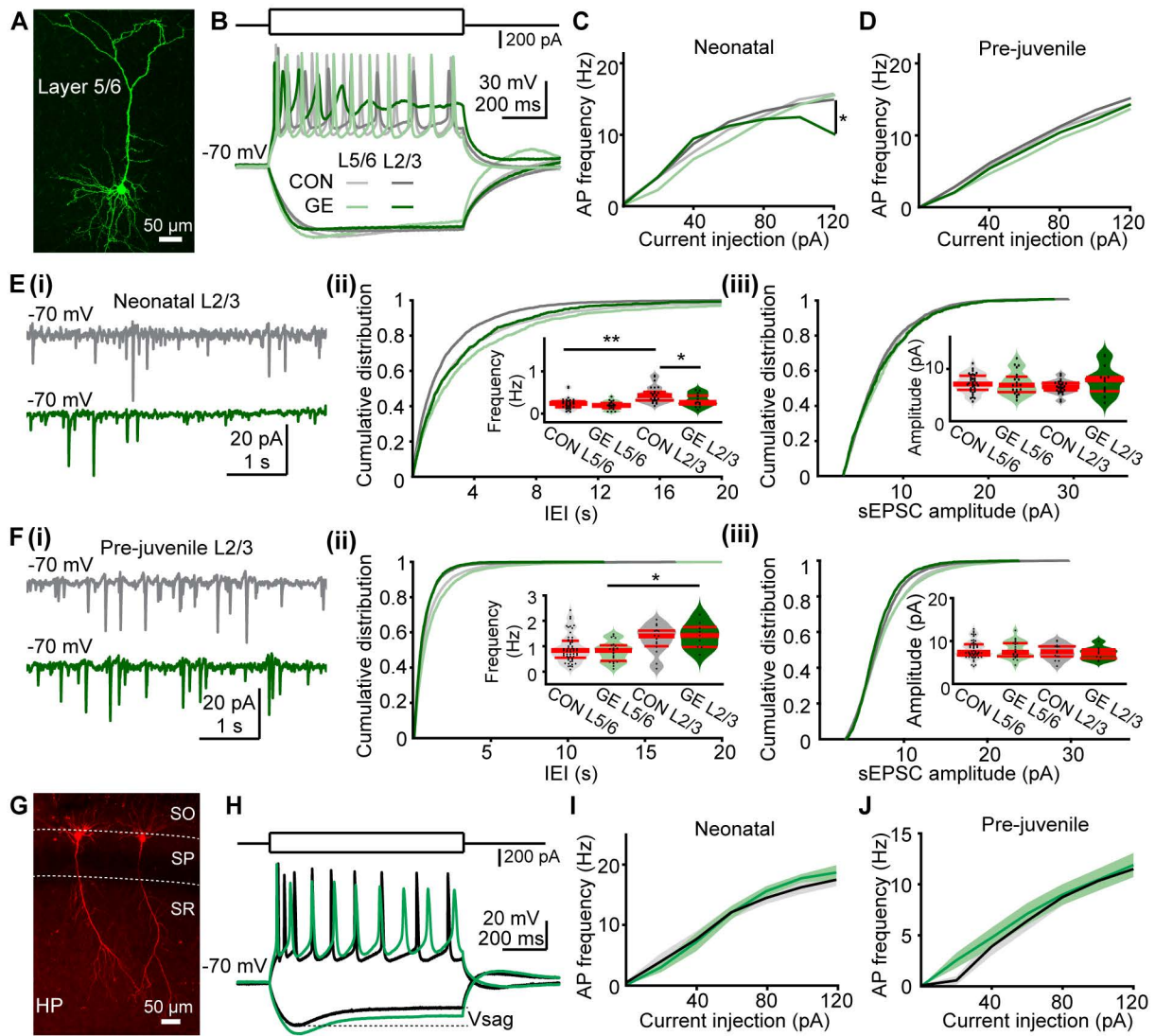


Figure 3 - Song et al.

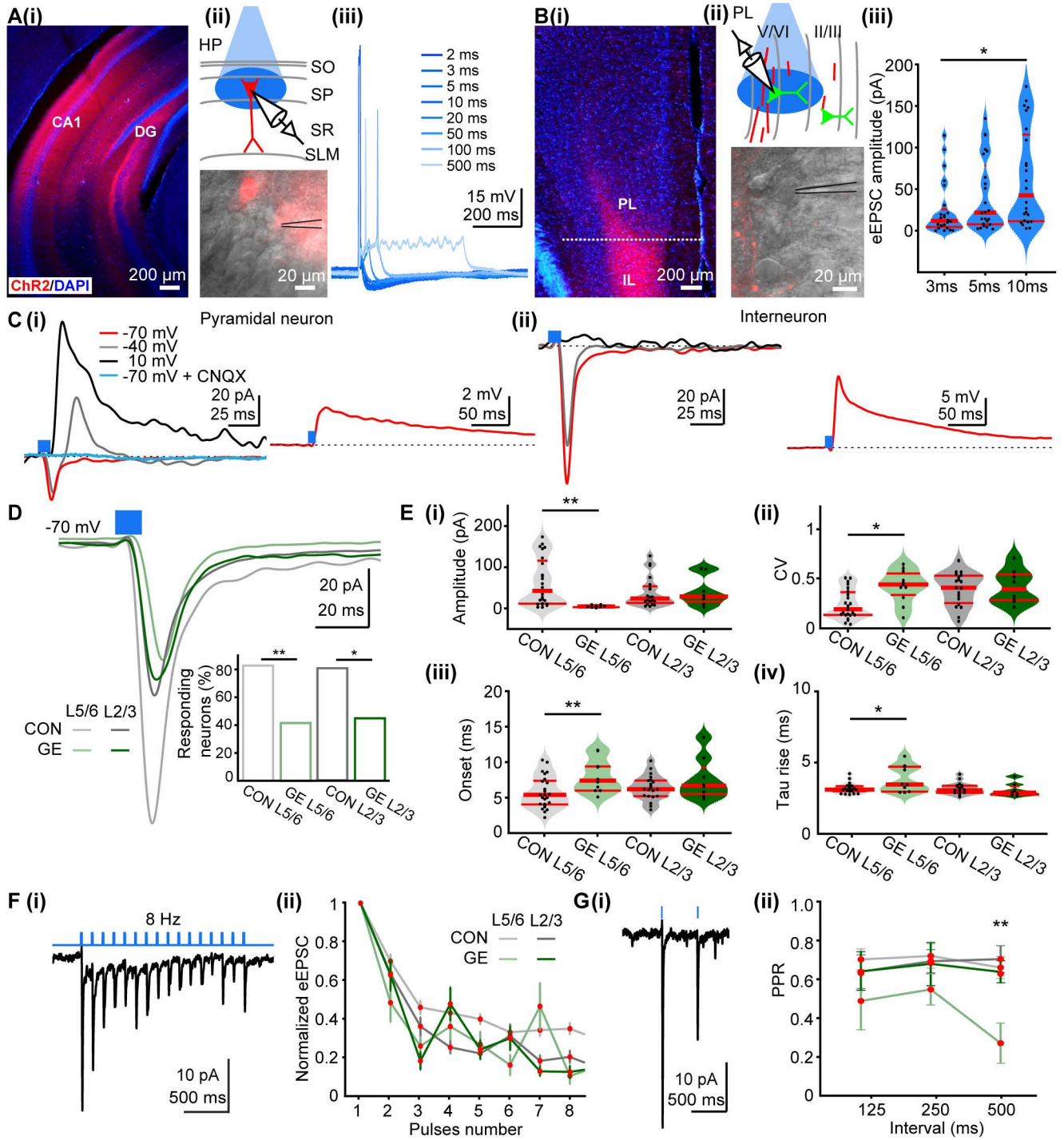


Figure 4 - Song et al.

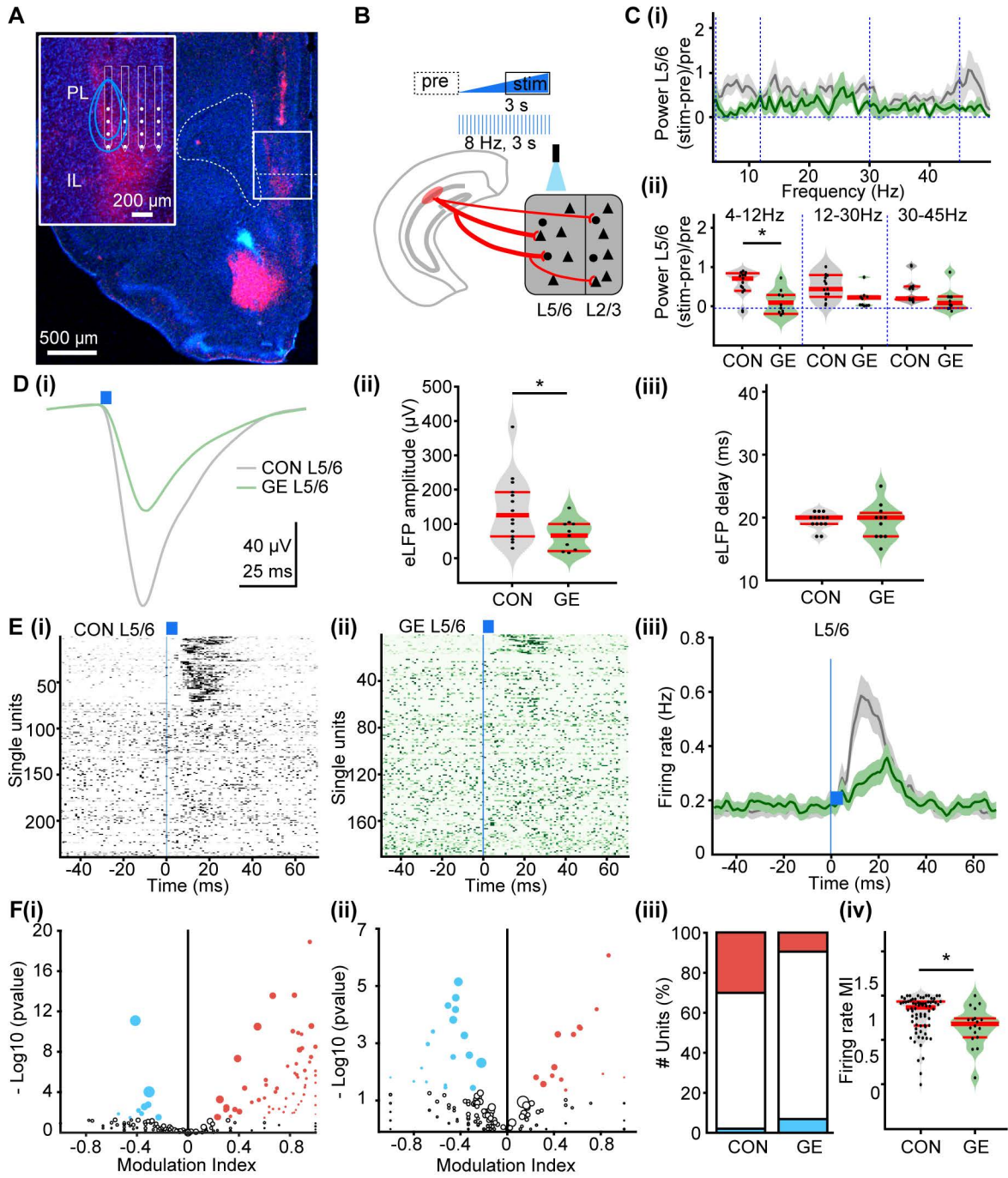


Figure 5 -Song et al.

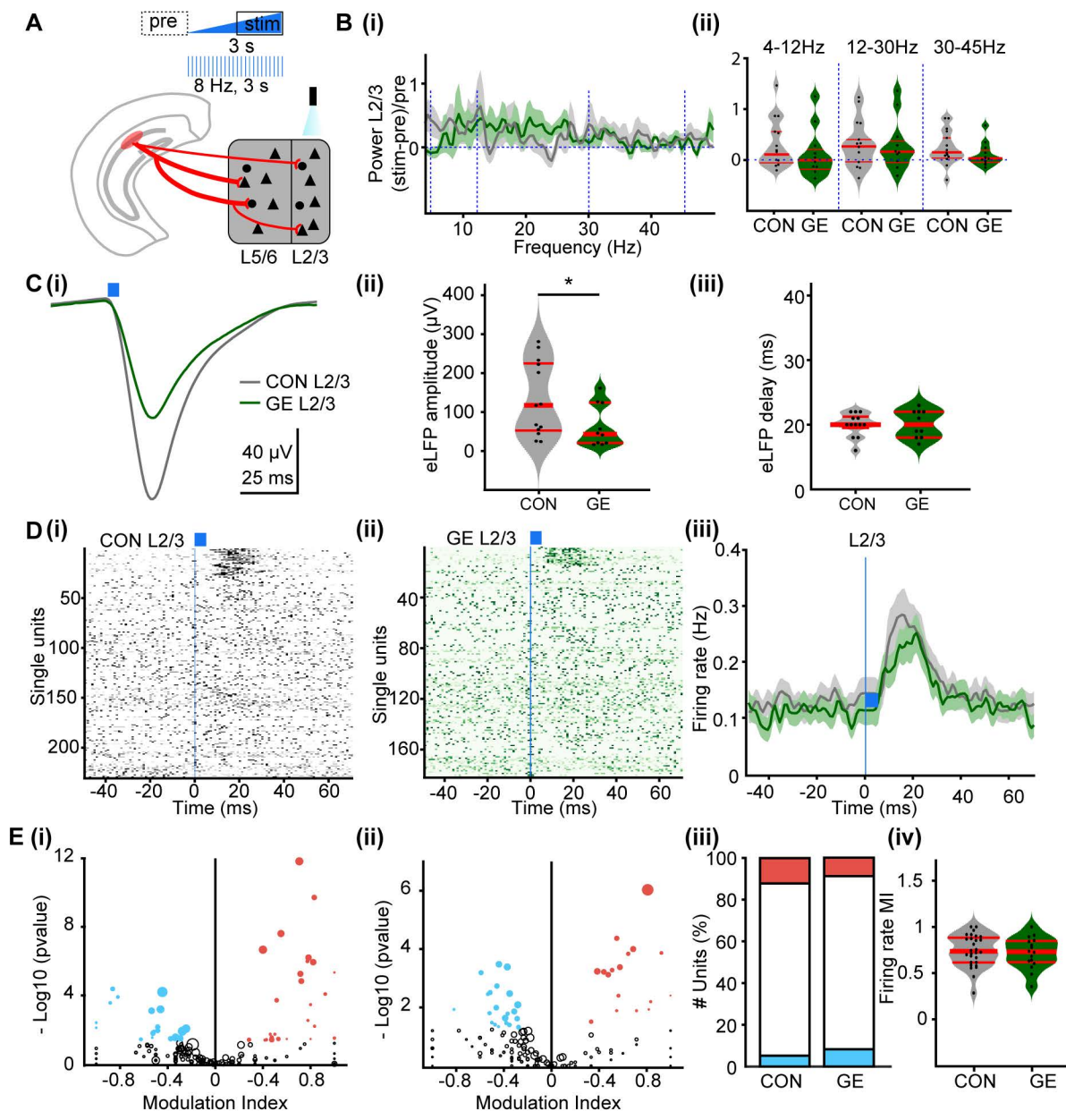


Figure 6 - Song et al.

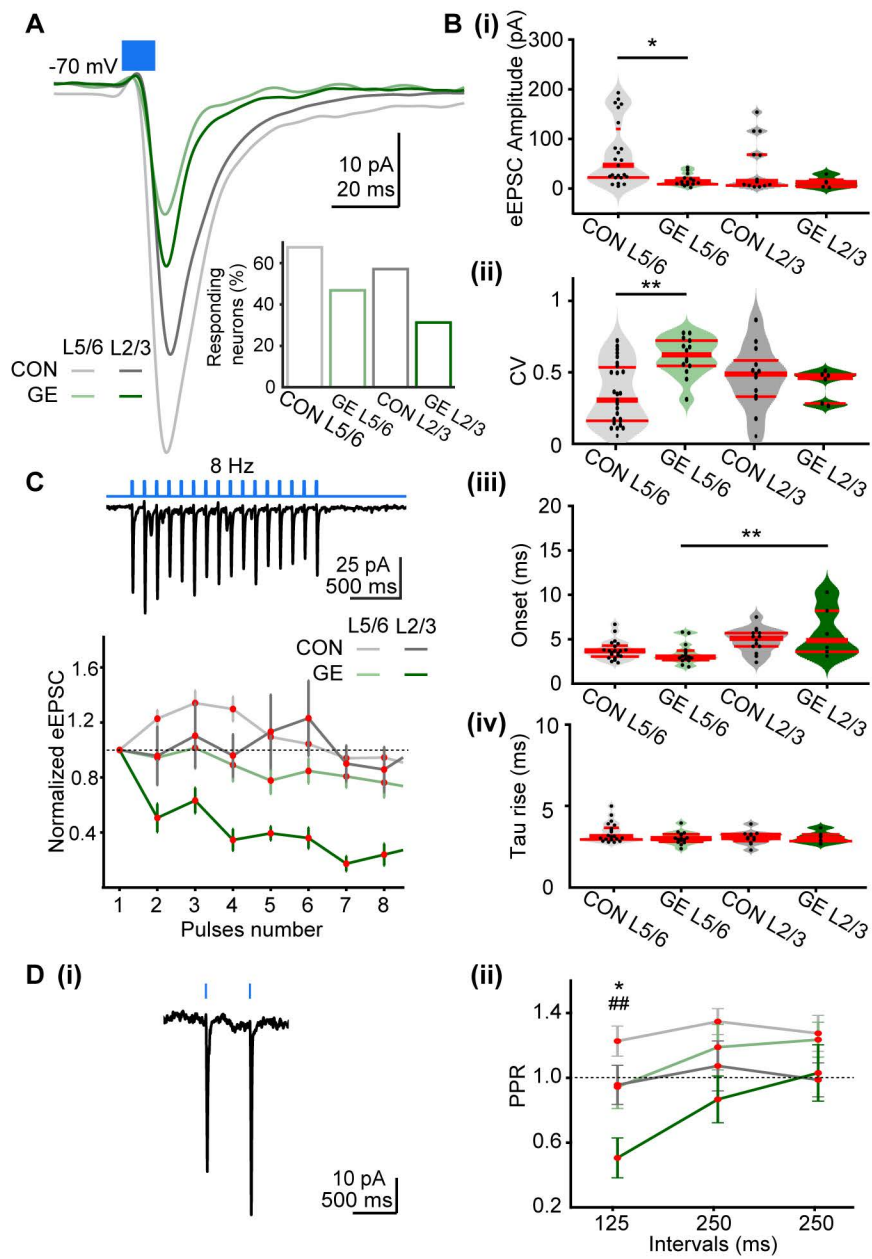


Figure 7 - Song et al.

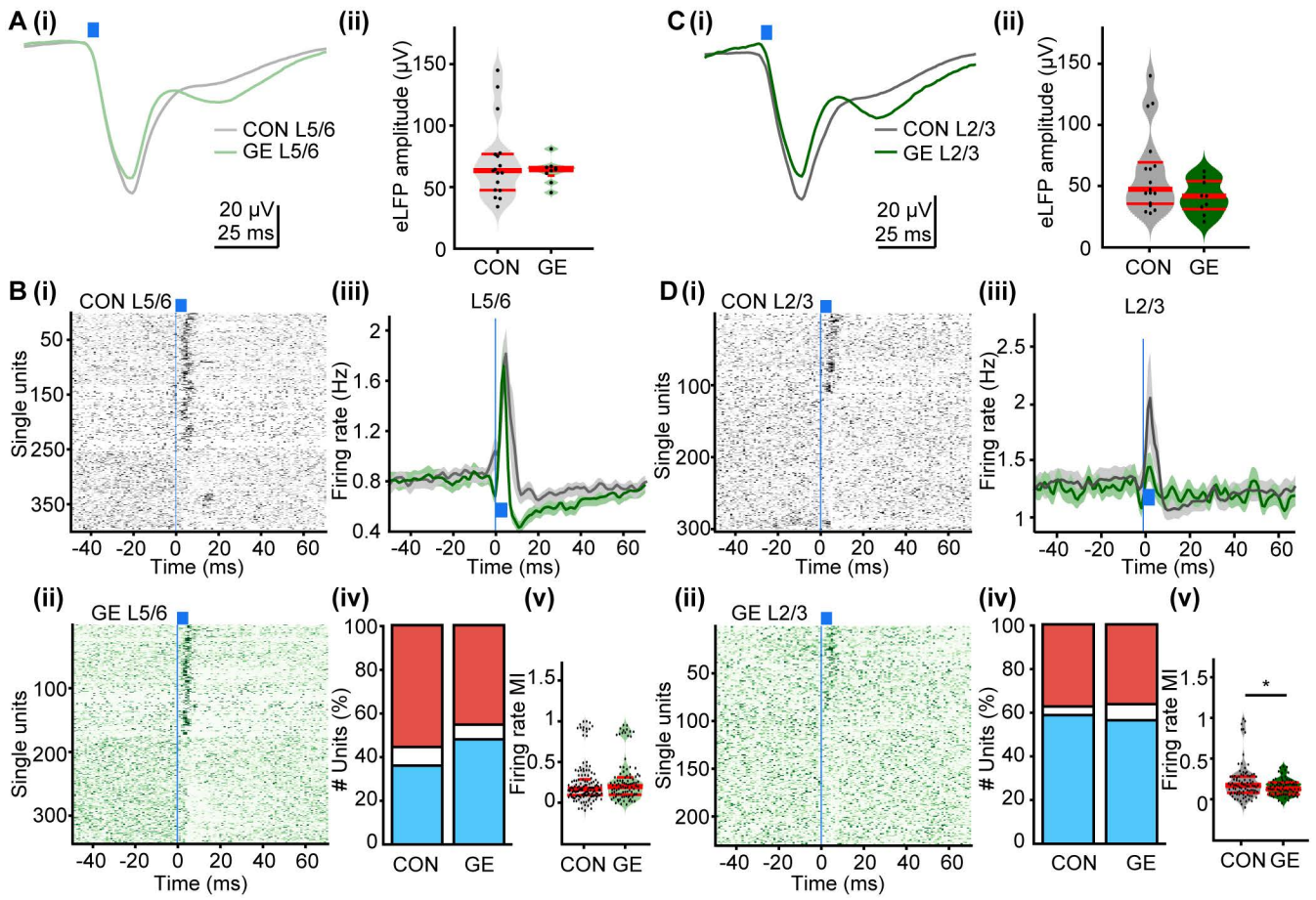


Figure 8 - Song et al.

4.4 Article 4

Developmental decrease of entorhinal-hippocampal communication in immune-challenged DISC1 knockdown mice

X Xu¹, **L Song**¹, R Kringel¹, IL Hanganu-Opatz¹

¹ Institute of Developmental Neurophysiology, Center for Molecular Neurobiology, University Medical Center Hamburg-Eppendorf, 20251 Hamburg, Germany

Nature Communication, (2021). Revision, DOI:10.21203/rs.3.rs-290304/v1

Personal contribution

I carried out part of *in vivo* electrophysiology and *in vitro* electrophysiology experiments. I assisted with histological investigations and image analysis. I assisted with formal analysis. I discussed, reviewed and edited the manuscript.

Developmental decrease of entorhinal-hippocampal communication in immune-challenged DISC1 knockdown mice

Xi Xia Xu*, Lingzhen Song, Rebecca Kringel, and Ileana L. Hanganu-Opatz*

Institute of Developmental Neurophysiology, Center for Molecular Neurobiology, University Medical Center Hamburg-Eppendorf, 20251 Hamburg, Germany

Running title: Abnormal entorhinal-hippocampal development

*Corresponding authors: Ileana L. Hanganu-Opatz
hangop@zmnh.uni-hamburg.de

Xi Xia Xu
xi Xia.xu@zmnh.uni-hamburg.de

Figures: 9

Tables: 1

Number of pages: 39

Number of words in Abstract: 152

Number of words in Introduction: 511

Number of words in Discussion: 1030

Abstract

The prefrontal-hippocampal dysfunction that underlies cognitive deficits in mental disorders emerges during early development. The contribution of the lateral entorhinal cortex (LEC), the cortical area that is tightly interconnected with both prefrontal cortex (PFC) and hippocampus (HP), to the early dysfunction is fully unknown. Here we show that the poorer LEC-dependent recognition memory detectable at pre-juvenile age follows the abnormal communication within LEC-HP-PFC networks of neonatal mice mimicking the combined genetic and environmental etiology (GE) of psychiatric risk. The prominent entorhinal drive to HP is weaker in GE mice as a result of sparser projections from LEC to CA1 and decreased efficiency of axonal terminals to activate the hippocampal circuits. In contrast, the direct entorhinal drive to PFC is not affected in GE mice, yet the PFC is indirectly compromised, as target of the under-activated HP. Thus, already at neonatal age, the entorhinal-hippocampal circuit is impaired, contributing to the disease-characteristic cognitive disability.

INTRODUCTION

The major burden of major psychiatric disorders, such as schizophrenia, is a lifelong cognitive disability^{1,2}. Its devastating impact on the daily life is augmented by the fact that the available medication causes a weak, if any, improvement of cognitive deficits concerning attention, processing speed, working and long-term memory, executive function, and social cognition, despite (almost) complete resolution of psychotic symptoms³. The pathophysiological substrate of these deficits has been identified to center on the prefrontal-hippocampal network⁴⁵. Abnormal prefrontal-hippocampal coupling during working memory tasks has been described in schizophrenia patients^{4,6}. It relates not only to local alterations at microscopic and macroscopic scales in both areas⁷ but also to connectivity dysfunction within large-scale networks⁸. In particular, the interactions between HP and entorhinal cortex (EC), which tightly communicate with each other along reciprocal pathways⁹, have been tackled in clinical and neuropathological investigations^{10, 11, 12, 13}. While some findings are still controversial, cytoarchitectural disorganization, cellular and synaptic deficits in layer 2 as well as aberrant axonal innervation have been detected in the EC of schizophrenia patients^{14, 15}. It has been hypothesized that these deficits result from developmental disturbance of migration, differentiation and wiring of entorhinal circuits. However, their underlying mechanisms and contribution to the cognitive impairment are currently unknown.

Broader network dysconnectivity as underlying mechanism of cognitive deficits has been also identified in rodent models of psychiatric disorders^{16, 17, 18}. While these models vary in their etiology, utility and validity, they provide precious insights into the neural basis of cognitive deficits that are difficult to obtain in humans¹⁹, especially when considering areas poorly investigated and less accessible, such as LEC. LEC lesion caused disease-characteristic altered mesolimbic dopaminergic transmission^{20, 21}. Being a direct correlate of cognitive performance²², gamma oscillations within entorhinal-hippocampal circuits are disrupted in mouse models of psychiatric illness²³.

Besides providing insights into the neurobiological substrate of disease, mouse models enable to test the neurodevelopmental origin of illness-related deficits. Recently, we showed

that already during early postnatal development, the neuronal activity and communication between limbic brain areas are profoundly compromised in a mouse model mimicking the combined genetic (knock-down of Disrupted-In-Schizophrenia 1 (*Disc1*)²⁴) and environmental (maternal immune activation (MIA)) etiology (GE) of psychiatric risk^{25, 26, 27, 28}, but largely normal in single-hit genetic (G, DISC1 alone) or environmental (E, MIA alone) model²⁵. Weaker PFC-HP communication at neonatal age results from dysfunction of local pyramidal-interneuronal interactions as well as sparsification of hippocampal projections targeting the PFC^{28, 29, 30}. At this age, LEC boosts the prefrontal-hippocampal circuits by projecting to PFC and HP³¹ and facilitating their oscillatory entrainment³². However, an in-depth characterization of the LEC role for PFC-HP communication in disease models is currently lacking.

To address this knowledge gap, here we combine *in vivo* electrophysiology and optogenetics with anatomical tracing and behavioral investigation to interrogate the developing entorhinal-hippocampal-prefrontal circuits in the GE mouse model. We show that in neonatal GE mice, sparser and less efficient projections from LEC cause weaker activation of HP. On its turn, the HP fails to sufficiently entrain the PFC, yet the direct entorhinal projections to PFC are largely intact.

RESULTS

Pre-juvenile GE mice have poorer recognition memory

Poorer associative memory has been identified both in first episode and chronic schizophrenia patients³³. This memory form requires LEC but not the medial entorhinal cortex (MEC) integrity^{34, 35}. The strong LEC input to HP provides non-spatial (contextual) information and facilitates the binding of information relating to objects, places, and contexts. To get first insights into the LEC function towards the end of development, we assessed the associative recognition memory in mice of pre-juvenile age (postnatal day (P) 17-18). At this age, the mice already have fully developed sensory and motor abilities required for processing of novelty³⁶. Two tasks were used: (i) novel object preference (distinct objects) (NOPd) task that requires an object-object association in adult mice³⁴ and (ii) object-location preference (OLP) task that

involves an object-location association. To confirm that LEC is involved in the two tasks, we firstly performed cFos staining. The detected post-task strong cFos expression in the LEC of CON mice (supplementary Fig.1) was complemented by a second approach directly testing whether LEC was necessary for the tasks. We injected AAV9_CaMKII_hM4Di_EGFP in LEC of P1 CON mice. The neuronal activity in LEC was decreased by exposure to the DREADD agonist 21 (compound 21, C21) 45 mins before the NOPd task (P17) or OLP task (P18). After C21 injection, CON mice were not able to recognize the novelty in both NOPd and OLP test phases (supplementary Fig.2). These data show that LEC was not only involved in, but also necessary for these two tasks.

To test whether GE mice show poorer LEC-dependent associative recognition memory, we investigated CON and GE mice in NOPd and OLP tasks. During the familiarization trial of the NOPd task, all mice spent equal time investigating the two objects placed in the arena (Fig.1a). During the test trial, all mice spent longer time interacting with the novel object than with the familiar one (paired-sample t-test; CON: $n=20$, $5.25 \pm 0.31s$ vs. $2.13 \pm 0.21s$, $p=4.63e-12$, $df=19$, $t=-15.15$; GE: $n=14$, $3.81 \pm 0.42s$ vs. $1.93 \pm 0.24s$, $p=0.002$, $df=13$, $t=-3.86$) (Fig.1a). However, GE mice had a poorer object discrimination than CON mice (0.30 ± 0.07 vs. 0.44 ± 0.03 , one-way ANOVA, $F_{(1,32)}=4.27$, $p=0.047$). The behavioral impairment was absent in one-hit G and one-hit E mice (supplementary Fig.3a). During the OLP task, the pre-juvenile mice had to associate object and location and distinguish, which object was placed in a new location (Fig.1b). In the test trial, CON mice spent significantly longer time with the new location-object than with the old location-object ($n=19$, $5.79 \pm 1.19s$ vs. $2.22 \pm 0.25s$, $p=0.009$, $df=18$, $t=-2.94$, paired-sample t-test). GE mice spent comparable time with the two objects ($n=16$, $2.98 \pm 0.34s$ vs. $3.38 \pm 0.32s$, $p=0.35$, $df=15$, $t=-0.96$, paired-sample t-test). Correspondingly, the object discrimination was significantly lower in GE mice than in CON mice (0.03 ± 0.08 vs. 0.38 ± 0.05 , one-way ANOVA, $F_{(1,33)}=12.68$, $p=0.0011$). One-hit G and one-hit E mice were also unable to recognize the object with a new location (supplementary Fig.4b). These data reveal that, besides deficits in object, location and recency recognition that have been previously identified

in GE mice²⁵, the LEC-dependent recognition abilities are also impaired in pre-juvenile GE mice.

Poor performance in NOPd and OLP tasks may result not only specifically from dysfunction of entorhinal networks but also from poorer motor abilities and/or enhanced anxiety. To exclude these confounding effects, we analyzed the velocity of mice during familiarization and test trials of NOPd and OLP tasks (supplementary Fig.3). The motor abilities of both groups were comparable as reflected by the similar velocity in the arena. We also analyzed the exploratory behavior of mice in the open field (10 min) at P16. All animals spent most of the time in the outer circle of the arena close to the walls and the distance covered in the inner circle was comparable between the groups (CON: 250±48cm; GE: 278±51cm). These data suggest that GE mice were not more anxious than CON mice.

Taken together, these results indicate that already at pre-juvenile age the LEC-dependent associative recognition memory is impaired in GE mice. This cognitive deficit complements the previously reported poor performance in other non-associative recognition tasks^{25, 27, 28}.

The oscillatory entrainment of LEC within prefrontal-hippocampal networks is impaired in GE mice throughout development

The above reported behavioral deficits might result from the developmental disruption of LEC function. To directly address this hypothesis, we investigated the oscillatory and firing activity of LEC and its embedding into PFC-HP networks. For this, we performed multi-site extracellular recordings of local field potential (LFP) and multiple-unit activity (MUA) from LEC, simultaneously with the CA1 area of intermediate/ventral HP (i/vCA1) and prelimbic subdivision (PL) of PFC of urethane-anesthetized P20–23 CON, GE mice *in vivo* (Fig.2). All investigated mice showed similar patterns of continuous network activity, which covered a broad frequencies spectrum and correspond to sleep-like rhythms mimicked by urethane anesthesia^{37, 38, 39}. While the oscillatory power in LEC as well as PFC and HP was comparable in CON and GE mice (Fig.2a), the firing activity (i.e. averaged single unit activity (SUA), CON:

n=12, GE: n=10, Wilcoxon rank-sum test) was significantly increased in both entorhinal layer 5/6 (5.22 ± 0.94 vs. 2.62 ± 0.88 , $p=0.027$, $zval=-2.20$, $ranksum=104$) and layer 2/3 (6.30 ± 0.86 vs. 3.18 ± 0.98 , $p=0.013$, $zval=-2.47$, $ranksum=100$) as well as in stratum pyramidale of hippocampal CA1 area (5.79 ± 1.05 vs. 2.65 ± 0.69 , $p=0.019$, $zval=-2.34$, $ranksum=102$) in GE mice (Fig.2b). The prefrontal firing activity was also increased in GE mice, yet below significance threshold (layer 5/6: 6.65 ± 1.34 vs. 3.53 ± 1.49 , $p=0.07$, $zval=-1.81$, $ranksum=110$; layer 2/3, 6.56 ± 1.31 vs. 4.11 ± 1.49 , $p=0.18$, $zval=-1.35$, $ranksum=117$, Wilcoxon rank-sum test). To assess the information flow within entorhinal-hippocampal-prefrontal networks, we used the generalized partial directed coherence (gPDC), a measure that reflects the directionality of network interactions in different frequency bands (Fig.2c, Wilcoxon rank-sum test). The information flow of LEC->PFC (0.079 ± 0.002 vs. 0.103 ± 0.013 , $p=0.008$, $zval=2.65$, $ranksum=254$) and HP->PFC (0.077 ± 0.002 vs. 0.089 ± 0.005 , $p=0.005$, $zval=2.80$, $ranksum=257$) was significantly reduced in GE mice (n=11) when compared to CON mice (n=15). The information flow of LEC->HP was comparable between the two groups (0.108 ± 0.005 vs. 0.115 ± 0.010 , $p=0.87$, $zval=0.016$, $ranksum=206$).

In line with previous studies^{25, 27, 28}, firing and coupling deficits at pre-juvenile age might reflect abnormal circuit wiring initiated at earlier stages of development. To test this hypothesis, we investigated the activity patterns within entorhinal-hippocampal-prefrontal networks in neonatal (P8-10) CON (n=14) and GE (n=14) mice (Fig.3). Extracellular recordings of LFP and MUA showed that discontinuous spindle-shaped oscillations with frequency components peaking in theta band (4-12 Hz) intermixed with irregular low amplitude beta-gamma band components (12-30 Hz) were the dominant pattern of entorhinal network activity of both groups of mice (supplementary Fig.5). The discontinuous oscillatory events classified as spindle-bursts were superimposed on a slow rhythm (2-4 Hz) that continuously entrained the neonatal LEC and related to respiration⁴⁰. The occurrence and duration of discontinuous oscillatory events (4-30 Hz) were comparable in CON and GE mice (supplementary Fig.6a). However, their power was significantly smaller ($p=0.04$, $F_{(1,23)}=4.69$, one-way ANOVA) in GE mice (4.81 ± 0.63) than CON mice (11.04 ± 2.60) (Fig.3a). Given that single-hit E and G mice were

indistinguishable in their activity patterns from CON mice (supplementary Fig.6b), single-hit models were not considered for the rest of investigations. The diminished network activity in LEC was accompanied, as previously reported²⁵, by the dysfunction of network activity in both HP and PFC (Fig.3a). While the oscillatory power in LEC, PFC and HP was significantly reduced in GE mice, the firing activity (SUA) was comparable (Wilcoxon rank-sum test) in entorhinal layer 5/6 (0.53 ± 0.14 vs. 0.32 ± 0.08 , $p=0.54$, $zval=-0.62$, $ranksum=189$), entorhinal layer 2/3 (0.37 ± 0.12 vs. 0.19 ± 0.07 , $p=0.30$, $zval=-1.03$, $ranksum=180$), stratum pyramidale of hippocampal CA1 area (0.32 ± 0.10 vs. 0.45 ± 0.16 , $p=0.26$, $zval=1.13$, $ranksum=228$) as well as prefrontal layer 5/6 (0.11 ± 0.05 vs. 0.24 ± 0.08 , $p=0.18$, $zval=1.36$, $ranksum=233$) (Fig.3b). In line with previous data²⁵, the firing activity in prefrontal layer 2/3 was significantly reduced in GE mice (0.17 ± 0.04 vs. 0.48 ± 0.14 , $p=0.04$, $zval=1.98$, $ranksum=246$).

Next, we questioned whether the dampening of oscillatory activity in LEC, HP and PFC during early development related to communication deficits within the limbic networks. For this, we firstly assessed the coupling by synchrony between LEC and PFC-HP pathway in neonatal CON ($n=14$) and GE ($n=14$) mice by calculating the coherence of oscillatory events and considering only the imaginary part of it that was not corrupted by volume conductance⁴¹. A tight theta-beta band LEC-HP, HP-PFC coupling of spindle-bursts was detected in neonatal CON mice (Fig.3c). In contrast, the imaginary coherence was significantly lower in GE mice (LEC-HP, 4-20 Hz: 0.286 ± 0.016 vs. 0.334 ± 0.020 , $p=0.04$, $F_{(1, 26)}=4.45$; 20-40 Hz: 0.331 ± 0.018 vs. 0.397 ± 0.019 , $p=0.012$, $F_{(1, 26)}=7.12$; HP-PFC: 0.345 ± 0.013 vs. 0.284 ± 0.014 , $p=0.002$, $F_{(1, 26)}=11.340$, one-way ANOVA). The LEC-PFC coherence was much higher than the coherence calculated for the shuffled data in both CON and GE mice, yet no frequency-specific coupling was detected. In a second step, gPDC was used to assess the directionality of information flow within entorhinal-hippocampal-prefrontal networks. In CON mice, we confirmed the previously reported drive HP->PFC as well as the stronger information flow LEC->HP than LEC->PFC^{32, 42}. The drive LEC->HP was significantly decreased in GE mice (0.084 ± 0.006 vs. 0.105 ± 0.005 , $p=0.008$, $F_{(1, 26)}=8.39$, one-way ANOVA), which, besides the previously reported local dysfunction in HP and PFC, might further contribute to the reduced drive HP->PFC

(0.069 ± 0.004 vs. 0.094 ± 0.006 , $p=0.002$, $F_{(1, 26)}=12.04$, one-way ANOVA) (Fig.3d). The weak entorhinal drive to PFC was comparable in CON and GE mice.

Taken together, these results uncover the functional pathways of communication within neonatal limbic circuits with the LEC boosting the hippocampal activity in CON but not GE mice.

Spatially distinct entorhinal projections to HP and PFC are sparser in neonatal GE mice

One possible source of dysfunction within entorhinal-hippocampal-prefrontal circuits is the abnormal connectivity between these areas. We previously showed that already at the end of the first postnatal week hippocampal CA1 area strongly innervated the PFC, whereas no direct prefrontal projections targeted the HP. Moreover, we identified projections from LEC to HP as well as PFC in neonatal rats^{25, 42}. However, it is unknown, whether the same or distinct entorhinal populations innervate PFC and HP. To elucidate anatomical integration of LEC within the neonatal HP-PFC pathway, we injected the retrograde tracers CTB555 in HP and CTB488 in PFC of the same P7 mouse and monitored the projections after 3 days. CTB555 injection confined to i/vCA1 labeled cells mainly in layer 2/3 of LEC (Fig.4a). CTB488 injection confined to prelimbic-infralimbic subdivisions of the PFC labeled cells in the same layers, yet in a distinct, more superficial part; labeled neurons were detected also in i/vCA1, confirming the previously described hippocampal projection to PFC. There was no overlap between the CTB555 and CTB488 labeled neurons in the superficial layers of LEC, indicating that the entorhinal HP- and PFC-projecting neurons had a distinct spatial organization. Moreover, assessment of histological identity of entorhinal neurons revealed that CA1-projecting neurons were calbindin-positive, whereas PFC-projecting neurons were reelin-positive (supplementary Fig.7).

The substrate of decreased functional coupling within entorhinal-hippocampal-prefrontal networks in GE mice might be the sparser anatomical projections between the three areas. To test this hypothesis, we quantified the density of entorhinal HP- and PFC-projecting neurons in CON (n=6) and GE mice (n=5) (Fig.4b, c). The density of HP-projecting neurons was higher than the density of PFC-projecting neurons in both CON and GE mice. GE mice

showed a significantly ($p=0.005$, $F_{(1, 9)}=13.44$, one-way ANOVA) reduced density of HP-projecting neurons (1556.14 ± 132.40) but a similar ($p=0.87$, $F_{(1, 9)}=0.03$, one-way ANOVA) density of PFC-projecting neurons (784.26 ± 94.51) when compared with CON mice (2156.84 ± 123.05 , 761.99 ± 105.82).

Another source of dysfunction within entorhinal-hippocampal-prefrontal circuits in GE mice might represent the LEC neurons *per se* that, due to abnormal properties, are not able to provide the activation relayed to downstream areas. To test this hypothesis, we performed *in vitro* whole-cell patch-clamp recordings from entorhinal neurons that were either retrogradely labeled by CTB488/Fluorogold (PFC-projecting neurons) or CTB555 (HP-projecting neurons). The passive membrane properties (RMP, C_m , R_{in} , T_m) of PFC- as well as HP-projecting neurons were similar in CON (27 neurons from 10 mice) and GE (12 neurons from 5 mice) mice (Table 1). All investigated neurons showed linear I–V relationships and their firing increased in response to depolarizing current injection. The active membrane properties (i.e. action potential (AP) threshold, AP amplitude, half-width, Rheobase, firing frequency) of entorhinal neurons did not differ between CON and GE mice (Table 1). These results suggest that circuit dysfunction of GE mice does not mainly relate to cellular abnormalities of entorhinal PFC- and HP-projecting neurons.

Weaker responsiveness of HP to optogenetic activation of LEC in neonatal GE mice

To directly test the functional communication along axonal pathways within entorhinal-hippocampal-prefrontal networks, we monitored the responsiveness of the three areas to the activation of LEC. For this, we selectively transfected pyramidal neurons in LEC of CON ($n=11$) and GE ($n=13$) mice with a highly efficient fast-kinetics double mutant ChR2 (H134R) by micro-injections performed at P1 (Fig.5a, supplementary Fig.8, 9).

First, we assessed the firing probability induced by light stimulation in entorhinal pyramidal neurons *in vivo*. Blue light pulses (473 nm, 3 ms) at a frequency of 8 Hz led shortly (<10 ms) after the stimulus to precisely timed firing of transfected neurons in the LEC of both CON and GE mice (Fig.5b). The used light power did not cause local tissue heating that might

interfere with neuronal spiking (supplementary Fig.10)^{43, 44}. The light-induced firing probability was similar for both CON and GE groups (Fig.5b). From the second pulse on, the firing of neurons from both groups gradually lost the precise timing to the stimulus and the response reliability, most likely due to the immaturity of entorhinal neurons unable to fire at the set frequency. Pulsed light stimulation in LEC led to rhythmic firing in HP, yet not in PFC (Fig.5b). Quantification of the hippocampal light-induced firing probability revealed that CA1 neurons were reliably activated by light pulses in CON, yet not GE mice, most likely due to the reduced number of entorhinal HP-projecting neurons and the sparser entorhinal projections in HP (Fig.4, supplementary Fig.11).

Second, to decide whether LEC activation boosts information flow within entorhinal-hippocampal-prefrontal networks, we investigated the synchrony of the three areas upon light stimulation. Ramp light stimulation (3 s, 473 nm) that enabled neurons to fire at their preferred and not a set frequency, augmented the 10-20 Hz LEC-HP coherence (0.14 ± 0.05) but not LEC-PFC coherence (-0.01 ± 0.02) in CON mice (Fig.5c). Of note, frequency-specific boosting of HP through LEC activation caused an indirect augmentation of HP-PFC synchrony in CON mice (0.19 ± 0.06). In GE mice, the stimulation-induced LEC-HP coherence increase was of lower magnitude (0.04 ± 0.03 vs. 0.14 ± 0.05 , $p=0.049$, $F_{(1,22)}=4.10$) and consequently, not sufficient to augment HP-PFC synchrony (-0.03 ± 0.04).

Taken together, these results indicate that LEC has a critical role for the activation of HP that on its turn boosts the entrainment of PFC. In contrast, the direct impact of entorhinal activity on PFC is low, if any. The LEC-driven activation of HP in GE mice is much weaker, being not further relayed to PFC.

The function of entorhinal projections targeting the HP and PFC is selectively compromised in neonatal GE mice

To experimentally backup the results above, we monitored the function of entorhinal projections targeting either the PFC or the HP. In all investigated P8-10 mice ($n=24$), LEC projected to the prelimbic and infralimbic sub-divisions of PFC, where it mainly targeted layer

5/6 neurons (Fig.6a). Light stimulation (3 ms, 473 nm, 8 Hz) of terminals (Fig.6b) in PFC of ChR2-transfected entorhinal neurons was performed simultaneously with extracellular LFP and MUA recordings in layer 5/6 of PL. Activation of entorhinal terminals caused a pronounced short-delay LFP response with a post-stimulus peak at 15 ms and augmented the neuronal firing in PFC of both CON and GE mice. The light-induced firing probability in layer 5/6 was low and comparable for CON and GE mice (0.010 ± 0.001 vs. 0.009 ± 0.001 , $p=0.41$, $z_{\text{val}}=-2.045$, $\text{ranksum}=15917$, Wilcoxon rank-sum test) (Fig.6c). Only 15 out 138 (~10.87%) prefrontal neurons in CON mice and 11 out 108 (~10.19%) in GE mice increased their firing upon stimulation ($p=0.97$, $\text{chi}=0.013$, Chi-square test) (Fig.6e, f).

To investigate the entorhinal projections to HP, we injected both Fluorogold and WGA tracers in the LEC of CON mice (Fig.7a). The presence of WGA labeled hippocampal neurons indicate that already at neonatal age, entorhinal projections target the HP. In line with previous studies⁴⁵, these projections accumulate in stratum lacunosum (SLM) of CA1 area (Fig.7b). The density of these projections significantly differed between CON and GE mice (supplementary Fig.11). To test the function of entorhinal innervation of HP and whether the sparser projections in GE mice caused the network and neuronal deficits described above, we firstly performed patch-clamp recordings from visually-identified CA1 pyramidal neurons during light stimulation of entorhinal terminals in SLM *in vitro* (supplementary Fig.12). In coronal slices from P9-10 mice, blue light pulses evoked excitatory postsynaptic currents (eEPSCs). The eEPSCs had a short latency (<9 ms) from stimulus onset and a fast kinetics. They were fully abolished by ionotropic AMPA receptor antagonists NBQX (10 μM) and NMDA receptor antagonists AP5 (50 μM) added to the bath solution. In GE mice, less neurons responded to light stimulation than in CON mice (9/42 vs. 16/26, $p=0.0021$, $\text{chi}=9.45$, Chi-square test). Moreover, GE mice had smaller eEPSC amplitude than CON mice (19.59 ± 9.04 vs. 45.62 ± 7.11 pA, $p=0.0042$, $z_{\text{val}}=2.86$, $\text{ranksum}=259$, Wilcoxon rank-sum test) and showed a higher degree of variability upon stimulation as mirrored by the larger coefficient of variation (0.52 ± 0.073 vs. 0.22 ± 0.052 , $p=0.0016$, $F_{(1, 23)}=12.81$, One-way ANOVA). The kinetics of eEPSCs from GE mice was also disrupted, the events having a significantly longer rise-time decay when compared with those

from CON mice (4.65 ± 0.23 vs. 5.51 ± 0.36 ms, $p = 0.036$, $F_{(1, 23)} = 4.98$, One-way ANOVA). These results suggest that the entorhinal inputs on CA1 neurons are less efficient in GE mice.

Second, we performed multi-site recordings of LFP and MUA in CA1 area during pulsed and ramp light stimulation of entorhinal terminals in HP (Fig.7). The field response evoked by light pulses in HP had a fast (~ 15 ms) latency in all investigated mice, yet a smaller amplitude ($23.37 \pm 3.91 \mu\text{V}$, $p = 0.018$, $z_{\text{val}} = 2.36$, $\text{ranksum} = 155$, Wilcoxon rank-sum test) in GE mice than CON mice ($51.49 \pm 13.06 \mu\text{V}$) (Fig.7c). Current source density analysis (CSD) of light-evoked LFP response revealed the sink in stratum lacunosum of CA1 area (i.e. ~ 150 - $200 \mu\text{m}$ below stratum pyramidale) (Fig.7d). The light-induced hippocampal firing probability was significantly ($p = 2.88 \times 10^{-7}$, $z_{\text{val}} = 5.13$, $\text{ranksum} = 7184$, Wilcoxon rank-sum test) lower in GE mice (0.013 ± 0.003) than in CON mice (0.072 ± 0.019) (Fig.7e). This is in line with the lower ($p = 0.02$, $\text{chi} = 5.43$, Chi-square test) number of responsive hippocampal units in GE mice (8 out of 73, $\sim 11\%$) than in CON mice (22 out of 81, $\sim 27\%$) (Fig.7f, g). These results indicate that the function of entorhinal projections in HP is impaired in GE mice, their efficiency to boost the hippocampal activity being decreased.

If the function of entorhinal projections to PFC but not to HP is largely intact in GE mice, the question arises, whether the weaker entorhinal drive to HP is still sufficient to entrain the neural activity in PFC. Light activation of entorhinal terminals in HP (Fig.8a) led to an increase of neuronal firing both in layer 5/6 (1.33 ± 0.10) and layer 2/3 (1.16 ± 0.09) of PFC in CON mice (Fig.8b, c). In contrast, the stimulation has a significantly weaker, if any, effect in the PFC of GE mice (layer 5/6, 0.94 ± 0.06 , $p = 0.0010$, $z_{\text{val}} = 3.28$, $\text{ranksum} = 250$; layer 2/3: 0.94 ± 0.06 , $p = 0.04$, $z_{\text{val}} = 2.083$, $\text{ranksum} = 221$; Wilcoxon rank-sum test). Correspondingly, the prefrontal-hippocampal coupling augmented in CON mice during stimulation (0.09 ± 0.03), yet not in GE mice (-0.02 ± 0.004 , $p = 0.03$, $F_{(1, 25)} = 5.18$, one-way ANOVA, Fig.8d).

To directly assess the entorhinal role within neonatal limbic circuits, we tested whether the decreased drive LEC->HP in GE mice can be replicated by temporally precise inhibition of entorhinal terminals in HP in CON mice (Fig.9). For this, we capitalized on the recently developed tool, the targeting-enhanced mosquito homolog of the vertebrate encephalopsin

(eOPN3) that has been developed to selectively suppress neurotransmitter release at presynaptic terminals through the Gi/o signaling pathway⁴⁶. Pulsed (473 nm, 5 ms, 8 Hz) light stimulation of eOPN3-expressing LEC terminals in HP of CON mice (n=13) significantly (paired-sample t-test; $p=0.008$, $df=12$, $t=3.17$) reduced the HP power (-0.36 ± 0.09) that reached values comparable ($p=0.158$, $F_{(1,24)}=2.12$, One way ANOVA) to the hippocampal power reduction in GE mice when compared with CON mice (-0.20 ± 0.08). Moreover, the selective silencing of LEC terminals in HP caused power decrease in the PFC (-0.16 ± 0.04) that was significantly ($p=0.016$, $F_{(1,24)}=6.75$, One way ANOVA) smaller than the prefrontal power reduction in GE mice (-0.41 ± 0.09). This result suggests that a disrupted entorhinal-hippocampal communication is one, but not the unique cause of abnormal prefrontal activity in GE mice. Correspondingly, the PFC-HP coherence was reduced in CON mice during silencing of entorhinal terminals in HP (-0.23 ± 0.03), reaching comparable ($p=0.79$, $zval=-0.27$, $ranksum=176$) values to those calculated for GE mice (-0.24 ± 0.07) (Fig.9d).

Taken together, these results uncover that, while the sparse entorhinal projections to PFC seem to be structurally and functionally normal in GE mice, the entorhinal-hippocampal communication is impaired and has indirect effects on the prefrontal activity.

DISCUSSION

Mouse models mimicking the dual etiology of psychiatric risk, such as abnormal DISC1 function and immune challenge early in life, reproduce the neuronal network and, to a certain amount, behavioral deficits reported for patients. These deficits have been hypothesized to originate during development. Indeed, mice of an age corresponding to second-third gestational trimester in humans show prefrontal-hippocampal dysfunction^{25, 27, 28, 29}, supporting the hypothesis of developmental miswiring in schizophrenia. The present results uncover novel mechanisms of miswiring in the neonatal brain and highlight the critical role of the LEC for the function of prefrontal-hippocampal circuits. We show that in GE mice (i) the patterns of oscillatory activity and coupling within LEC-HP-PFC networks are disrupted already at neonatal age, the entorhinal drive on HP being particularly reduced, (ii) the substrate of

abnormal LEC-HP coupling is sparser entorhinal projections and their poorer efficiency to excite the HP, (iii) the direct entorhinal drive to PFC is largely unaffected, and (iv) the LEC-dependent recognition memory emerging at pre-juvenile age is impaired.

The EC represents a part of medial temporal lobe that is highly interconnected with the hippocampus and subcortical areas, such as the amygdala⁴⁷. Related to its function and input-output connectivity, the EC has been divided into MEC that is involved in spatial navigation and spatial memory (“Where”)⁴⁸ and LEC that codes context (“What”) and temporal (“When”) information^{49, 50}. In contrast to MEC, the LEC function has been less well dissected. It codes for object features and context-related locations, being critical for the performance in associative recognition memory of adults³⁴. LEC is also involved in olfactory processing, as witnessed by lesions studies of LEC that led to olfactory anterograde amnesia⁵¹ but also facilitation of olfactory recognition⁵². Information transfer through LEC-HP synchrony is critical for olfactory associative learning⁵³. Given the LEC function and its tight embedding into large-scale circuits, it is not surprising that LEC came into the focus when investigating the pathophysiology of major psychiatric illnesses. Clinical, post-mortem and imaging studies identified structural and synaptic deficits in LEC of schizophrenia and bipolar disorder patients^{15, 54, 55, 56}. However, the mechanisms of these deficits remain largely unknown. It has been hypothesized that they result from abnormal development of LEC.

The present study addresses this hypothesis and uncovers the functional deficits of LEC-HP circuits and related behavior during development. Under physiological conditions, the neonatal LEC facilitates the hippocampal activation. In line with the density of projections, the direct entorhinal drive to HP is stronger than to PFC. The LEC-PFC coupling might occur via 3 distinct pathways: (i) monosynaptic connection from LEC to PFC, (ii) bi-synaptic transmission through direct synaptic connection from LEC to HP neurons, which further directly project to PFC, and (iii) polysynaptic transmission through direct synaptic connection from LEC to HP neurons, which do not directly further project to PFC but through interplay with other hippocampal neurons. The anatomical investigation of projections and the double-tracing with WGA and CTB (supplementary fig. 13) showed that the pathways (i) and (ii), which would lead

to high LEC-PFC coherence, are very weak, whereas the most prominent pathway (iii) mirrors the low LEC-PFC coherence. The prominent indirect and weak direct pathways together ensure the necessary level of neonatal prefrontal excitation and oscillatory activation, which are mandatory for adult prefrontal-related behavior⁵⁷.

The present study might also be instrumental for answering the question how non-sensory cortices, such as PFC, generate early oscillatory activity. Spontaneous activity from the periphery travels along axonal projections via brainstem and thalamic nuclei and boosts the entrainment of developing visual, barrel or auditory cortices in oscillatory rhythms that facilitate the emergence of characteristic functional topographies^{58, 59}. Such mechanisms are irrelevant for early prefrontal oscillations; here, it seems that LEC drives the activation patterns. This mechanism is not fully decoupled from sensory inputs, since LEC receives direct inputs from the olfactory bulb (OB). The blind and deaf mouse pups that do not actively whisker at neonatal age have already adult-like olfactory abilities⁶⁰. The OB not only processes and forwards the odor information to LEC, but also spontaneously generates early oscillatory activity that activates LEC^{40, 61}. Therefore, at neonatal age, the entorhinal direct drive to HP as well as direct and indirect to PFC, is controlled by the olfactory system.

In GE mice, LEC-dependent associative memory is impaired already at pre-juvenile age. The network impairment at this age is rather mild. In contrast, a prominent dysfunction within neonatal entorhinal-hippocampal-prefrontal networks has been identified and might be compensated to a certain amount throughout the development (see normal oscillatory power). However, the abnormal firing rates and communication within pre-juvenile circuits attest to circuit miswiring taking place before this age. While at neonatal age the direct LEC-PFC communication was largely intact, the LEC-HP communication was weaker as result of sparser and reduced efficiency of axonal projections to excite the hippocampal neurons. The effects of these deficits were detectable also in the downstream area, the PFC. Even if the passive and active membrane properties of entorhinal HP-projecting neurons were largely unaffected in GE mice, the function of axonal projections to HP was impaired. The origin of this impairment is still unknown. One possible source might represent the dysfunction of local circuits in LEC.

The cytoarchitecture of neonatal LEC was normal, yet subtle migration and differentiation deficits cannot be excluded as possible mechanisms, especially when considering that *Disc1* gene represents an intracellular hub of developmental processes. Neurons in deep layers of LEC have abnormal passive and active properties (R. Kringel & I.L. Hanganu-Opatz, unpublished observations) that might perturb the intracortical entorhinal connectivity. Another source of entorhinal dysfunction might be weak upstream input due to olfactory deficits. Robust olfactory deficits have been identified in schizophrenia patients and at-risk youth⁶². The shrinkage of the OB and the resulting abnormal olfactory processing have been considered as a byproduct of an early developmental disturbance⁶³. Thus, it can be hypothesized that the LEC disturbance and downstream limbic circuitry, at least in part, the result of an early miswiring of olfactory system. Currently, investigations of olfactory processing of mouse models of disease are lacking. Their achievement might open new perspectives for mechanistic understanding of schizophrenia and in the end, for early diagnostic (i.e. biomarkers) and design of therapeutic strategies.

MATERIALS AND METHODS

Animal Models. All experiments were performed in compliance with the German laws and the guidelines of the European Community for the use of animals in research and were approved by the local ethical committee (015/17, 015/18). Timed-pregnant C57BL/6J mice from the animal facility of the University Medical Center Hamburg-Eppendorf were used. The day of vaginal plug detection was defined as gestational day (G) 0.5, whereas the day of birth was defined as postnatal day (P) 0. Multisite extracellular recordings and behavioral testing were performed on pups of both sexes during neonatal development (i.e. P8-P10) as well as during pre-juvenile development (i.e. P16-P23). Heterozygous genetically engineered mutant DISC1 mice carrying a *Disc1* allele (*Disc1*Tm1Kara) on a C57BL6/J background were used. Due to two termination codons and a premature polyadenylation site, the allele produces a truncated transcript⁶⁴. Genotypes were determined using genomic DNA and following primer sequences:

forward primer 5'-TAGCCACTCTCATTGTCAGC-3', reverse primer 5'-

CCTCATCCCTTCCACTCAGC-3'. Mutant DISC1 mice were challenged by MIA, using the viral mimetic poly I:C (5mg/kg) injected intravenously (i.v.) into the pregnant dams at gestational day G9.5. The resulting offspring mimicking the dual genetic-environmental etiology of mental disorders were classified as GE mice (DISC1 knock-down + MIA). The offspring of wild-type C57BL/6J dams injected at G9.5 with saline (0.9%, i.v.) were classified as CON mice (control).

Electrophysiological recordings in vivo. For neonatal recordings in non-anesthetized state, 0.5% bupivacain / 1% lidocaine was locally applied on the neck muscles. For pre-juvenile recordings under anesthesia, mice were injected intraperitoneally (i.p.) with urethane (1 mg/g body weight; Sigma-Aldrich, MO, USA) prior to surgery. For both age groups, under isoflurane anesthesia (induction: 5%, maintenance: 2.5%) the head of the pup was fixed into a stereotaxic apparatus using two plastic bars mounted on the nasal and occipital bones with dental cement. The bone above the PFC (0.5 mm anterior to bregma, 0.1-0.5 mm right to the midline), hippocampus (3.5 mm posterior to bregma, 3.5 mm right to the midline), LEC (4 mm posterior to bregma, 6 mm right to the midline) was carefully removed by drilling a hole of <0.5 mm in diameter. After a 10 min recovery period on a heating blanket, mouse was placed into the setup for electrophysiological recording. Throughout the surgery and recording session the mouse was positioned on a heating pad with the temperature kept at 37°C.

A four-shank optoelectrode (NeuroNexus, MI, USA) containing 4x4 recording sites (0.4-0.8 MΩ impedance, 100 μm spacing, 125 μm intershank spacing) was inserted into the PL of PFC. A one-shank optoelectrode (NeuroNexus, MI, USA) containing 1x16 recordings sites (0.4-0.8 MΩ impedance, 50 μm spacing) was inserted into CA1 area. A one-shank optoelectrode (NeuroNexus, MI, USA) containing 1x16 recordings sites (0.4-0.8 MΩ impedance, 100 μm spacing) was vertically inserted into LEC by placing them parallel to the pup's plane. An optical fiber ending 200 μm above the top recording site aligned with each recording shank. A silver wire was inserted into the cerebellum and served as ground and reference electrode. Extracellular signals were band-pass filtered (0.1-9,000 Hz) and digitized (32 kHz) with a multichannel extracellular amplifier (Digital Lynx SX; Neuralynx, Bozeman, MO,

USA) and the Cheetah acquisition software (Neuralynx). Spontaneous (i.e. not induced by light stimulation) activity was recorded for 20 min at the beginning of each recording session as baseline activity. The position of recording electrodes in the PL, CA1 area of i/vHP and LEC was confirmed post mortem. Wide field fluorescence images were acquired to reconstruct the recording electrode position in brain slices of electrophysiologically investigated pups. Only pups with correct electrode position were considered for further analysis. In PL, the most medial shank was inserted to target layer 2/3, whereas the most lateral shank was located into layer 5/6. For the analysis of hippocampal LFP, the recording site located in the pyramidal layer, where SPWs reverse⁶⁵ was selected to minimize any non-stationary effects of large amplitude events. For the analysis of LEC LFP, the recording site that 700 μm above the pyramidal layer of CA1 was selected.

Viral transfection in pyramidal neurons of LEC and light stimulation. Transfection of pyramidal neurons with a ChR2 derivative (100 nl), a targeting-enhanced mosquito homolog of the vertebrate encephalopsin (eOPN3, 50 nl) or hM4D was achieved by injecting the construct AAV9-CaMKII-ChR2(H134R)-mCherry (Addgene, Watertown, MA, USA), AAV9-CaMKII-eOPN3-mScarlet or AAV9-CaMKII-hM4D(Gi)-EGFP (Addgene, Watertown, MA, USA) at a titer $> 1 \times 10^{13}$ vg/mL in LEC on the right hemisphere of P1 pup, respectively. In line with pilot experiments using 50, 100, and 150 nl volume, the used volume of 100 nl led to reliable transfection of a large number of neurons confined to LEC. The pups were placed in a stereotactic apparatus and kept under anesthesia with isoflurane (induction: 5%, maintenance: 2.5%) for the entire procedure. A 10 mm incision of the skin on the head was performed with small scissors. The bone above the LEC was carefully removed using a syringe. The injection was achieved via a 10 μl microsyringe pump controller. The injection speed (0.05 $\mu\text{l}/\text{min}$) was slow with the maintenance of the syringe in place for at least 8 min. To stimulate ChR2-expressing neurons, pulsatile (laser on-off, pulse 3 ms-long, 8 Hz, 3 s-long) or ramp (linearly increasing power, 3 s-long) light stimulations were delivered with an arduino uno (Arduino, Italy) controlled diode laser (473 nm; Omicron, Austria). Laser power was adjusted to trigger neuronal spiking in response to $>25\%$ of 3 ms-long light pulses at 8 Hz. To stimulate eOPN3-

expressing axons, pulsatile (laser on-off, pulse 5 ms-long, 8 Hz, 4 s-long) light stimulations were performed with an arduino uno (Arduino, Italy) controlled diode laser (473 nm; Omicron, Austria). Resulting light power was in the range of 20-40 mW/mm² at the fiber tip (i.e. 3-5 mW/mm² at the probe tip). To chemogenetically inhibit LEC by activating hM4D, DREADD agonist 21 (C21) was i.p. injected (3 mg / kg body weight).

In vitro whole-cell patch-clamp recordings. Whole-cell patch-clamp recordings were performed from neurons identified by their location in the LEC and their projections to PFC (CTB488 / Fluorogold retrograde-labeled neurons) or HP (CTB555 retrograde-labeled neurons). All recordings were performed at room temperature. Recording electrodes (5–8MΩ) were filled with K-gluconate based solution containing (in mM):130 K-gluconate, 10 Hepes, 0.5 EGTA, 4Mg-ATP, 0.3Na-GTP, 8 NaCl (285 mosmol kg-1H₂O, pH 7.4) and 0.5% biocytin for post hoc morphological identification of recorded cells. Capacitance artefacts were minimized using the built-in circuitry of the patch-clamp amplifier (HEKA EPC 10, HEKA Elektronik, Germany). The signals were low-pass filtered at 10 kHz and recorded online. All potentials were corrected for the liquid junction potential of the gluconate-based electrode solution, which, according to own measurement, was –8.65 mV. The resting membrane potential (RMP) was measured immediately after obtaining the whole-cell configuration. For the determination of input resistance (R_{in}), membrane time constant (T_m) and membrane capacitance (C_m), hyperpolarizing current pulses (–60 pA) of 600 ms in duration were applied from the resting membrane potential. Firing frequency was assessed at a depolarizing current pulse of 100 pA at the same length of 600 ms. Analysis was performed offline using custom-written scripts in the MATLAB environment.

For patch-clamp recordings accompanied by optogenetic stimulation, whole-cell recordings were performed from neurons located in the CA1 area of the HP from P9 or P10 mice that underwent transfection of LEC with AAV9-CaMKII-ChR2(H134R)-mCherry at P1. Two coronal slices including the i/vHP were used per animal. All recordings were performed from pyramidal neurons that were identified according to their shape, spiking pattern, and action potential width. For optogenetic stimulation *in vitro*, 470-nm light pulses were applied with a CoolLED system

(pE-2) attached to the upright microscope. Maximal light output at 470 nm was measured at 10 mW/mm² with optical power meter (Thorlabs, NJ, USA). For stimulation of entorhinal afferents targeting CA1 neurons, light was centered on the stratum lacunosum-moleculare (~150-200 μ m below the stratum pyramidale) and light pulses (10 ms, 15 s interval) were repetitively applied for up to 20 times. To block AMPA and NMDA receptors, 10 μ M 6-cyano-7-nitroquinoxaline-2, 3-dione (NBQX) and 50 μ M amino-5-phosphonovaleric acid (AP5) were added to the bath solution.

Light-evoked EPSCs (eEPSCs) were averaged over 20 stimuli. Their peak amplitude, onset (i.e. delay between light stimulus and time point at which the response speed exceeded 10 pA/ms) and rise-time were calculated. The coefficient of variation (CV) for a given measured variable was defined as the ratio between the standard deviation and the average value of 20 individual responses to light stimulation.

Behavioral protocols. The exploratory behavior and recognition memory of CON and GE mice were tested at pre-juvenile age using previously established experimental protocols⁶⁶. Briefly, all behavioral tests were conducted in a custom-made circular white arena, the size of which (D: 34 cm, H: 30 cm) maximized exploratory behavior, while minimizing incidental contact with testing objects⁶⁷. The objects used for testing of associative recognition were six differently shaped, textured and colored, easy to clean items that were provided with magnets to fix them to the bottom of the arena. Object sizes (H: 3 cm, diameter: 1.5-3 cm) were smaller than twice the size of the mouse and did not resemble living stimuli (no eye spots, predator shape). The objects were positioned at 10 cm from the borders and 8 cm from the center of the arena. After every trial the objects and arena were cleaned with 0.1 % acetic acid to remove all odors. A black and white CCD camera (VIDEOR TECHNICAL E. Hartig GmbH, Roedermark, Germany) was mounted 100 cm above the arena and connected to a PC via PCI interface serving as frame grabber for video tracking software (Video Mot2 software, TSE Systems GmbH, Bad Homburg, Germany).

Exploratory behavior in the open field. Pre-juvenile mice (P16) were allowed to freely explore the testing arena for 10 min. Additionally, the floor area of the arena was digitally subdivided in 8 zones (4 center zones and 4 border zones) using the zone monitor mode of the VideoMot 2 analysis software (VideoMot 2, TSE Systems GmbH). The time spent by pups in center and border zones, as well as the running distance and velocity was quantified.

Novel object preference (distinct objects) (NOPd) and object-location preference (OLP) tasks. All protocols for assessing associative recognition memory in P17 (NOPd) and P18 (OLP) mice consisted of familiarization and test trials. During the familiarization trial each mouse was placed into the arena containing two different objects and released with the back to the objects. After 10 min of free exploration of objects the mouse was returned to a temporary holding cage. Subsequently, the test trial was performed after a delay of 5 min post-familiarization. In NOPd task, the mice were allowed to investigate one familiar and one novel object with a different shape and texture for 5 min. The nature of this test is similar to the novel object preference test, except that the test trial involves an association between two different objects (an association of object-object). In OLP task, the mice were allowed to investigate one familiar and a copy of the old object that was previously presented for 5 min. This test examines whether animals recognize the location that was once occupied by a particular object (an association of object-location). Object interaction during the first 4 min was analyzed and compared between the groups. All trials were video-tracked and the analysis was performed using the Video Mot2 analysis software. The object recognition module of the software was used and a 3-point tracking method identified the head, the rear end and the center of gravity of the mouse. Digitally, a circular zone of 1.5 cm was created around each object and every entry of the head point into this area was considered as object interaction. Climbing or sitting on the object, mirrored by the presence of both head and center of gravity points within the circular zone, were not counted as interactions. Mice with low level of exploration (i.e. <20 cm/min) were excluded from further analysis. The discrimination index was defined as (time at novel object - time at old object) / time at both objects for NOPd and (time at displaced object - time at stationary object) / time at both objects for OLP.

cFos expression in mouse doing NOPd or OLP task. P16 CON mice were randomly divided into 4 groups (n=4 mice / group). The mice were allowed to freely explore the arena containing two different objects for 10 mins. This familiarization process continued for 3 days with 2 trials per day. On the third day (P18), 5 mins after the last familiarization trial, 3 mice from two groups were signed to perform the test trial (5 mins) of NOPd task, whereas one mouse to perform the familiarization trial. Similarly, for the other 2 groups, 3 mice were assigned to perform the test trial (5 mins) of OLP task and one mouse to perform the familiarization trial. The mice were perfused ~90 min after the last behavioral trial.

Retrograde tracing. For retrograde tracing, P7 mice received retrograde tracer CTB555 (Cholera Toxin Subunit B, Alexa Fluor 455 Conjugate) injections into HP (0.7mm anterior from the lambda, 2.4 mm from midline, 1.6 mm depth), and CTB488 (Cholera Toxin Subunit B, Alexa Fluor 488 Conjugate) injections into PFC (0.7mm anterior from to bregma, 0.1 mm from midline, 1.9 mm depth). The pups were placed in a stereotactic apparatus and kept under anesthesia with isoflurane (induction: 5%, maintenance: 2.5%) for the entire procedure. A 10 mm incision of the skin on the head was performed with small scissors. The bone above the HP and PFC was carefully removed using a syringe. A total volume of 0.1 μ l of CTB (2.5% in PBS) was delivered via a 10 μ l microsyringe pump controller into PFC or HP. The slow injection speed (0.05 μ l/min) and the maintenance of the syringe in place for at least 8 min ensured an optimal diffusion of the tracer. The pups were perfused at P10.

Anterograde tracing. To locate the innervated neurons in PFC by LEC, anterograde trans-synaptic tracer wheat germ agglutinin (WGA) (Thermo Fisher Scientific, USA) was used. To locate the LEC innervated neurons in HP, the mixed WGA and Fluorogold solution was used. Mice were injected at P8 with WGA unilaterally into LEC. A total volume of 0.1 μ l of WGA (2.5% in PBS) was delivered via a 10 μ l microsyringe pump controller. The slow injection speed (0.05 μ l/min) and the maintenance of the syringe in place for at least 8 min ensured an optimal diffusion of the tracer. 40 hours after the injection, the pups were perfused.

Histology and staining protocols. Histological procedures were performed as previously described^{26, 27}. Briefly, P8-10 and P18-23 mice were anesthetized with 10% ketamine (aniMedica) / 2% xylazine (WDT) in 0.9% NaCl solution (10 µg/g body weight, i.p.) and transcardially perfused with Histofix (Carl Roth) containing 4% paraformaldehyde. Brains were postfixed in Histofix for 24 h and sectioned coronally at 50 µm (immunohistochemistry) or 100 µm (quantification for CTB labeled neurons). Free-floating slices were permeabilized and blocked with PBS containing 0.8 % Triton X 100 (Sigma-Aldrich, MO, USA), 5% normal bovine serum (Jackson Immuno Research, PA, USA) and 0.05% sodium azide. For cFos staining, slices were incubated with mouse monoclonal Alexa Fluor-555 conjugated antibody against cFos (1:200, MAB377X, Merck Millipore, MA, USA), followed by 2h incubation with Alexa Fluor-488 goat anti-rabbit IgG secondary antibody (1:500, A11008, Merck Millipore, MA). For BDA staining, slices were incubated with streptavidin (Cy3, 1:500, ThermoFisher). For WGA staining, slices were incubated with goat anti-WGA IgG (1:500), followed by 2h incubation with Alexa Fluor-488 goat anti-rabbit IgG secondary antibody (1:500, A11008, Merck Millipore, MA). Slices were transferred to glass slides and covered with Fluoromount (Sigma-Aldrich, MO, USA). Wide-field fluorescence images were acquired to reconstruct the recording electrode position.

Quantification of cFos, CTB488, CTB555, WGA labeled neurons. All quantifications were carried out blind to the experimental condition. Using a light microscope, photographs of the relevant areas (LEC for cFos, CTB488, CTB555; PFC for WGA) were taken with a consistent light level (Olympus FX-100). 3~4 slices per animal were used (supplementary table.1). Sections were collected in three equally spaced series. To reduce the redundancy of information in neighboring slices, only one of the series was mounted or used for subsequent staining and analysis. Images were processed using ImageJ software. The number of cFos positive neurons, CTB488 positive neurons, CTB555 positive neurons and WGA positive neurons were counted manually in the interested regions.

Quantification of mCherry-labeled axons. High magnification images were acquired by confocal microscopy (DM IRBE, Leica Microsystems, Zeiss LSN700) from stratum lacunosum-moleculare of CA1 to quantify LEC axonal terminals labeled by BDA. Microscopic stacks were acquired as 2048x2048 pixel images (pixel size, 78 nm; Z-step, 500 nm). All images were similarly processed and analyzed using ImageJ software.

Data Analysis. Data were imported and analyzed offline using custom-written tools in Matlab software version 7.7 (Mathworks). The data were processed as following: (i) band-pass filtered (500-5000 Hz) to detect MUA as negative deflections exceeding five times the standard deviation of the filtered signals and (ii) low-pass filtered (<1500 Hz) using a third order Butterworth filter before downsampling to 1000 Hz to analyze the LFP. All filtering procedures were performed in a phase-preserving manner. The position of Dil-stained recording electrodes in PL (most medial shank confined to layer 2/3, most temporal shank confined to layer 5/6), CA1 and LEC was confirmed post-mortem by histological evaluation. Additionally, electrophysiological features (i.e. reversal of LFP and high MUA frequency over stratum pyramidale of CA1) were used for confirmation of the exact recording position in HP.

Detection of neonatal oscillatory activity. Discontinuous oscillatory events were detected using a previously developed unsupervised algorithm⁶⁸ and confirmed by visual inspection. Briefly, deflections of the root-mean-square of band-pass (3-100 Hz) filtered signals exceeding a variance-dependent threshold were assigned as network oscillations. The threshold was determined by a Gaussian fit to the values ranging from 0 to the global maximum of the root-mean-square histogram. Only oscillatory events >1 s were considered for further analysis. Time-frequency plots were calculated by transforming the data using the Morlet continuous wavelet.

Power spectral density. For power spectral density analysis, 1 s-long window of network oscillations were concatenated and the power was calculated using Welch's method with non-overlapping windows. For optical stimulation, we compared the average power during the 1.5

s-long time window preceding the stimulation to the last 1.5 s-long time window of light-evoked activity.

Single unit activity (SUA). SUA was detected and clustered using klusta (Rossant et al., 2016) and manually curated using phy (<https://github.com/cortex-lab/phy>). Data were imported and analyzed using custom-written tools in the MATLAB. Spikes occurring in a 20 ms-long time window after the start of a light pulse were considered to be light-evoked. Light-evoked spiking was calculated as the probability of at least one spike occurring in this period.

Firing rate. Single units were sorted using klusta described above. Spikes from all clustered units were summed up for each mouse. The firing rate was calculated for each animal by dividing the total number of spikes by the duration of the analyzed time window.

Spectral coherence. Co-occurring oscillatory activities were detected and extracted before coherence was calculated. Coherence was calculated using the coherence method. Briefly, the coherence was calculated (using the functions *cpsd.m* and *pwelch.m*) by cross-spectral density between the two signals and normalized by the power spectral density of each. The computation of the coherence C over frequency (f) for the power spectral density P of signal X and Y was performed according to the formula:

$$C_{XY}(f) = \left| \left(\frac{P_{XY}(f)}{\sqrt{P_{XX}(f)P_{YY}(f)}} \right) \right|$$

Directionality methods. To investigate the directionality of functional connectivity between PFC and HP, gPDC was used. gPDC is based on linear Granger causality measure in the frequency domain. The method attempts to describe the causal relationship between multivariate time series based on the decomposition of multivariate partial coherence computed from multivariate autoregressive models. The LFP signal was divided into 1s-long segments containing the oscillatory activity. After de-noising using Matlab wavelet toolbox, gPDC was calculated using a previously described algorithm^{69, 70}.

Estimation of light propagation. The spatial pattern of light propagation *in vivo* was estimated using a previously developed model⁴⁴ based on Monte Carlo simulation (probe parameters: light fiber diameter: 50 μm , numerical aperture: 0.22, light parameters: 594 nm, 0.6 mW).

Statistical analysis. Statistical analyses were performed in Matlab environment. Data were tested for normal distribution using the Kolmogorov-Smirnov test. Paired t-test or one-way ANOVA was performed to detect significant differences when the variance was normally distributed. Otherwise, non-parametric Wilcoxon rank sum test was used. Investigators were blinded to the group allocation when the quantifications of cFos expression, CTB488 and CTB555 positive neurons in LEC, and WGA positive neurons in PFC were performed. Chi-square test was used to detect the significance difference between two proportions. Data are presented as mean \pm sem. Significance levels of $p < 0.05$ (*), $p < 0.01$ (**) or $p < 0.001$ (***) were tested. Statistical parameters can be found in the main text.

Data availability

The data supporting the findings of this study is available with the article and its Supplementary Information file, or is available from the corresponding author upon request. Source data are provided with this paper.

Code availability

All the codes used in the current study are available from the corresponding author upon request.

References

1. van Os J, Kenis G, Rutten BPF. The environment and schizophrenia. *Nature* **468**, 203-212 (2010).
2. Howes OD, Murray RM. Schizophrenia: an integrated sociodevelopmental-cognitive model. *Lancet* **383**, 1677-1687 (2014).
3. Goldberg AD, Allis CD, Bernstein E. Epigenetics: A Landscape Takes Shape. *Cell* **128**, 635-638 (2007).
4. Meyer-Lindenberg A, *et al.* Neural correlates of genetically abnormal social cognition in Williams syndrome. *Nat Neurosci* **8**, 991-993 (2005).
5. Bähner F, Meyer-Lindenberg A. Hippocampal–prefrontal connectivity as a translational phenotype for schizophrenia. *Eur Neuropsychopharmacol* **27**, 93-106 (2017).
6. Rasetti R, Sambataro F, Chen Q, Callicott JH, Mattay VS, Weinberger DR. Altered Cortical Network Dynamics: A Potential Intermediate Phenotype for Schizophrenia and Association With ZNF804A. *Arch Gen Psychiatry* **68**, 1207-1217 (2011).
7. Meyer-Lindenberg A. From maps to mechanisms through neuroimaging of schizophrenia. *Nature* **468**, 194-202 (2010).
8. Kupferschmidt DA, Gordon JA. The dynamics of disordered dialogue: Prefrontal, hippocampal and thalamic miscommunication underlying working memory deficits in schizophrenia. *BNA* **2**, 2398212818771821 (2018).
9. Nilssen ES, Doan TP, Nigro MJ, Ohara S, Witter MP. Neurons and networks in the entorhinal cortex: A reappraisal of the lateral and medial entorhinal subdivisions mediating parallel cortical pathways. *Hippocampus* **29**, 1238-1254 (2019).
10. Arnold PJ. Dimensional Standardization and Production Scale in Mesoamerican Ceramics. *Lat Am Antiq* **2**, 363-370 (1991).
11. Arnold SE. Cellular and Molecular Neuropathology of the Parahippocampal Region in Schizophrenia. *Ann N Y Acad Sci* **911**, 275-292 (2000).
12. Baiano M, *et al.* Decreased entorhinal cortex volumes in schizophrenia. *Schizophr Res* **102**, 171-180 (2008).
13. Akil M, Lewis DA. Cytoarchitecture of the entorhinal cortex in schizophrenia. *Am J Psychiatry* **154**, 1010-1012 (1997).
14. Hemby SE, Ginsberg SD, Brunk B, Arnold SE, Trojanowski JQ, Eberwine JH. Gene Expression Profile for Schizophrenia: Discrete Neuron Transcription Patterns in the Entorhinal Cortex. *Arch Gen Psychiatry* **59**, 631-640 (2002).
15. Falkai P, Schneider-Axmann T, Honer WG. Entorhinal cortex pre-alpha cell clusters in schizophrenia: quantitative evidence of a developmental abnormality. *Biol Psychiatry* **47**, 937-943 (2000).

16. Bolkan SS, *et al.* Thalamic projections sustain prefrontal activity during working memory maintenance. *Nat Neurosci* **20**, 987-996 (2017).
17. Parnaudeau S, *et al.* Inhibition of Mediodorsal Thalamus Disrupts Thalamofrontal Connectivity and Cognition. *Neuron* **77**, 1151-1162 (2013).
18. Chun S, *et al.* Specific disruption of thalamic inputs to the auditory cortex in schizophrenia models. *Science* **344**, 1178-1182 (2014).
19. Insel TR. Rethinking schizophrenia. *Nature* **468**, 187-193 (2010).
20. Sumiyoshi T, *et al.* Enhanced locomotor activity in rats with excitotoxic lesions of the entorhinal cortex, a neurodevelopmental animal model of schizophrenia: Behavioral and in vivo microdialysis studies. *Neurosci Lett* **364**, 124-129 (2004).
21. Meyer F, Peterschmitt Y, Louilot A. Postnatal functional inactivation of the entorhinal cortex or ventral subiculum has different consequences for latent inhibition-related striatal dopaminergic responses in adult rats. *Eur J Neurosci* **29**, 2035-2048 (2009).
22. Fell J, *et al.* Human memory formation is accompanied by rhinal–hippocampal coupling and decoupling. *Nat Neurosci* **4**, 1259-1264 (2001).
23. Cunningham MO, *et al.* Region-Specific Reduction in Entorhinal Gamma Oscillations and Parvalbumin-Immunoreactive Neurons in Animal Models of Psychiatric Illness. *J Neurosci* **26**, 2767 (2006).
24. Brandon NJ, Sawa A. Linking neurodevelopmental and synaptic theories of mental illness through DISC1. *Nat Rev Neurosci* **12**, 707-722 (2011).
25. Hartung H, *et al.* From Shortage to Surge: A Developmental Switch in Hippocampal–Prefrontal Coupling in a Gene–Environment Model of Neuropsychiatric Disorders. *Cereb Cortex* **26**, 4265-4281 (2016).
26. Oberlander VC, Xu X, Chini M, Hanganu-Opatz IL. Developmental dysfunction of prefrontal–hippocampal networks in mouse models of mental illness. *Eur J Neurosci* **50**, 3072-3084 (2019).
27. Xu X, Chini M, Bitzenhofer SH, Hanganu-Opatz IL. Transient Knock-Down of Prefrontal DISC1 in Immune-Challenged Mice Causes Abnormal Long-Range Coupling and Cognitive Dysfunction throughout Development. *J Neurosci* **39**, 1222 (2019).
28. Xu X, Song L, Hanganu-Opatz IL. Knock-Down of Hippocampal DISC1 in Immune-Challenged Mice Impairs the Prefrontal–Hippocampal Coupling and the Cognitive Performance Throughout Development. *Cereb Cortex* **31**, 1240-1258 (2021).
29. Chini M, *et al.* Resolving and Rescuing Developmental Miswiring in a Mouse Model of Cognitive Impairment. *Neuron* **105**, 60-74.e67 (2020).
30. Comer AL, *et al.* Increased expression of schizophrenia-associated gene C4 leads to hypoconnectivity of prefrontal cortex and reduced social interaction. *PLoS Biol* **18**, e3000604 (2020).

31. Jones BF, Witter MP. Cingulate cortex projections to the parahippocampal region and hippocampal formation in the rat. *Hippocampus* **17**, 957-976 (2007).
32. Hartung H, Brockmann MD, Pöschel B, De Feo V, Hanganu-Opatz IL. Thalamic and Entorhinal Network Activity Differently Modulates the Functional Development of Prefrontal–Hippocampal Interactions. *J Neurosci* **36**, 3676 (2016).
33. Mathew I, et al. Medial Temporal Lobe Structures and Hippocampal Subfields in Psychotic Disorders: Findings From the Bipolar-Schizophrenia Network on Intermediate Phenotypes (B-SNIP) Study. *JAMA Psychiatry* **71**, 769-777 (2014).
34. Wilson DIG, Watanabe S, Milner H, Ainge JA. Lateral entorhinal cortex is necessary for associative but not nonassociative recognition memory. *Hippocampus* **23**, 1280-1290 (2013).
35. Staresina BP, Reber TP, Niediek J, Boström J, Elger CE, Mormann F. Recollection in the human hippocampal-entorhinal cell circuitry. *Nat Commun* **10**, 1503 (2019).
36. Krüger H-S, Brockmann MD, Salamon J, Ittrich H, Hanganu-Opatz IL. Neonatal hippocampal lesion alters the functional maturation of the prefrontal cortex and the early cognitive development in pre-juvenile rats. *Neurobiol Learn Mem* **97**, 470-481 (2012).
37. Wolansky T, Clement EA, Peters SR, Palczak MA, Dickson CT. Hippocampal Slow Oscillation: A Novel EEG State and Its Coordination with Ongoing Neocortical Activity. *J Neurosci* **26**, 6213 (2006).
38. Clement EA, Richard A, Thwaites M, Ailon J, Peters S, Dickson CT. Cyclic and Sleep-Like Spontaneous Alternations of Brain State Under Urethane Anaesthesia. *PLOS ONE* **3**, e2004 (2008).
39. Pagliardini S, Gosgnach S, Dickson CT. Spontaneous Sleep-Like Brain State Alternations and Breathing Characteristics in Urethane Anesthetized Mice. *PLOS ONE* **8**, e70411 (2013).
40. Gretenkord S, et al. Coordinated electrical activity in the olfactory bulb gates the oscillatory entrainment of entorhinal networks in neonatal mice. *PLoS Biol* **17**, e2006994 (2019).
41. Nolte G, Bai O, Wheaton L, Mari Z, Vorbach S, Hallett M. Identifying true brain interaction from EEG data using the imaginary part of coherency. *Clin Neurophysiol* **115**, 2292-2307 (2004).
42. Brockmann Marco D, Pöschel B, Cichon N, Hanganu-Opatz Ileana L. Coupled Oscillations Mediate Directed Interactions between Prefrontal Cortex and Hippocampus of the Neonatal Rat. *Neuron* **71**, 332-347 (2011).

43. Bitzenhofer SH, Ahlbeck J, Hanganu-Opatz IL. Methodological Approach for Optogenetic Manipulation of Neonatal Neuronal Networks. *Front Cell Neurosci* **11**, 239 (2017).
44. Stujenske JM, Spellman T, Gordon JA. Modeling the Spatiotemporal Dynamics of Light and Heat Propagation for In Vivo Optogenetics. *Cell Rep* **12**, 525-534 (2015).
45. Kitamura T, Macdonald CJ, Tonegawa S. Entorhinal-hippocampal neuronal circuits bridge temporally discontinuous events. *Learn Mem* **22**, 438-443 (2015).
46. Mahn M, et al. Efficient optogenetic silencing of neurotransmitter release with a mosquito rhodopsin. *Neuron* **109**, 1621-1635.e1628 (2021).
47. Witter MP, Wouterlood FG, Naber PA, Van Haeften T. Anatomical Organization of the Parahippocampal-Hippocampal Network. *Ann N Y Acad Sci* **911**, 1-24 (2000).
48. Moser EI, Moser M-B, McNaughton BL. Spatial representation in the hippocampal formation: a history. *Nat Neurosci* **20**, 1448-1464 (2017).
49. Tsao A, et al. Integrating time from experience in the lateral entorhinal cortex. *Nature* **561**, 57-62 (2018).
50. Wang C, et al. Egocentric coding of external items in the lateral entorhinal cortex. *Science* **362**, 945-949 (2018).
51. Staubli U, Fraser D, Kessler M, Lynch G. Studies on retrograde and anterograde amnesia of olfactory memory after denervation of the hippocampus by entorhinal cortex lesions. *Behav Neural Biol* **46**, 432-444 (1986).
52. Wirth S, Ferry B, Di Scala G. Facilitation of olfactory recognition by lateral entorhinal cortex lesion in rats. *Behav Brain Res* **91**, 49-59 (1998).
53. Igarashi KM, Lu L, Colgin LL, Moser M-B, Moser EI. Coordination of entorhinal-hippocampal ensemble activity during associative learning. *Nature* **510**, 143-147 (2014).
54. Bachus SE, Hyde TM, Herman MM, Egan MF, Kleinman JE. Abnormal cholecystokinin mRNA levels in entorhinal cortex of schizophrenics. *J Psychiatr Res* **31**, 233-256 (1997).
55. Benes FM, Berretta S. GABAergic Interneurons: Implications for Understanding Schizophrenia and Bipolar Disorder. *Neuropsychopharmacology* **25**, 1-27 (2001).
56. Pantazopoulos H, Lange N, Baldessarini RJ, Berretta S. Parvalbumin Neurons in the Entorhinal Cortex of Subjects Diagnosed With Bipolar Disorder or Schizophrenia. *Biol Psychiatry* **61**, 640-652 (2007).
57. Bitzenhofer SH, Pöplau JA, Chini M, Marquardt A, Hanganu-Opatz IL. Transient developmental increase of prefrontal activity alters network maturation and causes cognitive dysfunction in adult mice. *Neuron* **109**, 1350-1364, (2020).

58. Khazipov R, Sirota A, Leinekugel X, Holmes GL, Ben-Ari Y, Buzsáki G. Early motor activity drives spindle bursts in the developing somatosensory cortex. *Nature* **432**, 758-761 (2004).
59. Hanganu IL, Ben-Ari Y, Khazipov R. Retinal Waves Trigger Spindle Bursts in the Neonatal Rat Visual Cortex. *J Neurosci* **26**, 6728 (2006).
60. Welker W. Analysis of Sniffing of the Albino Rat. *Behaviour* **22**, 223-224 (1964).
61. Kostka JK, Gretenkord S, Spehr M, Hanganu-Opatz IL. Bursting mitral cells time the oscillatory coupling between olfactory bulb and entorhinal networks in neonatal mice. *J Physiol* **598**, 5753-5769 (2020).
62. Moberg PJ, *et al.* Meta-Analysis of Olfactory Function in Schizophrenia, First-Degree Family Members, and Youths At-Risk for Psychosis. *Schizophr Bull* **40**, 50-59 (2014).
63. Turetsky BI, *et al.* Structural anomalies of the peripheral olfactory system in psychosis high-risk subjects. *Schizophr Res* **195**, 197-205 (2018).
64. Kvajo M, *et al.* A mutation in mouse *Disc1* that models a schizophrenia risk allele leads to specific alterations in neuronal architecture and cognition. *PNAS* **105**, 7076-7081 (2008).
65. Bitzenhofer SH, Hanganu-Opatz IL. Oscillatory coupling within neonatal prefrontal-hippocampal networks is independent of selective removal of GABAergic neurons in the hippocampus. *Neuropharmacology* **77**, 57-67 (2014).
66. Kruger HS, Brockmann MD, Salamon J, Ittrich H, Hanganu-Opatz IL. Neonatal hippocampal lesion alters the functional maturation of the prefrontal cortex and the early cognitive development in pre-juvenile rats. *Neurobiol Learn Mem* **97**, 470-481 (2012).
67. Heyser CJ, Ferris JS. Object exploration in the developing rat: methodological considerations. *Dev Psychobiol* **55**, 373-381 (2013).
68. Cichon NB, Denker M, Grun S, Hanganu-Opatz IL. Unsupervised classification of neocortical activity patterns in neonatal and pre-juvenile rodents. *Front Neural Circuits* **8**, 50 (2014).
69. Baccala LA, Sameshima K. Partial directed coherence: a new concept in neural structure determination. *Biol Cybern* **84**, 463-474 (2001).
70. Baccala LA, Sameshima K, Takahashi DY. Generalized Partial Directed Coherence. In: *2007 15th International Conference on Digital Signal Processing* (2007).

Acknowledgements

We thank Dr. Joseph Gogos for providing the DISC1 mice and Dr. Simon Wiegert for providing AAV9-CaMKII-eOPN3-mScarlet. We also thank A. Marquardt, C. Tietze, A. Dahmann, and P. Putthoff for excellent technical assistance. This work was funded by grants from the European Research Council (ERC-2015-CoG 681577 to I.L.H.-O.), the German Research Foundation (SFB 936 B5 and Ha4466/11-1 to I.L.H.-O), Marie Curie Training Network euSNN (MSCA-ITN-H2020-860563 to I.L.H.-O), Horizon 2020 DEEPER 101016787 (to I.L.H.-O.) and Landesforschungsförderung Hamburg (LFF76, LFF73 to I.L. H.-O.).

Author contributions

I.L.H.-O., X.X. designed the experiments, X.X., L.S., and R.K carried out the experiments, X.X. analyzed the data, I.L.H.-O. and X.X. interpreted the data and wrote the paper. All authors discussed and commented on the manuscript.

Competing interests

The authors declare no competing financial interests.

Figure legends

Figure 1. The performance of pre-juvenile GE mice in associative recognition memory tasks. (a) Left, schematic of the protocol for NOPd task. Middle, violin plots displaying the interaction time (/min) spent by CON and GE with the objects during familiarization and test trials. Right, violin plots displaying the discrimination ratio in test trials (right). (b) Same as (a) for OLP task. In (a) and (b), black dotted line indicates chance level. For violin plots, black and red dots correspond to individual animals and the red horizontal lines display the median as well as 25th and 75th percentiles. * $p < 0.05$, *** $p < 0.001$.

Figure 2. Patterns of network activity in LEC, HP and PFC as well as functional communication within LEC-HP-PFC networks in pre-juvenile CON and GE mice. (a) Averaged power spectra $P(f)$ of oscillatory activity in CON and GE mice. Insets, violin plots displaying the power averaged for 1-30 Hz in CON and GE mice. (b) Violin plots displaying the firing rate in CON and GE mice. (c) Line plots displaying the information flow measured by gPDC within LEC-HP-PFC circuits. Insets, violin plots displaying the gPDC when averaged for 4-30 Hz. Right, schematic of information flow within LEC-HP-PFC circuits during pre-juvenile development as resolved by gPDC. The line thickness corresponds to the strength of information flow between brain regions. For violin plots, black and red dots correspond to individual animals and the red horizontal lines display the median as well as 25th and 75th percentiles. * $p < 0.05$, ** $p < 0.01$, *** $p < 0.001$.

Figure 3. Patterns of network activity in LEC, HP and PFC as well as functional communication within LEC-HP-PFC networks from neonatal CON and GE mice. (a) Left, digital photomontage reconstructing the location of the Dil-labeled 1×16-site recording electrode (orange) in a 100 μm -thick coronal section containing the LEC from a P9 mouse, the position of recording sites (white dots) over LEC layers when displayed at higher magnification. Bottom, averaged power spectra $P(f)$ of discontinuous oscillatory activity normalized to the baseline power $P_0(f)$ of time windows lacking oscillatory activity in CON and GE mice. Inset, violin plots displaying the average power spectra from 4-30 Hz in CON and GE mice. Middle,

same as (a) for HP. Right, same as (a) for PFC. **(b)** Violin plots displaying the firing rate in CON and GE mice. **(c)** Line plots of mean imaginary coherence for oscillatory activity simultaneously recorded in the LEC and HP, LEC and PFC, as well as HP and PFC of CON (black) and GE (red) mice. The bottom lines in the coherence plots correspond to the imaginary coherence calculated from shuffled data. Insets for each coherence plot, violin plots displaying the imaginary coherence when averaged for 4-30 Hz. Right, schematic of synchrony within LEC-HP-PFC networks during neonatal development as resolved by imaginary coherence. The line thickness corresponds to the coupling strength. **(d)** Same as (c) when the directional coupling within LEC-HP-PFC networks was estimated by gPDC. For violin plots, black and red dots correspond to individual animals and the red horizontal lines display the median as well as 25th and 75th percentiles. * $p < 0.05$, ** $p < 0.01$.

Figure 4. Long-range monosynaptic axonal projections connecting neonatal LEC, hippocampal CA1, and PFC. **(a)** Schematic of the retrograde tracer CTB488 injection in PFC and CTB555 injection in HP. Digital photomontage showing the CTB555 injection in the HP (left) and CTB488 injection in the PFC (middle) of a P10 CON mouse. Right, digital photomontage displaying CTB555- (red) and CTB488- (green) labeled neurons in LEC of the same mouse. Inset, labeled neurons in LEC shown at higher-magnification. The red arrow indicates rhinal fissure. **(b)** Left, schematic of the retrograde tracer CTB555 injection in HP. Middle, photographs depicting CTB555-labeled neurons (white dot) in the LEC of a P10 CON and GE mouse. Right, violin plot displaying the number of CTB555-labeled neurons in the LEC of CON and GE mice. **(c)** Same as **(b)** for CTB488 injection in PFC. For violin plots, black and red dots correspond to individual animals and the red horizontal lines display the median as well as 25th and 75th percentiles. * $p < 0.05$.

Figure 5. Light-induced activation of LEC. **(a)** Schematic of AAV9-CaMKII-ChR2-mCherry injection in the LEC. Right, photographs depicting the injection position in the LEC of a P10 CON mouse and the position of injection site (red) shown at higher-magnification. Blue lines correspond to the iso-contour lines for light power of 1 and 10 mW/mm², respectively. **(b)** Top,

representative raster plot and corresponding spike probability histogram for LEC, HP and PFC in response to 50 sweeps of 8 Hz pulse stimulation (3 ms pulse length, 473 nm) in LEC. Bottom, violin plot displaying firing probability of single unit in LEC, HP and PFC in response to 8 Hz light stimulation in LEC. **(c)** Line plots of coherence between LEC and HP, LEC and PFC, and HP and PFC during ramp stimulation of LEC pyramidal neurons normalized to coherence values before stimulation. * $p < 0.05$, ** $p < 0.01$, *** $p < 0.001$.

Figure 6. Prelimbic neurons innervated by LEC and light-induced activation of LEC terminals in PFC. **(a)** Schematic of the anterograde trans-synaptic WGA injection in LEC. Photograph depicting the injection position in LEC of a P10 CON mouse. Right, photographs depicting WGA-expressing neurons (green dots) in the PFC of a P10 CON mouse. WGA-labeled neurons in prelimbic layers displayed at a higher-magnification. PL, prelimbic subdivision of the PFC; IL, infralimbic subdivision of the PFC. **(b)** Schematic of the AAV9-CaMKII-ChR2-mCherry injection in the LEC and light stimulation of entorhinal axonal terminals in PFC. Right, photograph depicting mCherry-labeled axons in PL5/6 and PL2/3 of a P10 CON mouse. **(c)** Left, representative raster plot and corresponding spike probability histogram for prefrontal neurons in response to 50 sweeps of 8 Hz light stimulation. Right, violin plot displaying the firing probability of single unit in LEC, HP and PFC in response to 8 Hz light stimulation in LEC. **(d)** Averaged LFP traces recorded in the prelimbic layer 5/6 in response to light stimulation of LEC terminals in CON (black) and GE (red) mice. The blue line indicates the 3 ms-long pulse stimulation in PFC. **(e)** Left, raster plot depicting the firing of single cells in response to the first pulse stimulation from each sweep in CON mice. The blue line corresponds to the 3 ms-long pulse stimulation in PFC. Right, bubble plot depicting the modulation index of spiking response of prefrontal single units to pulse stimulation. Modulation index > 0 indicates increased firing activity, whereas values < 0 corresponds to decreased firing activity. The dot size mirrors the firing rate of single units. Inset, pie plot depicting the percentage of activated (black), inhibited (blue), and not changed (gray) prefrontal units upon light stimulation. **(f)** Same as **(e)** for GE mice.

Figure 7. Light-induced activation of LEC terminals in HP. (a) Left, schematic of the mixed Fluorogold (FG) and WGA injection in LEC. Middle, photographs depicting the neurons labeled by FG and WGA in the HP of a P10 CON mouse. Right, photographs of the region marked by the yellow box when displayed at a higher magnification. **(b)** Left, schematic of the AAV9-CaMKII-ChR2-mCherry injection in LEC and light stimulation of entorhinal terminals in HP. Middle, photographs depicting the LEC axons labeled by mCherry (red) in the HP of a P9 CON mouse. Blue lines correspond to the iso-contour lines for light power of 1 and 10 mW/mm², respectively. Right, mCherry-labeled axons in stratum lacunosum of CA1 displayed at a higher magnification. **(c)** Left, averaged hippocampal LFP in response to light stimulation of LEC terminals in CON and GE mice. The blue line indicates the pulse stimulation. Right, violin plots displaying the amplitude of the biggest response of the averaged LFP in HP. **(d)** Representative LFP sinks and sources in response to 50 sweeps pulsed light stimulation of LEC terminals in the HP from a P9 CON mouse and a P9 GE mouse. **(e)** Left, representative raster plot and corresponding spike probability histogram for hippocampal neurons in response to 50 sweeps of 8 Hz light stimulation. Right, violin plot displaying the firing probability in HP in response to 8 Hz light stimulation. **(f)** Left, raster plot depicting the firing of single hippocampal cells in response to the first pulse stimulation from each sweep in CON group. Right, bubble plot depicting the modulation index of spiking response of hippocampal single units to pulse stimulation. Modulation index > 0 indicates increased firing activity, whereas values < 0 correspond to decreased firing activity. The dot size mirrors the firing rate of single units. Inset, pie plot depicting the percentage of activated (black), inhibited (blue), and not changed (gray) prefrontal units upon light stimulation. **(g)** Same as (f) for GE mice. *p<0.05, ***p<0.001.

Figure 8. Firing activity in PFC during light-induced activation of LEC terminals in HP. (a) Schematic of AAV9-CaMKII-ChR2-mCherry injection in LEC and light stimulation of entorhinal axonal terminals in HP. **(b)** Line plot of firing activity of prelimbic layer 5/6 neurons during 3 s-long ramp stimulation (light blue shadow) of LEC terminals in HP normalized to the activity before stimulation for CON and GE mice. The horizontal dotted line corresponds to no changes of firing activity during the stimulation. Right, violin plots displaying the firing activity

of prelimbic layer5/6 neurons during 3 s-long ramp stimulation normalized to the activity before stimulation. **(c)** Same as **(b)** for prelimbic layer 2/3 neurons. **(d)** Line plots of HP-PFC coherence calculated during ramp stimulation of entorhinal terminals in HP and normalized to coherence values before stimulation. Inset, violin plot displaying the averaged 12-20 Hz coherence between HP and PFC during stimulation when normalized to coherence values before stimulation. For violin plots, black and red dots correspond to individual animals and the red horizontal lines display the median as well as 25th and 75th percentiles. * $p < 0.05$, ** $p < 0.01$.

Figure 9. Light-induced inhibition of entorhinal terminals in HP of CON mice. (a) Schematic of the stimulation protocol of LEC from AAV9_CaMKII_eOPN3_mScarlet-transfected P1 control mice. **(b)** Left, power of oscillatory activity in HP after stimulation of LEC axons in HP (post) normalized to the activity before the stimulation (pre) in CON (blue). Red line displays the relative HP power in non-stimulated GE mice. Right, violin plot displaying the average power reduction in 12-30 Hz range. **(c)** Same as (b) for PFC. **(d)** Left, line plots depicting the HP-PFC coherence after pulse stimulation of entorhinal terminals in HP (post) normalized to coherence values before stimulation (pre) (blue). Red line displays the relative HP-PFC coherence in GE mice. Right, violin plot displaying the coherence averaged for 12-30 Hz range. For violin plots, blue and red dots correspond to individual animals and the red horizontal lines display the median as well as 25th and 75th percentiles. * $p < 0.05$.

	HP-projecting neurons			PFC-projecting neurons			
	CON	GE	<i>p</i>	CON	GE	<i>p</i>	
Passive properties	RMP (mV)	-68.76 ± 8.19	-69.24 ± 7.44	0.12	-69.19 ± 4.47	-68.39 ± 5.47	0.99
	C _m (pF)	111.85 ± 21.99	118.96 ± 14.10	0.46	120.32 ± 22.02	119.53 ± 14.05	0.96
	R _{in} (MΩ)	606.99 ± 181.96	632.35 ± 102.39	0.62	481.20 ± 96.20	551.86 ± 93.68	0.27
	τ _m (ms)	67.24 ± 14.21	72.86 ± 16.08	0.17	58.95 ± 12.47	68.01 ± 12.95	0.29
Active properties	AP threshold (mV)	-41.16 ± 7.06	-42.20 ± 2.84	0.71	-42.94 ± 2.61	-44.05 ± 2.57	0.57
	AP amplitude (mV)	79.33 ± 5.29	77.88 ± 2.71	0.49	80.80 ± 3.38	81.21 ± 2.94	0.85
	Half-width (ms)	2.82 ± 0.45	2.61 ± 0.26	0.16	2.07 ± 0.31	1.92 ± 0.45	0.61
	Rheobase (pA)	45.61 ± 20.87	54.20 ± 16.42	0.69	56.07 ± 16.41	50.53 ± 8.27	0.49
	Firing frequency (Hz)	14.39 ± 4.53	14.79 ± 1.94	0.82	13.81 ± 3.05	16.67 ± 3.16	0.18

Table 1. Passive and active membrane properties of neurons in LEC of neonatal CON and GE mice.

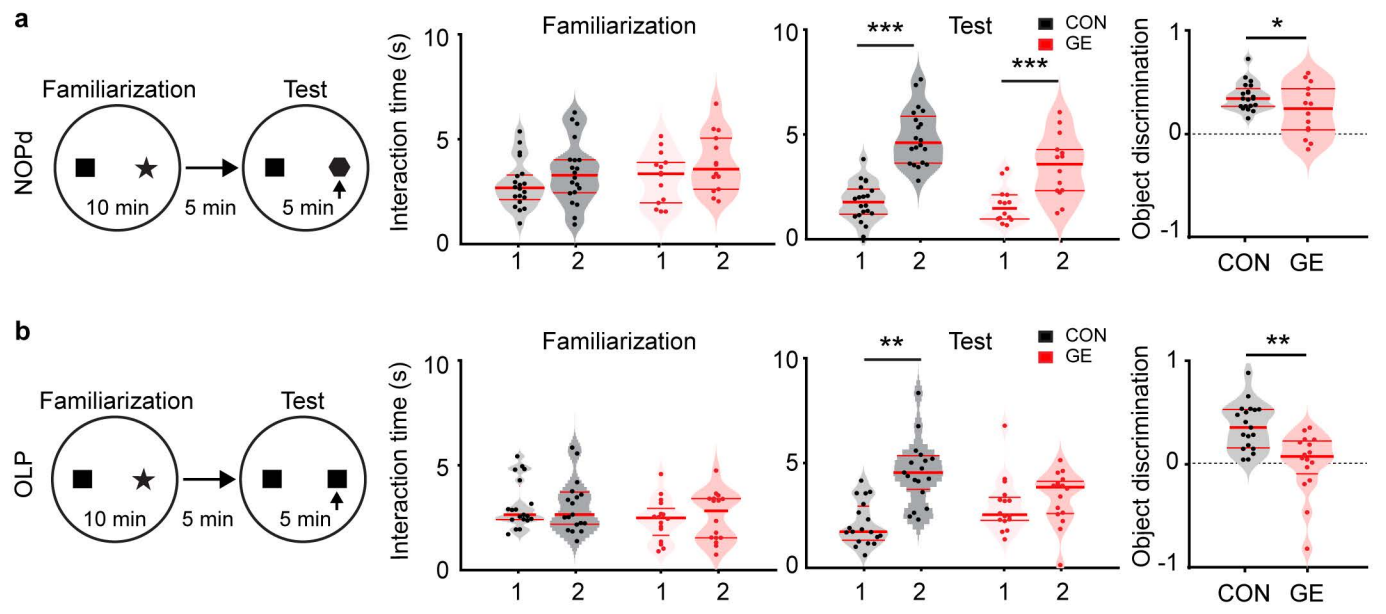


Figure 1- Xu et al.

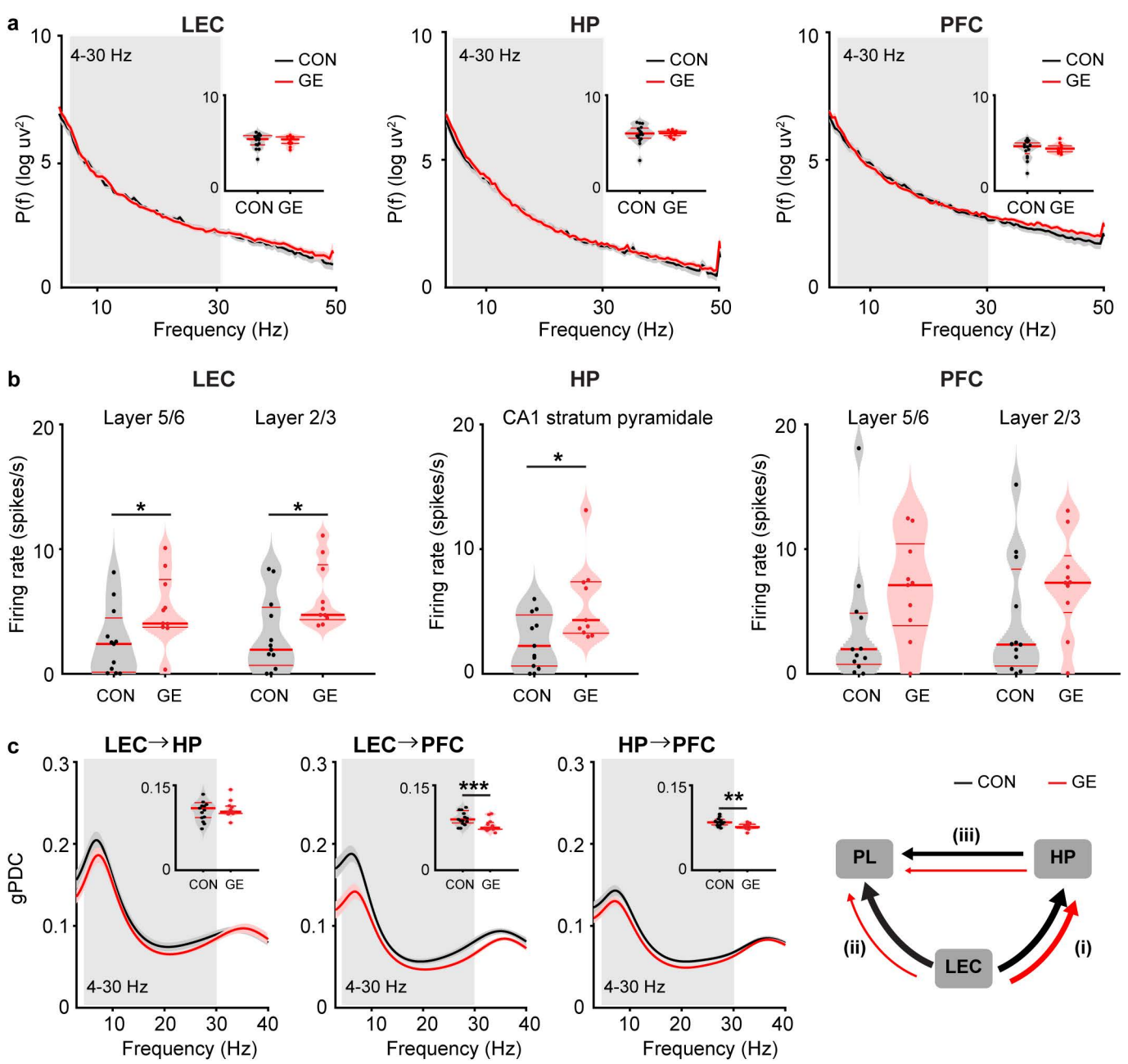
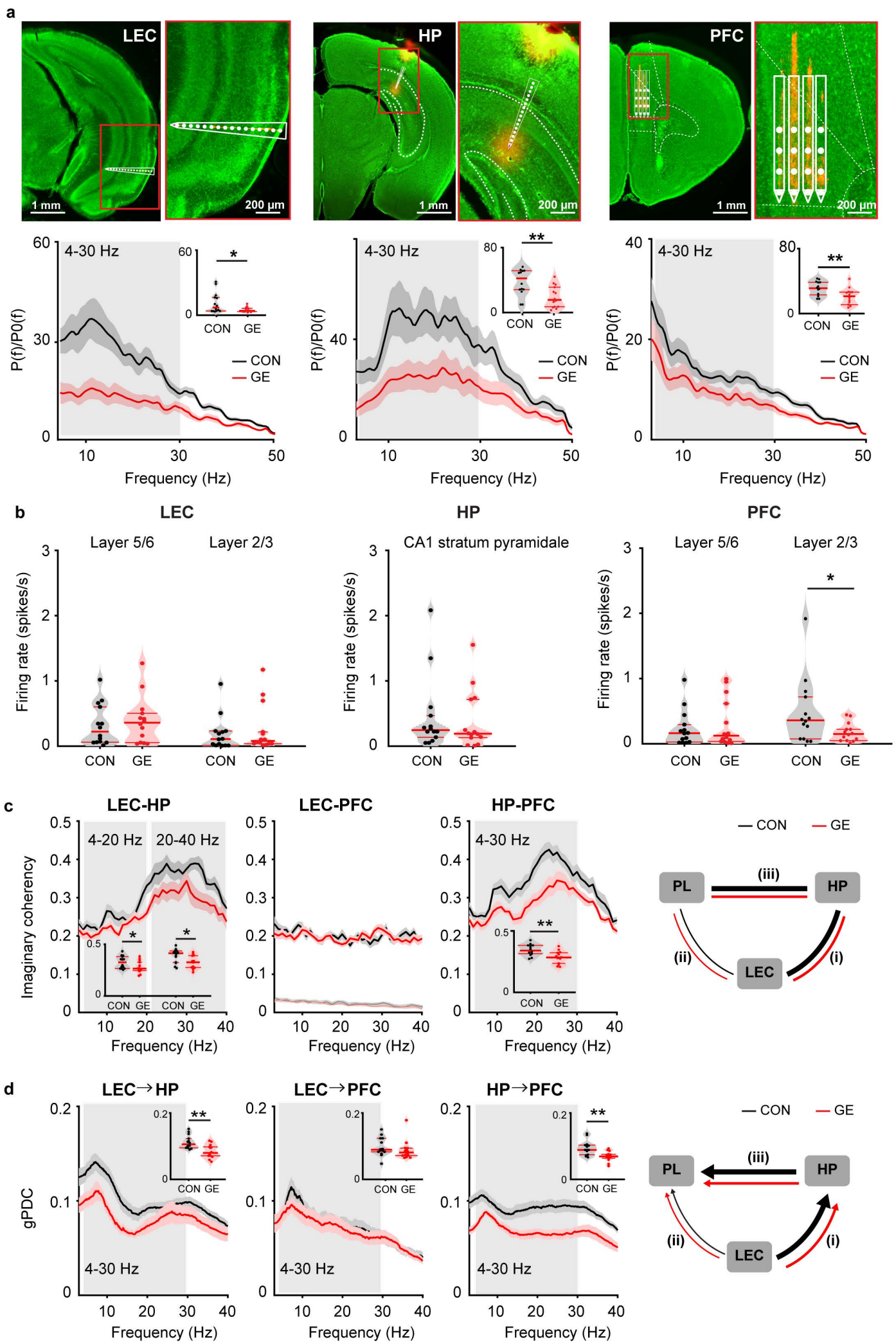


Figure 2- Xu et al.



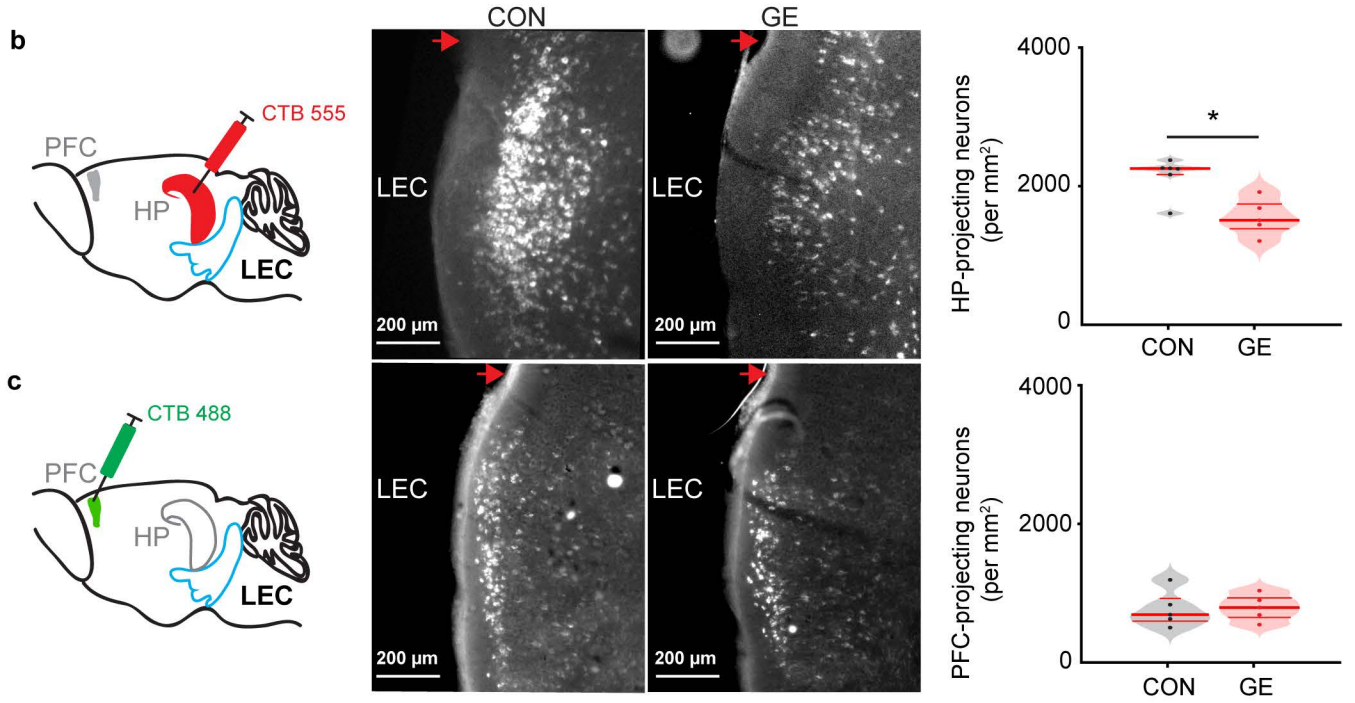
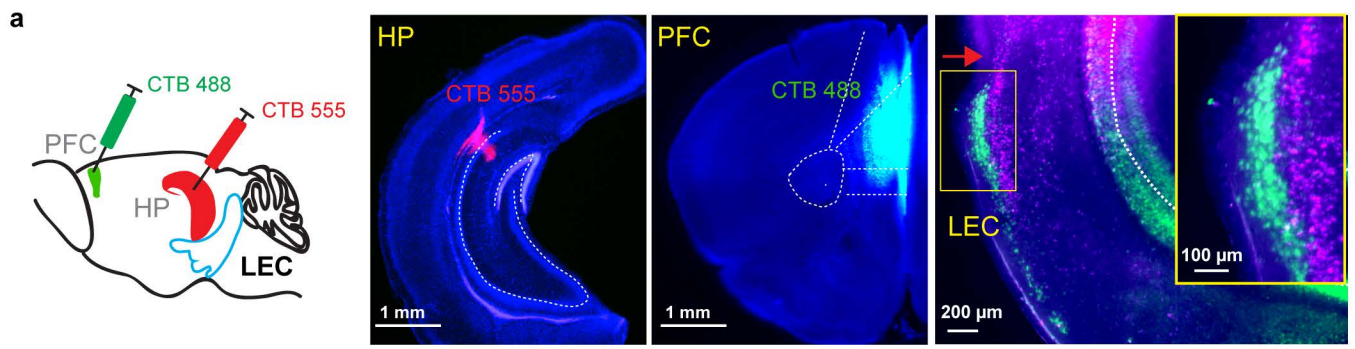


Figure 4- Xu et al.

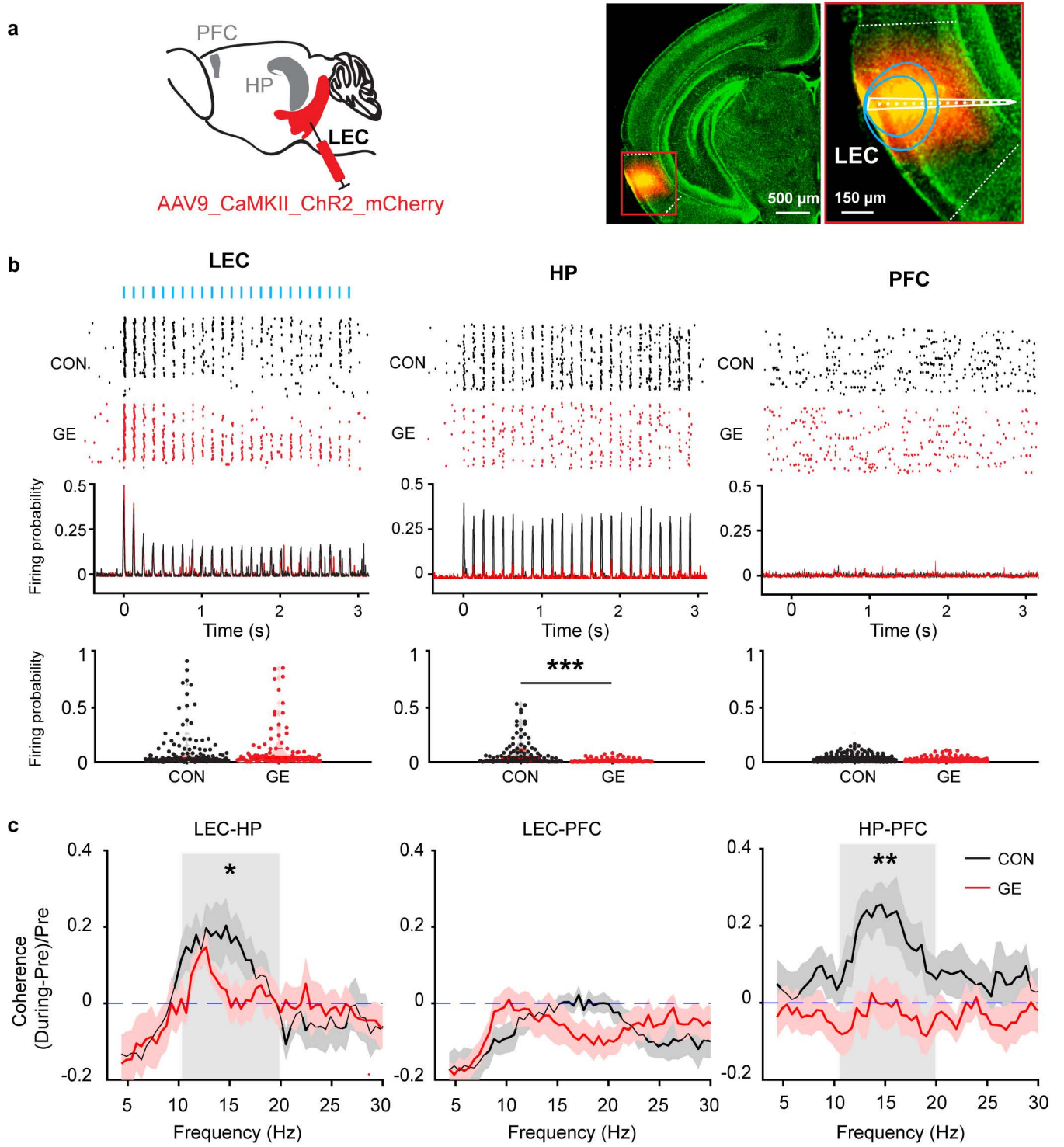


Figure 5- Xu et al.

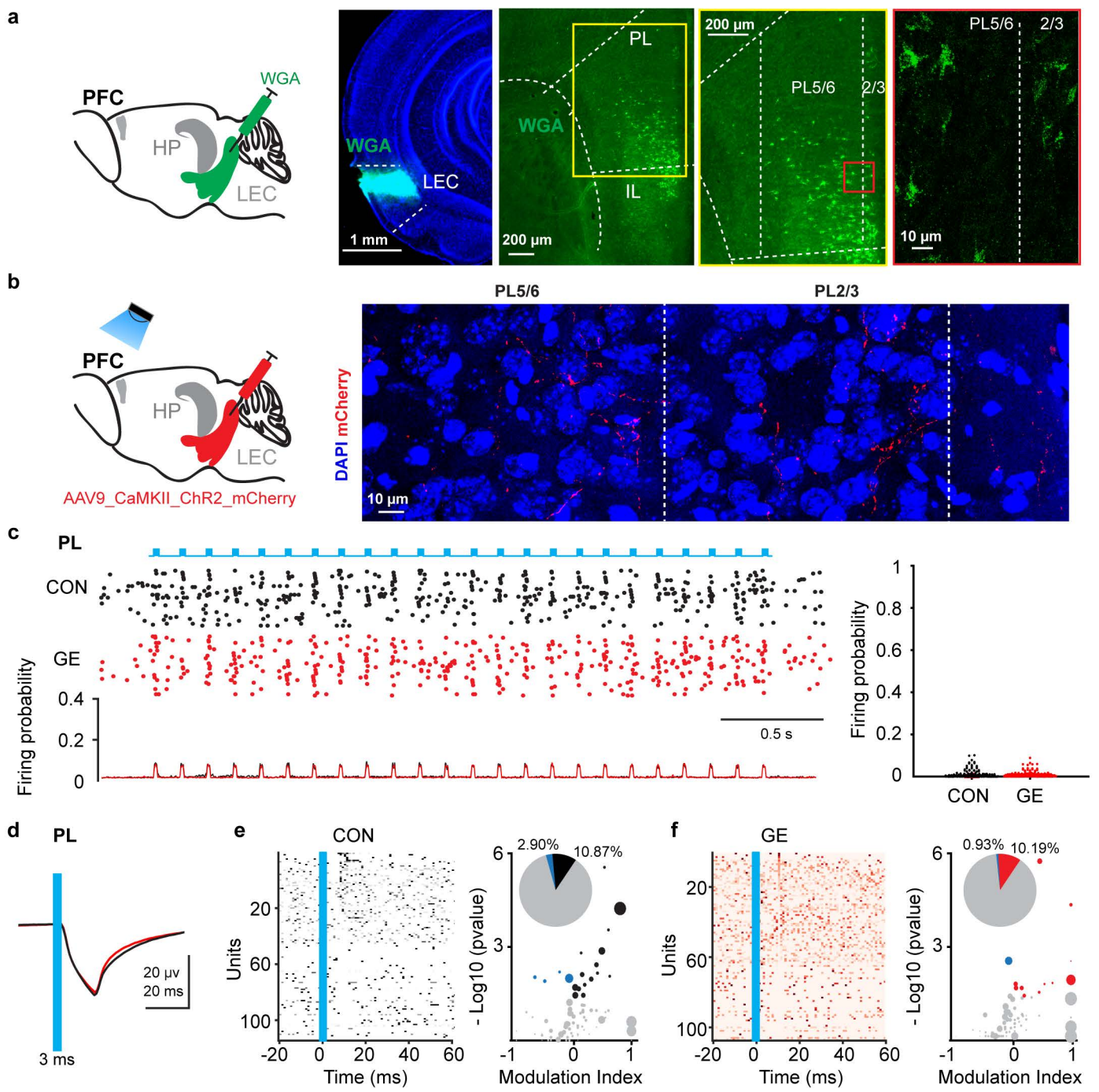


Figure 6- Xu et al.

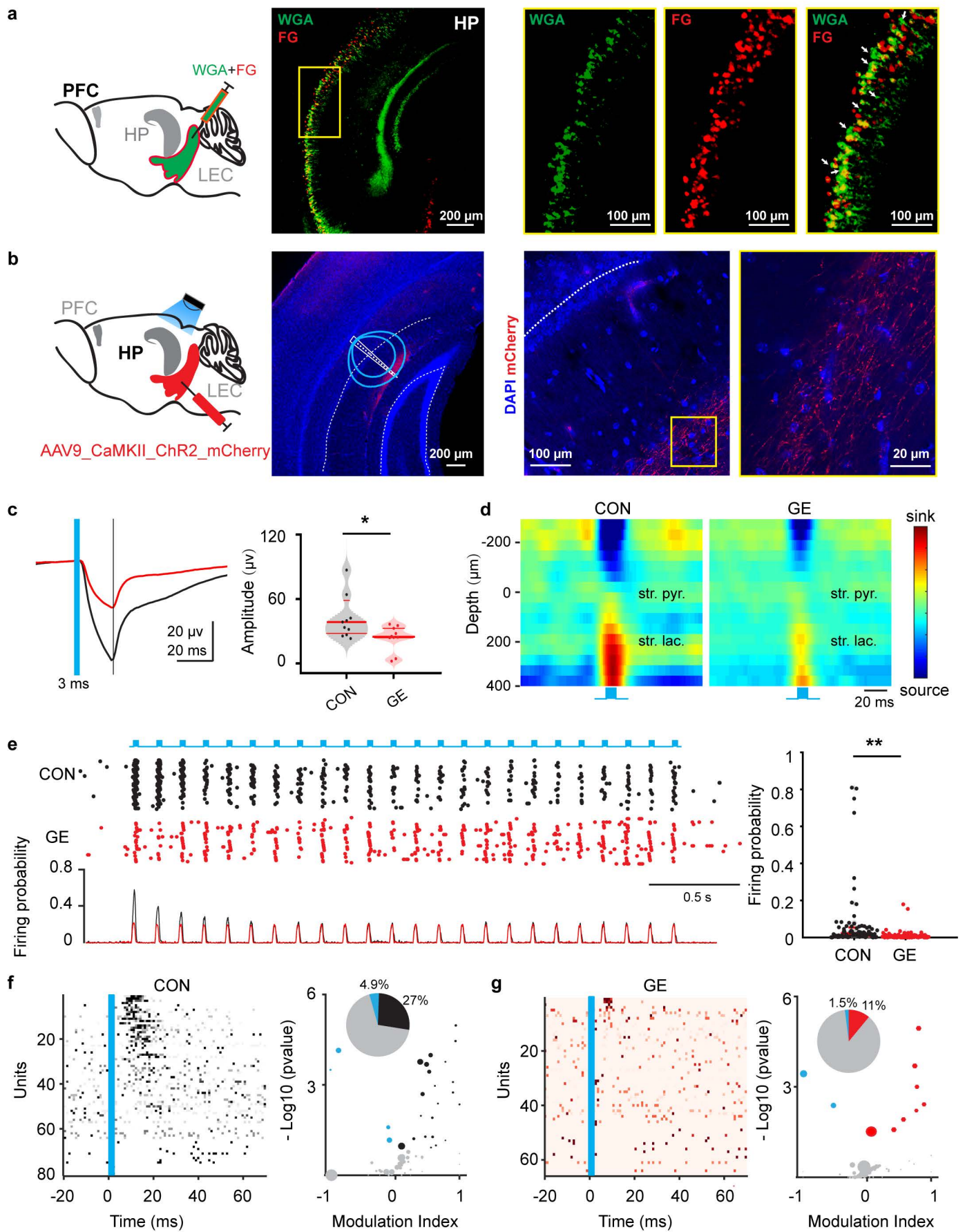


Figure 7- Xu et al.

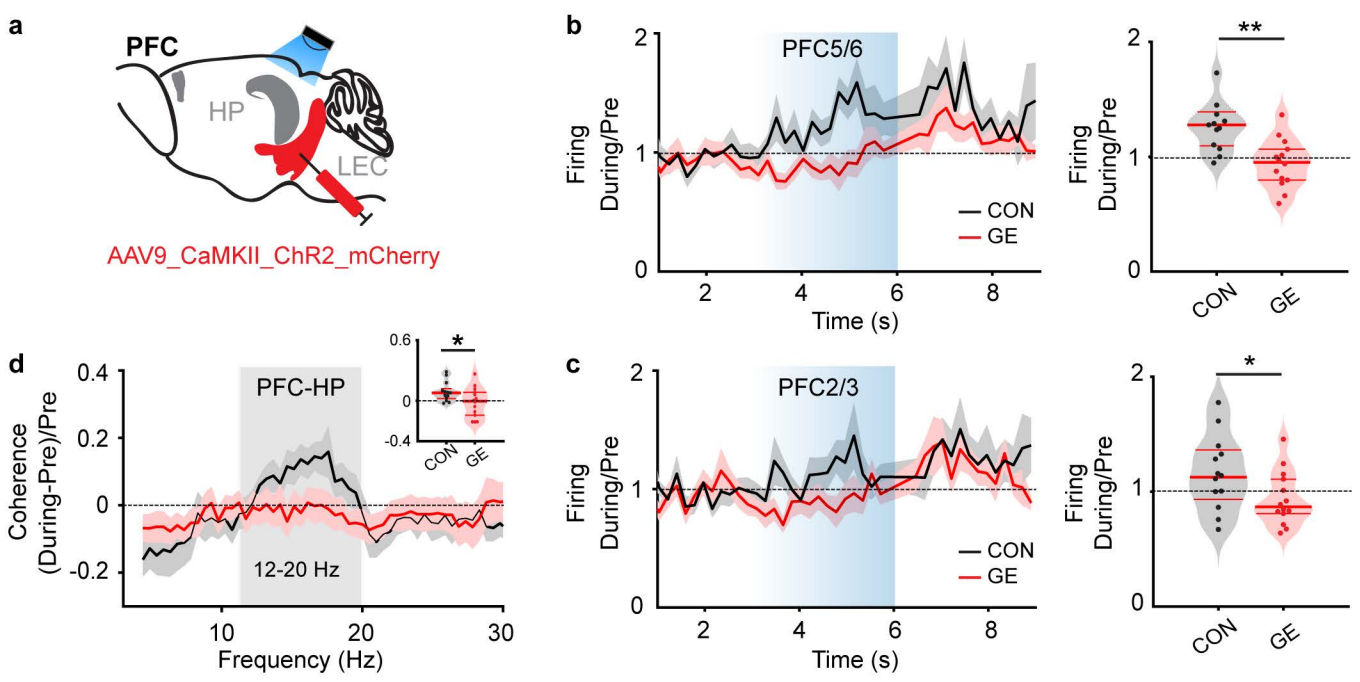


Figure 8- Xu et al.

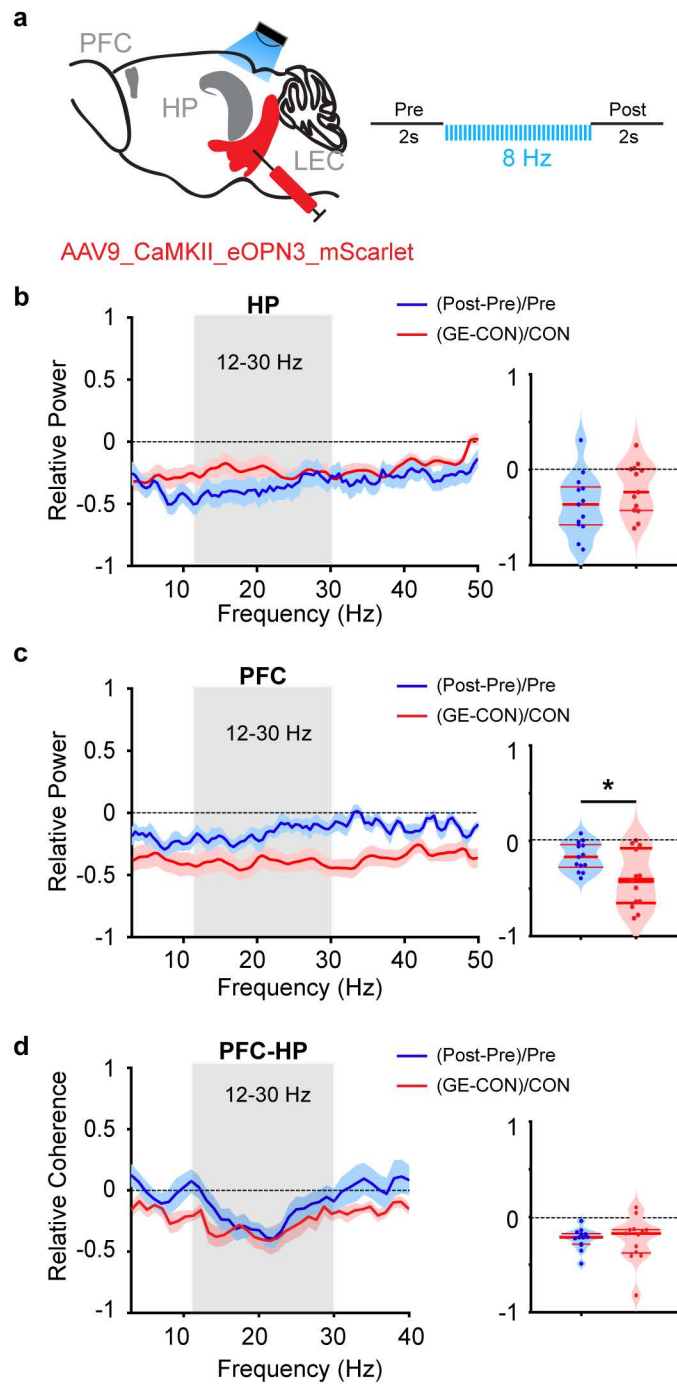
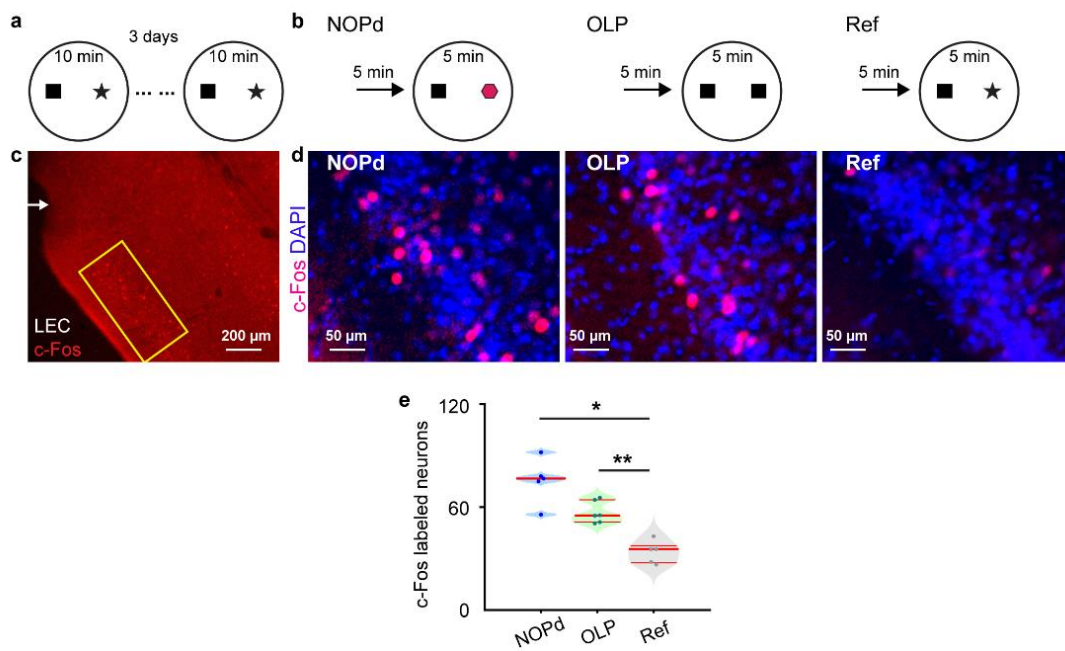


Figure 9- Xu et al.

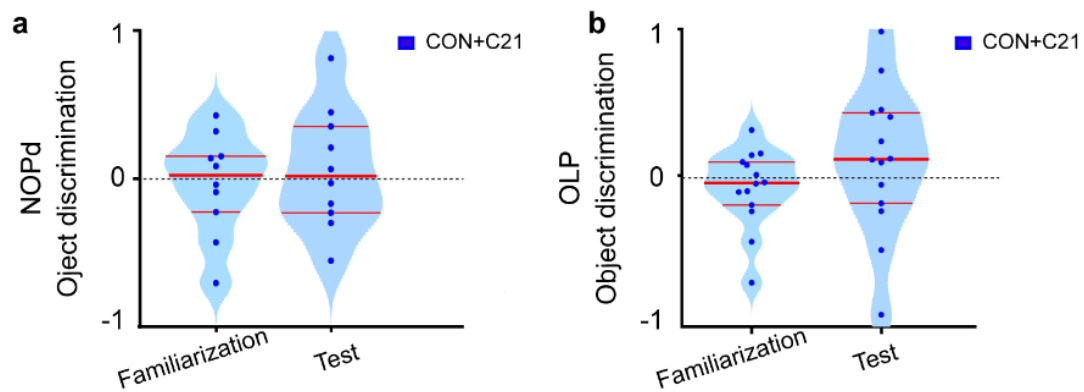
Supplementary information

**Developmental decrease of entorhinal-hippocampal
communication in immune-challenged DISC1
knockdown mice**

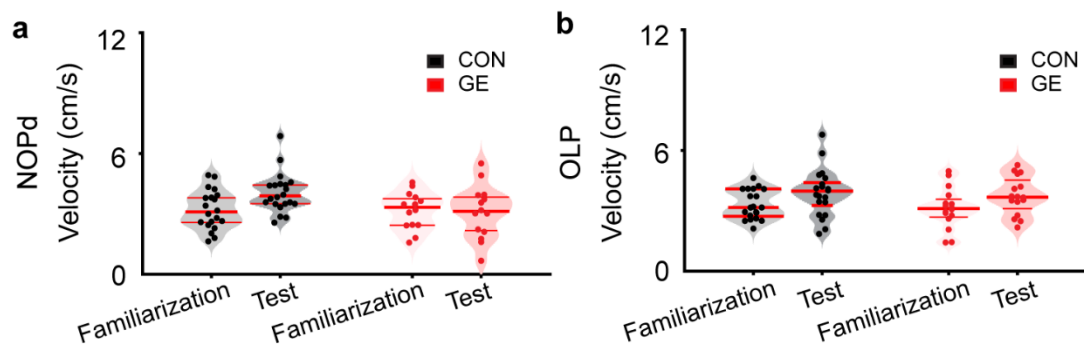
Xu et.al



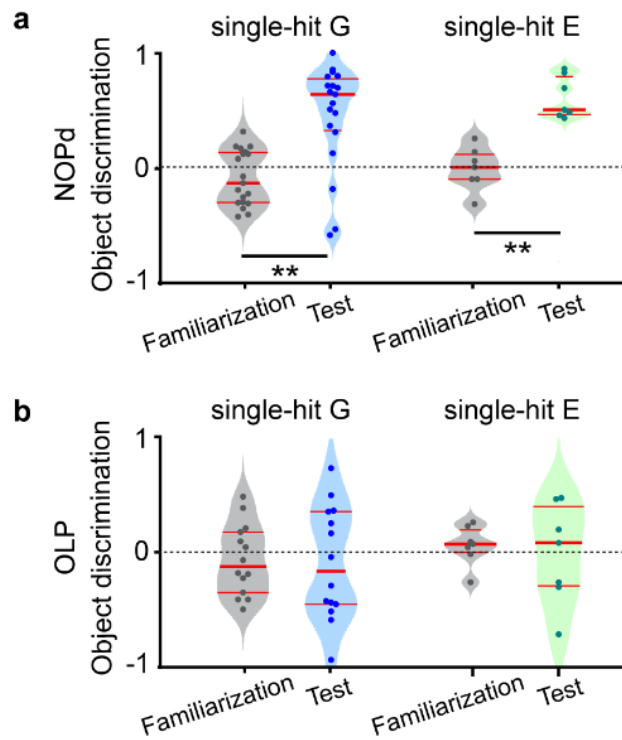
Supplementary fig.1 cFos immunoreactivity in LEC of mice tested in associative recognition tasks. **(a)** Schematic of the protocol for the familiarization trials (3 days, 2 trials per day). **(b)** Schematics of the protocol for NOPd test trial, OLP test trial, and reference trials (Ref). **(c)** Photomicrographs depicting cFos-expressing neurons (red) in the superficial layer of LEC from a P20 mouse, 90 mins after the test trial. **(d)** Photograph displaying the cFos-expressing cells (red dots) in LEC when stained for DAPI (blue) 90 mins after the NOPd test trial (left), OLP test trial (middle) and Ref trial (right). **(e)** Violin plots displaying the total number of cFos-positive neurons in the LEC of CON after NOPd task, OLP task, or Ref task. For violin plots, black and red dots correspond to individual animals and the red horizontal lines display the median as well as 25th and 75th percentiles. *p<0.05, **p<0.01.



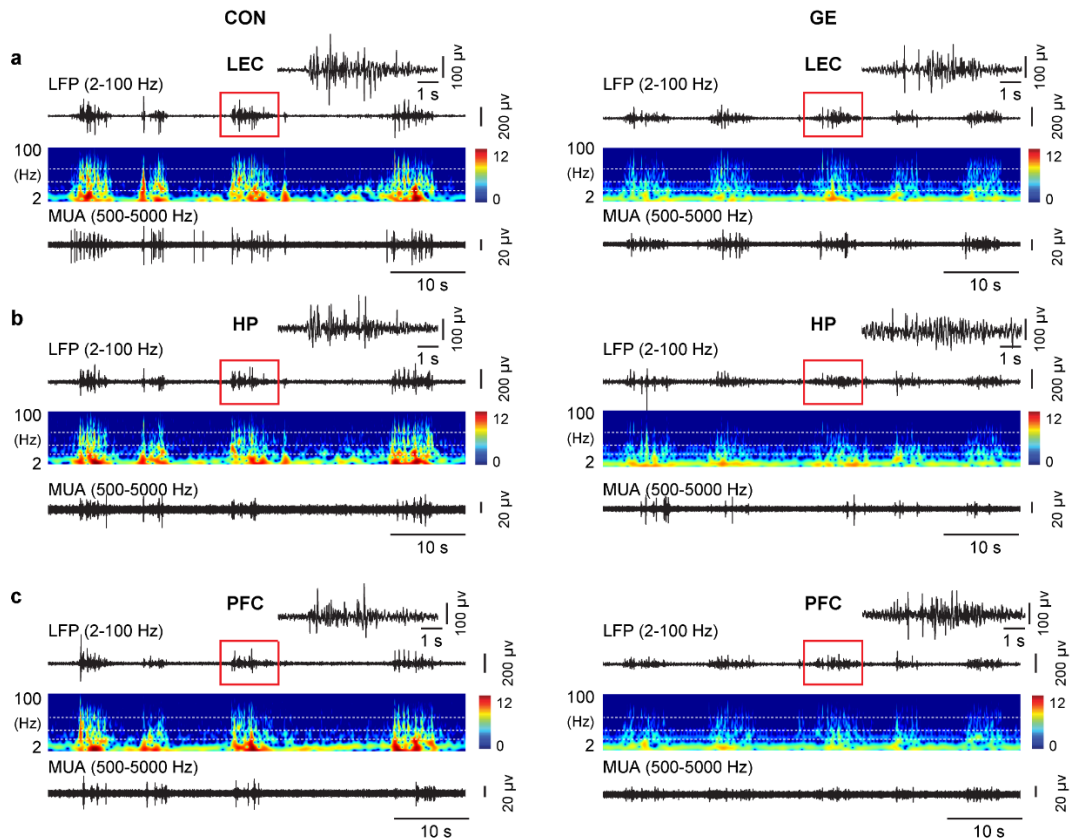
Supplementary fig.2 Poor performance of CON mice in NOPd and OLP tasks after silencing LEC activity by the DREADD agonist 21 (compound 21, C21). (a) Violin plots displaying the discrimination ratio in familiarization and test trials of NOPd task. (b) Same as (a) for OLP task. Black and red dots correspond to individual animals and the red horizontal lines display the median as well as 25th and 75th percentiles.



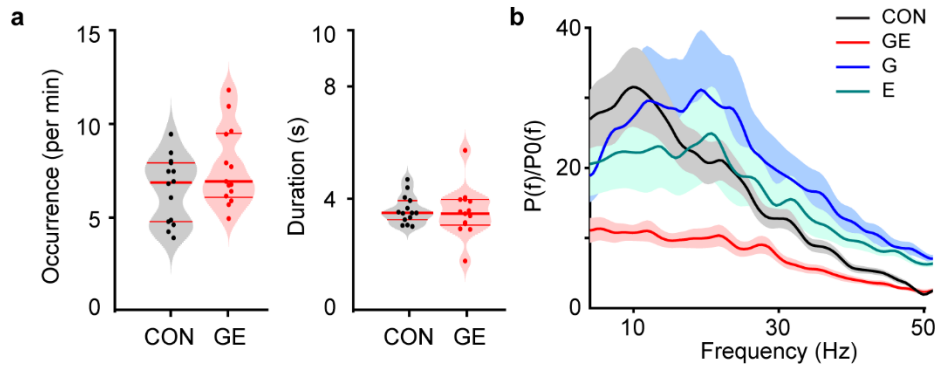
Supplementary fig.3 The velocity of pre-juvenile CON and GE mice in NOPd and OLP tasks. (a) Violin plots displaying the exploration velocity in familiarization and test trials of NOPd tasks. (b) The same display as (a) for OLP task. Black and red dots correspond to individual animals and the red horizontal lines display the median as well as 25th and 75th percentiles.



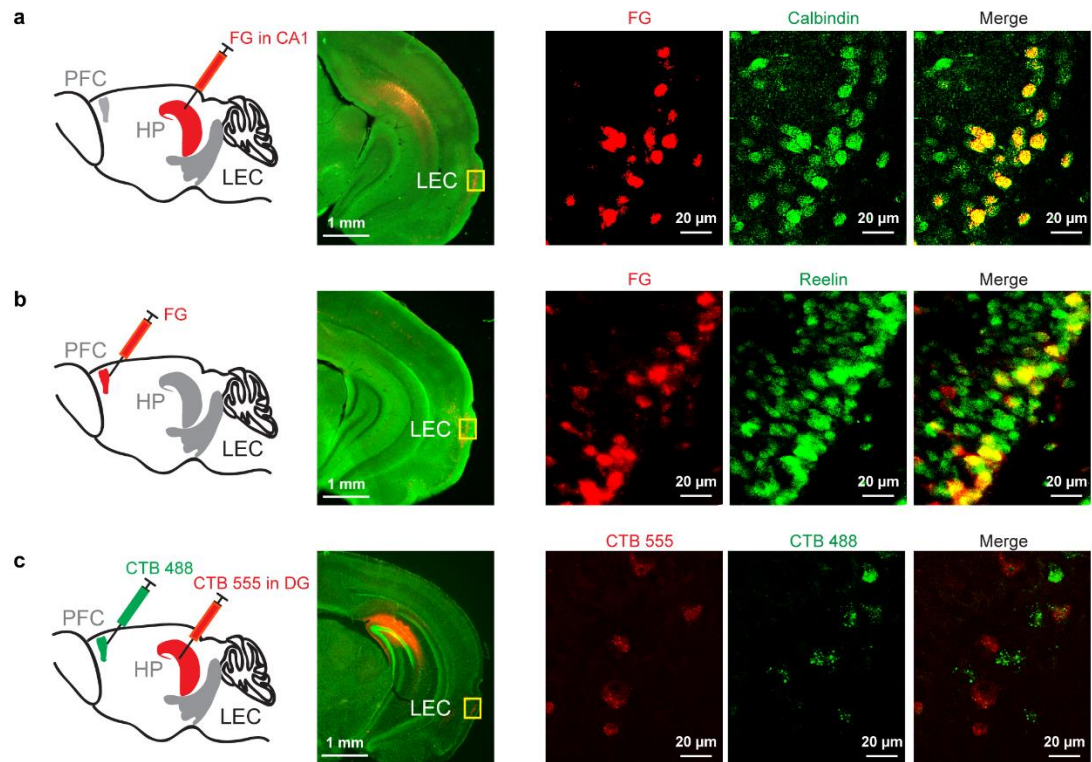
Supplementary fig.4 The performance of pre-juvenile single-hit G and E mice in associative recognition memory tasks. (a) Violin plots displaying the discrimination ratio in familiarization and test trials when averaged for single-hit G (DISC1 mice) and E (polyI:C-treated dams to induce MIA) mice. The black dotted line indicates chance level. **(b)** The same display as (a) for OLP task. Black and red dots correspond to individual animals and the red horizontal lines display the median as well as 25th and 75th percentiles. ** $p < 0.01$.



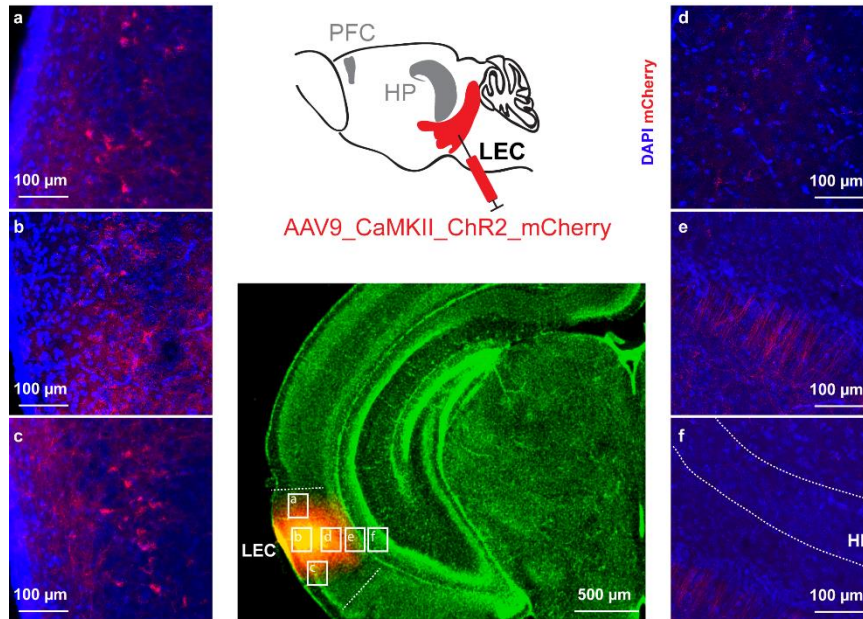
Supplementary fig.5 Discontinuous network activity in the LEC, HP and PFC of neonatal CON and GE mice. (a) Extracellular LFP recordings of discontinuous oscillatory activity in the LEC of a P9 CON mouse (left) and a P9 GE mouse (right) displayed after bandpass (2-100 Hz) filtering (top) together with the corresponding MUA (500-5000 Hz) (bottom). Traces are accompanied by the color-coded wavelet spectra of the LFP at identical time scale. **(b, c)** Same as (a) for HP and PFC, respectively.



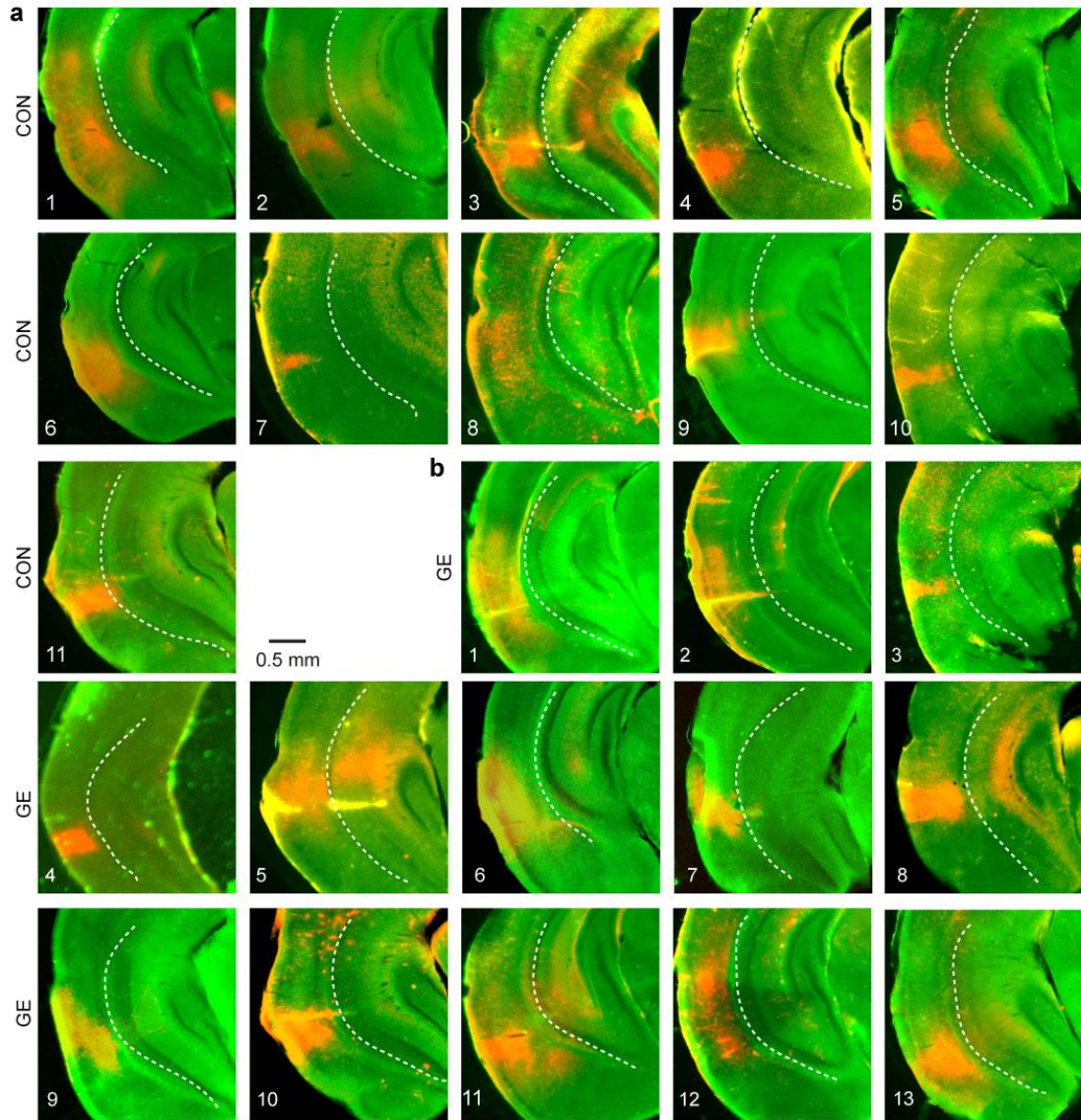
Supplementary fig.6 Patterns of network activity in the LEC of neonatal CON, GE, G, and E mice. (a) Violin plots displaying the occurrence and the duration of oscillatory activity in LEC recorded in CON and GE mice. **(b)** Averaged power spectra $P(f)$ of discontinuous oscillatory activity normalized to the baseline power $P_0(f)$ of time windows lacking oscillatory activity in CON, double-hit GE, single-hit G and single-hit E mice. For violin plots, black and red dots correspond to individual animals and the red horizontal lines display the median as well as 25th and 75th percentiles.



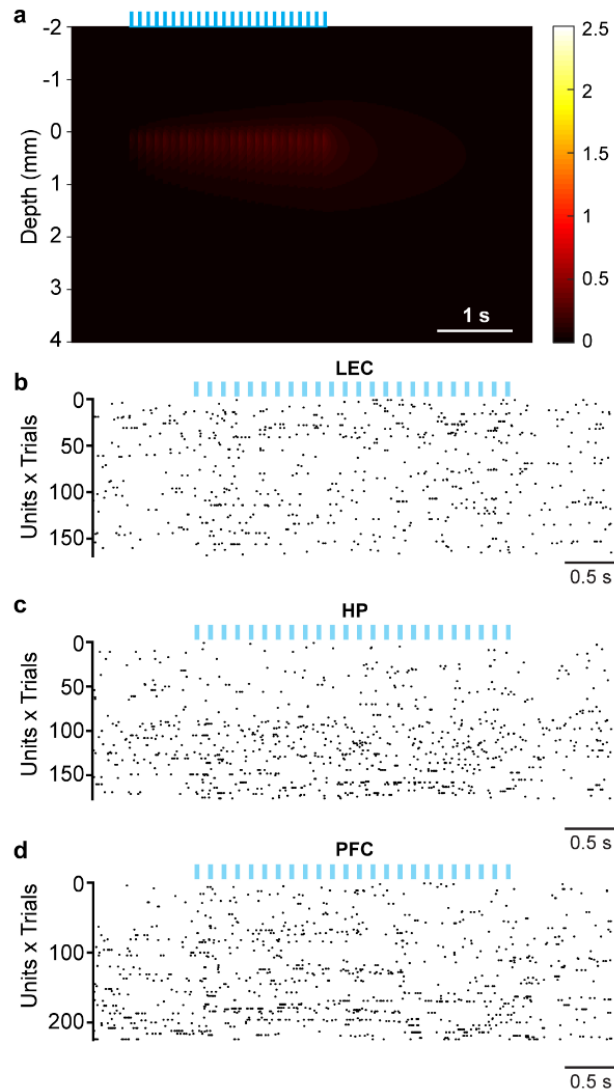
Supplementary fig.7 Co-localization of CA1-projecting neurons with reelin, and PFC-projecting neurons with calbindin in LEC. (a) Schematic of the retrograde FG injection in HP. Middle, photograph depicting FG-labeled neurons in the LEC of a P10 CON mouse. Right, FG and calbindin-labeled neurons in LEC. **(b)** Schematic of the retrograde FG injection in PFC. Middle, photograph depicting FG-labeled neurons in the LEC of a P10 CON mouse. Right, FG and reelin-labeled neurons in LEC. **(c)** Schematic of the retrograde CTB 488 injection in PFC, CTB 555 injection in DG. Middle, photograph depicting CTB 555-labeled neurons in the LEC of a P10 CON mouse. Right, CTB 488-labeled neurons and CTB 555-labeled neurons in the LEC.



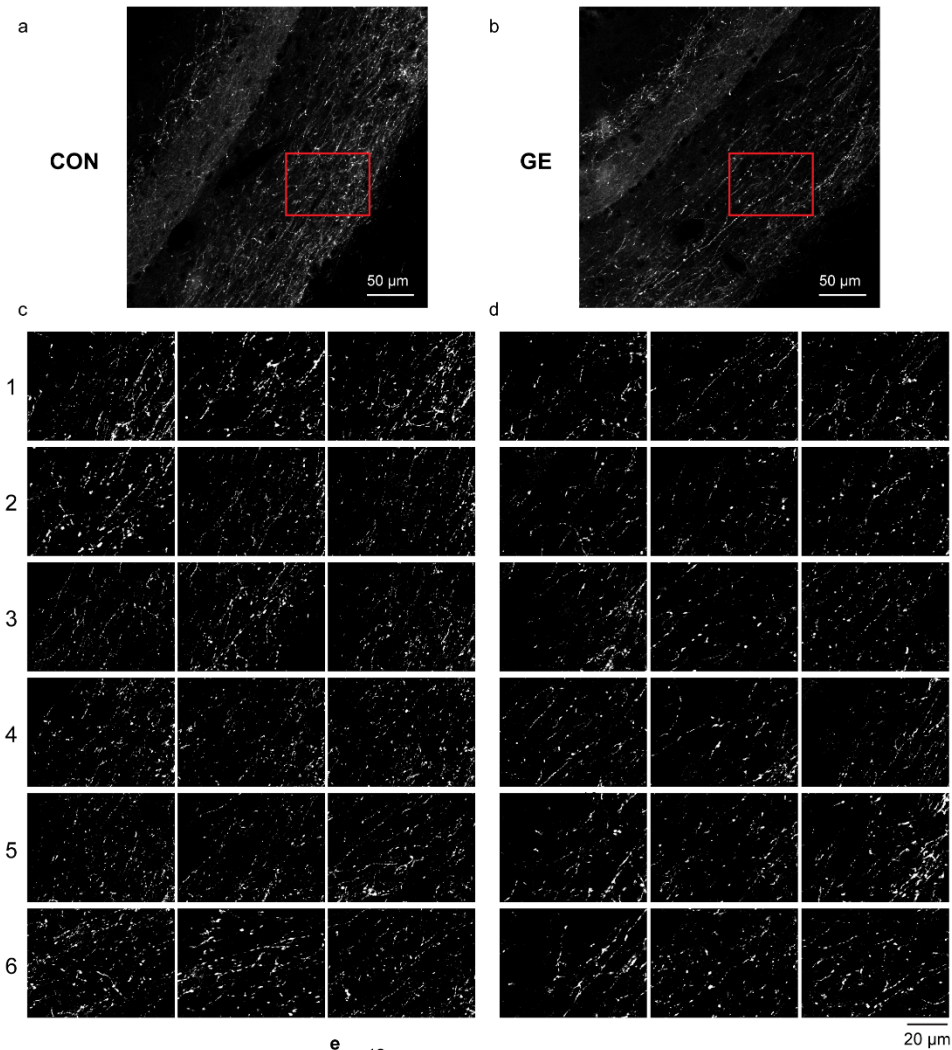
Supplementary fig.8 AAV9-CaMKII-ChR2-mCherry expression in LEC. AAV9-CaMKII-ChR2-mCherry injection in the LEC (middle) led to mCherry-labeled neurons in superficial layer of LEC (**a, b, c**), deep layer of LEC (**d**), axons from LEC to HP (**e**) and no transfected neurons in HP (**f**).



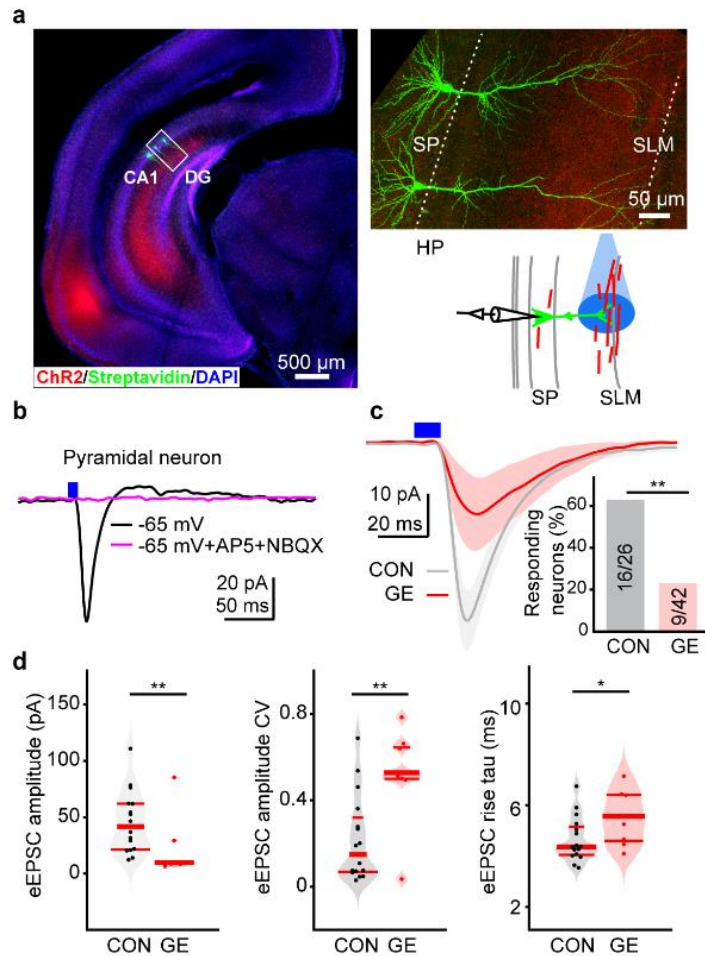
Supplementary fig.9 The injection position of AAV9-CaMKII-ChR2-mCherry in LEC for all the mice. (a) Photographs depicting the injection position for all CON mice used in the study. **(b)** Photographs depicting the injection position for all GE mice used in the study.



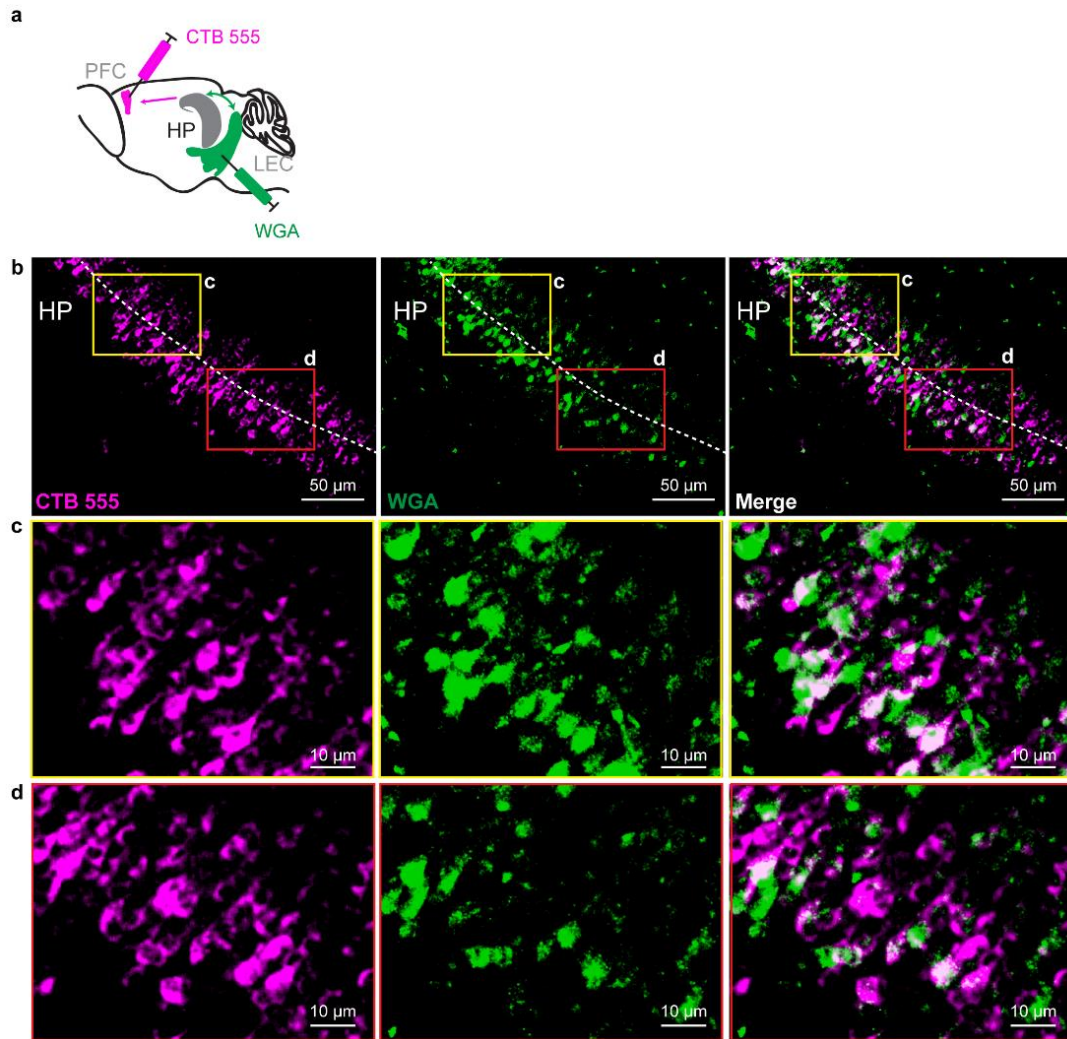
Supplementary fig.10 Pulses stimulation did not induce increased firing activity in opsin-free CON mice. (a) Heat map of temperature changes caused by the 8 Hz pulse stimulation estimated by the Monte Carlo model. **(b)** Representative raster plot of LEC firing activity in response to 30 sweeps of 8 Hz-pulsed stimulation (3 ms pulse length, 473 nm) in LEC of one P9 CON mice. **(c, d)** Same as (b) for HP and PFC, respectively.



Supplementary fig.11 LEC axons labeled by mCherry in HP. (a, b) Photographs exemplarily illustrating entorhinal axons in the HP of a P10 CON (a) and a GE mouse (b). **(c)** Axons from the area marked by a red box shown at higher-magnification. Totally 6 CON mice (each line indicated one mouse, each image indicated one slice) were used for the quantification. **(d)** Same display as (c) for 6 GE mice. **(e)** Violin plot displaying the averaged intensity of mCherry in CON and GE mice. For violin plots, black and red dots correspond to individual animals and the red horizontal lines display the median as well as 25th and 75th percentiles. *** $p < 0.0001$.



Supplementary fig.12 Synaptic properties of entorhinal inputs on CA1 pyramidal neurons in neonatal CON and GE mice. (a) Left, representative image showing ChR2 (H134R) (red) expression in a DAPI-stained coronal slice from a P10 CON mouse following LEC transfection at P1. Right, confocal image showing biocytin-filled CA1 neurons in HP from a P10 CON mouse displayed together with a schematic of light stimulation / recording protocol. **(b)** Representative light-evoked responses (blue vertical bar, 10 ms) recorded in a CA1 pyramidal neuron (black trace) at -65 mV. The response was abolished by bath application of NBQX and AP5 (purple trace). **(c)** Average light-evoked responses HP neurons from CON (n=16) and GE (n=9) neurons. Inset, bar diagram of the percentage of responsive CA1 neurons. **(d)** Violin plots displaying the amplitude (left), coefficient of variation of amplitudes (middle), and rise time (right) of light-evoked responses averaged for all CA1 neurons from CON (n=16) and GE (n=9) neurons. For violin plots, black and red dots correspond to individual investigated neurons and the red horizontal lines display the median as well as 25th and 75th percentiles. *p < 0.05, **p < 0.01.



Supplementary fig.13 LEC-PFC communication achieved by bi-synaptic and poly-synaptic transmission through HP neurons. (a) Schematic of the retrograde CTB 555 injection in PFC and retro-/anterograde WGA injection in LEC. **(b)** Photograph depicting CTB-labeled and WGA-labeled neurons in the CA1 of a P10 CON mouse. **(c, d)** Photograph depicting the labeled CA1 neurons from the area marked by yellow and red boxes in (b) at higher-magnification.

Experiments	Interested region	Slice thickness	Slice collection	Mice number
				CON, 6
CTB in HP	LEC			GE, 5
				CON, 6
CTB in PFC	LEC	100 um	Three equally spaced series, 3 series	GE,5
				CON, 6
AAV9_ mCherry in LEC	HP			GE,6
				NOPd, 5
cFos expression	LEC	50 um	Six equally spaced series, 3 series	OLP, 6
				Ref, 5

Supplementary table 1. Slice selection for quantification.

5 Discussion

The long-lasting burden of major psychiatric disorders, such as schizophrenia, results from the cognitive disruption in daily life (Insel, 2010). The impairment of long-range communication between two brain regions, hippocampus (HP) and prefrontal cortex (PFC), represents substrate of mnemonic and executive deficits (Godsil et al., 2013; Sigurdsson and Duvarci, 2015). Understanding organization in the HP-PFC circuit in multiple levels, such as anatomical and physiological mapping of individual neurons, their connectivity and function in both healthy and psychiatric diseases, is mandatory to open clinical treatment opportunities for mental disorders. Of note, elucidating developmental profiles of the HP-PFC network and their upstream brain region lateral entorhinal cortex (LEC) is an essential starting point.

5.1 Cellular substrates of functional LEC-HP-PFC network

Understanding the cellular basis of oscillatory synchrony in developing circuits is essential because several maturation processes rely on early network oscillations. Although most neurons are connected locally, a few "hub" neurons possess long-range connections that link large numbers of cells, thereby bestowing network-wide synchronicity. Neuronal populations that underlie cellular mechanisms of LEC-HP-PFC communication during development are identified in several recent optogenetic studies (Bitzenhofer et al., 2017; Ahlbeck et al., 2018; Xu et al., 2019; Chini et al., 2020; Xu et al., 2021).

The connection strength between HP and PFC increases along the septo-temporal axis of immature HP, similar to adult brains (O'Neill et al., 2013). The synchrony between HP and PL is stronger in i/vHP than in dHP as well. Pyramidal neurons of the i/vHP CA1 area, instead of dHP, project densely to layer V/VI of PL and being sparser to layer II/III (Ahlbeck et al., 2018); Song et al., revision). Correspondingly, selective light manipulation of CA1 pyramidal neurons in i/vHP entrains neonatal prelimbic activity in all frequency bands (Ahlbeck et al., 2018). While stimulation of CA1 pyramidal neurons in dHP leave the prelimbic network activity unaffected. Of note, augmentation of prelimbic activity is theta frequency-preference, which might be related to the preference of theta band firing of CA1 neurons in both physiological and light stimulation conditions (Xu et al., 2021). Silencing of interneurons in i/vHP leads to a significant augmentation of oscillatory activity within

both i/vHP and PL, suggesting that function of GABA is inhibitory at an early age. This observation, together with a large body of evidence (Kirmse et al., 2015; Valeeva et al., 2016; Chini et al., 2021), is challenging to the widely accepted concept that GABAergic signal is depolarizing and excitatory (Ben-Ari, 2002). The possible explanation might be that early investigations mainly were carried out *in vitro*, whereas recent ones were observed under physiological conditions and at the network level. Furthermore, the function of GABA depends on examining time windows and the brain areas (Murata and Colonnese, 2020). Both pyramidal neurons and interneurons in PL receive axonal innervation from HP (Song et al., revision), which is in line with studies conducted in adult mice (Marek et al., 2018; Liu et al., 2020). These finds reveal that already during neonatal development, might even earlier, the connection frame between HP and PFC is established, whose innervation density, synaptic plasticity, synaptic strength alter along with development (Song et al., revision).

Abnormal patterns of network activity and sharp waves, and reduced neuronal firing are observed in the i/vHP CA1 area of GE mice (Xu et al., 2021). These abnormalities are attributed to long-lasting morphological and synaptic deficits of CA1 pyramidal neurons, which cause the reduction of HP-PFC communication and poor cognitive behavior performance at pre-juvenile age. These results are consistent with previous reports (Kvajo et al., 2008; Niwa et al., 2010; Kvajo et al., 2011; Crabtree et al., 2017), where show DISC1 mutation results in impaired neuronal migration and cognitive impairments in adult mice. These morphological and functional deficits might result from that DISC1 mutation disturbs its interacts with proteins that bind to cytoskeletal and associated complexes, such as MAP1A, MIPT3, ATF4/5 and NUDE (Morris et al., 2003; Wang and Brandon, 2011). More importantly, when the suppression of DISC1 is restricted in HP CA1 pyramidal neurons, it is sufficient to reduce oscillatory entrainment of PL and hippocampal-prelimbic coupling (Xu et al., 2021). Prefrontal activity in $G_{HP}E$ mice is disorganized with lower power but unaffected firing activity, different from the reduced firing activity when DISC1 suppression is restricted to PL neurons (Crabtree et al., 2017; Xu et al., 2019). Direct light illumination of CA1 neurons in GE or $G_{HP}E$ mice cannot enhance the synchrony and directionality of hippocampal-prefrontal interaction, reflecting a weaker excitatory drive from HP to PL in these mice. This observation is in line with a previous study where shows that light-driven inhibition of hippocampal terminals in PFC disrupts the information interaction between HP and PFC and the performance of working memory (Spellman

et al., 2015). Thus, this thesis further confirms that hippocampal drive during early development is pivotal for the maturation of the PFC network and subsequent cognitive performance.

Sparser hippocampal projection in PL is observed in GE mice, and its ability in boosting prelimbic firing and entraining network activity is inefficient (Song et al., revision). These abnormalities present in the early postnatal developing network and persist throughout development till pre-juvenile age. Besides the decreased axonal density and efficiency, multiple presynaptic alterations of hippocampal terminals are found in GE mice. Altered short-term synaptic plasticity is observed in GE mice, supported by the impact of action potentials widening of CA1 neurons on neurotransmitter release by increasing the initial probability of presynaptic release and shifting short-term plasticity toward depression (Abbott and Regehr, 2004). Short-term facilitation of hippocampal terminals on prefrontal neurons is abolished in layer II/III neurons of GE at pre-juvenile age, suggesting that synaptic enhancement during development is absent or insufficient. The underlying mechanisms might be that DISC1 mutation and MIA interaction result in presynaptic dysregulation of synaptic vesicle recycling and release of neurotransmitters (Flores et al., 2011; Tang et al., 2016) or postsynaptic receptor desensitization that make the target neurons less sensitive to neurotransmitter (Zucker and Regehr, 2002). Though reduction of hippocampal projection is observed in layer V/VI of PL, functional abnormalities extend to layer II/III. This deficit might arise from, firstly the intracortical connectivity in PL amplifies these defects, and secondly, layer II/III pyramidal neurons in GE mice are themselves characterized by a simplified dendritic arborization, a striking reduced spine density and less synchronized to prefrontal oscillation in beta-low gamma frequency (Chini et al., 2020). By restricting DISC1 mutation to layer II/III pyramidal neurons, most structural and physiological deficits are replicated as whole-brain DISC1 mutation (Xu et al., 2019). These results are consistent with post-mortem findings of patients diagnosed with schizophrenia, that solely layer III prefrontal pyramidal neurons have reduced spine density (Kolluri et al., 2005). Overall, in addition to reduced innervation, alterations in synaptic plasticity may cumulatively impinge on the communication and function of the HP-PFC network.

Both HP and PFC receive monosynaptic innervation of LEC, mainly originating from upper layers, while there is almost no overlap between HP-projecting and PFC-

projecting neurons (Xu et al., Revision). Moreover, optogenetic manipulation of LEC neurons activates HP activity, which further entrains the prelimbic network. At least two entorhinal pathways, directly and indirectly, exist to activate PFC. These observations provide the first insight that LEC modulation on HP and PFC might be affected differently in GE mice. Indeed, solely the number of HP-projecting neurons in LEC reduces and entorhinal drive to HP is weaker, while direct LEC-PFC communication is largely intact in GE mice. This specific alteration might be related to complex components of layer II in LEC. HP-projecting neurons lay outside PFC-projecting neurons without overlapping in layer II, and these neurons are Reelin positive and Calbindin positive, respectively. Layer II in LEC comprises a mixture of multipolar large fan cells expressing Reelin and medium-sized multipolar pyramidal neurons expressing Calbindin (Witter et al., 2017). There are subtle physiological differences between overarching Reelin and Calbindin classes (Canto and Witter, 2012; Leitner et al., 2016), which might be differently affected in GE mice. Although passive and active membrane properties of these neurons are largely unaffected, the function of their axonal projections in HP is impaired in GE mice. One possible source might be dysfunction of the LEC local circuit, supported by our observation of reduced oscillatory power and aberrant firing activity in GE mice (Xu et al., Revision). Given DISC1 gene represents an intracellular hub of multiple developmental processes (Brandon and Sawa, 2011), subtle migration and differentiation deficits cannot be excluded in the LEC of GE mice. The other possible source is that neurons in deep layers of LEC have abnormal passive and active properties in GE mice (Rebecca Kringel, unpublished observations), which might perturb the intracortical entorhinal connectivity.

These findings provide a conceptual framework for studying different neuronal populations and subtypes, their function and connectivity in the LEC-HP-PFC network and how they are affected in pathological conditions.

5.2 LEC acts as an upstream region for the HP-PFC network

LEC is critical for coding context and temporal information in associative recognition memory, whose volume abnormally decreases in psychiatric disorders (Prasad et al., 2004; Baiano et al., 2008). In addition, LEC is a favorable biomarker of mild cognitive impairment and mild Alzheimer's disease (Zhou et al., 2016). Consistent with these findings, our study confirms the presence of LEC-dependent associative behavior impairment in pre-juvenile GE mice (Xu et al., Revision), which may play a significant

role in psychopathology and cognitive disturbances of mental disorders. The LEC is most directly and bidirectionally connected to HP, which in turn are strongly connected directionally with PFC (Witter et al., 2000; Kerr et al., 2007; Agster and Burwell, 2009). Although the direct entorhinal drive to PFC is low and largely intact in neonatal GE mice, its communication diminishes indirectly. Disruption of entorhinal-hippocampal communication cannot further relay information to PFC and is sufficient to affect PFC activation (Xu et al., Revision). The big difference of direct LEC-PFC connection in developing brains from adult brains is that in adults, LEC projects to layers I, II and VI of PFC, and reciprocal projections terminate in deep layers of LEC (Jones and Witter, 2007; Agster and Burwell, 2009), while reciprocal projections from PFC to LEC do not exist in neonatal mice (Hartung et al., 2016a). The PFC connects with many cortical and subcortical areas (McGarry and Carter, 2017; Collins et al., 2018; Anastasiades et al., 2019), through which extend pathways can indirectly influence early LEC networks. These results highlight the critical role of LEC as one upstream region of HP-PFC circuits during early development and uncover a novel mechanism of prefrontal miswiring in mental disorders.

This mechanism is not fully decoupled from sensory inputs since LEC is one of the primary sources of olfactory inputs at neonatal age when blind and deaf mouse pups are not actively whiskering but have already adult-like olfactory abilities (Welker, 1964). In sensory systems, endogenous activation of the sensory periphery drives local circuitry and further entrains developing visual, barrel, or auditory cortices in oscillatory rhythms that facilitate the emergence of distinct functional topographies (Khazipov et al., 2004; Dupont et al., 2006; Hanganu et al., 2006). Knowledge gain might be instrumental for answering how non-sensory cortices, such as PFC, generate early patterns of oscillatory activity, which ensure the necessary level of excitation and activation at neonatal age that are mandatory for adult prefrontal-related behavior. Such mechanisms are irrelevant for early prefrontal oscillations; here, it seems that LEC drives activation patterns. LEC receives direct projections from OB (Xu and Wilson, 2012; Gretenkord et al., 2019). The OB processes and forwards odor information to LEC and spontaneously generates patterns of early oscillatory activity that activate LEC (Gretenkord et al., 2019; Kostka et al., 2020). Therefore, the olfactory system can control direct entorhinal drive to HP and direct and indirect drive to PFC at neonatal age. Robust olfactory deficits have been identified in schizophrenia patients and at-risk youth (Moberg et al., 2014; Takahashi et al., 2018). The reduced size of

OB and abnormal olfactory processing have been considered a byproduct of an early developmental disturbance (Turetsky et al., 2018). Thus, it can be hypothesized that disruption of LEC and its downstream limbic circuitry involved in cognitive memory is, at least in part, the result of an early miswiring of the olfactory system.

Currently, investigations of olfactory processing in mouse models of psychiatric disease are lacking. Their achievement might open new perspectives for a mechanistic understanding of the neuropathology of mental disorders.

5.3 Excitation-inhibition imbalance in psychiatric disorders

Network excitability (involving both long-range afferent from other regions and short-range fibers within local microcircuits) is central to the production of synchronized neuronal activity (Egorov and Draguhn, 2013). The excitatory connection in LEC-HP-PFC circuits is the main topic of the present thesis, while attention must be given to GABAergic interneurons and excitation-inhibition (E/I) balance.

During brain development, GABAergic interneurons generated in ganglionic eminences tangentially migrate to target brain regions and assemble into the GABAergic signaling system (Lim et al., 2018). The maturation of GABAergic circuits allows cortical networks to generate oscillations of higher amplitude and faster frequencies, eventually in the high gamma range, a hallmark of mature circuits (Bitzenhofer et al., 2020). Interneurons integrate into the developing cortex in coordination with glutamatergic pyramidal neurons to establish circuit-level E/I balance (Bartolini et al., 2013). Several studies have reported E-I imbalances selectively in PFC and consistent PFC-dependent long-term cognitive or social abilities in individuals with ASD and schizophrenia or mice carrying mutations of mental disorders risk genes (Filice et al., 2016; Robertson et al., 2016; Ajram et al., 2017; Zick et al., 2018; Sohal and Rubenstein, 2019). For example, the number of GABAergic interneurons reduces, and the typical correlation between GABA concentrations and gamma-band coherence is disrupted in their brains. Tangential migration of MGE-derived interneurons, PV cells in particular, and their function and PFC-dependent cognition are reported to be impaired following genetic perturbations of DISC1 (Steinecke et al., 2012; Delevich et al., 2020). Moreover, shifted E-I ratio arise from increased inhibition in superficial layers of PFC is recently reported in GE mice (Chini et al., 2021). Another study by transient activation of layer II/III pyramidal neurons in mice of P7-11 observes a premature growth of dendrites and spines, desynchronized firing pattern and a lower amplitude

/frequency of gamma oscillations, which might be related to PV interneurons and altered E/I balance in PFC (Bitzenhofer et al., 2021). Despite opposite effects on pyramidal neurons in the above two studies, similar diminished mPFC-dependent cognitive abilities are observed. Excitation-inhibition imbalance in PL might underlie numerous neurological and behavioral abnormalities found in GE mice.

The number of activated prefrontal neurons by stimulation of hippocampal or entorhinal terminals increases along with development, same for the number of inhibited neurons (Song et al., revision; Xu et al., revision). The increased number of activated neurons results from denser hippocampal projections and enhanced synaptic strength of glutamatergic innervation along with development (Song et al., revision), which might also be the truth for entorhinal projections. The inhibition might arise from feed-forward inhibition of interneurons directly targeted by these projections or from activated interneurons that directly connect with light-activated pyramidal neurons. Multiple mechanisms, e.g., more interneurons are recruited, synaptic strength on interneurons increases or interaction between pyramidal neurons and interneurons change along with development, might underlie the developmental alteration in the number of inhibited neurons. Of note, the ratio between activated neurons and inhibited neurons dramatically changes in GE mice since early development (Song et al., revision; Xu et al., revision; personal observation). The disrupted depression-to-facilitation shift of hippocampal inputs on layer II/III prelimbic neurons in GE mice might contribute to their inability in modulating prelimbic E/I balance (Jia et al., 2021). Another study investigating ASD mice shows that hippocampal innervation pattern in PFC changes from mainly targeting pyramidal neurons to preferentially targeting PV interneurons (Phillips et al., 2019), which is a contributing factor to aberrant HP-PFC signaling.

There is converging evidence sustaining the hypothesis that even minor deviations from normal during early development, e.g., E/I imbalance, might unify the framework for understanding circuit dysfunction characterizing psychiatric disorders (Sohal and Rubenstein, 2019). Our results provide insights into the mechanism of how upstream inputs can shape E/I balance in downstream brain areas throughout development, i.e., altering innervation patterns and strength on pyramidal neurons and interneurons.

5.4 Concluding remarks

This thesis provides several new findings of morphological and physiological features of the LEC-HP-PFC network throughout development. Multiple connectivity deficits of this network might be the underlying cause of poor cognitive performance in a mice model of psychiatric risk mediated by gene-environment interaction. We confirm and expand previous literature that CA1 pyramidal neurons of i/vHP are crucial input sources driving the maturation of the prelimbic network during early development. Sparser and less efficient hippocampal projections in PL underlie the reduction of HP-PFC communication in neonatal GE mice. These abnormalities present till pre-juvenile age, which cumulatively contributes to impairments of cognitive behavior in these mice. Importantly, LEC functions as an upstream region for the HP-PFC synchrony, and its disturbances profoundly affect the oscillatory and firing activities of HP. The impairment of entorhinal-hippocampal connectivity, such as decreased entorhinal projections and their inefficiency in entraining network activity, relays furtherly to PFC and cumulatively affects the development of PFC physiology and ultimately cause cognitive abnormalities. These findings point out cellular and synaptic mechanisms of early communication dysfunction centered in the LEC-HP-PFC network in psychiatric disorders, providing insights into how appropriate functional connectivity underlies cognitive processes. The present thesis brings us new perspectives for understanding mental disorders and is helpful for early diagnostic and design of therapeutic strategies in the end.

6 General Summary

6.1 English summary

The hippocampal-prefrontal network decoupling, which starts long before detectable symptomatology, has been implicated in the pathophysiology of neuropsychiatric disorders. Characteristics of the long-range connectivity between hippocampus and prefrontal cortex during development and its deficits in mental diseases are poorly understood. To fill this knowledge gap, combined *in vivo* and *in vitro* electrophysiology and optogenetic with in-depth morphological and behavior assessment were employed to dissect cellular mechanisms underlying hippocampal-prefrontal synchrony.

The intermediate/ventral hippocampus is found to be coupled more strongly with the prefrontal cortex than the dorsal hippocampus. Furthermore, we show that theta coupling within the hippocampal-prefrontal network is driven by prefrontal cortex-projecting pyramidal neurons in CA1, as activation of these neurons at theta rhythm leads to entrainment of the local prefrontal circuit. Employing a mouse model of combined genetic and environmental risk factors, we report that the hippocampus exhibits morphological and functional disturbances, characterized by simplified dendritic arborization, reduced synaptic density of CA1 neurons, reduced sharp waves and neuronal firing, already at neonatal age. These deficits are replicated by restricting DISC1 mutation to a subset of CA1 pyramidal neurons. Reduced hippocampal drive to the prefrontal cortex throughout development, characterized by sparser axonal projections and less efficiency of these axons, is one mechanism of hippocampal-prefrontal decoupling and is predictive of cognitive abnormalities at pre-juvenile age. The involvement of the lateral entorhinal cortex in regulating hippocampal-prefrontal communication has been investigated. We show that the lateral entorhinal cortex modulates prefrontal oscillations directly and indirectly. While the direct pathway is largely intact in the mouse model mimicking aspects of etiology of psychiatric illness, the indirect pathway is impaired specifically through the decreased entorhinal drive of the hippocampal circuit. Less and inefficient entorhinal projections that cannot relay information from lateral entorhinal cortex to prefrontal cortex are observed in hippocampus of disease mice, further disturbing the maturation of prelimbic circuit and being another fundamental mechanism underlying the cognitive disruption in mental disorders.

These results open up mechanistic insights into understanding the communication between hippocampus and prefrontal cortex throughout development. Elucidation of cellular substrates that underlie hippocampal-prefrontal information processing is crucial for understanding cognitive functions, especially their impairments in psychiatric diseases.

6.2 German summary

Die Entkopplung des hippocampalen-präfrontalen Netzwerks, die lange vor nachweisbaren Symptomen beginnt, wird mit der Pathophysiologie neuropsychiatrischer Erkrankungen in Verbindung gebracht. Die Charakteristika der interarealen Konnektivität zwischen Hippokampus und präfrontalem Kortex während der Entwicklung und ihrer Defizite bei psychischen Erkrankungen sind kaum verstanden. Um diese Wissenslücke zu schließen, wurden *in vivo* und *in vitro* Elektrophysiologie und Optogenetik mit detaillierter morphologischer Untersuchung und Verhaltensbewertung kombiniert, um zelluläre Mechanismen zu analysieren, die der hippocampalen-präfrontalen Synchronie zugrunde liegen.

Der intermediäre/ventrale Hippokampus ist stärker mit dem präfrontalen Kortex gekoppelt als der dorsale Hippokampus. Darüber hinaus zeigen wir, dass eine Kopplung im Theta Frequenzbereich innerhalb des hippocampalen-präfrontalen Netzwerks durch Pyramidenneuronen in CA1 angetrieben wird, die zum präfrontalen Kortex projizieren, da die Aktivierung dieser Neurone im Theta-Rhythmus sich auf das lokale präfrontale Netzwerk überträgt. Anhand eines Mausmodells kombinierter genetischer und umweltbedingter Risikofaktoren zeigen wir, dass der Hippokampus bereits im Neugeborenenalter morphologische und funktionelle Störungen aufweist, die durch vereinfachte dendritische Verzweigung, reduzierte synaptische Dichte von CA1-Neuronen, reduzierte Sharp-Wave Aktivität und neuronales Feuern gekennzeichnet sind. Diese Defizite werden durch die Begrenzung der DISC1-Mutation auf einen Teil der CA1 Pyramidenneurone repliziert. Ein verminderter hippocampaler Antrieb des präfrontalen Kortex während der gesamten Entwicklung, gekennzeichnet durch spärlichere axonale Projektionen und eine geringere Effizienz dieser Axone, ist ein Mechanismus der hippocampalen-präfrontalen Entkopplung und steht im direkten Zusammenhang mit kognitiven Anomalien im präjuvenilen Alter. Die Beteiligung des lateralen entorhinalen Kortex an der Regulierung der hippocampalen-präfrontalen Kommunikation wurde untersucht. Wir zeigen, dass der laterale

entorhinale Kortex präfrontale Oszillationen direkt und indirekt moduliert. Während der direkte Weg im Mausmodell, welches Aspekte der Ätiologie psychiatrischer Erkrankungen nachahmt, weitgehend intakt ist, wird der indirekte Weg speziell durch den verminderten entorhinalen Antrieb des hippocampalen Netzwerks beeinträchtigt. Weniger und ineffiziente entorhinale Projektionen, die keine Informationen vom lateralen entorhinalen Kortex zum präfrontalen Kortex weiterleiten können, wurden im Hippokampus erkrankter Mäuse beobachtet, was die Reifung des prälimbischen Netzwerks weiter stört und ein weiterer grundlegender Mechanismus ist, der kognitiven Störungen bei psychiatrischen Erkrankungen zugrunde liegt.

Diese Ergebnisse eröffnen mechanistische Einblicke in das Verständnis der Kommunikation zwischen Hippokampus und präfrontalem Kortex während der Entwicklung. Die Aufklärung der zellulären Elemente, die der hippocampalen-präfrontalen Informationsverarbeitung zugrunde liegen, ist entscheidend für das Verständnis kognitiver Funktionen und insbesondere ihrer Beeinträchtigung bei psychiatrischen Erkrankungen.

7 Bibliography

- Abbott LF, Regehr WG (2004) Synaptic computation. *Nature* 431:796-803.
- Adhikari A, Topiwala MA, Gordon JA (2010) Synchronized activity between the ventral hippocampus and the medial prefrontal cortex during anxiety. *Neuron* 65:257-269.
- Agster KL, Burwell RD (2009) Cortical efferents of the perirhinal, postrhinal, and entorhinal cortices of the rat. *Hippocampus* 19:1159-1186.
- Ahlbeck J, Song L, Chini M, Bitzenhofer SH, Hanganu-Opatz IL (2018) Glutamatergic drive along the septo-temporal axis of hippocampus boosts prelimbic oscillations in the neonatal mouse. *Elife* 7:e33158.
- Ajram LA, Horder J, Mendez MA, Galanopoulos A, Brennan LP, Wichers RH, Robertson DM, Murphy CM, Zinkstok J, Ivin G, Heasman M, Meek D, Tricklebank MD, Barker GJ, Lythgoe DJ, Edden RAE, Williams SC, Murphy DGM, McAlonan GM (2017) Shifting brain inhibitory balance and connectivity of the prefrontal cortex of adults with autism spectrum disorder. *Transl Psychiatry* 7:e1137.
- Allene C, Cattani A, Ackman JB, Bonifazi P, Aniksztejn L, Ben-Ari Y, Cossart R (2008) Sequential generation of two distinct synapse-driven network patterns in developing neocortex. *J Neurosci* 28:12851-12863.
- Amaral D, Lavenex P (2006) "Hippocampal Neuroanatomy". In: Andersen, P., Morris, R., Amaral, D., Bliss, T. and O'Keefe, J., *The Hippocampus Book*. Oxford University Press, Oxford:37-115.
- Amaral DG, Witter MP (1989) The three-dimensional organization of the hippocampal formation: a review of anatomical data. *Neuroscience* 31:571-591.
- American Psychiatric Association (2013) *Diagnostic and Statistical Manual of Mental Disorders: Fifth Edition*. Arlington: American Psychiatric Association.
- Anastasiades PG, Boada C, Carter AG (2019) Cell-Type-Specific D1 Dopamine Receptor Modulation of Projection Neurons and Interneurons in the Prefrontal Cortex. *Cereb Cortex* 29:3224-3242.
- Anderson CM, Torres F, Faoro A (1985) The EEG of the early premature. *Electroencephalogr Clin Neurophysiol* 60:95-105.
- Anderson P, Morris R, Amaral D, Bliss T, O'Keefe J (2006) "The hippocampal formation". In: Andersen, P., Morris, R., Amaral, D., Bliss, T. and O'Keefe, J., *The Hippocampus Book*. Oxford University Press, Oxford.
- Axmacher N, Henseler MM, Jensen O, Weinreich I, Elger CE, Fell J (2010) Cross-frequency coupling supports multi-item working memory in the human hippocampus. *Proc Natl Acad Sci USA* 107:3228-3233.
- Baccalá LA, Sameshima K (2001) Partial directed coherence: a new concept in neural structure determination. *Biological cybernetics* 84:463-474.
- Bahner F, Demanuele C, Schweiger J, Gerchen MF, Zamoscik V, Ueltzhoffer K, Hahn T, Meyer P, Flor H, Durstewitz D, Tost H, Kirsch P, Plichta MM, Meyer-Lindenberg A (2015) Hippocampal-dorsolateral prefrontal coupling as a species-conserved cognitive mechanism: a human translational imaging study. *Neuropsychopharmacology* 40:1674-1681.
- Baiano M, Perlini C, Rambaldelli G, Cerini R, Dusi N, Bellani M, Spezzapria G, Versace A, Balestrieri M, Mucelli RP, Tansella M, Brambilla P (2008) Decreased entorhinal cortex volumes in schizophrenia. *Schizophr Res* 102:171-180.
- Bannerman DM, Rawlins JN, McHugh SB, Deacon RM, Yee BK, Bast T, Zhang WN, Pothuizen HH, Feldon J (2004) Regional dissociations within the hippocampus--memory and anxiety. *Neurosci Biobehav Rev* 28:273-283.

- Barnea-Goraly N, Raman M, Mazaika P, Marzelli M, Hershey T, Weinzimer SA, Aye T, Buckingham B, Mauras N, White NH, Fox LA, Tansey M, Beck RW, Ruedy KJ, Kollman C, Cheng P, Reiss AL, Diabetes Research in Children N (2014) Alterations in white matter structure in young children with type 1 diabetes. *Diabetes Care* 37:332-340.
- Bartolini G, Ciceri G, Marin O (2013) Integration of GABAergic interneurons into cortical cell assemblies: lessons from embryos and adults. *Neuron* 79:849-864.
- Behrens MM, Ali SS, Dao DN, Lucero J, Shekhtman G, Quick KL, Dugan LL (2007) Ketamine-induced loss of phenotype of fast-spiking interneurons is mediated by NADPH-oxidase. *Science* 318:1645-1647.
- Behuet S, Cremer JN, Cremer M, Palomero-Gallagher N, Zilles K, Amunts K (2019) Developmental Changes of Glutamate and GABA Receptor Densities in Wistar Rats. *Front Neuroanat* 13:100.
- Bell MJ, Hallenbeck JM (2002) Effects of intrauterine inflammation on developing rat brain. *J Neurosci Res* 70:570-579.
- Ben-Ari Y (2002) Excitatory actions of gaba during development: the nature of the nurture. *Nat Rev Neurosci* 3:728-739.
- Benchenane K, Peyrache A, Khamassi M, Tierney PL, Gioanni Y, Battaglia FP, Wiener SI (2010) Coherent theta oscillations and reorganization of spike timing in the hippocampal- prefrontal network upon learning. *Neuron* 66:921-936.
- Benetti S, Mechelli A, Picchioni M, Broome M, Williams S, McGuire P (2009) Functional integration between the posterior hippocampus and prefrontal cortex is impaired in both first episode schizophrenia and the at risk mental state. *Brain* 132:2426-2436.
- Birnbaum R, Weinberger DR (2017) Genetic insights into the neurodevelopmental origins of schizophrenia. *Nat Rev Neurosci* 18:727-740.
- Bitzenhofer SH, Popplau JA, Hanganu-Opatz I (2020) Gamma activity accelerates during prefrontal development. *Elife* 9:e56795.
- Bitzenhofer SH, Popplau JA, Chini M, Marquardt A, Hanganu-Opatz IL (2021) A transient developmental increase in prefrontal activity alters network maturation and causes cognitive dysfunction in adult mice. *Neuron* 109:1350-1364 e1356.
- Bitzenhofer SH, Ahlbeck J, Wolff A, Wiegert JS, Gee CE, Oertner TG, Hanganu-Opatz IL (2017) Layer-specific optogenetic activation of pyramidal neurons causes beta-gamma entrainment of neonatal networks. *Nat Commun* 8:14563.
- Blankenship AG, Feller MB (2010) Mechanisms underlying spontaneous patterned activity in developing neural circuits. *Nat Rev Neurosci* 11:18-29.
- Blanton MG, Lo Turco JJ, Kriegstein AR (1990) Endogenous neurotransmitter activates N-methyl-D-aspartate receptors on differentiating neurons in embryonic cortex. *Proc Natl Acad Sci USA* 87:8027-8030.
- Bota M, Dong HW, Swanson LW (2005) Brain architecture management system. *Neuroinformatics* 3:15-48.
- Bragin A, Jandó G, Nádasdy Z, Hetke J, Wise K, Buzsáki G (1995) Gamma (40-100 Hz) oscillation in the hippocampus of the behaving rat. *J Neurosci* 15:47-60.
- Brandon NJ, Sawa A (2011) Linking neurodevelopmental and synaptic theories of mental illness through DISC1. *Nat Rev Neurosci* 12:707-722.
- Brockmann MD, Poschel B, Cichon N, Hanganu-Opatz IL (2011) Coupled oscillations mediate directed interactions between prefrontal cortex and hippocampus of the neonatal rat. *Neuron* 71:332-347.
- Brown AS (2012) Epidemiologic studies of exposure to prenatal infection and risk of schizophrenia and autism. *Dev Neurobiol* 72:1272-1276.

- Buzsáki G, Draguhn A (2004) Neuronal oscillations in cortical networks. *Science* 304:1926-1929.
- Buzsáki G, Wang XJ (2012) Mechanisms of gamma oscillations. *Annu Rev Neurosci* 35:203-225.
- Buzsáki G, Anastassiou CA, Koch C (2012) The origin of extracellular fields and currents--EEG, ECoG, LFP and spikes. *Nat Rev Neurosci* 13:407-420.
- Buzsáki G (1986) Hippocampal sharp waves: their origin and significance. *Brain research* 398:242-252.
- Buzsáki G (2002) Theta oscillations in the hippocampus. *Neuron* 33:325-340.
- Buzsáki G, Watson BO (2012) Brain rhythms and neural syntax: implications for efficient coding of cognitive content and neuropsychiatric disease. *Dialogues in clinical neuroscience* 14:345-367.
- Buzsáki G, Leung LW, Vanderwolf CH (1983) Cellular bases of hippocampal EEG in the behaving rat. *Brain research* 287:139-171.
- Cabungcal JH, Counotte DS, Lewis E, Tejeda HA, Piantadosi P, Pollock C, Calhoon GG, Sullivan E, Presgraves E, Kil J, Hong LE, Cuenod M, Do KQ, O'Donnell P (2014) Juvenile antioxidant treatment prevents adult deficits in a developmental model of schizophrenia. *Neuron* 83:1073-1084.
- Canto CB, Witter MP (2012) Cellular properties of principal neurons in the rat entorhinal cortex. I. The lateral entorhinal cortex. *Hippocampus* 22:1256-1276.
- Canto CB, Wouterlood FG, Witter MP (2008) What does the anatomical organization of the entorhinal cortex tell us? *Neural Plast* 2008:381243.
- Cappaert NLM, Van Strien NM, Witter MP (2015) Hippocampal Formation. In: *The Rat Nervous System*, pp 511-573.
- Carlen M (2017) What constitutes the prefrontal cortex? *Science* 358:478-482.
- Chao HT, Chen H, Samaco RC, Xue M, Chahrour M, Yoo J, Neul JL, Gong S, Lu HC, Heintz N, Ekker M, Rubenstein JL, Noebels JL, Rosenmund C, Zoghbi HY (2010) Dysfunction in GABA signalling mediates autism-like stereotypies and Rett syndrome phenotypes. *Nature* 468:263-269.
- Cheriyian J, Kaushik MK, Ferreira AN, Sheets PL (2016) Specific Targeting of the Basolateral Amygdala to Projectionally Defined Pyramidal Neurons in Prelimbic and Infralimbic Cortex. *eNeuro* 3.
- Chini M, Pfeffer T, Hanganu-Opatz IL (2021) Developmental increase of inhibition drives decorrelation of neural activity. *bioRxiv*.
- Chini M, Popplau JA, Lindemann C, Carol-Perdiguer L, Hnida M, Oberlander V, Xu X, Ahlbeck J, Bitzenhofer SH, Mulert C, Hanganu-Opatz IL (2020) Resolving and Rescuing Developmental Miswiring in a Mouse Model of Cognitive Impairment. *Neuron* 105:60-74 e67.
- Cichon NB, Denker M, Grun S, Hanganu-Opatz IL (2014) Unsupervised classification of neocortical activity patterns in neonatal and pre-juvenile rodents. *Front Neural Circuits* 8:50.
- Clancy B, Darlington RB, Finlay BL (2001) Translating developmental time across mammalian species. *Neuroscience* 105:7-17.
- Cloarec R, Riffault B, Dufour A, Rabiei H, Gouty-Colomer LA, Dumon C, Guimond D, Bonifazi P, Eftekhari S, Lozovaya N, Ferrari DC, Ben-Ari Y (2019) Pyramidal neuron growth and increased hippocampal volume during labor and birth in autism. *Sci Adv* 5:eaav0394.
- Colgin LL (2015) Theta-gamma coupling in the entorhinal-hippocampal system. *Curr Opin Neurobiol* 31:45-50.
- Colgin LL (2016) Rhythms of the hippocampal network. *Nat Rev Neurosci* 17:239-249.

- Colgin LL, Denninger T, Fyhn M, Hafting T, Bonnevie T, Jensen O, Moser MB, Moser EI (2009) Frequency of gamma oscillations routes flow of information in the hippocampus. *Nature* 462:353-357.
- Collins DP, Anastasiades PG, Marlin JJ, Carter AG (2018) Reciprocal Circuits Linking the Prefrontal Cortex with Dorsal and Ventral Thalamic Nuclei. *Neuron* 98:366-379 e364.
- Cooper RA, Richter FR, Bays PM, Plaisted-Grant KC, Baron-Cohen S, Simons JS (2017) Reduced Hippocampal Functional Connectivity During Episodic Memory Retrieval in Autism. *Cereb Cortex* 27:888-902.
- Cox DD, Dean T (2014) Neural networks and neuroscience-inspired computer vision. *Curr Biol* 24:R921-R929.
- Crabtree GW, Sun Z, Kvajo M, Broek JA, Fenelon K, McKellar H, Xiao L, Xu B, Bahn S, O'Donnell JM, Gogos JA (2017) Alteration of Neuronal Excitability and Short-Term Synaptic Plasticity in the Prefrontal Cortex of a Mouse Model of Mental Illness. *J Neurosci* 37:4158-4180.
- Crepel V, Aronov D, Jorquera I, Represa A, Ben-Ari Y, Cossart R (2007) A parturition-associated nonsynaptic coherent activity pattern in the developing hippocampus. *Neuron* 54:105-120.
- Delevich K, Jaaro-Peled H, Penzo M, Sawa A, Li B (2020) Parvalbumin Interneuron Dysfunction in a Thalamo-Prefrontal Cortical Circuit in *Disc1* Locus Impairment Mice. *eNeuro* 7.
- Deshmukh SS, Knierim JJ (2011) Representation of non-spatial and spatial information in the lateral entorhinal cortex. *Front Behav Neurosci* 5:69.
- Dupont E, Hanganu IL, Kilb W, Hirsch S, Luhmann HJ (2006) Rapid developmental switch in the mechanisms driving early cortical columnar networks. *Nature* 439:79-83.
- Egorov AV, Draguhn A (2013) Development of coherent neuronal activity patterns in mammalian cortical networks: common principles and local heterogeneity. *Mech Dev* 130:412-423.
- Eichenbaum H, Yonelinas AP, Ranganath C (2007) The medial temporal lobe and recognition memory. *Annu Rev Neurosci* 30:123-152.
- Ennaceur A, Delacour J (1988) A new one-trial test for neurobiological studies of memory in rats. 1: Behavioral data. *Behavioural brain research* 31:47-59.
- Fanselow MS, Dong HW (2010) Are the dorsal and ventral hippocampus functionally distinct structures? *Neuron* 65:7-19.
- Feinberg I (1982) Schizophrenia: caused by a fault in programmed synaptic elimination during adolescence? *J Psychiatr Res* 17:319-334.
- Feller MB, Scanziani M (2005) A precritical period for plasticity in visual cortex. *Curr Opin Neurobiol* 15:94-100.
- Fernández-Ruiz A, Oliva A, Fermino de Oliveira E, Rocha-Almeida F, Tingley D, Buzsáki G (2019) Long-duration hippocampal sharp wave ripples improve memory. *Science* 364:1082-1086.
- Filice F, Vorckel KJ, Sungur AO, Wohr M, Schwaller B (2016) Reduction in parvalbumin expression not loss of the parvalbumin-expressing GABA interneuron subpopulation in genetic parvalbumin and shank mouse models of autism. *Mol Brain* 9:10.
- Flint AC, Dammerman RS, Kriegstein AR (1999) Endogenous activation of metabotropic glutamate receptors in neocortical development causes neuronal calcium oscillations. *Proc Natl Acad Sci USA* 96:12144-12149.

- Flores R, 3rd, Hirota Y, Armstrong B, Sawa A, Tomoda T (2011) DISC1 regulates synaptic vesicle transport via a lithium-sensitive pathway. *Neurosci Res* 71:71-77.
- Freund TF, Antal M (1988) GABA-containing neurons in the septum control inhibitory interneurons in the hippocampus. *Nature* 336:170-173.
- Fuster JM (2000) Executive frontal functions. *Exp Brain Res* 133:66-70.
- Fuster JM, Bressler SL (2015) Past makes future: role of pFC in prediction. *J Cogn Neurosci* 27:639-654.
- Gabbott PL, Warner TA, Jays PR, Salway P, Busby SJ (2005) Prefrontal cortex in the rat: projections to subcortical autonomic, motor, and limbic centers. *J Comp Neurol* 492:145-177.
- Garaschuk O, Linn J, Eilers J, Konnerth A (2000) Large-scale oscillatory calcium waves in the immature cortex. *Nat Neurosci* 3:452-459.
- Genovese G, Fromer M, Stahl EA, Ruderfer DM, Chambert K, Landen M, Moran JL, Purcell SM, Sklar P, Sullivan PF, Hultman CM, McCarroll SA (2016) Increased burden of ultra-rare protein-altering variants among 4,877 individuals with schizophrenia. *Nat Neurosci* 19:1433-1441.
- Giovanoli S, Engler H, Engler A, Richetto J, Voget M, Willi R, Winter C, Riva MA, Mortensen PB, Feldon J, Schedlowski M, Meyer U (2013) Stress in puberty unmasks latent neuropathological consequences of prenatal immune activation in mice. *Science* 339:1095-1099.
- Girardeau G, Benchenane K, Wiener SI, Buzsaki G, Zugaro MB (2009) Selective suppression of hippocampal ripples impairs spatial memory. *Nat Neurosci* 12:1222-1223.
- Godsil BP, Kiss JP, Spedding M, Jay TM (2013) The hippocampal-prefrontal pathway: the weak link in psychiatric disorders? *Eur Neuropsychopharmacol* 23:1165-1181.
- Grayton HM, Fernandes C, Rujescu D, Collier DA (2012) Copy number variations in neurodevelopmental disorders. *Prog Neurobiol* 99:81-91.
- Gretenkord S, Kostka JK, Hartung H, Watznauer K, Fleck D, Minier-Toribio A, Spehr M, Hanganu-Opatz IL (2019) Coordinated electrical activity in the olfactory bulb gates the oscillatory entrainment of entorhinal networks in neonatal mice. *PLoS Biol* 17:e2006994.
- Griguoli M, Cherubini E (2017) Early Correlated Network Activity in the Hippocampus: Its Putative Role in Shaping Neuronal Circuits. *Front Cell Neurosci* 11:255.
- Hafting T, Fyhn M, Molden S, Moser MB, Moser EI (2005) Microstructure of a spatial map in the entorhinal cortex. *Nature* 436:801-806.
- Hanganu-Opatz IL (2010) Between molecules and experience: role of early patterns of coordinated activity for the development of cortical maps and sensory abilities. *Brain Res Rev* 64:160-176.
- Hanganu IL, Ben-Ari Y, Khazipov R (2006) Retinal waves trigger spindle bursts in the neonatal rat visual cortex. *J Neurosci* 26:6728-6736.
- Hartung H, Brockmann MD, Poschel B, De Feo V, Hanganu-Opatz IL (2016a) Thalamic and Entorhinal Network Activity Differently Modulates the Functional Development of Prefrontal-Hippocampal Interactions. *J Neurosci* 36:3676-3690.
- Hartung H, Cichon N, De Feo V, Riemann S, Schildt S, Lindemann C, Mulert C, Gogos JA, Hanganu-Opatz IL (2016b) From Shortage to Surge: A Developmental Switch in Hippocampal-Prefrontal Coupling in a Gene-Environment Model of Neuropsychiatric Disorders. *Cereb Cortex* 26:4265-4281.

- Hartwich K, Pollak T, Klausberger T (2009) Distinct firing patterns of identified basket and dendrite-targeting interneurons in the prefrontal cortex during hippocampal theta and local spindle oscillations. *J Neurosci* 29:9563-9574.
- Herweg NA, Aritz T, Leicht G, Mulert C, Fuentemilla L, Bunzeck N (2016) Theta-Alpha Oscillations Bind the Hippocampus, Prefrontal Cortex, and Striatum during Recollection: Evidence from Simultaneous EEG-fMRI. *J Neurosci* 36:3579-3587.
- Heyser CJ, Ferris JS (2013) Object exploration in the developing rat: methodological considerations. *Developmental psychobiology* 55:373-381.
- Hirvonen J, Kreisl WC, Fujita M, Dustin I, Khan O, Appel S, Zhang Y, Morse C, Pike VW, Innis RB, Theodore WH (2012) Increased in vivo expression of an inflammatory marker in temporal lobe epilepsy. *J Nucl Med* 53:234-240.
- Hoover WB, Vertes RP (2007) Anatomical analysis of afferent projections to the medial prefrontal cortex in the rat. *Brain Struct Funct* 212:149-179.
- Igarashi KM, Lu L, Colgin LL, Moser MB, Moser EI (2014) Coordination of entorhinal-hippocampal ensemble activity during associative learning. *Nature* 510:143-147.
- Insausti R, Amaral DG (2004) Hippocampal Formation. In: *The Human Nervous System*, pp 871-914.
- Insausti R, Herrero MT, Witter MP (1997) Entorhinal cortex of the rat: cytoarchitectonic subdivisions and the origin and distribution of cortical efferents. *Hippocampus* 7:146-183.
- Insel TR (2010) Rethinking schizophrenia. *Nature* 468:187-193.
- Jay TM, Witter MP (1991) Distribution of hippocampal CA1 and subicular efferents in the prefrontal cortex of the rat studied by means of anterograde transport of Phaseolus vulgaris-leucoagglutinin. *J Comp Neurol* 313:574-586.
- Ji K, Miyauchi J, Tsirka SE (2013) Microglia: an active player in the regulation of synaptic activity. *Neural Plast* 2013:627325.
- Jia DW, Costa RP, Vogels TP (2021) Developmental depression-facilitation shift controls excitation-inhibition balance. *bioRxiv*.
- Jones BF, Witter MP (2007) Cingulate cortex projections to the parahippocampal region and hippocampal formation in the rat. *Hippocampus* 17:957-976.
- Kahn RS (2020) On the Origins of Schizophrenia. *Am J Psychiatry* 177:291-297.
- Karlsson KA, Mohs EJ, di Prisco GV, Blumberg MS (2006) On the co-occurrence of startles and hippocampal sharp waves in newborn rats. *Hippocampus* 16:959-965.
- Keresztes A, Ngo CT, Lindenberger U, Werkle-Bergner M, Newcombe NS (2018) Hippocampal Maturation Drives Memory from Generalization to Specificity. *Trends Cogn Sci* 22:676-686.
- Kerr KM, Agster KL, Furtak SC, Burwell RD (2007) Functional neuroanatomy of the parahippocampal region: the lateral and medial entorhinal areas. *Hippocampus* 17:697-708.
- Khazipov R, Sirota A, Leinekugel X, Holmes GL, Ben-Ari Y, Buzsáki G (2004) Early motor activity drives spindle bursts in the developing somatosensory cortex. *Nature* 432:758-761.
- Kilb W, Kirischuk S, Luhmann HJ (2011) Electrical activity patterns and the functional maturation of the neocortex. *Eur J Neurosci* 34:1677-1686.
- Kirmse K, Kummer M, Kovalchuk Y, Witte OW, Garaschuk O, Holthoff K (2015) GABA depolarizes immature neurons and inhibits network activity in the neonatal neocortex in vivo. *Nat Commun* 6:7750.
- Kjelstrup KB, Solstad T, Brun VH, Hafting T, Leutgeb S, Witter MP, Moser EI, Moser MB (2008) Finite scale of spatial representation in the hippocampus. *Science* 321:140-143.

- Knierim JJ, Neunuebel JP, Deshmukh SS (2014) Functional correlates of the lateral and medial entorhinal cortex: objects, path integration and local-global reference frames. *Philos Trans R Soc Lond B Biol Sci* 369:20130369.
- Knuesel I, Chicha L, Britschgi M, Schobel SA, Bodmer M, Hellings JA, Toovey S, Prinssen EP (2014) Maternal immune activation and abnormal brain development across CNS disorders. *Nat Rev Neurol* 10:643-660.
- Kolluri N, Sun Z, Sampson AR, Lewis DA (2005) Lamina-specific reductions in dendritic spine density in the prefrontal cortex of subjects with schizophrenia. *Am J Psychiatry* 162:1200-1202.
- Komuro H, Rakic P (1996) Intracellular Ca²⁺ fluctuations modulate the rate of neuronal migration. *Neuron* 17:275-285.
- Kostka JK, Gretenkord S, Spehr M, Hanganu-Opatz IL (2020) Bursting mitral cells time the oscillatory coupling between olfactory bulb and entorhinal networks in neonatal mice. *J Physiol* 598:5753-5769.
- Krstic D, Madhusudan A, Doehner J, Vogel P, Notter T, Imhof C, Manalastas A, Hilfiker M, Pfister S, Schwerdel C, Riether C, Meyer U, Knuesel I (2012) Systemic immune challenges trigger and drive Alzheimer-like neuropathology in mice. *J Neuroinflammation* 9:151.
- Kruger HS, Brockmann MD, Salamon J, Ittrich H, Hanganu-Opatz IL (2012) Neonatal hippocampal lesion alters the functional maturation of the prefrontal cortex and the early cognitive development in pre-juvenile rats. *Neurobiol Learn Mem* 97:470-481.
- Kvajo M, McKellar H, Arguello PA, Drew LJ, Moore H, MacDermott AB, Karayiorgou M, Gogos JA (2008) A mutation in mouse *Disc1* that models a schizophrenia risk allele leads to specific alterations in neuronal architecture and cognition. *Proc Natl Acad Sci USA* 105:7076-7081.
- Kvajo M, McKellar H, Drew LJ, Lepagnol-Bestel AM, Xiao L, Levy RJ, Blazeski R, Arguello PA, Lacefield CO, Mason CA, Simonneau M, O'Donnell JM, MacDermott AB, Karayiorgou M, Gogos JA (2011) Altered axonal targeting and short-term plasticity in the hippocampus of *Disc1* mutant mice. *Proc Natl Acad Sci USA* 108:E1349-1358.
- Lasztocki B, Klausberger T (2014) Layer-specific GABAergic control of distinct gamma oscillations in the CA1 hippocampus. *Neuron* 81:1126-1139.
- Laubach M, Amarante LM, Swanson K, White SR (2018) What, If Anything, Is Rodent Prefrontal Cortex? *eNeuro* 5.
- Lazaro MT et al. (2019) Reduced Prefrontal Synaptic Connectivity and Disturbed Oscillatory Population Dynamics in the *CNTNAP2* Model of Autism. *Cell Rep* 27:2567-2578 e2566.
- Lee AR, Kim JH, Cho E, Kim M, Park M (2017) Dorsal and Ventral Hippocampus Differentiate in Functional Pathways and Differentially Associate with Neurological Disease-Related Genes during Postnatal Development. *Front Mol Neurosci* 10:331.
- Leinekugel X, Khazipov R, Cannon R, Hirase H, Ben-Ari Y, Buzsáki G (2002) Correlated bursts of activity in the neonatal hippocampus in vivo. *Science* 296:2049-2052.
- Leitner FC, Melzer S, Lutcke H, Pinna R, Seeburg PH, Helmchen F, Monyer H (2016) Spatially segregated feedforward and feedback neurons support differential odor processing in the lateral entorhinal cortex. *Nat Neurosci* 19:935-944.
- Lema Tome CM, Tyson T, Rey NL, Grathwohl S, Britschgi M, Brundin P (2013) Inflammation and alpha-synuclein's prion-like behavior in Parkinson's disease--is there a link? *Mol Neurobiol* 47:561-574.

- Lieberman JA, Perkins D, Belger A, Chakos M, Jarskog F, Boteva K, Gilmore J (2001) The early stages of schizophrenia: speculations on pathogenesis, pathophysiology, and therapeutic approaches. *Biol Psychiatry* 50:884-897.
- Lim L, Mi D, Llorca A, Marin O (2018) Development and Functional Diversification of Cortical Interneurons. *Neuron* 100:294-313.
- Liu X, Dimidschstein J, Fishell G, Carter AG (2020) Hippocampal inputs engage CCK+ interneurons to mediate endocannabinoid-modulated feed-forward inhibition in the prefrontal cortex. *Elife* 9.
- Long Z, Duan X, Mantini D, Chen H (2016) Alteration of functional connectivity in autism spectrum disorder: effect of age and anatomical distance. *Sci Rep* 6:26527.
- Maharajh K, Teale P, Rojas DC, Reite ML (2010) Fluctuation of gamma-band phase synchronization within the auditory cortex in schizophrenia. *Clinical Neurophysiology* 121:542-548.
- Maingret N, Girardeau G, Todorova R, Goutierre M, Zugaro M (2016) Hippocampocortical coupling mediates memory consolidation during sleep. *Nat Neurosci* 19:959-964.
- Marek R, Jin J, Goode TD, Giustino TF, Wang Q, Acca GM, Holehonnur R, Ploski JE, Fitzgerald PJ, Lynagh T, Lynch JW, Maren S, Sah P (2018) Hippocampus-driven feed-forward inhibition of the prefrontal cortex mediates relapse of extinguished fear. *Nat Neurosci* 21:384-392.
- McCabe AK, Easton CR, Lischalk JW, Moody WJ (2007) Roles of glutamate and GABA receptors in setting the developmental timing of spontaneous synchronized activity in the developing mouse cortex. *Dev Neurobiol* 67:1574-1588.
- McGarry LM, Carter AG (2017) Prefrontal Cortex Drives Distinct Projection Neurons in the Basolateral Amygdala. *Cell Rep* 21:1426-1433.
- McGlashan TH (1996) Early detection and intervention in schizophrenia: research. *Schizophr Bull* 22:327-345.
- McGrath JJ, Eyles DW, Pedersen CB, Anderson C, Ko P, Burne TH, Norgaard-Pedersen B, Hougaard DM, Mortensen PB (2010) Neonatal vitamin D status and risk of schizophrenia: a population-based case-control study. *Arch Gen Psychiatry* 67:889-894.
- Meier MH, Caspi A, Reichenberg A, Keefe RS, Fisher HL, Harrington H, Houts R, Poulton R, Moffitt TE (2014) Neuropsychological decline in schizophrenia from the premorbid to the postonset period: evidence from a population-representative longitudinal study. *Am J Psychiatry* 171:91-101.
- Meyer-Lindenberg AS, Olsen RK, Kohn PD, Brown T, Egan MF, Weinberger DR, Berman KF (2005) Regionally specific disturbance of dorsolateral prefrontal-hippocampal functional connectivity in schizophrenia. *Arch Gen Psychiatry* 62:379-386.
- Milad MR, Wright CI, Orr SP, Pitman RK, Quirk GJ, Rauch SL (2007) Recall of fear extinction in humans activates the ventromedial prefrontal cortex and hippocampus in concert. *Biol Psychiatry* 62:446-454.
- Millar JK, Wilson-Annan JC, Anderson S, Christie S, Taylor MS, Semple CA, Devon RS, St Clair DM, Muir WJ, Blackwood DH, Porteous DJ (2000) Disruption of two novel genes by a translocation co-segregating with schizophrenia. *Hum Mol Genet* 9:1415-1423.
- Miller EK, Cohen JD (2001) An integrative theory of prefrontal cortex function. *Annu Rev Neurosci* 24:167-202.

- Minzenberg MJ, Laird AR, Thelen S, Carter CS, Glahn DC (2009) Meta-analysis of 41 functional neuroimaging studies of executive function in schizophrenia. *Arch Gen Psychiatry* 66:811-822.
- Moberg PJ, Kamath V, Marchetto DM, Calkins ME, Doty RL, Hahn CG, Borgmann-Winter KE, Kohler CG, Gur RE, Turetsky BI (2014) Meta-analysis of olfactory function in schizophrenia, first-degree family members, and youths at-risk for psychosis. *Schizophr Bull* 40:50-59.
- Mohns EJ, Blumberg MS (2010) Neocortical activation of the hippocampus during sleep in infant rats. *J Neurosci* 30:3438-3449.
- Montchal ME, Reagh ZM, Yassa MA (2019) Precise temporal memories are supported by the lateral entorhinal cortex in humans. *Nat Neurosci* 22:284-288.
- Morris JA, Kandpal G, Ma L, Austin CP (2003) DISC1 (Disrupted-In-Schizophrenia 1) is a centrosome-associated protein that interacts with MAP1A, MIPT3, ATF4/5 and NUDEL: regulation and loss of interaction with mutation. *Hum Mol Genet* 12:1591-1608.
- Mukai J, Tamura M, Fenelon K, Rosen AM, Spellman TJ, Kang R, MacDermott AB, Karayiorgou M, Gordon JA, Gogos JA (2015) Molecular substrates of altered axonal growth and brain connectivity in a mouse model of schizophrenia. *Neuron* 86:680-695.
- Murata Y, Colonnese MT (2020) GABAergic interneurons excite neonatal hippocampus in vivo. *Sci Adv* 6:eaba1430.
- Nadarajah B, Parnavelas JG (2002) Modes of neuronal migration in the developing cerebral cortex. *Nat Rev Neurosci* 3:423-432.
- Nelson MD, Saykin AJ, Flashman LA, Riordan HJ (1998) Hippocampal volume reduction in schizophrenia as assessed by magnetic resonance imaging: a meta-analytic study. *Arch Gen Psychiatry* 55:433-440.
- Ngo CT, Alm KH, Metoki A, Hampton W, Riggins T, Newcombe NS, Olson IR (2017) White matter structural connectivity and episodic memory in early childhood. *Dev Cogn Neurosci* 28:41-53.
- Nilssen ES, Doan TP, Nigro MJ, Ohara S, Witter MP (2019) Neurons and networks in the entorhinal cortex: A reappraisal of the lateral and medial entorhinal subdivisions mediating parallel cortical pathways. *Hippocampus* 29:1238-1254.
- Niwa M, Kamiya A, Murai R, Kubo K, Gruber AJ, Tomita K, Lu L, Tomisato S, Jaaro-Peled H, Seshadri S, Hiyama H, Huang B, Kohda K, Noda Y, O'Donnell P, Nakajima K, Sawa A, Nabeshima T (2010) Knockdown of DISC1 by in utero gene transfer disturbs postnatal dopaminergic maturation in the frontal cortex and leads to adult behavioral deficits. *Neuron* 65:480-489.
- O'Mara SM, Commins S, Anderson M, Gigg J (2001) The subiculum: a review of form, physiology and function. *Prog Neurobiol* 64:129-155.
- O'Neill PK, Gordon JA, Sigurdsson T (2013) Theta oscillations in the medial prefrontal cortex are modulated by spatial working memory and synchronize with the hippocampus through its ventral subregion. *J Neurosci* 33:14211-14224.
- Oberlander VC, Xu X, Chini M, Hanganu-Opatz IL (2019) Developmental dysfunction of prefrontal-hippocampal networks in mouse models of mental illness. *Eur J Neurosci* 50:3072-3084.
- Owen MJ, Sawa A, Mortensen PB (2016) Schizophrenia. *The Lancet* 388:86-97.
- Padilla-Coreano N, Canetta S, Mikofsky RM, Alway E, Passecker J, Myroshnychenko MV, Garcia-Garcia AL, Warren R, Teboul E, Blackman DR, Morton MP, Hupalo S, Tye KM, Kellendonk C, Kupferschmidt DA, Gordon JA (2019) Hippocampal-Prefrontal Theta Transmission Regulates Avoidance Behavior. *Neuron* 104:601-610 e604.

- Paintlia MK, Paintlia AS, Barbosa E, Singh I, Singh AK (2004) N-acetylcysteine prevents endotoxin-induced degeneration of oligodendrocyte progenitors and hypomyelination in developing rat brain. *J Neurosci Res* 78:347-361.
- Paolicelli RC, Bolasco G, Pagani F, Maggi L, Scianni M, Panzanelli P, Giustetto M, Ferreira TA, Guiducci E, Dumas L, Ragozzino D, Gross CT (2011) Synaptic pruning by microglia is necessary for normal brain development. *Science* 333:1456-1458.
- Paus T, Keshavan M, Giedd JN (2008) Why do many psychiatric disorders emerge during adolescence? *Nat Rev Neurosci* 9:947-957.
- Phillips ML, Robinson HA, Pozzo-Miller L (2019) Ventral hippocampal projections to the medial prefrontal cortex regulate social memory. *Elife* 8:e44182.
- Place R, Farovik A, Brockmann M, Eichenbaum H (2016) Bidirectional prefrontal-hippocampal interactions support context-guided memory. *Nat Neurosci* 19:992-994.
- Poulton R, Caspi A, Moffitt TE, Cannon M, Murray R, Harrington H (2000) Children's self-reported psychotic symptoms and adult schizophreniform disorder: a 15-year longitudinal study. *Arch Gen Psychiatry* 57:1053-1058.
- Prasad KM, Patel AR, Muddasani S, Sweeney J, Keshavan MS (2004) The entorhinal cortex in first-episode psychotic disorders: a structural magnetic resonance imaging study. *Am J Psychiatry* 161:1612-1619.
- Prins JR, Eskandar S, Eggen BJL, Scherjon SA (2018) Microglia, the missing link in maternal immune activation and fetal neurodevelopment; and a possible link in preeclampsia and disturbed neurodevelopment? *J Reprod Immunol* 126:18-22.
- Rasetti R, Sambataro F, Chen Q, Callicott JH, Mattay VS, Weinberger DR (2011) Altered cortical network dynamics: a potential intermediate phenotype for schizophrenia and association with ZNF804A. *Arch Gen Psychiatry* 68:1207-1217.
- Reichenberg A, Caspi A, Harrington H, Houts R, Keefe RS, Murray RM, Poulton R, Moffitt TE (2010) Static and dynamic cognitive deficits in childhood preceding adult schizophrenia: a 30-year study. *Am J Psychiatry* 167:160-169.
- Rein B, Yan Z (2020) 16p11.2 Copy Number Variations and Neurodevelopmental Disorders. *Trends Neurosci* 43:886-901.
- Ribiani E, Rosati A, Romanelli M, Cruciani L, Incalza F, Di Renzo GC (2007) Perinatal infections and cerebral palsy. *Minerva ginecologica* 59:151-157.
- Robertson CE, Ratai EM, Kanwisher N (2016) Reduced GABAergic Action in the Autistic Brain. *Curr Biol* 26:80-85.
- Rousset CI, Chalon S, Cantagrel S, Bodard S, Andres C, Gressens P, Saliba E (2006) Maternal exposure to LPS induces hypomyelination in the internal capsule and programmed cell death in the deep gray matter in newborn rats. *Pediatr Res* 59:428-433.
- Sachs NA, Sawa A, Holmes SE, Ross CA, DeLisi LE, Margolis RL (2005) A frameshift mutation in *Disrupted in Schizophrenia 1* in an American family with schizophrenia and schizoaffective disorder. *Mol Psychiatry* 10:758-764.
- Sargolini F, Fyhn M, Hafting T, McNaughton BL, Witter MP, Moser MB, Moser EI (2006) Conjunctive representation of position, direction, and velocity in entorhinal cortex. *Science* 312:758-762.
- Schizophrenia Working Group of the Psychiatric Genomics C (2014) Biological insights from 108 schizophrenia-associated genetic loci. *Nature* 511:421-427.
- Schomburg EW, Fernandez-Ruiz A, Mizuseki K, Berenyi A, Anastassiou CA, Koch C, Buzsaki G (2014) Theta phase segregation of input-specific gamma patterns in entorhinal-hippocampal networks. *Neuron* 84:470-485.

- Sekar A, Bialas AR, de Rivera H, Davis A, Hammond TR, Kamitaki N, Tooley K, Presumey J, Baum M, Van Doren V, Genovese G, Rose SA, Handsaker RE, Schizophrenia Working Group of the Psychiatric Genomics C, Daly MJ, Carroll MC, Stevens B, McCarroll SA (2016) Schizophrenia risk from complex variation of complement component 4. *Nature* 530:177-183.
- Sellgren CM, Gracias J, Watmuff B, Biag JD, Thanos JM, Whittredge PB, Fu T, Worringer K, Brown HE, Wang J, Kaykas A, Karmacharya R, Goold CP, Sheridan SD, Perlis RH (2019) Increased synapse elimination by microglia in schizophrenia patient-derived models of synaptic pruning. *Nat Neurosci* 22:374-385.
- Sheroziya MG, von Bohlen Und Halbach O, Unsicker K, Egorov AV (2009) Spontaneous bursting activity in the developing entorhinal cortex. *J Neurosci* 29:12131-12144.
- Siapas AG, Wilson MA (1998) Coordinated interactions between hippocampal ripples and cortical spindles during slow-wave sleep. *Neuron* 21:1123-1128.
- Siapas AG, Lubenov EV, Wilson MA (2005) Prefrontal phase locking to hippocampal theta oscillations. *Neuron* 46:141-151.
- Sigurdsson T, Duvarci S (2015) Hippocampal-Prefrontal Interactions in Cognition, Behavior and Psychiatric Disease. *Front Syst Neurosci* 9:190.
- Sigurdsson T, Stark KL, Karayiorgou M, Gogos JA, Gordon JA (2010) Impaired hippocampal-prefrontal synchrony in a genetic mouse model of schizophrenia. *Nature* 464:763-767.
- Sipila ST, Huttu K, Soltesz I, Voipio J, Kaila K (2005) Depolarizing GABA acts on intrinsically bursting pyramidal neurons to drive giant depolarizing potentials in the immature hippocampus. *J Neurosci* 25:5280-5289.
- Sipilä ST, Huttu K, Yamada J, Afzalov R, Voipio J, Blaesse P, Kaila K (2009) Compensatory enhancement of intrinsic spiking upon NKCC1 disruption in neonatal hippocampus. *J Neurosci* 29:6982-6988.
- Sirota A, Montgomery S, Fujisawa S, Isomura Y, Zugaro M, Buzsaki G (2008) Entrainment of neocortical neurons and gamma oscillations by the hippocampal theta rhythm. *Neuron* 60:683-697.
- Sohal VS, Rubenstein JLR (2019) Excitation-inhibition balance as a framework for investigating mechanisms in neuropsychiatric disorders. *Mol Psychiatry* 24:1248-1257.
- Spellman T, Rigotti M, Ahmari SE, Fusi S, Gogos JA, Gordon JA (2015) Hippocampal-prefrontal input supports spatial encoding in working memory. *Nature* 522:309-314.
- Spitzer NC (2006) Electrical activity in early neuronal development. *Nature* 444:707-712.
- Spratt PWE, Ben-Shalom R, Keeshen CM, Burke KJ, Jr., Clarkson RL, Sanders SJ, Bender KJ (2019) The Autism-Associated Gene Scn2a Contributes to Dendritic Excitability and Synaptic Function in the Prefrontal Cortex. *Neuron* 103:673-685 e675.
- Steinecke A, Gampe C, Valkova C, Kaether C, Bolz J (2012) Disrupted-in-Schizophrenia 1 (DISC1) is necessary for the correct migration of cortical interneurons. *J Neurosci* 32:738-745.
- Stiles J, Jernigan TL (2010) The basics of brain development. *Neuropsychol Rev* 20:327-348.
- Strange BA, Witter MP, Lein ES, Moser EI (2014) Functional organization of the hippocampal longitudinal axis. *Nat Rev Neurosci* 15:655-669.

- Stujenske JM, Spellman T, Gordon JA (2015) Modeling the Spatiotemporal Dynamics of Light and Heat Propagation for In Vivo Optogenetics. *Cell Rep* 12:525-534.
- Supèr H, Soriano E (1994) The organization of the embryonic and early postnatal murine hippocampus. II. Development of entorhinal, commissural, and septal connections studied with the lipophilic tracer Dil. *J Comp Neurol* 344:101-120.
- Suzuki WA, Amaral DG (1994) Topographic organization of the reciprocal connections between the monkey entorhinal cortex and the perirhinal and parahippocampal cortices. *J Neurosci* 14:1856-1877.
- Szczurkowska J, Cwetsch AW, dal Maschio M, Ghezzi D, Ratto GM, Cancedda L (2016) Targeted in vivo genetic manipulation of the mouse or rat brain by in utero electroporation with a triple-electrode probe. *Nat Protoc* 11:399-412.
- Takahashi M, Nishida H, Redish AD, Lauwereyns J (2014) Theta phase shift in spike timing and modulation of gamma oscillation: a dynamic code for spatial alternation during fixation in rat hippocampal area CA1. *J Neurophysiol* 111:1601-1614.
- Takahashi T, Nakamura M, Sasabayashi D, Komori Y, Higuchi Y, Nishikawa Y, Nishiyama S, Itoh H, Masaoka Y, Suzuki M (2018) Olfactory deficits in individuals at risk for psychosis and patients with schizophrenia: relationship with socio-cognitive functions and symptom severity. *Eur Arch Psychiatry Clin Neurosci* 268:689-698.
- Tamnes CK, Herting MM, Goddings AL, Meuwese R, Blakemore SJ, Dahl RE, Guroglu B, Raznahan A, Sowell ER, Crone EA, Mills KL (2017) Development of the Cerebral Cortex across Adolescence: A Multisample Study of Inter-Related Longitudinal Changes in Cortical Volume, Surface Area, and Thickness. *J Neurosci* 37:3402-3412.
- Tang W, Thevathasan JV, Lin Q, Lim KB, Kuroda K, Kaibuchi K, Bilger M, Soong TW, Fivaz M (2016) Stimulation of Synaptic Vesicle Exocytosis by the Mental Disease Gene DISC1 is Mediated by N-Type Voltage-Gated Calcium Channels. *Front Synaptic Neurosci* 8:15.
- Tau GZ, Peterson BS (2010) Normal development of brain circuits. *Neuropsychopharmacology* 35:147-168.
- Tort AB, Komorowski RW, Manns JR, Kopell NJ, Eichenbaum H (2009) Theta-gamma coupling increases during the learning of item-context associations. *Proc Natl Acad Sci USA* 106:20942-20947.
- Turetsky BI, Moberg PJ, Quarmley M, Dress E, Calkins ME, Ruparel K, Prabhakaran K, Gur RE, Roalf DR (2018) Structural anomalies of the peripheral olfactory system in psychosis high-risk subjects. *Schizophr Res* 195:197-205.
- Uher R (2014) Gene-environment interactions in severe mental illness. *Front Psychiatry* 5:48.
- Valeeva G, Tressard T, Mukhtarov M, Baude A, Khazipov R (2016) An Optogenetic Approach for Investigation of Excitatory and Inhibitory Network GABA Actions in Mice Expressing Channelrhodopsin-2 in GABAergic Neurons. *J Neurosci* 36:5961-5973.
- Valeeva G, Janackova S, Nasretidinov A, Rychkova V, Makarov R, Holmes GL, Khazipov R, Lenck-Santini PP (2019) Emergence of Coordinated Activity in the Developing Entorhinal-Hippocampal Network. *Cereb Cortex* 29:906-920.
- Vanderwolf CH (1969) Hippocampal electrical activity and voluntary movement in the rat. *Electroencephalogr Clin Neurophysiol* 26:407-418.
- Von Neumann J (1958) *The computer and the brain*. Yale University Press.
- Wang Q, Brandon NJ (2011) Regulation of the cytoskeleton by Disrupted-in-schizophrenia 1 (DISC1). *Mol Cell Neurosci* 48:359-364.

- Weinberger DR (1987) Implications of normal brain development for the pathogenesis of schizophrenia. *Arch Gen Psychiatry* 44:660-669.
- Welker WI (1964) Analysis of Sniffing of the Albino Rat. *Behaviour* 22:223–244.
- Wierenga LM, Langen M, Oranje B, Durston S (2014) Unique developmental trajectories of cortical thickness and surface area. *Neuroimage* 87:120-126.
- Wierzynski CM, Lubenov EV, Gu M, Siapas AG (2009) State-dependent spike-timing relationships between hippocampal and prefrontal circuits during sleep. *Neuron* 61:587-596.
- Witter MP (2010) "Connectivity of the Hippocampus". In: Cutsuridis V., Graham B., Cobb S., Vida I., *Hippocampal Microcircuits*. Springer Series in Computational Neuroscience Springer, New York.
- Witter MP, Wouterlood FG, Naber PA, Van Haefen T (2000) Anatomical organization of the parahippocampal-hippocampal network. *Ann N Y Acad Sci* 911:1-24.
- Witter MP, Doan TP, Jacobsen B, Nilssen ES, Ohara S (2017) Architecture of the Entorhinal Cortex A Review of Entorhinal Anatomy in Rodents with Some Comparative Notes. *Front Syst Neurosci* 11:46.
- Xu W, Wilson DA (2012) Odor-evoked activity in the mouse lateral entorhinal cortex. *Neuroscience* 223:12-20.
- Xu X, Song L, Hanganu-Opatz IL (2021) Knock-Down of Hippocampal DISC1 in Immune-Challenged Mice Impairs the Prefrontal-Hippocampal Coupling and the Cognitive Performance Throughout Development. *Cereb Cortex* 31:1240-1258.
- Xu X, Chini M, Bitzenhofer SH, Hanganu-Opatz IL (2019) Transient Knock-Down of Prefrontal DISC1 in Immune-Challenged Mice Causes Abnormal Long-Range Coupling and Cognitive Dysfunction throughout Development. *J Neurosci* 39:1222-1235.
- Yan J, Cui Y, Li Q, Tian L, Liu B, Jiang T, Zhang D, Yan H (2019) Cortical thinning and flattening in schizophrenia and their unaffected parents. *Neuropsychiatr Dis Treat* 15:935-946.
- Yang JW, Hanganu-Opatz IL, Sun JJ, Luhmann HJ (2009) Three patterns of oscillatory activity differentially synchronize developing neocortical networks in vivo. *J Neurosci* 29:9011-9025.
- Zhou M, Zhang F, Zhao L, Qian J, Dong C (2016) Entorhinal cortex: a good biomarker of mild cognitive impairment and mild Alzheimer's disease. *Rev Neurosci* 27:185-195.
- Zhou Y, Shu N, Liu Y, Song M, Hao Y, Liu H, Yu C, Liu Z, Jiang T (2008) Altered resting-state functional connectivity and anatomical connectivity of hippocampus in schizophrenia. *Schizophr Res* 100:120-132.
- Zick JL, Blackman RK, Crowe DA, Amirikian B, DeNicola AL, Netoff TI, Chafee MV (2018) Blocking NMDAR Disrupts Spike Timing and Decouples Monkey Prefrontal Circuits: Implications for Activity-Dependent Disconnection in Schizophrenia. *Neuron* 98:1243-1255 e1245.
- Zucker RS, Regehr WG (2002) Short-term synaptic plasticity. *Annu Rev Physiol* 64:355-405.

8 List of abbreviations

ACC	Anterior cingulate cortex
ADHD	Attention deficit hyperactivity disorder
AMPA	α -amino-3-hydroxy-5-methyl-4-isoxazole propionic acid
ANOVA	Analysis of variance
AP5	Amino-5-phosphonovaleric acid
ASD	Autism spectrum disorders
BDA	Biotin dextran amine
BLA	Basolateral amygdala
CA	Cornu ammonis
CAG	Cytomegalovirus enhancer fused to chicken beta-actin
CaMKII	Calcium calmodulin-dependent kinase 2
cGDP	Cortical giant depolarizing potentials
ChR2	Channelrhodopsin-2
ChR2(ET/TC)	Channelrhodopsin-2 E123T T159C
ChR2(H134R)	Channelrhodopsin-2 H134R
CLA	Clastrum
CNQX	6-cyano-7-nitroquinoxaline-2,3-dione
CNV	Copy number variants
CON	Controls
CTB	Cholera toxin subunit B
CV	Coefficient of variation
dACC	Dorsal anterior cingulate cortex
DAB	Diaminobenzidine
DAPI	4,6-diamidino-2-phenylindole
DG	Dentate gyrus
dHP	Dorsal hippocampus
DISC1	Disrupted in schizophrenia 1
DNA	Deoxyribonucleic acid
E	Embryonic
EC	Entorhinal cortex
EEG	Electroencephalography
E/I	Excitation-inhibition
ENOs	Early network oscillations
EPSC	Excitatory postsynaptic current
eSPW	Early sharp-wave complex
FG	FluoroGold
fMRI	Functional magnetic resonance imaging
GABA	gamma aminobutyric acid
GDPs	Giant depolarizing potentials
GE	Genetic-environmental challenged mice
G _{HP} E	DISC1 knockdown confined to HP in immune-challenged mice
GLM	Generalized linear model
gPDC	Generalized partial directed coherence
GWAS	Genome-wide association studies
HP	Hippocampus
HP-PFC	Hippocampal-prefrontal
i/vHP	Intermediate-ventral hippocampus
IL	Infralimbic cortex

IPSC	Inhibitory postsynaptic current
IUE	<i>In utero</i> electroporation
ISI	Inter-spike-interval
LEC	Lateral entorhinal cortex
LEC-HP-PFC	Lateral entorhinal-hippocampal-prefrontal
LFP	Local field potential
MD	Mediodorsal thalamus
MEC	Medial entorhinal cortex
MGE	Medial ganglionic eminence
MI	Modulation index
MIA	Maternal immune activation
mPFC	Medial prefrontal cortex
MS	Medial septal
NBQX	6-cyano-7-nitroquinoxaline-2, 3-dione
NMDA	N-Methyl-D-aspartic acid
NOR	Novel object recognition
NOPd	Novel object preference (distinct objects)
OB	Olfactory bulb
OF	Open field
OLP	Object-location preference
P	Postnatal
PBS	Phosphate buffered saline
PFA	Paraformaldehyde
PFC	Prefrontal cortex
PL	Prelimbic cortex
PLV	Phase locking value
PV	Parvalbumin
REM	Rapid eye movement
RR	Recency recognition
RSC	Retrosplenial cortex
sEPSC	Spontaneous excitatory postsynaptic current
SLM	Stratum lacunosum-moleculare
SNP	Single nucleotide polymorphisms
SNV	Single-nucleotide variants
SP	Stratum pyramidale
SPA	Synchronous plateau assemblies
SPWs	Sharp waves
SPW-Rs	Sharp waves-ripples complexes
STR	Striatum
SUA	Single unit activity
vGLUT1	Vesicular glutamate transporter 1
VM	Ventromedial thalamus
VTA	Ventral tegmental area
WGA	Wheat germ agglutinin

9 Acknowledgements

First of all, I would like to express my sincere gratitude to my supervisor Prof. Ileana L. Hanganu-Opatz, for providing me with the opportunity to do the doctoral degree within her group, for her support and availability, for tolerating and correcting my occasional mistakes in the laboratory and personal life. With her continuous supervision, I improved my skills in various aspects of scientific life to conduct research. I am also indebted to Prof. Michael Frotscher, who accepted me as his co-worker, and the China Scholarship Council (CSC), who awarded me the stipend, which enabled my study in Hamburg. Moreover, I also would like to thank the other members of my thesis committee involving Prof. Marc Spehr and Prof. Dietmar Kuhl, for their valuable time.

I am particularly grateful to Dr. Xiaxia Xu for patiently tutoring me in *in vivo* electrophysiology and data analysis, for always available for helpful discussions of the experiments. I also would like to thank all of the other current and former colleagues from "OpatzLab" who shared their knowledge, experience and many beautiful moments throughout the last 4 years. In particular, they are Mattia, Steven, Johanna, Marilena, Yunan, Henrik, Jastyn, Joachim, Sebastian and Sabine. Special thanks to Dr. Sebastian Bitzenhofer for translating the "General Summary" into German. I am thankful for the support I received from Peggy, Annette and Achim, outstanding technicians whose contributions were invaluable to this thesis. I wish to thank my co-authors for their contributions to the studies.

Finally, I wish to thank my family and boyfriend for their loving and unconditional support, interest and encouragement. Communication via social media never weakens our bonding.

10 Curriculum Vitae

2017 – 2021: PhD student at Institute of Developmental Neurophysiology, Center for Molecular Neurobiology, University Medical Center Hamburg-Eppendorf, Hamburg, Germany.

2015 – 2017: Associate research specialist at Institute of Structural Neurobiology, Center for Molecular Neurobiology, University Medical Center Hamburg-Eppendorf, Hamburg, Germany.

2012 – 2015: Master of Science, College of Veterinary Medicine, Northwest A&F University, Shaanxi, China.

2008 – 2012: Bachelor of Science, College of Life Science, Shandong Agricultural University, Shandong, China.

Publications and Reprints

X Xu¹, **L Song**¹, IL Hanganu-Opatz. Knock-down of hippocampal DISC1 in immune-challenged mice impairs the prefrontal–hippocampal coupling and the cognitive performance throughout development. *Cerebral Cortex*, (2021) 31: 1240-1258

L Song¹, X Xu¹, P Putthoff, D Fleck, M Spehr, IL Hanganu-Opatz. Sparser and less efficient projections from hippocampus to prefrontal cortex account for network dysfunction in a mouse model with schizophrenialike etiology. *The Journal of Neuroscience*, (2021) Revision.

X Xu, **L Song**, R Kringel, IL Hanganu-Opatz. Developmental decrease of entorhinal gate disrupts prefrontal-hippocampal communication in immune-challenged DISC1 knockdown mice. *Nature Communication*, (2021). Revision, DOI: 10.21203/rs.3.rs-290304/v1

J Ahlbeck, **L Song**, M Chini, SH Bitzenhofer, IL Hanganu-Opatz. Glutamatergic drive along the septotemporal axis of hippocampus boosts prelimbic oscillations in the neonatal mouse. *eLife*, (2018) 7:e33158

K Li, X Cheng, J Jiang, J Wang, J Xie, X Hu, Y Huang, **L Song**, M Liu, L Cai, L Chen, S Zhao. The toxic influence of paraquat on hippocampal neurogenesis in adult mice. *Food Chem Toxicol*, (2017) 106(Pt A):356-366

X Chai, S Zhao, L Fan, W Zhang, X Lu, H Shao, S Wang, **L Song**, AV Failla, B Zobiak, HG Mannherz, M Frotscher. Reelin and cofilin cooperate during the migration of cortical neurons: a quantitative morphological analysis. *Development*, (2016) 143(6):1029-40

11 Eidesstattliche Versicherung

Ich versichere ausdrücklich, dass ich die Arbeit selbständig und ohne fremde Hilfe verfasst, andere als die von mir angegebenen Quellen und Hilfsmittel nicht benutzt und die aus den benutzten Werken wörtlich oder inhaltlich entnommenen Stellen einzeln nach Ausgabe (Auflage und Jahr des Erscheinens), Band und Seite des benutzten Werkes kenntlich gemacht habe.

Ferner versichere ich, dass ich die Dissertation bisher nicht einem Fachvertreter an einer anderen Hochschule zur Überprüfung vorgelegt oder mich anderweitig um Zulassung zur Promotion beworben habe. Ich erkläre mich einverstanden, dass meine Dissertation vom Dekanat der Medizinischen Fakultät mit einer gängigen Software zur Erkennung von Plagiaten überprüft werden kann.